EXPERIMENTAL AND NUMERICAL STUDY OF SYNGAS COMBUSTION

BY

SANUSI YINKA SOFIHULLAHI

A Dissertation Presented to the

DEANSHIP OF GRADUATE STUDIES

KING FAHD UNIVERSITY OF PETROLEUM & MINERALS

DHAHRAN, SAUDI ARABIA

In Partial Fulfillment of the

Requirements for the Degree of

DOCTOR OF PHILOSOPHY

In

MECHANICAL ENGINEERING

MAY, 2015

KING FAHD UNIVERSITY OF PETROLEUM & MINERALS

DHAHRAN- 31261, SAUDI ARABIA

DEANSHIP OF GRADUATE STUDIES

This dissertation, written by **SANUSI YINKA SOFIHULLAHI** under the direction of his dissertation advisor and approved by his dissertation committee, has been presented and accepted by the Dean of Graduate Studies, in partial fulfillment of the requirements of **DOCTOR OF PHILOSOPHY IN MECHANICAL ENGINEERING.**

Dr. Esmail M. A. Mokheimer
(Advisor)

Dr. Zuhair M. Gasem
Department Chairman

Dr. Mohamed A. Habib
(Co-Advisor)

Dr. Salam A. Zummo
Dean of Graduate Studies

Dr. Ahmed F. Ghoniem (MIT)
(Member)

2/7/15
Date

Dr. Syed A. M. Said
(Member)

Dr. Amro M. Al-Qutub
(Member)

DEDICATION

قُلْ إِنَّنِي هَدَانِي رَبِّي إِلَىٰ صِرَاطٍ مُّسْتَقِيمٍ دِينًا قِيَمًا مِّلَّةَ إِبْرَاهِيمَ حَنِيفًا ۚ وَمَا كَانَ مِنَ الْمُشْرِكِينَ (١٦١)

قُلْ إِنَّ صَلَاتِي وَنُسُكِي وَمَحْيَايَ وَمَمَاتِي لِلَّهِ رَبِّ الْعَالَمِينَ (١٦٢)

لَا شَرِيكَ لَهُ ۖ وَبِذَٰلِكَ أُمِرْتُ وَأَنَا أَوَّلُ الْمُسْلِمِينَ (١٦٣)

(161) Say (O Muhammad صلى الله عليه وسلم): "Truly, my Lord has guided me to a Straight Path, a right religion, the religion of Ibrahim (Abraham), Hanifa [i.e. the true Islamic Monotheism - to believe in One God (Allah i.e. to worship none but Allah, Alone)] and he was not of Al-Mushrikun."

(162) Say (O Muhammad صلى الله عليه وسلم): "Verily, my Salat (prayer), my sacrifice, my living, and my dying are for Allah, the Lord of the 'Alamin (mankind, jinn and all that exists).

(163) "He has no partner. And of this I have been commanded, and I am the first of the Muslims."

--Sooratul-An’aam, 161 – 163

ACKNOWLEDGMENTS

All praise and thanks are due to Almighty Allah for his mercy and guidance throughout my Ph.D. program. My gratitude goes to the authority of KFUPM for giving me the privilege to do my Ph.D. studies and funding my research through the center for clean water and clean energy, as well as funding my research visit to MIT.

I am also grateful to the authority of Ahmadu Bello University, Zaria for granting me study fellowship.

I would like to express my profound gratitude and deep regard to my dissertation advisor, Dr. Esmail Mokheimer for his guidance and support throughout this research work. I thank him for his patience, motivation, enthusiasm, insightful comments and mentorship during the research and dissertation writing. I also appreciate his effort in facilitating my visit to MIT. Special thanks to my co-advisor Dr. M.A. Habib for his continuous supervision, fruitful discussions and important ideas in the course of this work. I am indeed grateful to Dr. A. F. Ghoniem for his immense contribution towards the completion of this research by giving me the privilege to visit and work in his lab. Special thanks to Dr. S.A.M. Said and Dr. Amro M. Al-Qutub for their immense contributions to my research work.

I would like to acknowledge the assistance of Mr. Karam in setting up the experiment, Dr. Santosh, Soufiene, Zach and John for their assistance and for answering my many questions during my visit to MIT. I will also like to acknowledge my colleagues in KFUPM especially Fahad Al-Zahrahani and other members of the combustion research group.

My deepest thanks, love and gratitude goes to all my family especially my parents for their prayer, encouragement and support. Extraordinary thanks to my wife Anike and my lovely kids, Abdulsalam, Abdulmujeeb and Sakeenah. Thank you for your love, patience and understanding.

I would also like to say thank you to all my friends and member of the Nigeria community in KFUPM for their concern and advice throughout my study.

Thank you all for making my Ph.D. a reality!!!

TABLE OF CONTENTS

LIST OF TABLES

LIST OF FIGURES

LIST OF ABBREVIATIONS

CFD	Computational fluid dynamics
EDC	Eddy-dissipation-concept
FFT	Fast Fourier transform
ISAT	In situ adaptive tabulation
LBO	Lean blow off
LBV	Lean blow off velocity
LHV	Lower heating value
MW	Mega watts
$OASPL$	Overall sound pressure level
PLIF	Planar Laser Induced Fluorescence
PPM	Part per million
PIV	Particle image velocimetry
PV	Photovoltaic
PVC	Precessing vortex core
SG	Specific gravity
SMR	Steam methane reforming
SPL	Sound pressure level
Syngas	Synthetic gas
TRI	Turbulence–radiation interactions
UNFCCC	United Nations framework convention on climate change
WI	Wobbe index
WSGGM	Weighted sum of gray gas model

LIST OF SYMBOLS

a_i	Blackbody radiation fraction
b	Temperature exponent
c	speed of sound (m/s)
CO	Carbon monoxide
CO_2	Carbon dioxide
C_p	specific heat at constant pressure (J/kgK)
$D_{j,m}$	diffusion flux of specie j (m^2/s)
E_a	Activation energy (kJ/kmolK)
f	Frequency (Hz)
G_k	Turbulence production energy (J/m^3s)
H_2	Hydrogen gas
$H(f)$	Heaviside function
I^*	amplitude of the normalized intensity
I (t)	integrated intensity over a time interval
k	Turbulent kinetic energy (m^2/s^2)
k_i	Wave number(m^{-1})
K_r	Rate constant (m^3/s)
k_q	Thermal conductivity (W/mK)
m	Unit of length
M	Mach no
NOx	Nitrogen oxide
P_{CO_2}	Partial pressure of carbondioxide
P_{H_2o}	Partial pressure of water
P'	sound pressure at the far field (N/m^2)
P(t)	pressure measured over a time interval (N/m^2)
$\hat{P}_i$	Pressure magnitude (N/m^2)
P_{ij}	the compressive stress tensor (N/m^2)
$\dot{q}'$	un-steady heat release (W)
R_j	species equation source term (kg/m^3s)
S_i	cross sectional area (m^2)
S	radiation beam length
$S_\emptyset$	energy source term (W/m^3)
t	Time (s)
t_{ij}	Viscous stress tensor (N/m^2)
T_{ij}	Lighthill stress tensor (N/m^2)
T	Temperature (K)
T_b	burned gas temperature (T)
T_u	unburned gas temperature (T)

T_w	Wall temperature (T)
T_a	ambient temperature (T)
u'	velocity perturbation (m/s)
u_i	Fluid velocity component in the x_i (m/s)
u_n	Fluid velocity normal to the surface (m/s)
$\hat{u}_i$	Velocity magnitude (m/s)
v_i	surface velocity components in the x_i direction (m/s)
v_n	surface velocity normal to the surface (m/s)
x	Distance (m)
Y_j	Mass fraction of specie j

Greek symbols

α_s	swirl constant
$\delta(f)$	Dirac delta function
ε	Turbulent dissipation rate (m^2/s^3)
ϵ	Emissivity
μ	dynamic viscosity (Ns/m^2)
μ_t	turbulent viscosity (Ns/m^2)
ω	angular frequency (rad/s)
Ø	Equivalence ratio
ρ	Density (kg/m^3)
τ	phase delay
$\tau^*.$	time scale (s)
θ_{qp}	phase angle
∩	characteristics swirl number

ABSTRACT

Full name : SANUSI YINKA SOFIHULLAHI

Dissertation title : Experimental and Numerical Study of Syngas Combustion

Major Field : Mechanical Engineering

Date of degree : May 2015

The electricity consumption in Saudi Arabia increased continuously in the last two decades. This trend is expected to continue due to increase in population and industrialization. Most of the power plants in Saudi Arabia are currently operated by fossil fuel (oil and gas), with 46 % of its (Saudi Arabia) power generated using gas turbines. The Saudi authority is set to meet its ever increasing power requirement by 2020 via renewable energy sources. This will free up oil and natural gas that are burned cheaply for export. Areas being targeted include the use of abundant solar energy to produce syngas fuel by solar steam methane reforming. The syngas produced, could have increased energy level by up to 30% per unit volume of methane. Syngas produced via solar methane reforming are, however, susceptible to mixture variation. Hence, fuel-flexible combustor becomes imperative. Thus, the aim of this study is to investigate experimentally and numerically two different swirl stabilized combustors: premixed and non-premixed combustor. Different mixtures of methane (CH_4) and hydrogen (H_2) are used as the characteristic syngas. In non-premixed combustor, the effect of hydrogen enrichment of methane on the combustion characteristics and emissions were studied at different operating conditions (fuel energy inputs and equivalence ratio). The addition of 30% hydrogen extends the lean blow off regime of the combustor by ~103%. The

extended lean blow off of hydrogen-enriched methane was explored to achieve zero NOx emission. This is critical towards achieving zero NOx emission power plants (ZEPP). The premixed swirl combustor was experimentally studied to show the dependence of hydrogen on the thermo-acoustic instability. The heat release and the pressure oscillation were observed to be positively coupled, with the instabilities triggered at maximum coupling (θ_{qp} approaches zero). Similar flame shapes were observed at the same extinction strain rate (irrespective of the CH_4/H_2 mixture) and linked to the instability in the combustor. The collapse of the overall sound pressure level (OASPL) and phase data with the extinction strain rates suggest that the stability of the combustor and its acoustic foot print for different operating conditions can be encapsulated in a single parameter (extinction strain rate). This implies that the dynamic state (instabilities) of the combustor can be determined for any arbitrary change in fuel.

In the second part of the work, a numerical model was developed and validated using the temperature, carbon dioxide and NOx emissions data obtained in the non-premixed combustor. A Modified-2sCM2 mechanism, proposed in this study, gave good predictions of the combustor temperature, major species and NOx emissions. Numerical results further show that there exists an equivalence ratio where the emissions (CO and NOx) from the combustor are optimum for any given fuel composition. The numerical model developed was further used to investigate the combustion of different syngas (CO/H_2) compositions in a 200 MW package boiler. Among the tested syngas compositions, 50% CO: 50% H_2 syngas had the lowest emissions with the best combustion characteristics. The NOx emission decreased by approximately 30% when the amount of excess air supplied was increased from 5% to 25%.

ABSTRACT (*ملخص الرسالة*)

الاسم الكامل: **سنوسي يانكا صفي الله**

عنوان الرسالة: **دراسة تجريبية وعددية لاحتراق الغاز المصنع**

التخصص: **هندسة ميكانيكية**

تاريخ الدرجة العلمية: **مايو 2015**

تزايد استهلاك الكهرباء في المملكة العربية السعودية زيادة مستمرة في العقدين الماضيين. ومن المتوقع أن يستمر هذا الاتجاه في زيادة استهلاك الطاقة الكهربية نظرا لزيادة عدد السكان والتصنيع في المملكة. وتعمل معظم محطات توليد الكهرباء في المملكة العربية السعودية في الوقت الراهن بالوقود الأحفوري (النفط والغاز)، علما بأن 46٪ من الطاقة الكهربية المنتجة في المملكة العربية السعودية يتم توليدها باستخدام توربينات الغاز. ولذلك تعمل السلطات السعودية على تلبية متطلبات الطاقة المتزايدة بحلول عام 2020 عن طريق مصادر الطاقة المتجددة. هذا سيوفر النفط والغاز الطبيعي الذي يتم حرقه للتصدير. وتشمل التطبيقات المستهدفة لاستخدام الطاقة الشمسية الوفيرة إنتاج الوقود الغازي المصنع من إعادة تشكيل الميثان (الغاز الطبيعي) باستخدام الطاقة الشمسية والبخار. إن الغاز المصنع المنتج بهذه الطريقة تزيد الطاقة الناتجة عند حرقه بنسبة تصل إلى 30٪ لكل وحدة حجم من غاز الميثان (الغاز الطبيعي) مقارنة بالميثان (الغاز الطبيعي) المستخدم. لكن الغاز المصنع عن طريق الطاقة الشمسية معرض لتغير تركيبه الكيميائي مع تغير الطاقة الشمسية المتاحة. وبالتالي، يصبح الاحتراق المرن للوقود حتمي. وبالتالي، فإن الهدف من هذه الدراسة إجراء تجارب معملية وعددية لدراسة الاحتراق المخلوط مع الهواء وغير المخلوط. و لقد تم في هذه الدراسة تمثيل الغاز المصنع باستخدام خليط من الميثان (CH_4) والهيدروجين (H_2) بنسب مختلفة. في الاحتراق غير المخلوط، تم دراسة تأثير نسب خلط الهيدروجين مع غاز الميثان على خصائص الاحتراق والانبعاثات في ظروف تشغيل مختلفة (مدخلات الطاقة من الوقود ونسبة التكافؤ). ولقد وجد أن إضافة 30٪ هيدروجين توسع مدى استقرار نظام الاحتراق بنسبة تقارب ~ 103٪ مع تحقيق الانبعاثات الصفرية لأكاسيد النيتروجين. هذا أمر بالغ الأهمية من أجل منع انبعاثات أكاسيد النيتروجين من محطات الطاقة. وقد تم تجريبيا دراسة الاحتراق المخلوط في نظام احتراق يحتوي على باعث دوامات (swirler) وذلك لإظهار اعتماد عدم الاستقرار الصوت-حراري للهب على نسب الهيدروجين في خليط الوقود الصناعي. وقد لوحظت العلاقة الطردية بين إطلاق النار وتذبذب الضغط الصوتي. وقد لوحظت أشكال مماثلة اللهب عند نفس معدل التمدد (بغض النظر عن نسب خليط CH_4 / H_2) كما تم التمكن من تمثيل تأثير مجموعة من المتغيرات في نظام الاحتراق بمعامل واحد وهو معدل التمدد مما يمكننا بسهولة من تحديد مدى الاستقرار الديناميكي لنظام الاحتراق بناءا على نوع الوقود.

في الجزء الثاني من العمل، قد تم تطوير نموذج عددي والتحقق من صحته بمقارنة درجات الحرارة، بيانات انبعاثات ثاني أكسيد الكربون وأكاسيد النيتروجين التي تم الحصول عليها الدراسة التجريبية لنظام الاحتراق الغير مخلوط التي تم لإجرائها سابقا. A آلية sCM22 .إن أنموذج الاحتراق 2sCM2-المعدل و المقترح في هذه الدراسة، أعطى توقعات جيدة لدرجة حرارة الاحتراق، والأنواع الرئيسية وانبعاثات أكاسيد النيتروجين. كما تظهر النتائج العددية أيضا أنه يوجد نسبة تكافؤ مثالية للاحتراق حيث انبعاثات (أول أكسيد الكربون وأكاسيد النيتروجين) من الاحتراق هي المثلى لتكوين أي وقود معين. كما تم أيضا استخدام النموذج العددي الذي تم تطويره في دراسة احتراق الوقود المصنع في مرجل بخاري سعة 200 ميغاواط مع تغيير نسب وجود (CO / H_2) في الوقود المصنع و لقد وجد أن أفضل تركيب للغاز المصنع هو خليط (50% CO: 50% H_2). وقد لوحظ أيضا أن انبعاث أكاسيد النيتروجين ينخفض بنحو 30٪ عند زيادة كمية الهواء الزائد من 5٪ إلى 25٪.

CHAPTER 1

INTRODUCTION

The world total electricity consumption in 2009 is estimated at 20,132TWh [1]. World electricity demand is expected to grow by about 56 percent between 2010 and 2040 [2]. The expected increase in electricity demand will be produced mainly by fossil fueled power plant. Gas turbines are the most widely-used technologies for generating electricity. Most of gas turbines are run on natural gas which has methane (CH_4) as its main component. The emissions from gas turbine combustor are mainly carbon dioxide (CO_2) and water vapor, but it may also contain carbon monoxide (CO), nitric oxide (NOx) and un-burned hydrocarbon. The continuous increase in the emission of greenhouse gases from the combustion of natural gas has been of great concern to the international community. The United Nations Framework convention on climate change (UNFCCC) is attempting to achieve stabilization of greenhouse gas (CO_2) concentrations to avert the threats of serious or irreversible climate damage [3]. This is in line with Kyoto protocols that have similarly reiterated the need for reduction in greenhouse gases. Researchers have estimated that the marginal damage costs of carbon dioxide emissions are on average of $93/ton of C [4]. The greenhouse gas stabilization can be achieved through drastic reduction and control of global CO_2 emissions. Reductions in CO_2 emissions when confronted with increasing power requirements can

be achieved by the gradual replacement of methane with carbon-less fuel such as hydrogen (H_2) as well as exploitation of renewable energy sources. There is also increasing stringent regulations on pollutant emissions especially NOx from power plants. Operating the combustors under a lean-premixed condition has been previously reported to lower the combustor temperature and thus, reduces NOx emission. Lean premixed combustors are, however, susceptible to thermo-acoustic instabilities [5-7]. The instabilities in the combustor can lead to severe structural damage. In addition to environmental concerns, the increase in energy consumption is expected to match the expected population and economic growth. This will lead to rapid depletion in the fossil fuel deposit and future energy crisis if other energy sources are not explored. Therefore, harnessing power through renewable sources which are sustainable and environmental friendly becomes imminent. The Saudi Arabia authority is also worried by its persistence increase in its energy consumption. Figure 1.1 shows that the peak load of electricity consumed in Saudi Arabia increases by nearly 100% within a decade. The electricity peak load is forecasted to increase by more than 150% within 2005 to 2020 time frame (Fig. 1.2).

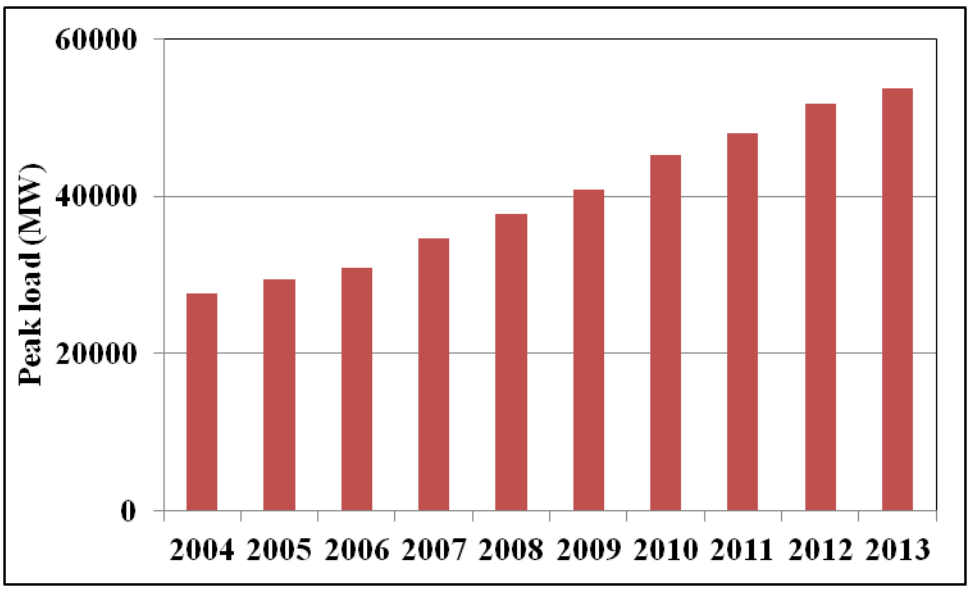

Figure 1.1: The peak load of electricity consumption in Saudi Arabia [8].

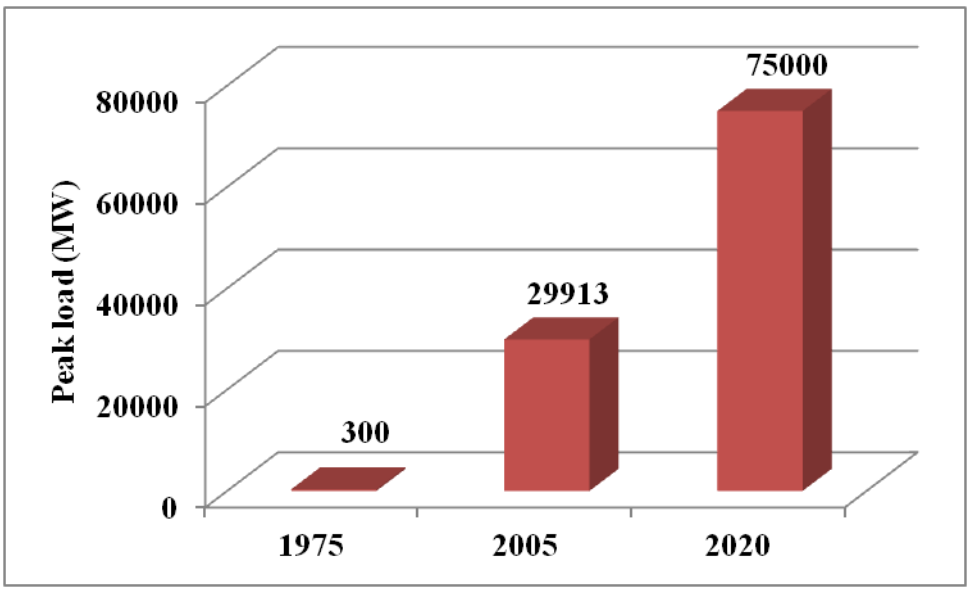

Figure 1.2: Electricity consumption trend in Saudi Arabia [8].

Currently, Saudi Arabia produced most of its electric power using fossil fuel (oil and gas) and about 46 % of the electricity produced in Saudi Arabia is from gas turbine power

plants [9]. This implies that increased energy demand means more fuels will be burned. This will lead to cheap burning of oil and gas that ought to be used in earning foreign income as well as increasing the emission of greenhouse gases. In order to stem the trend, the Saudi authority has set a goal of producing almost half of its power through clean energy solutions (renewable fuels) by 2020. The abundant solar energy, in excess of 3.61–7.96 kWh/m^2 [10] monthly average daily solar global radiation intensity, will be used to meet domestic power needs. This will free up oil and natural gas hitherto used for export. This approach is a sustainable and environmental friendly means of generating electricity. Under the Saudi green energy program, the government plans to invest about $109 billion to create a solar industry that will generate a third of its electricity by 2032 [11]. Currently, about three megawatts of solar power plants are working in Saudi Arabia. In addition, the Saudi government is embarking on solar power plant (PV) of nearly 100 MW in the city of Makah [12]. The King Abdullah City for Atomic and renewable energy is also mandated to build 41,000 MW of power from renewable energy over the next two decades [12]. Other area being targeted by the intervention plan is in the solar hybrid system and solar methane reforming for the production of synthetic (syngas) gas.

1.1 Syngas Fuel

Syngas primarily consist of carbon monoxide and hydrogen, and may also contain carbon dioxide. Syngas are mostly produced by the reforming of natural gas or biomass gasification. Syngas are produced by steam methane reforming as given in Eq. 1.1 [13]

$$\boldsymbol{CH_4 + H_2O \leftrightarrow CO + 3H_2} \qquad \boldsymbol{\Delta H_{298} = 206 kJ/mol} \qquad (1.1)$$

Reforming reactions is strongly endothermic, so the forward reaction is favored by high temperatures and low pressures. Syngas produced from steam methane reforming (SMR) consist of varying proportion of carbon monoxide (CO) and hydrogen (H_2) and may also contain methane (CH4) depending on its conversion efficiency. The syngas produced from this method will have enhanced fuel energy from an approximately 31.4MJ/m^2 (methane) to about 40.8MJ/m^2 of methane. This representing about 30% increase in fuel energy level. The steam required for this process can be generated from solar energy there by converting solar thermal energy to chemical energy of the fuel. The continuous variation in solar radiation through the day and across the year will have strong effect on the syngas conversion efficiency and resulting fuel thermal energy. When the syngas produced by SMR is integrated to gas turbine in an in-situ operation, the fuel variation will affect the heat release rate, emissions and stability of the combustor. Most of the conventional gas turbines are designed to operate within 5% Wobbe index [14]. The Wobbe index (WI) is the measure of amount of energy delivered to the burner. It is also an indicator of the interchangeability of fuel gases from the designed fuel. Wobbe index is calculated as;

$$\boldsymbol{Wobbe\ index} = \frac{\boldsymbol{LHV}}{\sqrt{\boldsymbol{SG}}} \tag{1.2}$$

Where LHV is the lower heating value and SG is the specific gravity of the fuel relative to air.

The interchangeability of fuel or variation in fuel compositions will have significant effect on the corresponding heating values. Thus, the design of flexible burner that will accommodate more variation in the Wobbe index is still an active research area.

1.2 Motivation of the Study

Saudi Arabia is blessed with abundant solar energy and natural gas. The abundant solar energy can be use for producing syngas via steam methane reforming technology. This is in line with the Saudi government green energy programs. According to the program, they plan to generate one-third of their electricity requirements by 2032 from renewable sources (majorly solar) [11]. The syngas produced could be used to power gas turbines or boilers (in the case of steam turbines) for electricity generation. Syngas, however, have varying compositions and/or heating values depending on the prevailing conditions. The variation in the operating conditions of the combustor will significantly affect the combustor stability and emissions. This could lead to severe structural damage in the combustor and increase pollutant emission beyond the acceptable limit. Understanding the effects of fuel energy level and changing composition of fuel deliver to the burner on the flame structure, stability and emissions is critical towards designing a fuel-flexible combustor. In addition, water tube package boilers are widely used for steam generation in powering steam turbines and other industrial applications. It is therefore imperative to understand the performance of water tube boilers when fired by syngas of different compositions.

1.3 Objective

The aim of the present work is to experimentally and numerically study the combustion characteristics, stability and emissions in swirl combustors using syngas fuel of different compositions. The following are the specific objectives:

1. To investigate the effects of different fuel energy levels and fuel compositions on the combustion characteristics and emission in a non-premixed swirl stabilized (a model gas turbine) combustor using methane and hydrogen as the characteristics syngas.
2. To identify distinct operating modes in a premixed combustor and characterize the thermo-acoustic instabilities for different methane / hydrogen fuel mixtures.
3. To develop a numerical model to simulate the observed flame characteristics and emission observed in the model combustor.
4. To investigate the combustion characteristics of syngas (CO/H_2) composition in 200 MW package boiler.

1.4 Methodology

In this section, the procedure used in achieving the dissertation objectives is outlined as follows:

1. Experiments were performed in a non-premixed combustor at different fuel energy inputs (0.92-4.59 MW/m^3) and hydrogen contents (0-50% H_2) in CH_4/H_2 mixtures, under ultra-lean conditions ($Ø \leq 0.5$). The equivalence ratio sweep test was carried out to determine the lean blow off (LBO) limit. Temperatures along the combustor axis and the emissions at the combustor exit were recorded.
2. The equivalence ratio sweep tests were also carried out in a premixed swirl stabilized combustor at different methane and hydrogen fuel compositions. The dynamic pressure and Chemiluminescence intensity were recorded at each

equivalence ratio. Instantaneous and global images of the flames were also taken at all operating conditions.

3. A numerical model was developed to simulate the observed flame characteristics and emission observed in the non-premixed model combustor using ANSYS Fluent 14. The numerical model was used to carry out parametric studies on the effect of swirl number and wall boundary conditions on the emissions from the combustor.
4. The numerical model was used to investigate the combustion characteristics and emissions in a 200 MW package boiler fired by different syngas (CO/H_2) compositions of 25% CO/75% H_2, 50% CO/50% H_2, 75% CO/25% H_2 and compared to a base case of 100% CH_4.

1.5 Dissertation Structure

This dissertation is divided into seven chapters:

Chapter 1 includes the introduction, objectives and the methodology used in achieving the dissertation objectives**.**

Chapter 2. A comprehensive review of previous work on the effect of different fuel compositions on the combustion characteristics, emissions and the thermo-acoustic instability were discussed in this chapter. The later part of the chapter explained the numerical approach used in the combustion modeling. The basic equations, turbulence model, combustion model and chemical mechanisms used were also discussed.

In **chapter 3,** the experimental setup and conditions used in studying the combustion of hydrogen-enriched methane at different fuel energy inputs in a non-premixed combustor

as well as the obtained results were discussed. The focus in this chapter is on the combustion characteristics and emissions.

The effect of different fuel compositions (H_2/CH_4) on the onset of the thermo-acoustic instabilities was presented in **chapter 4**. The equivalence ratio sweep tests were performed in a premixed combustor. The dynamic pressure, heat release and Chemiluminescence images were used to identify distinct operating modes in the combustor.

Results of numerical simulations carried out in a model gas turbine combustors were discussed in **chapter 5**. Three Different chemical mechanisms for methane combustion were first compared and a Modified two-step mechanism of methane for use under ultra-lean conditions was proposed. Parametric studies on the effect of wall boundary conditions and swirl numbers were also reported.

The numerical investigation on the use of different syngas compositions in a 200 MW package boiler is presented in **chapter 6**. The effect of excess air on the emissions from the boiler is also reported in this chapter.

The conclusions that highlight the key findings in this work and recommendations for future work are reported in **chapter 7.**

CHAPTER 2

LITERATURE REVIEW

2.1 Type of Flames

Burners are classified based on how the fuel and oxidizer are mixed. Burners can, thus, be classified as a premixed, on premixed or partially premixed burner. Figure 2.1 shows a schematic diagram to illustrate different kinds of burner arrangements.

2.1.1 Premixed Flames

In a premixed flame, the fuel and the oxidizer are mixed at the molecular level prior to the occurrence of any significant chemical reaction (combustion begins). Combustion occurs as flame front propagates into the unburned reactants. Premixed flames are shorter and more intense than non-premixed flames. They are susceptible to combustion instability, flashback, and blow off. Premixed flames, however, eliminate the local hotspot observed in a non-premixed combustor, thus, reducing the tendency of high NOx formation.

2.1.2 Non-Premixed Flames

Non-premixed burners are generally referred to as diffusion burner. In a non-premixed burner, the fuel and oxidizers are separated and unmixed prior to combustion. The reactions occur only at the interface between the fuel and the oxidizer where the mixing and reactions both take place. Non-premixed flames are limited by the rate of molecular diffusion of the fuel and oxidizer to the flame front. Thus, time is needed for convection

and diffusion, both being responsible for turbulent mixing is typically much larger than the time needed for combustion reactions to occur. Non-premixed burner can be found in furnace and some gas turbine applications. The non-premixed gas turbine combustors show more stability in operation than other type of combustor.

2.1.3 Partially-Premixed Flames

Partially premixed burners combine the properties of both the premixed and non-premixed flames. In partially premixed burner, some fraction of the fuel is pre mixed with the oxidizer prior to combustion. Partially premixed takes different forms such as

a) when an additional oxidizer or fuel stream enters a premixed system
b) when a diffusion flame becomes lifted off the burner so that some premixing takes place prior to combustion
c) lean premixed combustors with diffusion pilot flames and/or cooling air jets
d) those with imperfectly mixed inlet flows premixed jets
e) discharging into a quiescent atmosphere

partially premixed is often used for stability and safety reasons because it helps anchor the flame but also reduces the chance of flash back, which is sometimes a problem in fully premixed burners.

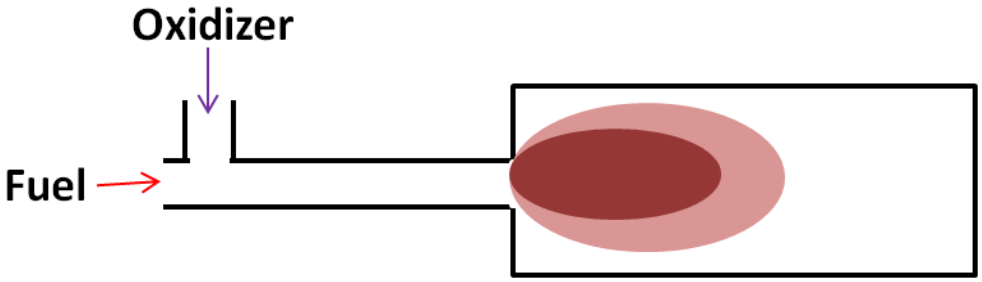

a) Premixed burner

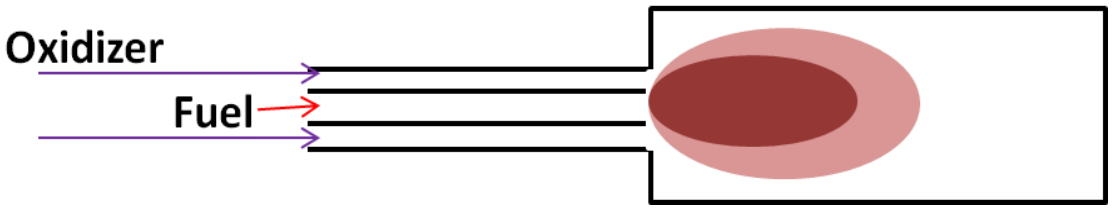

b) Non Premixed burner

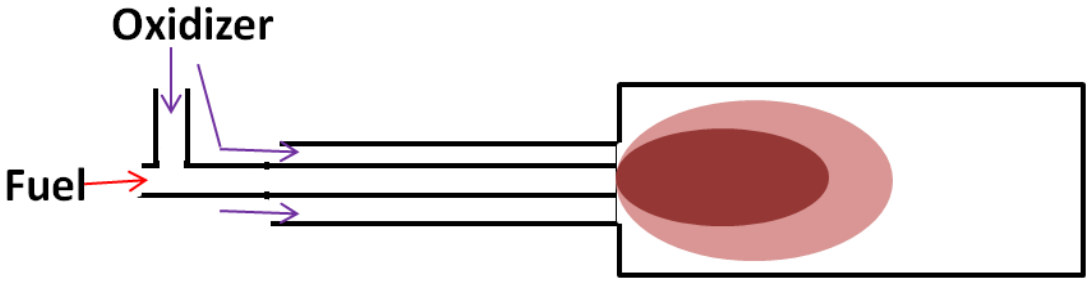

c) Partially Premixed burner

Figure 2.1 : Schematic diagram of different types of burner [15]

2.2 Syngas Combustion

Synthesis gas (syngas) is an environmentally clean fuel and has the potential to become a major fuel toward the near zero pollutant emissions. The use of syngas as a fuel is in line with meeting the ever-increasing stringent environmental policy. Syngas has also been adjudged a potential energy source for the future due to its wide availability as a product of biofuel and fossil fuel gasification [16], as well as a product of methane reforming.

Syngas can be produced by steam methane reforming process. The steam required for this process can be generated from solar energy, thereby converting solar thermal energy into chemical energy of the fuel. The continuous variations in solar radiation through the day and across the year as well as absence of solar radiation at night will have strong effects on the syngas conversion efficiency and the resultant fuel thermal energy. This affects the heat release rate, emission characteristics and stability of the flame making pilot study necessary. Syngas has been successfully used and proved to be beneficial in commercial plants. Several studies have been carried out with focus on the emissions from syngas combustion. Gadde et al. [17] carried out extensive testing on SGT6-5000F combustion system over a range of syngas fuels and achieved NOx and CO emissions of less than 15 PPM and 10 PPM, respectively, over the expected load range. They also observed less than 5 PPM NOx and less than 1 PPM CO emissions when syngas are tested on SGT5-4000F combustion system which shows improvement as compared to less than 25 PPM NOx and less than10 PPM CO on natural gas combustion system with steam injection. Sainchez et al. [18] showed that the use of syngas increases the gas turbine power by 3–7% at generator terminals and 5–10% increase in gas turbine efficiency (LHV based) but resulted in much higher carbon dioxide emissions. Oluyede et al. [19] reported that firing syngas in conventional gas turbine has the potential to result in enhanced power output with an increase of 20-25% when compared with the natural gas due to significant flow rate increase (≈ 14% increase over natural gas). They however, noted that the increase in power output is accompanied by an increase in the moisture content of the combustion products, this is due to higher hydrogen content in the syngas which can contribute significantly to the overheating of the turbine component parts. Performance test of

syngas on a GE7EA gas turbine carried out by Lee et al. [20] has shown that fuel with high hydrogen content emits more NOx, but does not emit CO even in a low load condition while the turbine did not generate combustion pulsation, unlike methane. Khalil et al. [21] experimentally studied syngas in a cylindrical combustor with swirling air injection and observed very low-level of NOx (3 PPM) with CO (70 PPM) emissions. When they preheated the air to 600 K, they observed low-level of CO (10 PPM) with an increase in NOx (10 PPM). They concluded that higher air inlet temperature resulted in higher flame temperature that aids the formation of thermal NOx and reduces CO by accelerating the conversion of CO to carbon dioxide (CO_2). The increased inlet temperatures enable the combustor to sustain the flame at lower equivalence ratios. Blow off regime is also of interest in syngas study because of its varying composition. This occurs when the characteristic reaction time is longer than the flow residence time in the burner. Fuel compositions and their corresponding flow characteristics are known to have significant effect on the combustor blow off limits. Noble et al. [22] experimentally showed that the percentage of H_2 in the fuel dominates the mixtures blow off characteristics. Lieuwen et al. [16] suggested that the percentage of hydrogen in the fuel is the most significant fuel parameter that initiates flame blow off due to the hydrogen flame's resistant to stretch induced extinction. Researchers have carried various works on developing chemical mechanism for syngas modeling [23-31]. Most of the developed mechanisms have been validated against experimental values of laminar flame speeds [32-35]. Other researchers have studied the effect of different fuel compositions [36], nitrogen and carbon dioxide dilutions [37, 38], preheat temperatures and pressures [39, 40] as well as emissions [41-43] on the accuracy of the developed mechanisms. Syngas

mechanisms developed have also been used variously in CFD modeling of syngas.

Ghenai et al. [44] carried out numerical investigation on syngas and methane using *k-ε* turbulence model. They observed that the gas temperature for the all five syngas compositions studied is lower than that of methane and this was attributed to their lower heating value as well as the mixtures of combustible and non-combustibles constituents present in the syngas. They concluded that for the same fuel mass flow rate, the power generated and the average NOx mass fraction for syngas are lower than that of methane while higher mass of CO_2 was emitted. Louis et al. [45] simulated non-adiabatic combustion of syngas (40% CO, 40% H_2, and 20% N_2) using CFX software and obtained a good agreement between calculated species concentrations and suction probe measurements.

2.3 Hydrogen-Enriched Methane Mixtures (CH_4/H_2)

The increasing stringent regulation on emission control is of great concern to gas turbine operators and designers. For instance, Kyoto protocols have reiterated the need for reduction in greenhouse gas emission to militate against the effect of global warming. This gas (CO_2) is, however, a direct product of CH_4 combustion. The reduction of greenhouse gas emission in the face of ever-increasing power requirement can only be possible by the gradual replacement of methane with carbon-less fuel such as hydrogen (H_2). Also, the regulation on NOx emission has necessitated the need for combustion to take place under leaner conditions. Lean burning is an efficient way of achieving a near Zero NOx emission. Methane (CH_4) is, however, susceptible to blow off under very lean condition. This is attributed to its high ignition temperature and low flame propagation

speed with ensuing poor lean burning [46]. Consequently, addition of fuel such as hydrogen with low ignition energy, high burning velocity and high diffusivity [47, 48] with a wider flammability range will improve the flame stability of methane under lean condition [49]. In furtherance of the aforementioned, Emadi et al. [50] have shown that the addition of 20% and 40% H_2 to CH_4 improves its blow off limit by about 7% and 35%, respectively, and stabilizes the flame in a wider range of equivalence ratio. Ilbas et al. [51] reported that increasing the H_2 percentage in H_2 -CH_4 mixtures widened the flammability limits. Studies have also shown that flames of CH_4 enriched with H_2 are less influenced by the flow field, indicating H_2 high resistance to extinction strain rate [52]. In a related study, Zhang et al. [53] used Damkohler number to show that increasing hydrogen fraction in natural gas flame widens its extinction limits. Beside the H_2 fraction, initial pressure and temperature have also been reported to have combined effect on flame stability [54]. The addition of hydrogen to methane has also been reported to affect the location where the flame is stabilized from the combustor inlet. Studies by Littlejohn [55] showed that lifted flame shifts closer to the nozzle exit with increasing hydrogen fraction. They attributed the change in the flame position to the increase in the turbulent flame speed as the hydrogen fraction increases. Other factors that have effect on combustion characteristics and flame stability are swirl number [56, 57], dual fuel injection [58], and the insertion of a bluff body that increases the inlet velocity [59]. Research has also been carried out at fundamental level to study the influence of hydrogen on the combustion characteristics of methane. The enrichment of methane with hydrogen has been observed to increase the laminar burning velocity [60-63] and reduce the ignition delay time [64] and laminar flame thickness as well as the dependence of the

laminar burning velocity on the flame stretch [65]. The increase of laminar burning velocity with hydrogen addition is attributed to the flooding of the reaction zone with H, O and OH radicals that have strong positive correlation with the burning velocity [46, 66, 67]. The improved lean burn ability of methane enriched with hydrogen can be explored to achieve near zero NOx emission. This becomes imperative because of increasing stringent environmental regulation on NOx emission. Ilbas [68] has shown that the observed NO emission from H_2 combustion to be higher than those of pure CH_4 and CH_4-H_2 combustion. Cozzi et al. [69] has similarly observed a monotonic increase in both CO and NOx emissions for H_2 fractions in natural gas - H_2 mixtures ranging from 0% up to 80%. Combustion under lean condition will lower the maximum combustor temperature necessary for NOx formation while enhancing the thermal efficiency of the combustion system. Burning CH_4 under very lean condition might result in local flame extinction and thus, increase the emission of CO and unburnt hydrocarbon. Tuncer et al. [70] has however, shown that lower lean blow off (LBO) associated with hydrogen addition can be explored to reduce NOx emissions. They, however, reported that hydrogen enrichment could cause an abrupt change in the dominant acoustic mode. In a similar work, Schefer et al. [71] reported that the extension of the stability limit allows stable burner operation at the lower flame temperatures resulting in low NOx emissions. Park et al. [72], reported the efficiency of NOx reduction to be highly dependent on the excess air ratio. Khalil et al. [73, 74] reported that in a premixed combustor, CO emission is substantially reduced with hydrogen enrichment leading to minimal effect on NO emission.

2.4 Combustion Instability

Most modern gas turbine combustors are operated under lean-premixed conditions to reduce the pollutant emission (especially Nox). Premixing the fuel and air eliminates local hotspot, thus, reduces the flame temperature and thermal NOx formation. Other advantages of lean premixed operation include increased combustion intensity, shorter flame lengths and better fuel burnout [75]. Lean premixed flames are, however, susceptible to thermo-acoustic instabilities [5-7]. These instabilities are sustained by the feedback loop between pressure and heat-release fluctuations and can limit the operating range of the combustor [76] as well as lead to severe structural damage [6, 77, 78]. The thermo-acoustic instabilities become more complicated under swirling flow with flow features such as re-circulation zone and precessing of vortex core (PVC). These unsteady vortices may couple resonantly with the flame front and subsequently cause the so-called flame-vortex combustion instabilities [79]. Several works have been done to understand the phenomenon that lead to onset of combustion instabilities. Specific attention has been given to the flame-vortex instabilities [79-82] where various reasons were suggested for driving the instabilities. The presence, shape, and dynamics of large-scale coherent precessing vortex core (PVC) were reported to result in thermo-acoustically self-excited flame in the combustors [76, 80]. Kim [82] shows that the swirl number variation within the combustor leads to the formation of a coherent structure, which drives strong self-sustained combustion instabilities, while, Huang [79] further shows that the inlet swirl number plays a dominant role in determining the amplitudes of wave motions. Emadi [5] stated that the coupling between heat release and pressure fluctuation was due to the effect of pressure fluctuation on the bulk velocity. He suggested that fluctuations trigger

the developing shear layer vortex causes variation in flame surface which results in unsteady heat release. Other factors such as the inlet temperature [83], equivalence ratio [84-86] and fuel composition [87, 88] have effects on the acoustic footprint of the combustor. Speth et al.[89] studied the dynamic regimes of a swirl-stabilized combustor and observed that stable helical flames were anchored within the inner recirculation zone near the lean blowout limit. They observed the flame become quasi-stable and oscillate weakly at intermediate equivalence ratios and become unstable at higher equivalence ratios due to vortex formation in the outer recirculation zone. In this study, we investigated the flame-vortex combustion instabilities with emphasis on identifying and characterizing the dynamic mode of a swirl stabilized combustor using the flame extinction strain rate. This is a follow-up to the work of Speth et al. [89, 90] where they characterized dynamic operating modes of the combustor and used a single parameter (flame consumption speeds) to correlate the dependence of the combustor dynamics on the equivalence ratio and fuel composition. This study was extended by Hong [91] in a laboratory scale backward-facing step combustor burning lean premixed, propane/hydrogen/air. They show that the operating parameters of the combustor can be scaled as a function of a normalized flame consumption speed taken into consideration the density of the reactant and the product. This idea was further extended in the present study by the characterization of the acoustic response of a swirl stabilized combustor using extinction strain rate.

2.5 CH_4/H_2-Air Chemical Reaction Mechanism

Several researchers have investigated the combustion dynamics and emission experimentally. The cost of a robust experimental analysis can be prohibitive because the dynamics and stability of the flame as well as emission are geometry dependent. Thus, combustion studies using computational fluid dynamics (CFD) approach have become imperative. The numerical study enables the researcher to get more insight on the flame dynamics in a cheaper and safer way. The accuracy of combustion modeling, however, depends on correct representation of the physical geometry as well as the use of appropriate models (i.e. turbulence, radiation, and chemistry models). The chemistry model is a key element for accurate predictions of the various flame properties such as flame shapes, temperature, flame speed, species concentrations and emissions. Detailed chemical mechanism such as GRI 3.0 Mechanism [23] has been reported to give good prediction of this properties at fundamental level (1-D). Owing to computational expense, the reduced and global mechanisms having reasonable degree of accuracy are mostly used in CFD calculations. Norton [92] used the one-step global mechanism by Westbrook and Dryer[93] to model the combustion characteristics of CH_4-air mixtures in micro-combustor. Yin [94] reported that the one step reaction mechanism gave similar adiabatic temperature with the detailed mechanism in the fuel lean region (Ø=0.5-1.0) with significant over prediction as the equivalence ratio increases. The over prediction in the temperature and it ensuing effect on the prediction of the species led to the development of global mechanism with more steps. Da-Silva [95] used a two step global mechanism of methane (2sCM1) with irreversible CO/CO_2 step to model combustion in a cylindrical combustor and obtain a good radial and axial prediction of the combustion

temperature. The mechanism, however, under predicts the CO species in the flame core. Further details on the chemical mechanisms used in modeling CH_4/H_2-air combustion are given in section 5.2.

2.6 Computational Fluid Dynamics of Reacting Flows

Computational fluid dynamics modeling of combustion involve the proper selection and implementation of a suitable model to faithfully represent the complex physical and chemical phenomenon associated with the combustion process. The mathematical model describing combustion process is based on the conservation equations of mass, momentum, species and energy as well as equations for turbulence and radiation models. The generalized equation which governs the conservation of mass, momentum and energy as well as the equations for species transport can be written as [96-98]:

$$\frac{\partial}{\partial x_j}\left(\overline{\rho}\overline{u}_j\emptyset + \overline{\rho}\overline{\mathbf{u}_\mathbf{j}'\emptyset'}\right) = \frac{\partial}{\partial X_j}\left(\Gamma_{\emptyset'}\frac{\partial \emptyset}{\partial x_j}\right) + \overline{\rho}S_\emptyset \tag{2.1}$$

2.6.1 Continuity and Momentum Equation

$$\frac{\partial}{\partial x_j}\left(\rho u_j\right) = \mathbf{0} \tag{2.2}$$

Momentum equation:

$$\frac{\partial(\rho u_i u_j)}{\partial x_j} = -\frac{\partial P}{\partial x_i} + \frac{\partial(t_{ij}+\tau_{ij})}{\partial x_j} \tag{2.3}$$

Where t_{ij} is the viscous stress tensor and is given in equation (4) [44]:

$$t_{ij} = \mu\left[\left(\frac{\partial u_i}{\partial x_j} + \frac{\partial u_j}{\partial x_i}\right) - \frac{2}{3}\frac{\partial u_k}{\partial x_k}\delta_{ij}\right] \tag{2.4}$$

$\delta_{ij} = 1$ if $i = j$, $\delta_{ij} = 0$ if $i \neq j$

2.6.2 Turbulence Modeling

Turbulent flows are characterized by fluctuating velocity fields. These fluctuations mix transported quantities such as momentum, energy, and species concentration, and cause the transported quantities to fluctuate as well. Presence of turbulence usually dominates all other flow phenomena and results in increased energy dissipation, mixing, heat transfer and drag. Because these fluctuations can be of small scale and high frequency, they are too computationally expensive to simulate directly in practical engineering calculations. Instead, the instantaneous (exact) governing equations can be time-averaged and resulting in a modified set of equations that are computationally less expensive to solve. However, the modified equations contain additional unknown variables, and turbulence models are needed to determine these variables in terms of known quantities.

The time average Reynolds stress tensor is defined as

$$\boldsymbol{\tau_{ij}} = -\boldsymbol{\rho}\overline{\boldsymbol{u_i'u_j'}} \tag{2.5}$$

$$\boldsymbol{\tau_{ij}} = \boldsymbol{\mu_t}\left[\left(\frac{\partial \boldsymbol{u_i}}{\partial \boldsymbol{x_j}} + \frac{\partial \boldsymbol{u_j}}{\partial \boldsymbol{x_i}}\right) - \frac{\boldsymbol{2}}{\boldsymbol{3}}\frac{\partial \boldsymbol{u_k}}{\partial \boldsymbol{x_k}}\boldsymbol{\delta_{ij}}\right] - \frac{\boldsymbol{2}}{\boldsymbol{3}}\left(\boldsymbol{\rho k \delta_{ij}}\right) \tag{2.6}$$

There are various Turbulence model in existence, it is, however, unfortunate fact that no single turbulence model is universally accepted as being superior for all classes of problems. The choice of turbulence model will depend on considerations such as the physics encompassed in the flow, the established practice for a specific class of problem, the level of accuracy required, the available computational resources, and the amount of time available for the simulation. In the present study, two equations Reynolds-averaged

Navier–Stokes equations (RANS) turbulence models were considered, the renormalization group (RNG) and the realizable k-ε turbulence model. The models solved the equations for the turbulent kinetic energy equation (eq.2.7) and the turbulent dissipation rate equation (eq.2.8). The main difference in the model is how the turbulence viscosity is computed.

$$\frac{\partial(\rho k u_j)}{\partial x_j} = \frac{\partial\left[\left(\mu+\frac{\mu_t}{\sigma_k}\right)\left(\frac{\partial(k)}{\partial x_j}\right)\right]}{\partial x_j} + G_k - \rho\varepsilon \tag{2.7}$$

$$\frac{\partial(\rho \varepsilon u_j)}{\partial x_j} = \frac{\partial\left[\left(\mu+\frac{\mu_t}{\sigma_\varepsilon}\right)\left(\frac{\partial(\varepsilon)}{\partial x_j}\right)\right]}{\partial x_j} + C_{\varepsilon 1}\frac{\varepsilon}{k} - C_{\varepsilon 2}\rho\frac{\varepsilon^2}{k} \tag{2.8}$$

Where G_k represents the production of turbulence kinetic energy and it is defined as:

$$G_k = \mu_t\left[\left(\frac{\partial u_i}{\partial x_j}+\frac{\partial u_j}{\partial x_i}\right)\right]\frac{\partial u_i}{\partial x_j} - \frac{2}{3}\frac{\partial u_i}{\partial x_j}\delta_{ij}\left[\mu_t\frac{\partial u_k}{\partial x_k}+\rho k\right] \tag{2.9}$$

Realizable $k-\varepsilon$ Model

The realizable $k-\varepsilon$ model proposed by Shih et al. [97, 99] sensitize Cμ to the mean flow (mean deformation) and the turbulence, thus, making it variable. The immediate benefit of the realizable k-ε model is that it more accurately predicts the spreading rate of both planar and round jets. It is also likely to provide superior performance for flows involving rotation, boundary layers under strong adverse pressure gradients, separation, and recirculation [100].

The solution of the transport equations for k and ε are used to compute the turbulent viscosity as:

$$\mu_t = \rho C_\mu \frac{k^2}{\varepsilon} \tag{2.10}$$

The variable C_μ for realizable $k-\varepsilon$ is computed from:

$$\boldsymbol{C_\mu = \frac{1}{A_0 + A_s \frac{kU^*}{\varepsilon}}} \tag{2.11}$$

Where:

$$\boldsymbol{U^* \equiv \sqrt{\left(S_{ij}S_{ij} + \widetilde{\Omega_{ij}}\widetilde{\Omega_{ij}}\right)}} \tag{2.12}$$

$$\boldsymbol{\widetilde{\Omega_{ij}} = \overline{\Omega}_{ij} - 3\varepsilon_{ijk}\omega_k \quad S_{ij} = \frac{1}{2}\left(\frac{\partial \overline{u_i}}{\partial x_j} + \frac{\partial \overline{u_j}}{\partial x_i}\right)} \tag{2.13}$$

$$\boldsymbol{A_0 = 4.04, A_s = \sqrt{6}cos\emptyset} \tag{2.14}$$

$$\boldsymbol{\emptyset = \frac{1}{3}\cos^{-1}\left(\sqrt{6}W\right)} \tag{2.15}$$

$$\boldsymbol{W = \frac{S_{ij}S_{jk}S_{ki}}{\overline{S}^3}} \tag{2.16}$$

$$\boldsymbol{\overline{S} = \sqrt{S_{ij}S_{ij}}} \tag{2.17}$$

The model constants are given as:

$$C_{2\varepsilon} = 1.9 \;\; \sigma_k = 1.0 \;\; \sigma_\varepsilon = 1.2$$

RNG $k-\varepsilon$ Model

The RNG-based k-e turbulence model was derived from the instantaneous Navier-Stokes equations, using a mathematical technique called renormalization group (RNG) methods [101]. The RNG $k-\varepsilon$ model [102, 103] has an additional term in its ε equation that significantly improves the accuracy for rapidly strained flow. It also accounts for the effect of swirl on turbulence, thus, enhancing the accuracy of swirling flow. The analytically-derived differential formula for effective viscosity also accounts for low-

Reynolds-number effects. A comprehensive details of the model and application can be found in [104].

To account for the effect of swirl or rotation, the turbulence viscosity is calculated as:

$$\boldsymbol{\mu_t = \mu_{t0}\, f\left(\alpha_s, \cap, \frac{k}{\varepsilon}\right)} \tag{2.18}$$

Where μ_{t0} is the turbulent viscosity calculated without the swirl modification and given as:

$$\boldsymbol{\mu_{t0}\ = \rho C_\mu \frac{k^2}{\varepsilon}} \tag{2.19}$$

$\cap$ is the characteristics swirl number and α_s is the swirl constant set as 0.07.

The model constants are given as:

$$C_\mu = 0.0845\,, C_{1\varepsilon} = 1.42,\ \ C_{2\varepsilon} = 1.68$$

For the purpose of the near wall treatment, the standard wall function was used in this study to couple the field variables and the corresponding cell variables near the wall.

2.6.3 Energy Equation

The energy equation was solved to account for heat transfer due to conduction, species diffusion, viscous dissipation as well as energy source terms [44, 59].

$$\boldsymbol{\frac{\partial \rho u_i h}{\partial x_i} = \frac{\partial}{\partial x_i}\left(k_f \frac{\partial T}{\partial x_i}\right) + \sum_j \frac{\partial}{\partial x_i}\left(h_j \rho D_{j,m} \frac{\partial Y_j}{\partial x_i}\right) + S_\emptyset} \tag{2.20}$$

$S_\emptyset$ is the energy source term including the reaction source term and radiation heat exchange.

The heat loss from combustor wall is modeled using convective-radiative equation given as [59]:

$$\dot{\boldsymbol{q}} = \boldsymbol{h}(\boldsymbol{T_w} - \boldsymbol{T_a}) + \boldsymbol{\varepsilon_w \sigma}(\boldsymbol{T_w^4} - \boldsymbol{T_a^4}) \tag{2.21}$$

Heat conduction has been reported to have effect on the combustion characteristics for given wall properties [59, 92, 105]as such, the heat transfer within the combustor wall thickness is computed from;

$$\frac{\boldsymbol{\partial}}{\boldsymbol{\partial x_i}}\left(\boldsymbol{k_q}\frac{\boldsymbol{\partial T}}{\boldsymbol{\partial x_i}}\right) = \mathbf{0} \tag{2.22}$$

h is the effective heat transfer coefficient; T_{w} is the temperature on the wall; T_a is the ambient temperature.

2.6.4 Radiation Model

Radiation is an important heat transfer phenomenon in combustion, thus, it is necessary to solve radiative heat transfer equations to improve combustion simulation results. Heat losses from the reacting gases to the combustion chamber wall may significantly change the temperature of the flame and eventually affect the chemical kinetic of the product species like CO, NOx or soot particles. Moreover, the radiative heat flux must be determined to evaluate correctly the thermal exchanges with walls. Due to the complexity of radiation and the non-linear interactions between reacting flows, heat transfer and turbulence, Proper care should be taken in choosing the radiation model for combustion simulation. Bidi [106] numerically studied the effect of radiation modeling of methane–air combustion using discrete ordinate method with the weighted sum of gray gas model (WSGGM). They concluded that radiation effects of non-gray gases of hot combustion products influence the temperature and species concentration profiles. Centeno [107],

similarly, used discrete ordinates method to account for the turbulence–radiation interactions (TRI) with weighted-sum-of-gray-gases (WSGG) for the participating species. They observed numerical results considering radiation to be in good agreement with experimental data and concluded that inclusion of TRI had important influence on global results, such as the flame peak temperature and radiant fraction. In the present study, the radiative transfer equation (RTE) was solved using the discrete ordinates (DO) radiation model [108]. WSGG model was also adopted in computing the gas emissivity as [109]:

$$\boldsymbol{\epsilon = \sum_i a_i(T)\left[1 - \exp\left(-k_i\left(P_{H_2o} + P_{CO_2}\right)S\right]\right.} \tag{2.23}$$

The fractiona_i of the blackbody radiation for a given spectral regions is given as:

$$\boldsymbol{a_i(T) = \sum_j b_{i,j}\left(\frac{T}{T_{ref}}\right)^{j-1}} \tag{2.24}$$

S is the radiation beam length; P_{H2O} and P_{CO2} are the partial pressures of the absorbing gases (H_2O and CO_2). k_i is the absorption coefficient. The coefficients of the WSGG used are obtained from [110].

2.6.5 Species Transport Model

The mixing and transport of chemical species can be modeled by solving conservation equations describing convection, diffusion, and reaction sources for each component species given in equation (2.25).

The species equation that solves the convection–diffusion equation for the j^{th} species is given thus:

$$\frac{\partial \rho u_i Y_j}{\partial x_i} = -\frac{\partial}{\partial x_i}\rho D_{j,m}\frac{\partial Y_j}{\partial x_i} + R_j \quad (2.25)$$

R_j is the species equation source term, which is the net rate of production or consumption of species j by chemical reaction and $D_{j,m}$ is the diffusion flux of species j .

The source term in the species equation for species l is computed using the eddy-dissipation-concept (EDC) model that includes detailed chemical mechanisms in turbulent flows [111].

$$R_l = \frac{\rho(\varepsilon^*)^2}{\tau^*[1-(\varepsilon^*)^3]}\left(Y_j{}^* - Y_j\right) \quad (2.26)$$

$Y_j{}^*$ is the fine scale mass fraction that is obtained after reaction over the time scale τ^*. The length fraction of the fine scales is modeled as [112].

$$\varepsilon^* = C_\varepsilon\left(\frac{v\varepsilon}{k^2}\right)^{1/4} \quad (2.27)$$

The species are assumed to react in the fine structures over time scale τ^*. Reactions proceed over this time scale τ^*governed by the Arrhenius rates of Equation, and are integrated numerically using the ISAT algorithm [113].

$$\tau^* = C_\tau\left(\frac{v}{\varepsilon}\right)^{1/2} \quad (2.28)$$

Where the volume fraction constant C_ε= 2.1377 and time scale constant C_τ =0.4082.

2.7 NOx Model

NOx is modeled through the post-processing of the main combustion calculation. This is based on the assumption that:

1) NOx concentrations in combustion systems are generally low and have a negligible effect on the flow field [114].
2) Rate of reaction for NOx is much slower than that of the combustion reaction. Thus, NOx mechanism can be decouple from the main combustion mechanism [115].
3) NOx chemistry has negligible influence on the predicted flow field, temperature, and major combustion product concentrations [99].

The NOx calculations that are carried out in the current study are thermal and prompt NOx. The thermal NOx is computed using the extended Zeldovich mechanism with the assumption of quasi-steady state for N and H atoms and partial equilibrium for O [116, 117], while prompt NO is modeled using the expressions proposed by De Soete [118].

2.8 Acoustic Model

The acoustic model presented in this work is limited to the prediction of the acoustic frequencies and the sound pressure level.

2.8.1 Modeling of Acoustic Frequency

The acoustics frequency of the combustor was modeled by the linear one-dimensional wave equation [119].

$$\frac{1}{\overline{c^2}}\frac{\partial^2 P'}{\partial t^2} - \frac{\partial^2 P'}{\partial x^2} = 0 \qquad (2.29)$$

The velocity perturbation $u'(x,t) satisfies$

$$\frac{\partial u'}{\partial t} = -\frac{1}{\bar{\rho}}\frac{\partial P'}{\partial x} \tag{2.30}$$

For such waves the acoustic pressure and velocity for nth block can be written as

$$\boldsymbol{P_i'(x,t) = \hat{P}_i(x)e^{-i\omega t}} \tag{2.31}$$

$$\boldsymbol{u_i'(x,t) = \hat{u}_i(x)e^{-i\omega t}} \tag{2.32}$$

For flow under consideration, the Mach number is low (M<<0.1) such that the mode shapes in each block take the form[91].

$$\boldsymbol{\hat{P}_i(x) = A_i^+ e^{-jK_i x} + A_i^- e^{jK_i x}} \tag{2.33}$$

$$\boldsymbol{\hat{u}_i(x) = \frac{A_i^+}{(\rho c)_i} e^{-jK_i x} - \frac{A_i^-}{(\rho c)_i} e^{jK_i x}} \tag{2.34}$$

Where ρ is the density, c is the speed of sound in each block and K is the wave number.

The wave number expressed as

$$\boldsymbol{K_i = \frac{\omega}{c}} \tag{2.35}$$

$\omega = 2\pi f$ is the natural frequency of the system, A_i^+ and A_i^- are arbitrary constant.

Details of the matching conditions in each block are given in chapter 4.

CHAPTER 3

EXPERIMENTAL STUDY OF COMBUSTION CHARACTERISTICS AND EMISSIONS IN A NON-PREMIXED SWIRL COMBUSTOR

Experiments were carried out to study the effect of hydrogen enrichment of methane on the combustor stability and emission under ultra-lean conditions ($Ø \leq 0.5$). The effect of varying fuel energy input and equivalence ratio were also studied.

3.1 Experimental Setup

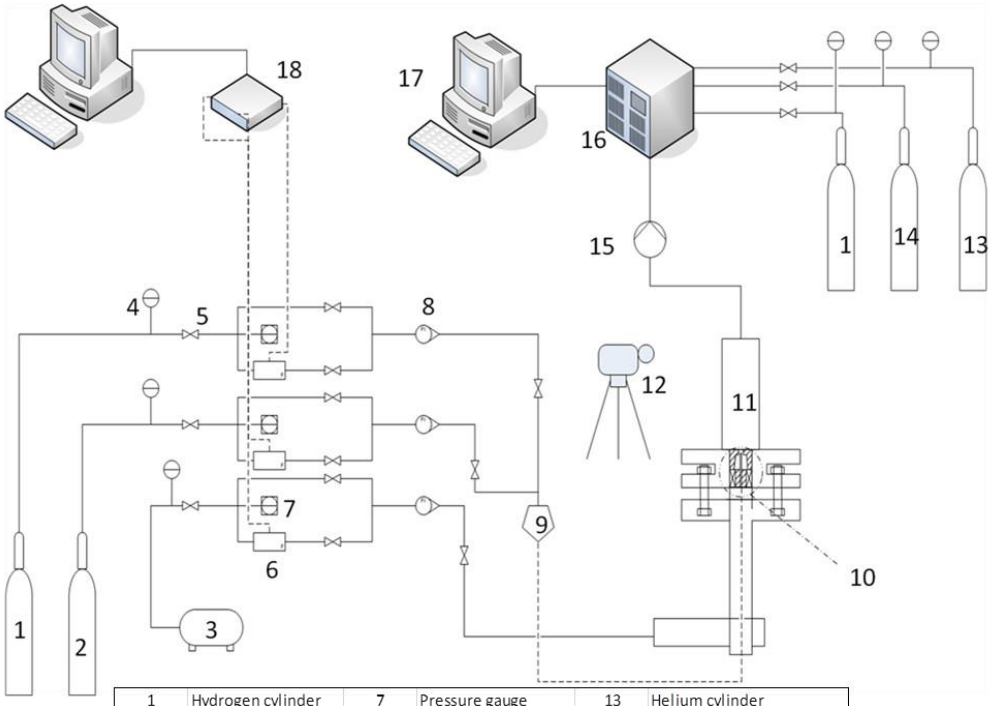

1	Hydrogen cylinder	7	Pressure gauge	13	Helium cylinder
2	Methane cylinder	8	One way valve	14	Air Cylinder
3	Air compressor	9	Fuel Mixer	15	Exhaust gas suction pump
4	Pressure regulator	10	Combustor burner	16	Gas chromatograhpy
5	Valve	11	Combustion chamber	17	computer set
6	Mass flow controller	12	Digital camera setup	18	MFC interface

Figure 3.1: Schematic diagram of the experimental set up of a gas turbine model combustor

The schematic layout of the experimental setup of a model non-premixed gas turbine combustor is given in Fig. 3.1. The setup was used to study the effect of H_2 enrichment on CH_4-air combustion. CH_4 and H_2 gases with 99.9 % purity are supplied from compressed gas cylinders through pressure regulators within the acceptable limit of the flow controller (8-10 bars). Dry air is supplied from a compressor via an air dryer. Fuel (mixtures of CH_4 and H_2) and air were metered using mass flow controllers by Bronkhorest HIGH-TECH with uncertainty of ±0.5 %. CH_4 and H_2 are initially mixed in a T junction upstream the fuel mixer which serves as a choke that enhance turbulence and improve homogeneity of the fuel mixtures. The fuel mixtures are, then, delivered to a 6 mm diameter stainless tube, which is 2 m long from the fuel nozzle where subsequent mixing occurs. Air is supplied via four 6 mm-tubes that are evenly distributed around a 50.8mm diameter pipe, 1.2 m upstream of the swirler. This allowed enough residence time for the flow to be fully developed before entering the combustor burner. The enlarged view of the burner that consists of the air swirler, air orifice and fuel nozzle is given in Fig. 3.2. The swirler has a diameter of 53 mm and height of 25 mm with 19 mm center body. A hole of 6.35 mm was drilled in the center body to allow passage for a pipe through which the fuel can be delivered. Eight vanes at angle of 45 degree are used to generate the required swirling flow and deliver it to an air orifice inlet diameter of 22 mm just above the swirler. The air orifice with a slant angle of 88^o has a sudden area reduction to 16 mm diameter, 8 mm from the dump plane. The sudden area reduction is to increase the air side velocity and turbulence level to enhance the fuel-air mixing and flame stabilization. The fuel nozzle installed on 6.35 mm diameter pipe consists of 5 mm bluff body with 16 fuel channels (0.45 mm × 0.13 mm) round the bluff body. The

inserted bluff body was used to generate the required fuel side velocity to stabilize the flame as well as to improve the symmetry of the fuel injection. This fuel symmetry will also help in the setting of the boundary condition for numerical modeling. The fuel nozzle is lowered 3 mm into the swirling air upstream of the combustor dump plane to further enhance turbulence mixing of the fuel and air, thus, improving the combustor lean burning. The dump plane is set as the reference for later measurements. The sudden expansion from 16 mm fuel-air passage into combustion chamber create outer recirculation zone that anchors and stabilizes the flame in the vicinity of the combustor center line. Quartz tube of 67 mm diameter and 300 mm long was used to simulate the combustion chamber. The combustion chamber has a thickness of 2 mm and is air cooled by natural convection.

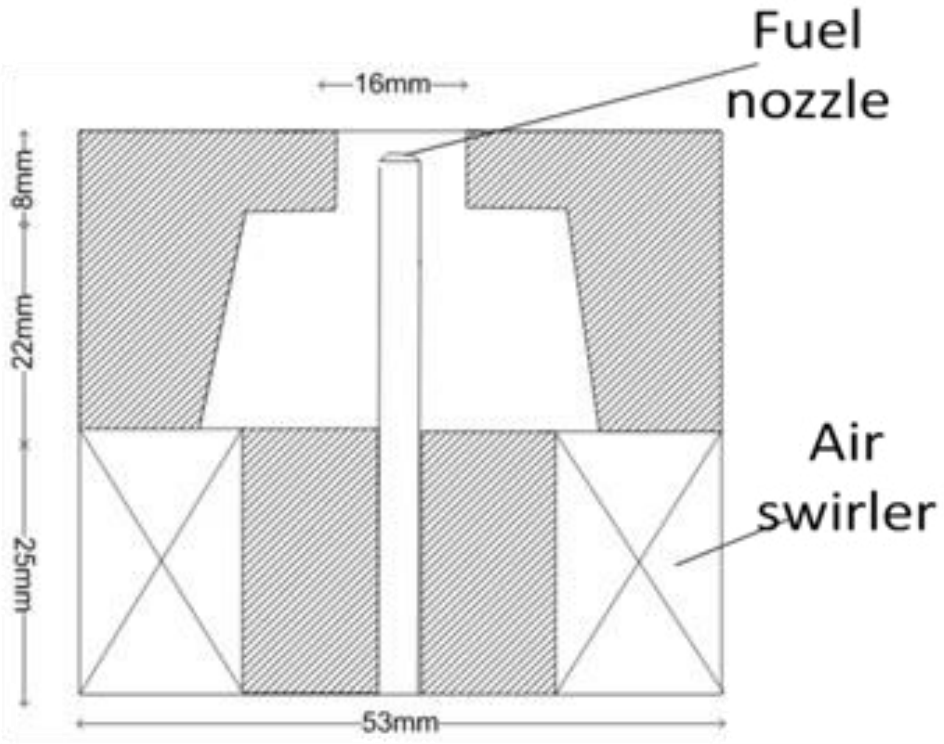

Figure 3.2: Combustor burner

3.2 Experimental Procedures

Experiments were initially carried out with 100% methane, 0.92 MW/m^3 fuel energy input under ultra-lean condition (i.e. $\emptyset \leq 0.5$) to determine the lean blow off (LBO) limit. Temperature profiling along the combustor center line as well as emission from the combustor were also recorded. The reported equivalence ratio throughout this work is based on air-fuel ratio such that $\emptyset < 1$ is referred to as lean mixtures. The LBO limit was obtained by carrying out equivalence ratio sweep test. This is achieved by gradually decreasing the equivalence ratio by 0.01 from $\emptyset = 0.5$ up to blow off. Temperature profiling along the combustor axis was carried out using type R-thermocouple from Omega instruments with measuring range of 1723K and accuracy of 0.25%. A high-speed camera was positioned at a fixed location to capture the size and shape of the flame under varying equivalence ratio. Gas chromatography (GC) was used to measure the species concentration at 50 mm from the exit plane of the combustor. The GC used for the species measurement is from Bruker Corporation with model no 450-GC. The GC has a flame ionization detector (FID) and a thermal conductivity detector (TCD). The FID was used for detecting and measuring the unburnt hydrocarbon while the TCD was used in measuring CO_2, O_2 and N_2 on dry basis. The combustion products were sucked via a water-cooled probe to freeze the combustion while delivering it to the GC. In measuring the NOx emission, UEI AGA5000 exhaust gas analyzer that has 1 PPM resolution and accuracy of $\pm 5\%$ was used. The measured NOx values are corrected to 15% O_2. The effect of hydrogen enrichment with methane on the LBO, temperature profile and emission was then studied. This was accomplished with addition of 10% hydrogen up to 50% hydrogen on volume basis while keeping the overall fuel energy input constant at

0.92 MW/ m^3. The experiment was repeated under similar conditions with the fuel energy input increased to 1.83, 2.75, 3.69 and 4.59 MW/ m^3. Fuel energy of 3.69 and 4.59 MW/ m^3 fall within the categories of industrial gas turbines that have operating range between 3.5 and 20 MW/ m^3-bar [108]. All experiments were conducted under atmospheric conditions. The summary of the volumetric flow rates at different fuel energy inputs is given in Table 3.1.

Table 3.1: Volumetric flow rate of the fuel components

Fuel energy (MW/m^3)	Percentage of Hydrogen (H_2) by volume	Volume flow rate of CH_4 (Liter/min.)	Volume flow rate of H_2 (Liter/min.)
0.92	0	1.91	0
	10	1.84	0.2
	20	1.76	0.44
	30	1.68	0.72
	40	1.58	1.05
	50	1.45	1.45
1.83	0	3.81	0
	10	3.68	0.41
	20	3.54	0.88
	30	3.36	1.44
	40	3.16	2.1
	50	2.91	2.91
2.75	0	5.72	0
	10	5.53	0.61
	20	5.3	1.33
	30	5.04	2.16

	40	4.73	3.16
	50	4.36	4.36
3.67	0	7.62	0
	10	7.37	0.82
	20	7.07	1.77
	30	6.72	2.88
	40	6.31	4.21
	50	5.81	5.81
4.59	0	9.53	0
	10	9.21	1.02
	20	8.84	2.2
	30	8.41	3.6
	40	7.89	5.26
	50	7.26	7.26

3.3 Results and Discussion

The current section presents the experimental results of the effect of hydrogen enrichment of methane on the LBO limit, combustion temperature and CO_2 and NOx emissions.

3.3.1 Stability Limit

Lean blow off limit

Figure 3.3 depicts the effect of hydrogen enrichment of methane in the range of 0% H_2 up to 50% H_2. For clarity purpose, 0% H_2 refers to 0% H_2 /100% CH_4, while 50% H_2 refers to 50% H_2 /50% CH_4 on volume basis. At 0% H_2, the lean blow off limit was observed to

be within the vicinity of $\emptyset = 0.35$ (Fig.3.3) for all fuel energy inputs under study. This indicates that the combustor was able to achieve a very lean burning. Increasing the H_2 content generally reduces the LBO equivalence ratio. This is due to H_2 lower ignition temperature as well as higher H_2 resistance to flame stretch and extinction. The hydrogen resistance to flame extinction favors stable burning at lower temperature as compared to CH_4. In a related work by Ren et al.[120], H_2 was similarly reported to sustain vigorous burning than CH_4 at low temperature due to its higher flame speed. In the present work, addition of 10% H_2 was observed to lower the LBO equivalence ratio by 21.3% and 18.4% at fuel energy of 2.75 MW/m^3 and 3.67 MW/m^3, respectively. A continuous downward trend was generally observed as the H_2 content was further increased. It is important to state that as the H_2 content and fuel energy input are increased in the combustor, the amount of air required to achieving LBO equivalence ratio increases. We are however constrained by the capacity of the mass flow controller for the air. Thus, we could not obtain the LBO equivalence ratio at conditions of very high air requirement and they are not presented. Figure 3.4 shows the effect of combustor fuel energy on the LBO equivalence ratio. At 0% H_2, increasing the fuel energy in the combustor marginally lowers the LBO equivalence ratio. This can be attributed to the increase of the thermal energy level of the combustor that favors continuous ignition of the incoming fuel. It can be concluded that at 0% H_2, the thermal state of the combustor has no significance influence on the LBO limit. On the contrary, increasing the fuel energy input in the presence of H_2 results in an increase in the LBO equivalence ratio. More insight on the effect at higher fuel energy is given in Fig.3.5. Increasing the fuel energy input increases the fuel flow rate and the corresponding air flow rate at blow off. This increases the lean

blow off velocity (LBV) but may not be translated to increase in the LBO equivalence ratio for the cases of H_2 enriched mixtures. On the other hand, the increase in hydrogen content results in a reduced air flow rates. The relative air flow rates at higher H_2 content is further reduced at higher fuel energy input leading to more stability. Figure 3.5 shows that the lean blow off velocity of H_2 enriched methane mixtures are generally higher than those of CH_4. Increasing the H_2 fraction increases the blow off velocity at the same fuel energy. This is due to the resistance of H_2 to stretch at higher velocity. It should be noted that the fuel energy input and H_2 content have coupled effect on blow off velocity. For instance, at 1.83 MW/m^3 fuel energy, increasing the H_2 content from 0% H_2 to 30 %, increases the blow off velocity by about 103%, while increasing the fuel energy to 2.75 MW/m^3 increases the LBV by 20%. This shows that the effect of H_2 on flame extinction outweigh the effect of the fuel energy input. The LBV is observed to have a linear relationship with the fuel energy (Fig. 3.5) and/or H_2 percent (not shown). We therefore used Minitab software to obtain a multiple regression equation. This equation can predict the dependence of lean blow off velocity (LBV) as function of the hydrogen content in the fuel mixtures and the fuel energy input as shown in equation (3.1).

$$\boldsymbol{LBV = 0.2762H + 4.3716E + 0.7458} \quad (3.1)$$

Where H represents the % H_2 in the mixtures on volume basis and E is the combustor fuel energy input in MW/m^3.

The predicted values of the LBV and experimental values were plotted in Fig 3.6. The experimental values were correlated with a mean error of about 7%. The backward step procedure using the predicted lean blow off velocity (LBV) was used to obtain the

predicted LBO equivalence ratio at different hydrogen contents in CH_4 mixtures as shown in Fig. 3.7. This procedure was used to predict the LBO equivalence ratio within a good accuracy especially with fuel mixtures containing H_2.

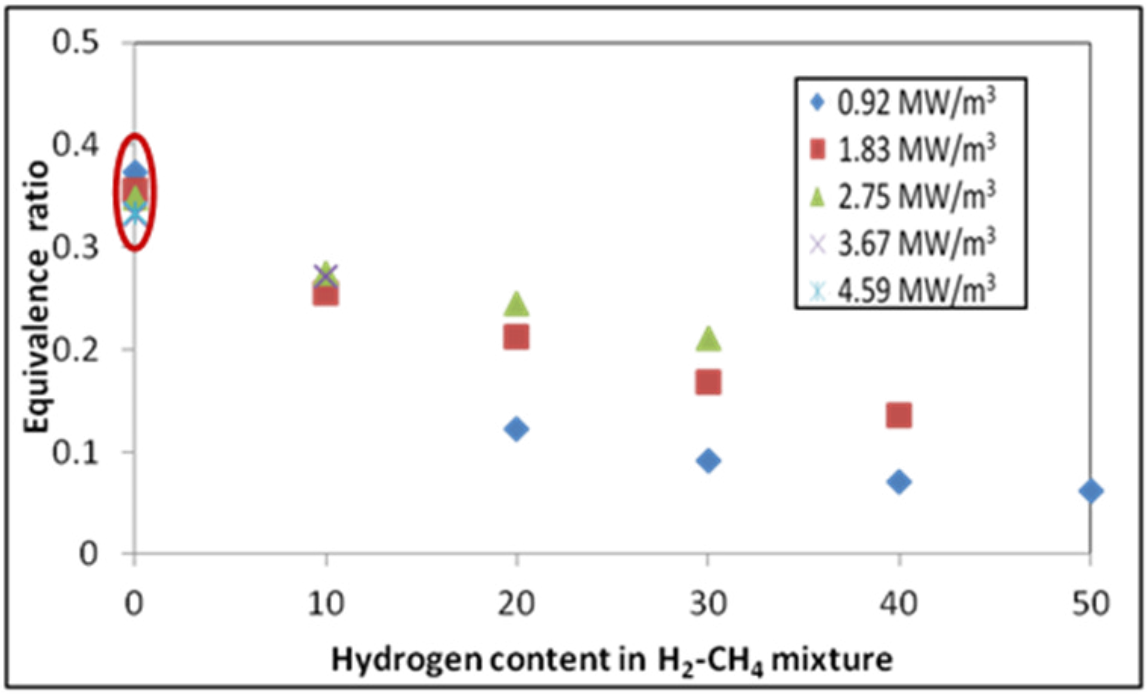

Figure 3.3 : Effect of hydrogen content on the lean blow off equivalence ratio

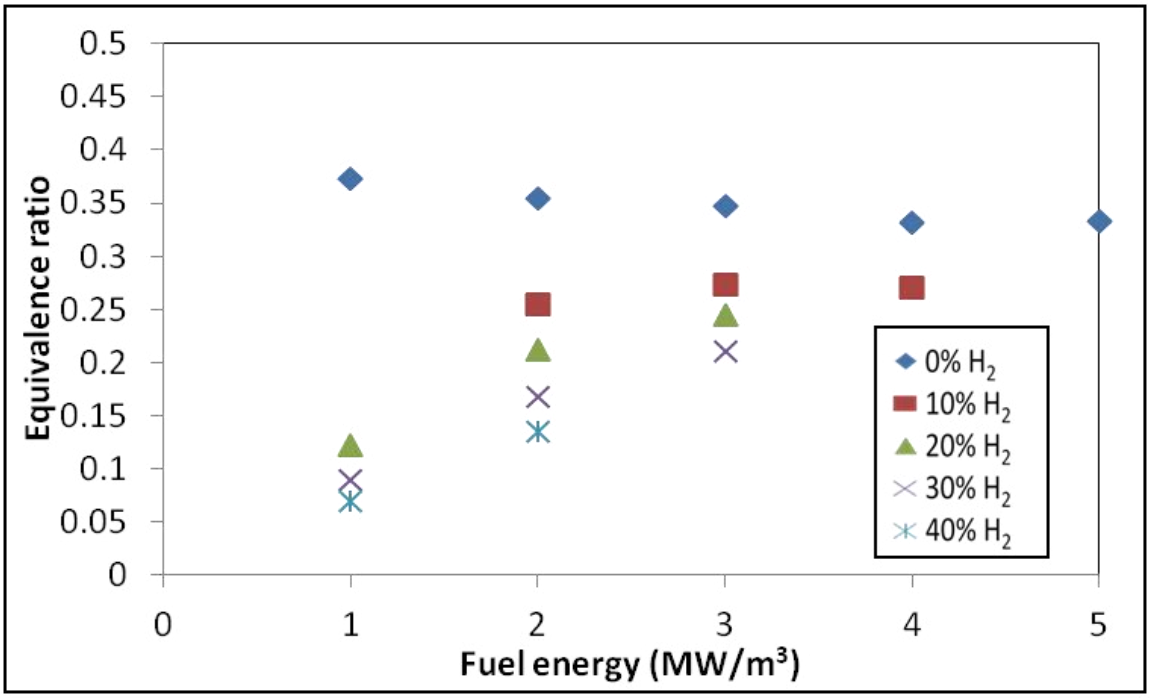

Figure 3.4: Effect of fuel energy input on the lean blow off equivalence ratio.

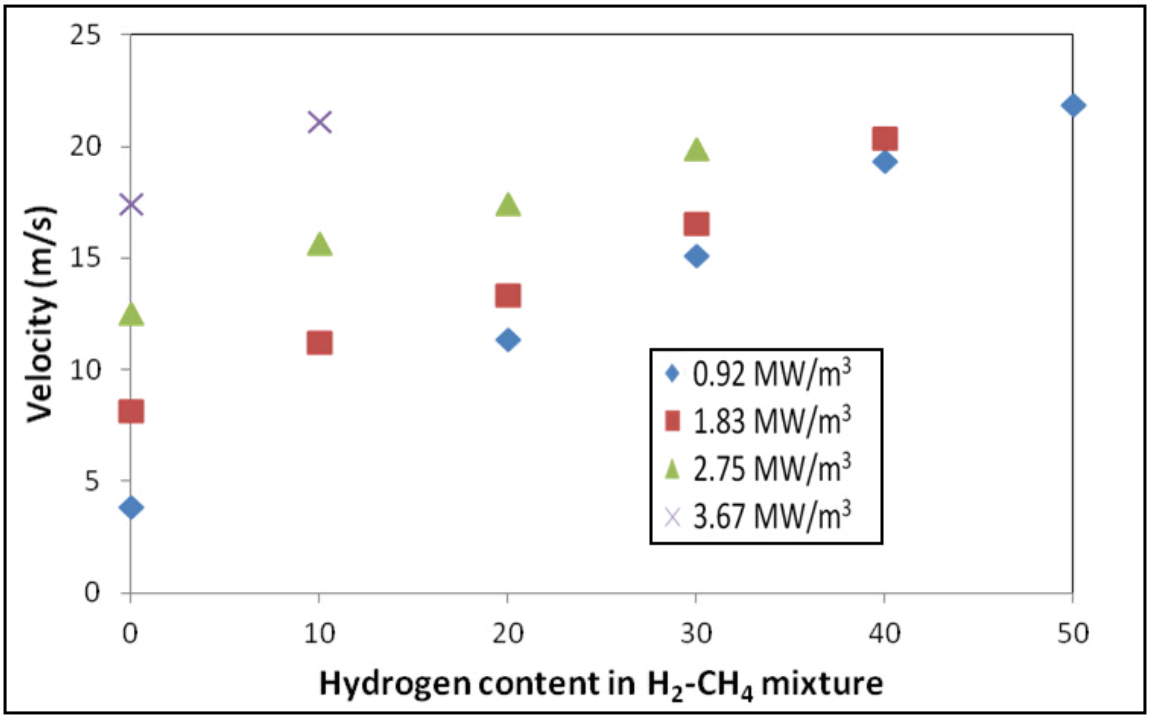

Figure 3.5: Effect of hydrogen content on the lean blow velocity

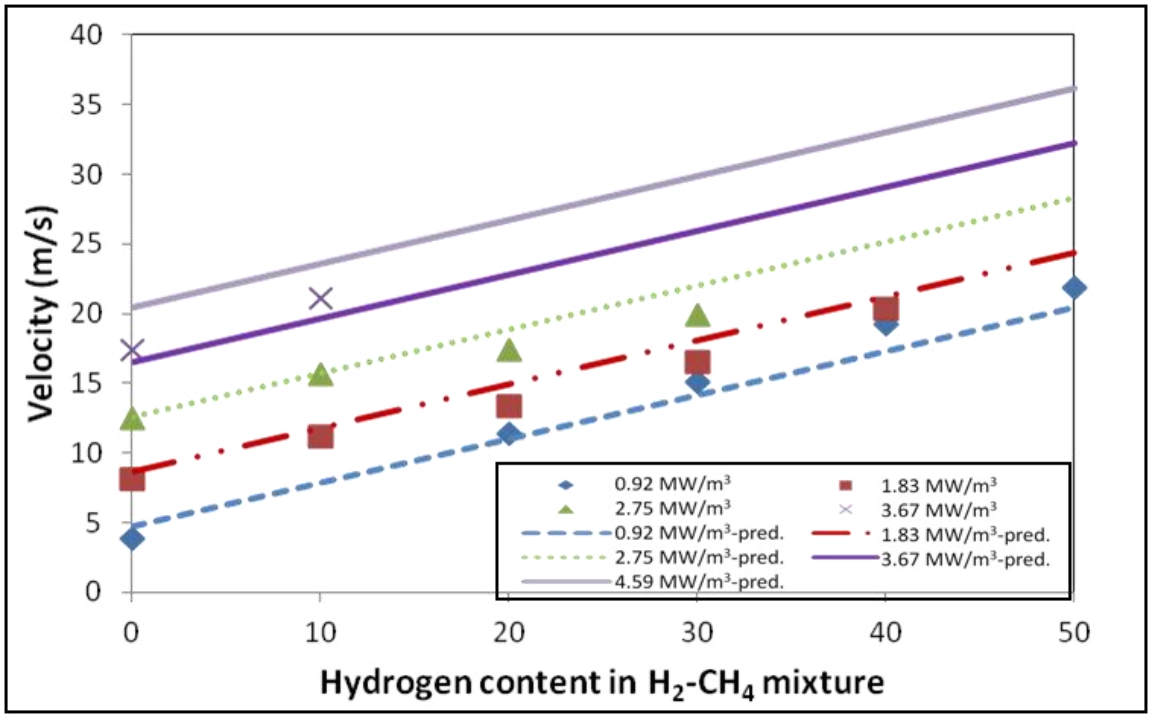

Figure 3.6: Comparison of the observed and predicted lean blow off velocity at different Hydrogen contents

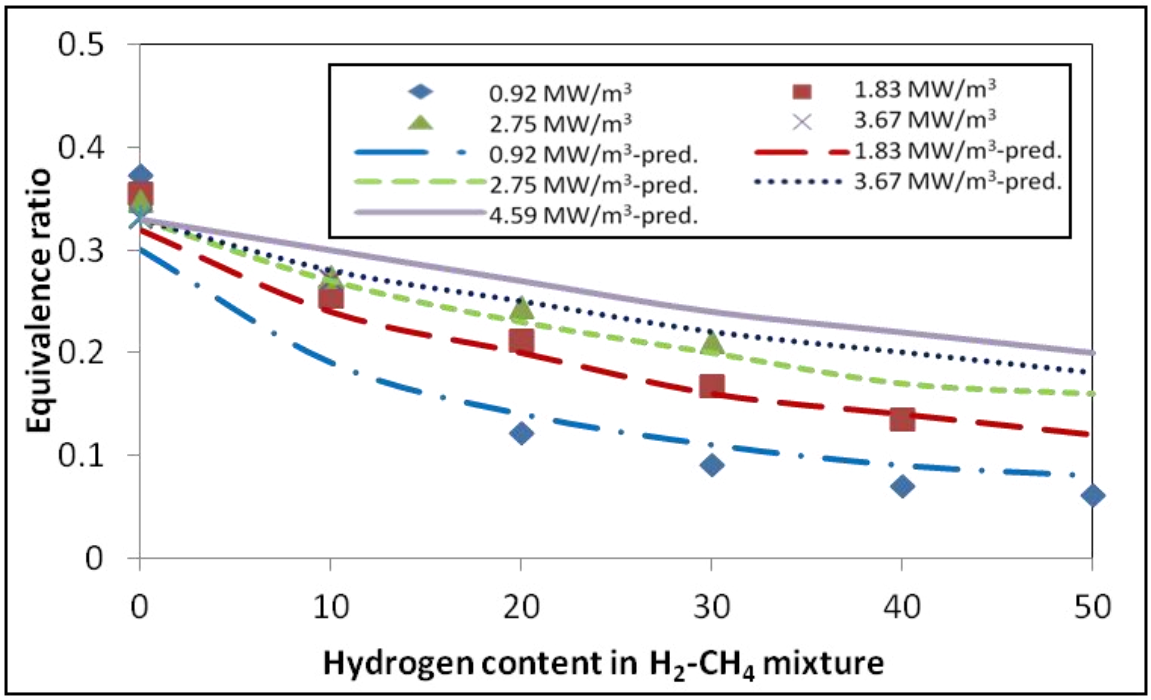

Figure 3.7 : Comparison of the observed and predicted equivalence ratio at different Hydrogen contents

Flame shape

Figure 3.8 shows the direct flame photographs taken at different H_2 contents and different equivalence ratios. Deep blue flames were observed at 0% H_2 and at equivalence ratio$\emptyset = 0.5$. The heights of these flames were observed to decrease without any significant change in color as the equivalence ratio is lowered towards the LBO limits. Enrichment of methane with 10% H_2, at a fixed equivalence ratio increases the flame height with the formation of yellow luminous plume towards the flame tip. The height, width and brightness of the yellow plume were observed to increase with increasing H_2 percent. Similar observation was reported by Cozzi et al.[69]. Based on their flame emission spectra measurement, they attributed the yellowish plume to soot formation in the flame. They similarly observed the yellow plume to extend above the visible blue zone and concluded that the height and brightness of the yellow plume increase with hydrogen content up to 60% in CH_4 - H_2 fuel mixture. The yellow plumes progressively disappear as hydrogen content in CH_4 - H_2 fuel mixtures becomes more than 60%. The increasing presence of hydrogen increases the rate of reaction and reduces the reaction zone (reduction in the blue flame, see Fig.3.8). The reduction in the reaction zone resulted in soot formation due to incomplete burning of CH4. At 50% H_2, decreasing the equivalence ratio reduces both the height and luminosity of the yellow plume in the flame, with blue flame formation similar to 0% H_2 achieved at $\emptyset$ = 0.25. The advantage of H_2 addition is in the extension of the LBO limit (Fig. 3.3) allowing the flame to burn leaner. The lean burning of the fuel lowers the flame temperature and NOx emission (see section 3.3.3). The effect of fuel energy input on the flame structure at 50% H_2 is shown in Fig. 3.9. It is noteworthy to state that changing the fuel energy input, equivalence ratio

and hydrogen content affect the combustor acoustic level. However, it is not quantitatively measured and thus, not reported. At low fuel energy input to the combustor (0.92 MW/m^3), the fuel burns quietly with long blue flame. As the fuel energy is increased (1.83-4.5 MW/m^3), the flame was observed to enter another mode of increased sound level as well as increased height and brightness of the yellow plume. This can be attributed to higher rate of heat release in the combustor. Lowering the equivalence ratio increases the combustor sound level. It, however, decreases yellow plume indicating near zero soot formation at ∅=0.25. The decrease in the soot formation is due to the increase in the turbulence level in the combustor. The increased turbulence enhanced the mixing of the fuel and air in the combustor thereby eliminating fuel rich zones, which, enabled the complete combustion of the fuel to be achieved.

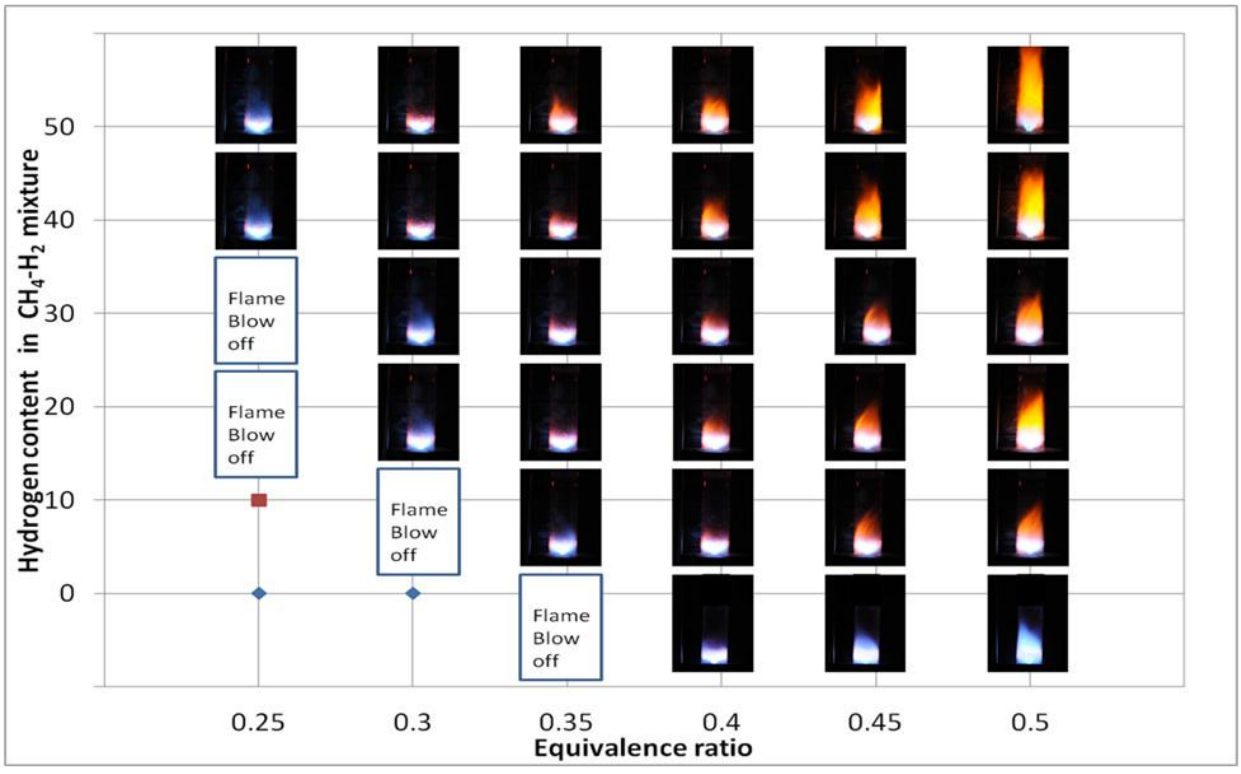

Figure 3.8: Effect of the Hydrogen content on the flame structure at 3.67 MW/m^3.

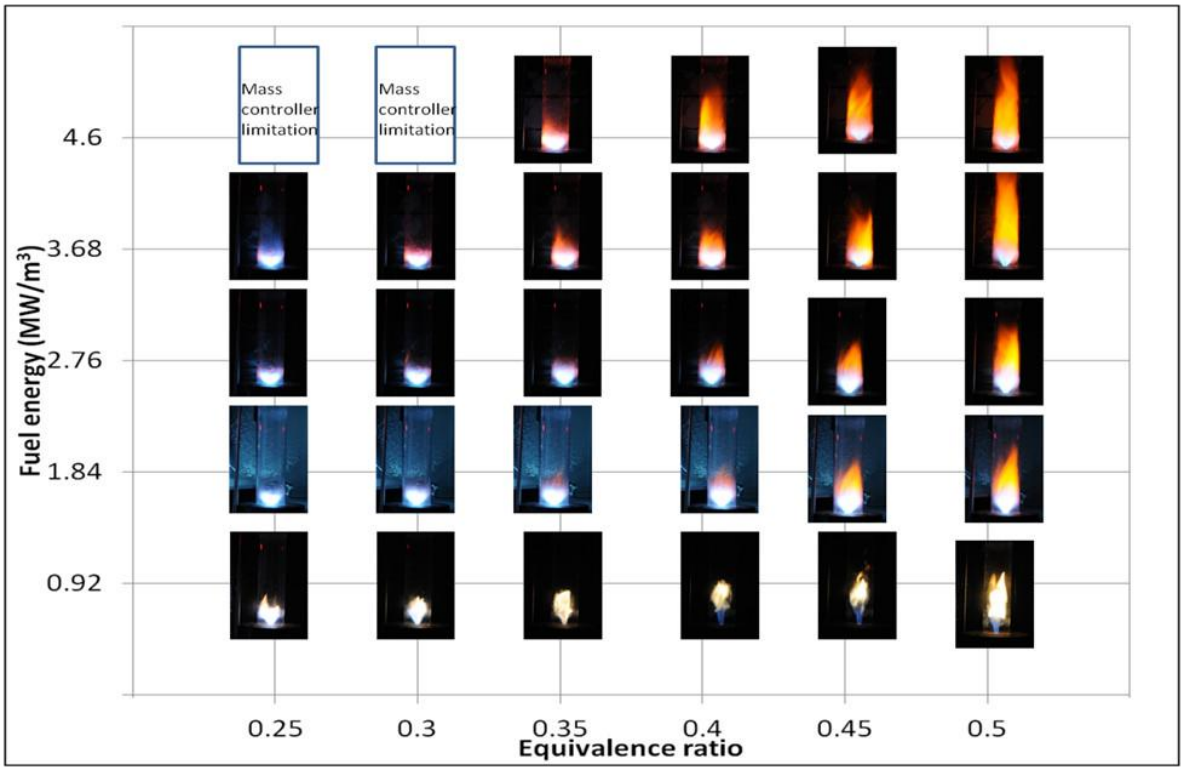

Figure 3.9: Effect of fuel energy on the flame structure at 50% H_2.

3.3.2 Thermal Field

Temperature distribution along the centerline of the combustion tube was obtained at different H_2 contents, equivalence ratios and energy inputs. Figure 3.10a shows the axial temperature profile along the combustor center line for the case 0% H_2. The axial distance refers here to the distance from the combustor burner (dump plane). Measured temperature was observed to decrease with increasing axial distance due to the continuous mixing of the combustion product with the excess air supplied which serves as the heat sink, thus, lowers the flame temperature. It can also be attributed to the cooling of the combustor by the ambient air. Increasing the fuel energy input to the combustor generally increases the temperature level in the flame (Fig.3.10a). As the

methane is enriched up to 50% H_2 (Fig.3.10b), higher temperatures were observed at all locations in the combustor as compared to the case of 0% H_2. For example, at axial distance of 10 cm, temperature of 1321 K was observed for 0% H_2 as compared to 1454 K for 50% H_2 at the same fuel energy input. This is due to higher adiabatic flame temperature of H_2 as compared to CH_4. This shows that besides the fuel energy input, the fuel composition also affects the temperature level of the flame. Therefore, care must be taken when changing fuel supply to the combustor to avoid rupture of the combustor material. Fig.3.10c similarly shows the temperature profiles at 50% H_2 but at lower equivalence ratio (Ø=0.25). The extensive data presented shows the thermal characteristics of the flame at different conditions (fuel energy, equivalence ratio and H_2 percent) and can serve as basis for the validation of numerical model. This can give more insight in to the combustion characteristics such as effect of hydrogen on the turbulence level and how it improves the localized extinction of methane in a more cost-effective way. The influence of the H_2 content on the temperature level of the flame is presented in Fig 3.11a. It can be observed that 10 % H_2 enrichment causes significant increase in the temperature of the burnt gases. Similar temperature profiles are observed for the cases of 20% and 30% H_2. While fuel with 50% H_2 gave the highest temperature values, they are, however, similar to the values obtained for 40% H_2 especially downstream of the combustor. Similar trend was observed for Ø = 0.4 but with lower temperature range. The rise in temperature levels with H_2 enrichment was observed to decrease downstream of the combustor. At Ø = 0.4 (Fig. 3.11b) there is no observed monotonic increase in temperature level with H_2 content. The case of 50% H_2 gives the highest temperature in the flame. It can be concluded that the effect of H_2 enrichment is more significant on the

local maximum temperature which affects NOx formation as will be seen in section 3.3.3. The increase of excess air is an efficient way to lower the temperature of the combustor as shown in Fig. 3.12. Decreasing the equivalence ratio reduces the temperature at different locations in the flame. For the same fuel energy input, the change in the equivalence ratio from 0.5 to 0.25 results in the reduction of the combustion temperature by 15% and 22% at 10 cm and 20 cm from the dump plane, respectively. The combustor average temperature at varying operating conditions is presented in Fig.3.13. The figure shows that the average combustor temperature can be lowered by either allowing the fuel to burn leaner, thus, increasing the amount of air that serves as heat sink, decreasing the amount of fuel supplied to the combustor that reduces the fuel energy or by decreasing the hydrogen content in the H_2-CH_4 mixtures. Because more energy is required to improve the combustor output, lean burning of methane enriched with hydrogen can be seen as the most efficient way of lowering the combustor temperature and NOx emission. This is achieved without the combustor suffering from neither low energy output nor lean stability problem.

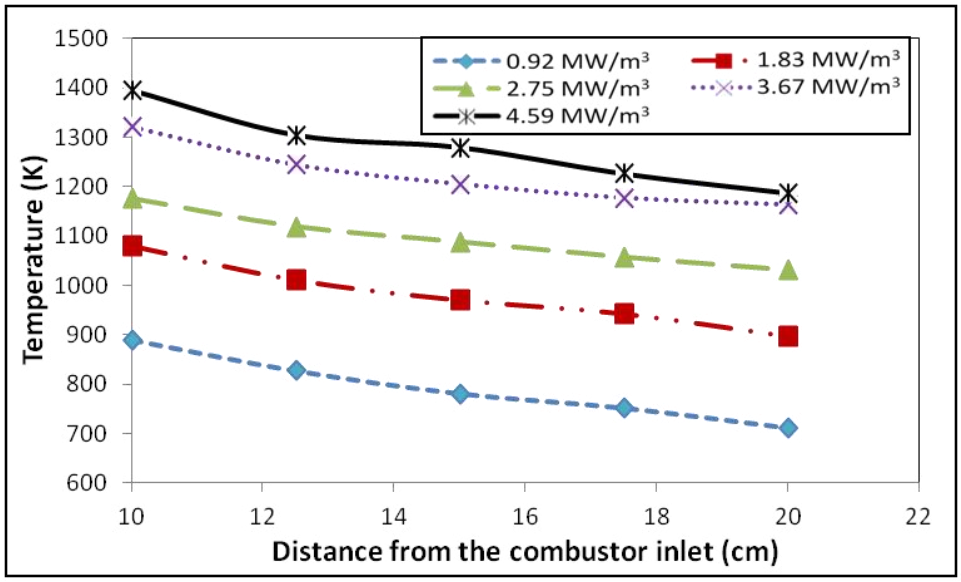

a) 0% H_2: equivalence ratio = 0.5.

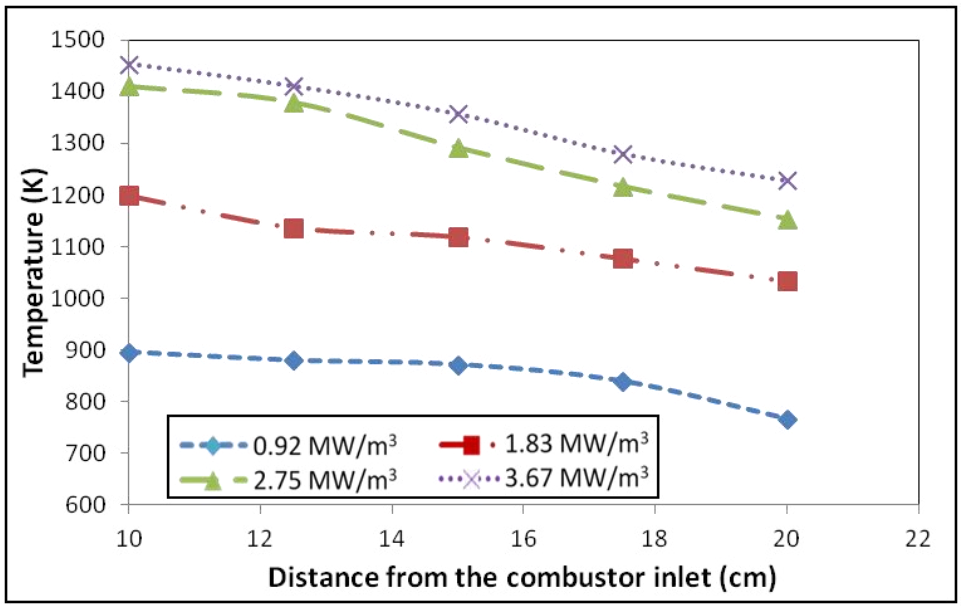

b) 50% H_2: equivalence ratio = 0.5.

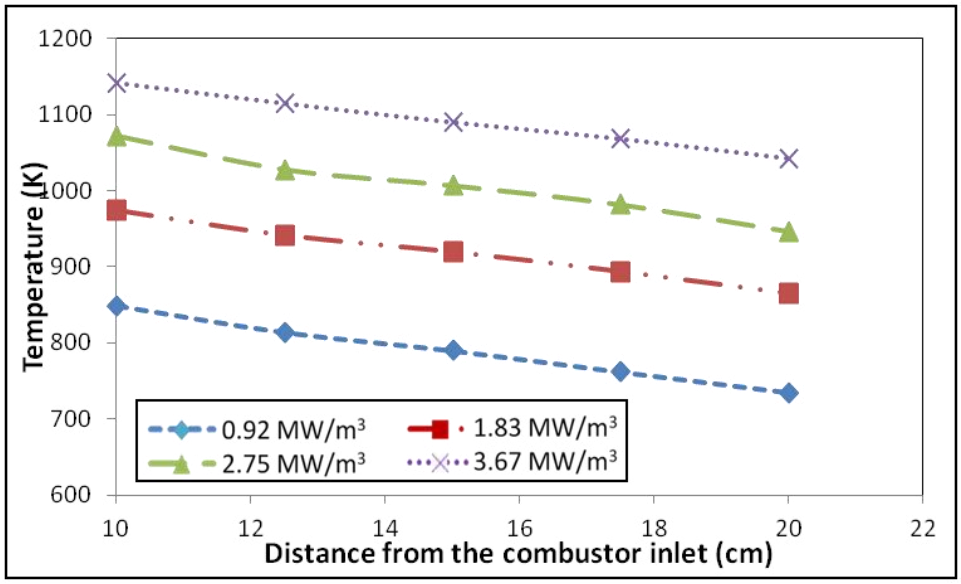

c) 50% H_2: equivalence ratio = 0.25.

Figure 3.10 : Effect of fuel energy on the axial temperature profile of the combustor.

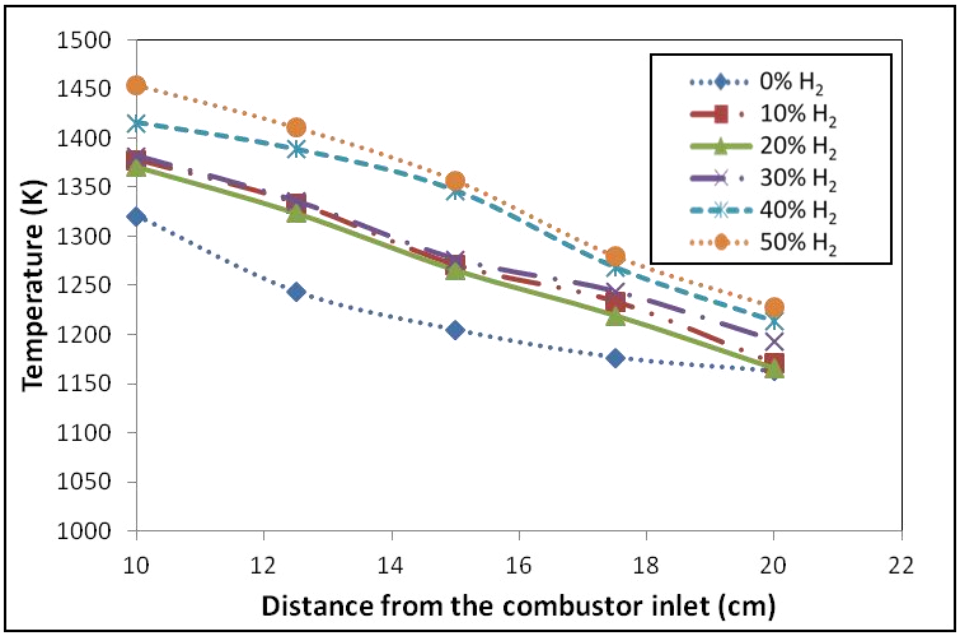

a) 3.67 MW/m^3: equivalence ratio = 0.5.

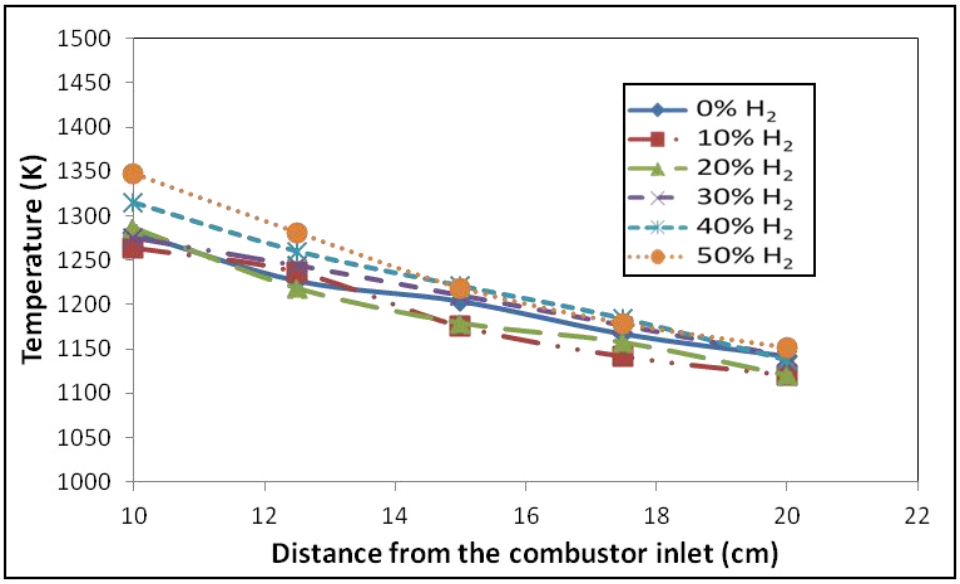

b) 3.67 MW/m^3: equivalence ratio = 0.4.

Figure 3.11: Effect of H_2 content on the axial temperature profile of the combustor.

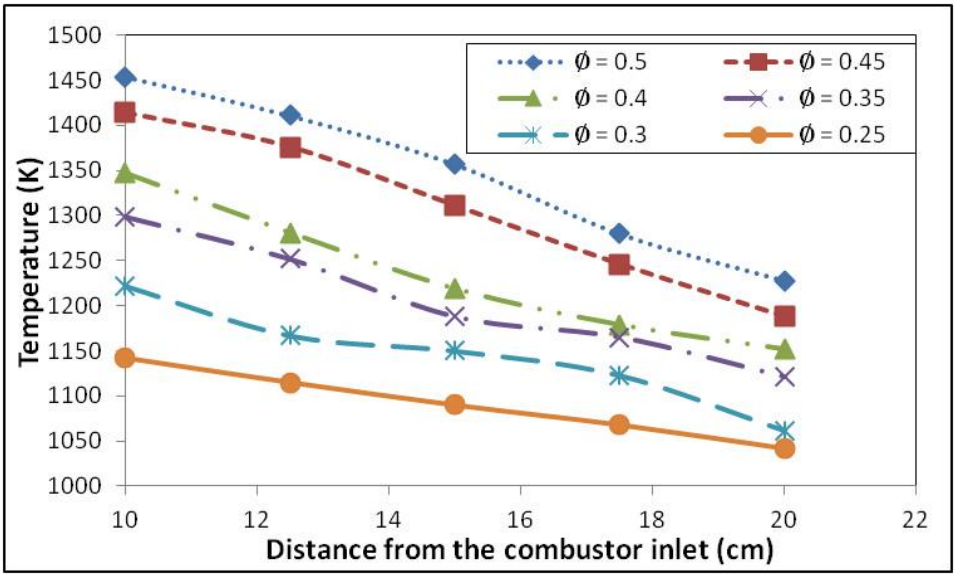

Figure 3.12: Axial temperature profile at different equivalence ratios. 3.67 MW/m^3:50% H_2.

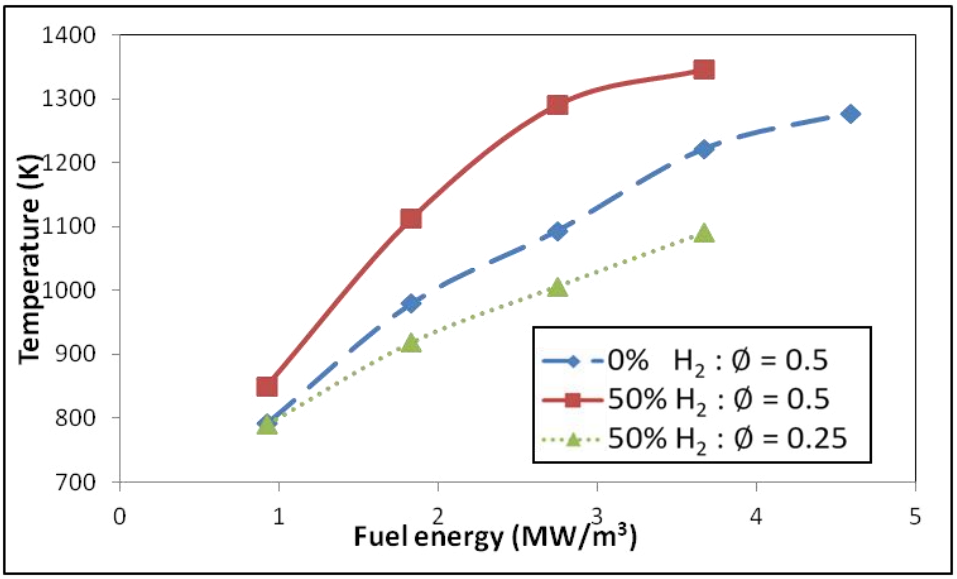

Figure 3.13: Average combustor temperature

3.3.3 Emissions

CO_2 Emissions

One of the advantages of replacing CH_4 with H_2 is in the reduction of CO_2 emission that is responsible for global warming. The effect of H_2 content or the CO_2 emission at 3.67 MW/m^3 fuel energy input is shown in Fig.3.14. At $\emptyset$ = 0.5, increasing the H_2 content from 0% to 50% H_2 lead to a decrease in the CO_2 emission by about 30% on volume basis. The decrease in the CO_2 is expected because the addition of H_2 lowers the carbon content of the fuel supplied. Values obtained serve as reference in validating the numerical model. Similar trend was observed at $\emptyset$ = 0.4 but with lower CO_2 values. The decrease in the equivalence ratio increases the amount of air added and thus, increases the combustor volume flow rate on the basis of which CO_2 is obtained from the GC. The relative percent of CO_2 with air is, thus, lowered at lower equivalence ratio. The effect of fuel energy on the measured CO_2 emission is given in Fig. 3.15. Qualitatively, the increase in fuel energy input does not have significant effect on the CO_2 emission on

volume basis. The quantity of CO_2 emitted (kg/hr) however increases. Further details on the amount of CO_2 emitted (kg/hr) at any given conditions are presented in section 5.4.4

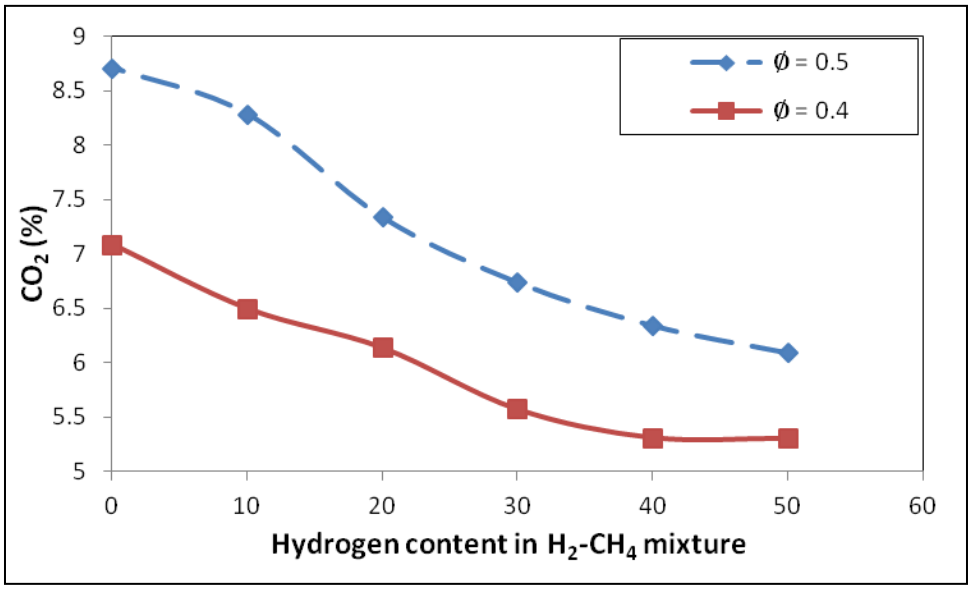

Figure 3.14: Effect of hydrogen content on CO_2 emissions at 3.67 MW/m^3

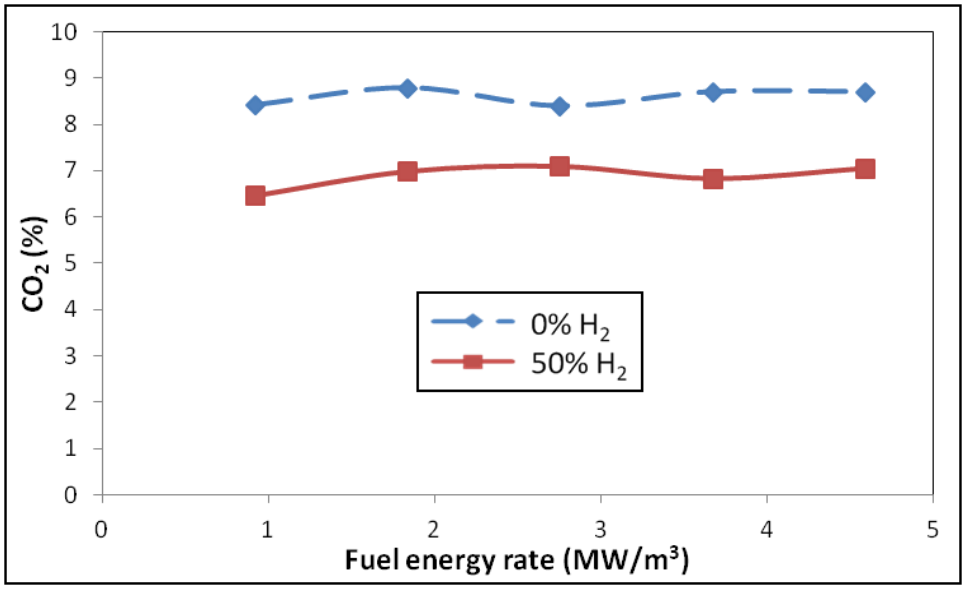

Figure 3.15: Effect of fuel energy on CO_2 emissions at Ø=0.5.

NOx Emissions

Figure 3.16 shows the NOx emissions at different H_2 contents and equivalence ratio. Increasing the H_2 content leads to an increase in NOx emission as shown in Fig. 3.16a. This can be attributed to higher adiabatic flame temperature of H_2 compared to CH_4 gas. Similar trend was observed by Ghoniem et al. [121], Bose et al. [122] and Askari [123]. They similarly attribute the increased NOx formation to the high flame temperature experienced in hydrogen combustion. The increased temperature may also be due to smaller ignition delay time for hydrogen-enriched fuel case as compared to pure methane fuel case that lead to local hotspot within the combustion chamber [124]. For the case of 0% H_2, decreasing the equivalence ratio to 0.4 was observed to lead to zero NOx formation in the combustor. This equivalence ratio ($\emptyset$ = 0.4) is, however, close to the average blow off equivalence ratio of 0.35 for pure methane. Zero NOx was similarly achieved at 10% H_2 and $\emptyset$ = 0.4 with the extension of the LBO equivalence ratio from 0.35 to 0.27. Further increase in the H_2 at $\emptyset$ = 0.4 raises the NOx emission from the combustor. For the combustor under study, the $\emptyset$ = 0.3 is observed to be sufficiently low enough to achieve zero NOx at higher H_2 content without suffering from instability that will result from LBO. Figure 3.16b shows that decreasing the equivalence ratio results in a monotonic decrease in the NOx. This is due to the decrease in the combustion temperature. The supply of excess air serves as heat sink to reduce the overall combustor temperature. Its other advantage lies in the increase in the overall volume flow rate, which reduces the residence time required for NOx formation. The reduction in the residence time will, however, have effect on the overall combustion efficiency due to local flame extinction. Zero NOx was also observed at $\emptyset$ = 0.3 for case of 40% H_2 and at

Ø=0.45 for pure methane. The effect of H_2 on the NOx emission (Fig 3.16b) can be observed to be similar to the effect of H_2 on temperature profile. Figure 3.17 shows that at Ø = 0.5, increasing the fuel energy to 1.8 MW/m^3 initially increases the NOx level due to the expected increase in the combustor temperature that favors NOx formation. Further increase in the fuel energy input leads to monotonic decrease in the NOx emission. The increase in the fuel energy input does not only increase the combustor temperature but also increases volume flow rate that lower the residence time of the combustion product and thus, decreases the NOx formation and emission. At a much lower equivalence ratio (Ø=0.3) there is a monotonic decrease in the NOx with the increase of the fuel energy input. This implies that, the combustor is should be operated under actual gas turbine operating conditions (>3.5 MW/m^3) in order to achieve low NOx emission.

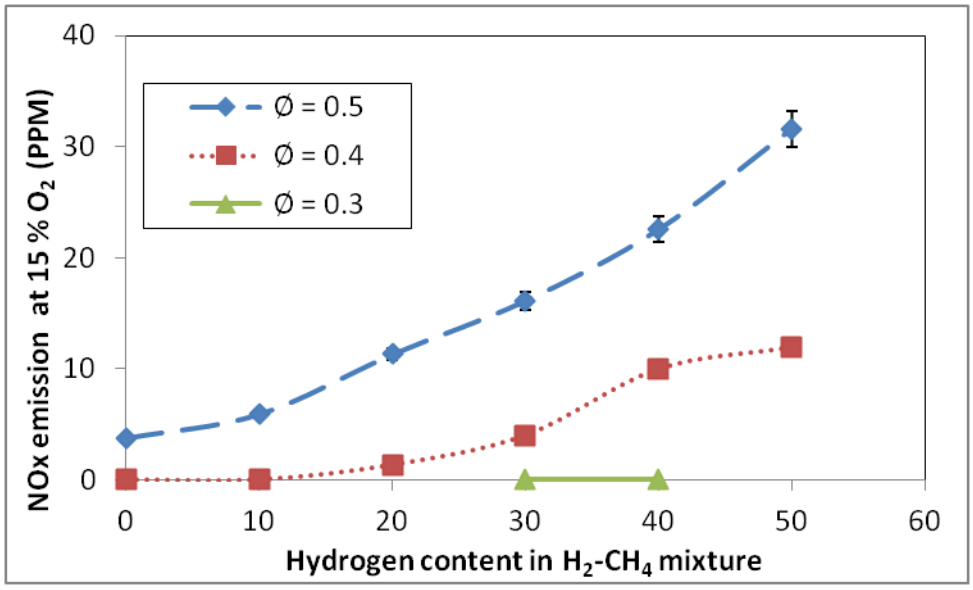

a) Effect of hydrogen content

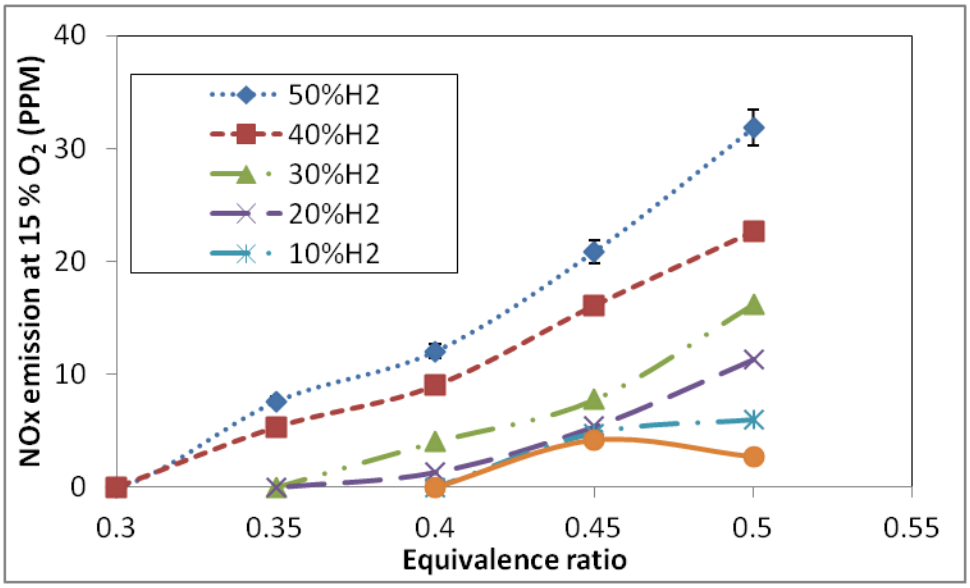

b) Effect of Ø

Figure 3.16: NOx emissions at 4.59 MW/m^3.

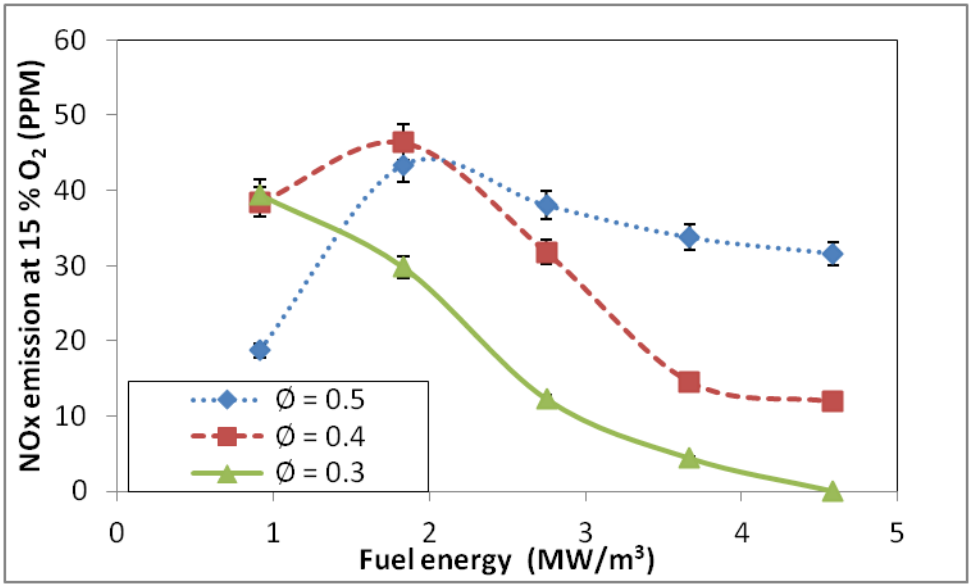

Figure 3.17: Effect of fuel energy on NOx emissions at 50% H_2.

In Fig. 3.18, we generally observed that for combustor temperature of about 1200K, the measured NOx emissions are of a single digit (less than 10 PPM). A 9 PPM NOx

emission was similarly observed in the upgraded version of Siemens SGT6-5000F gas turbine that has dual fuel capabilities [125]. This model of Siemens gas turbine has recently being deployed for use in Qurayyah [126] and Jazan [127] power plants. This study will serve as guide to the gas turbine operators when changing the fuel compositions supplied to the combustor on the expected combustor temperature and NOx emission.

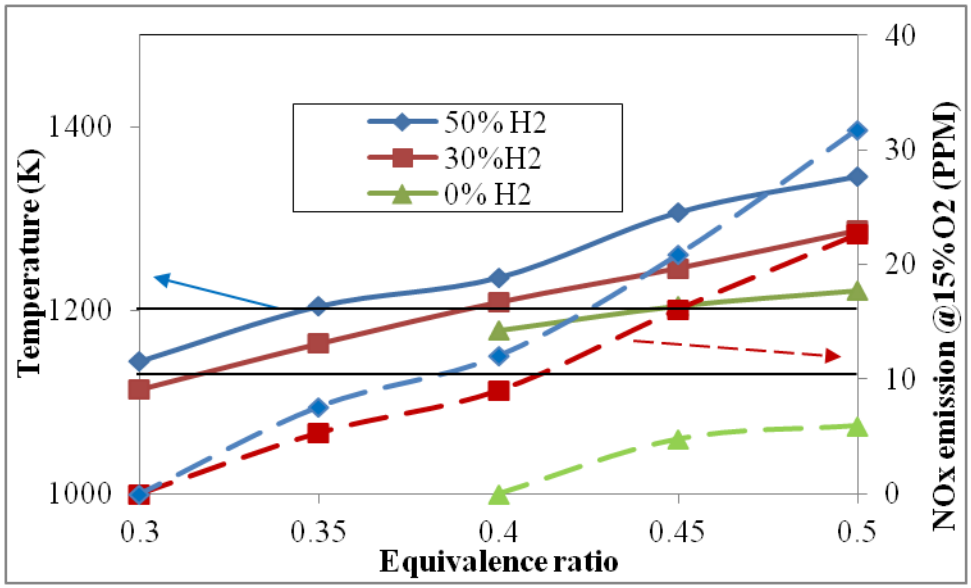

Figure 3.18: Combustor temperature and NOx emissions at different operating conditions. Temperature (continuous lines), NOx emissions (dashed lines).

3.4 Empirical Modeling of NOx Emission.

NOx are formed in the combustor by three major routes: The thermal, prompt and fuel NOx. The fuel NOx are formed by the oxidation of ionized nitrogen in the fuel while, Prompt NOx are formed under fuel-rich conditions. Prompt NOx also requires a short residence time. Thermal NO_x are formed by the reaction of atmospheric oxygen and

nitrogen at high temperatures. Thermal NOx depends on the molar concentrations of nitrogen and oxygen in the combustor.

For the combustor under study, there is no fuel NOx and the combustion takes place at ultra-lean conditions, thus, the dominant NOx formation route is thermal. In this section, the empirical modeling of NOx emission from the model gas turbine combustor was carried out based on the approach of Li and Thompson [128].

Thermal NOx modeling.

Thermal NOx was modeled by extended Zeldovich reaction mechanism which is highly dependent on temperature. The Zeldovich reaction mechanism is given as:

$$O + N_2 \leftrightarrow N + NO \quad (3.2)$$

$$N + O_2 \leftrightarrow O + NO \quad (3.3)$$

$$N + OH \leftrightarrow H + NO \quad (3.4)$$

High temperature is required for breaking the diatomic bond of nitrogen (N_2) (see eq. 3.2), whereas the activation energy for the oxidation of N atom is small in the presence of sufficient oxygen (eq. 3.3) such as in the case of fuel lean conditions. Reaction three (eq. 3.4) contributes to the thermal NOx formation at near stoichiometry and in fuel rich flame. These conditions are obtainable in non-premixed flames.

The NO formed in the combustor can be expressed as;

$$\frac{d[NO]}{dt} = k_{f1}[O][N_2] + k_{f2}[N][O_2] + k_{f3}[N][OH] - k_{r1}[NO][N] - k_{r2}[NO][O] + k_{r3}[NO][H] \quad (3.5)$$

Equation 3.2 is the rate limiting equation for the extended Zeldovich reaction mechanism which is dependent on the combustor temperature and availability of oxygen in the reaction zone. The NOx formed in the combustor can be expressed as:

NOx = f (Temperature, excess air) (3.6)

Temperature = f (firing rate, fuel composition, equivalence ratio) (3.7)

And excess air can be expressed as:

Excess air = f (equivalence ratio) (3.8)

NOx formed in the combustor can be expressed as:

NOx = f (firing rate, fuel composition, equivalence ratio) = f (P, H, Ø) (3.9)

We can assume a general solution of

$$\boldsymbol{NO_x = aP^x(1-\emptyset)^y(1+zH)} \quad (3.10)$$

P^x in the right hand side is the contribution of increased combustor firing rate to NOx production, such that when P is zero (no fuel supplied), there will be no (zero) NOx formed in the combustor. The deviation by the amount of excess air supplied from stoichiometry is accounted for by $(1-\emptyset)^y$. This means that for $\emptyset = 1$ there is no excess air supplied and zero NOx is expected to be form in the combustor. The effect of hydrogen addition to methane on the combustor NOx formation is given by $(1+zH)$. The addition of hydrogen to methane will increase the adiabatic temperature that will favor NOx formation. Isolating each of these term we have:

$$\boldsymbol{NO_x = bP^x} \quad (3.11)$$

$$\boldsymbol{NO_x = c(1-\emptyset)^y} \quad (3.12)$$

$$\boldsymbol{NO_x = d(1+zH)} \quad (3.13)$$

a, x, y and z are model constants, while, b, c, d are arbitrary constants that depend on the combustor operating conditions.

For a given equivalence ratio and hydrogen content in the fuel, constant b can be computed as:

$$\boldsymbol{b = a(1-\emptyset)^{y}(1+zH)} \quad (3.14)$$

For a given fuel energy input and hydrogen content in the fuel, constant c can be computed as:

$$\boldsymbol{c = aP^{x}(1+zH)} \quad (3.15)$$

For a given equivalence ratio and fuel energy input, constant d can be computed as:

$$\boldsymbol{d = aP^{x}(1-\emptyset)^{y}} \quad (3.16)$$

The procedure for obtaining the constant x,y,z and a in equation is outlined here under:

1. At a given equivalence ratio and hydrogen content in the fuel, experimentally measured NOx at different power input is expressed as given in eq. (3.11).
2. Constants x and b are then determined from the obtained equation.
3. Constant b obtained in step 2 and operating conditions ($\emptyset \; and \; H$) are substituted in eq. (3.14).
4. Equation 3.14 is thereby expressed as a function of a, y and z.
5. Procedures 1- 4 is then repeated for equation (3.12) for a given fuel energy input and hydrogen content in the fuel to obtain constants c and y using experimentally measured NOx at different equivalence ratio. Equation (3.15) is, thus, expressed as a function of a, x and z.

6. Constants y and x are substituted in equations obtained in steps 4 and 5 respectively given two new equations as a function of a and z
7. The new equations obtained in step 6 was solved simultaneously to obtain constants a and z
8. Constants a, x, y and z obtained are then substituted in NO generalized equation given in equation (3.10).

The generalized equation obtained is given as:

$$\boldsymbol{NO = 0.25P^{-1.5}(1-\emptyset)^{-5.53}(1+0.4H)} \quad (3.17)$$

Where NO is in PPM, $\emptyset$ is the air/fuel equivalence ratio P is the fuel energy input in MW/m^3 and H is the hydrogen content in the fuel (%).

The NO generalized equation given in equation (3.17) was used to predict the NOx emissions for the combustor and compared with the measured values at different operating conditions.

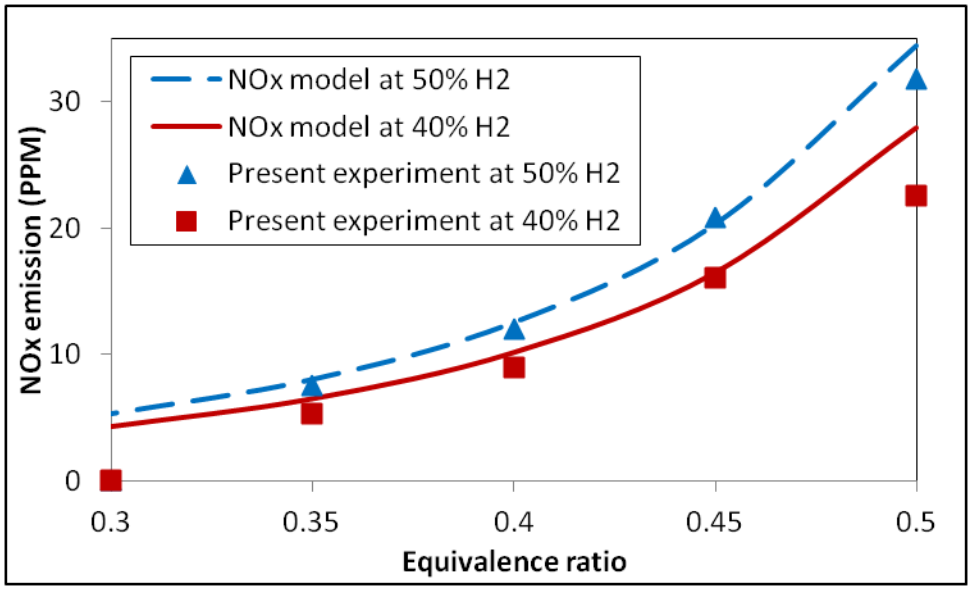

Figure 3.19: Comparison of experimental and modeled NOx at different equivalence ratios.

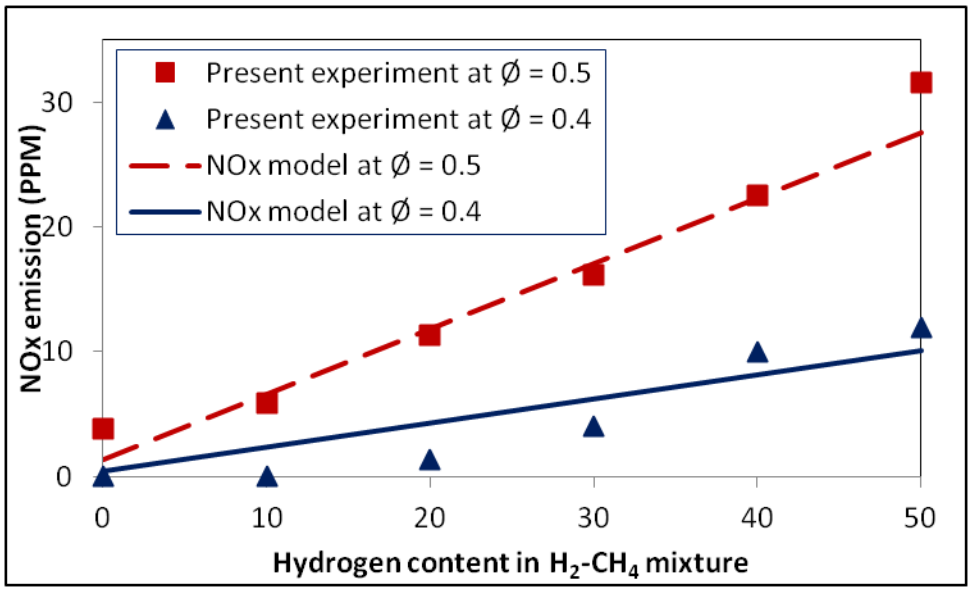

Figure 3.20: Comparison of experimental and modeled NOx at different hydrogen contents in H_2 -CH_4

In Fig.3.19 and Fig.3.20, we showed that the NOx model presented gave a fair prediction of the experimental values. However, the model could not capture the zero NOx observed

in the experiment. This can be attributed to the fact that the model neglects the effect of combustion residence time. The combustion residence time is also a critical factor to NOx formation within the combustor (see section 5.4).

CHAPTER 4

EXPERIMENTAL STUDY OF COMBUSTION INSTABILITY IN A PREMIXED SWIRL COMBUSTOR

In this section, the details of the experimental study carried out to characterize the acoustic response of a premixed swirl stabilized combustor over a range of fuel composition (CH_4/H_2) and operating conditions (equivalence ratio) is presented. Prior studies have shown the dependence of extinction strain rate on the equivalence ratio [129] and hydrogen [130] composition. Tests were initially carried out using methane -air from near stoichiometry up to the combustor blow off. The role of hydrogen addition on the combustor scaling was studied by increasing the hydrogen content in methane up to 50% on volume basis.

4.1 Experimental Setup

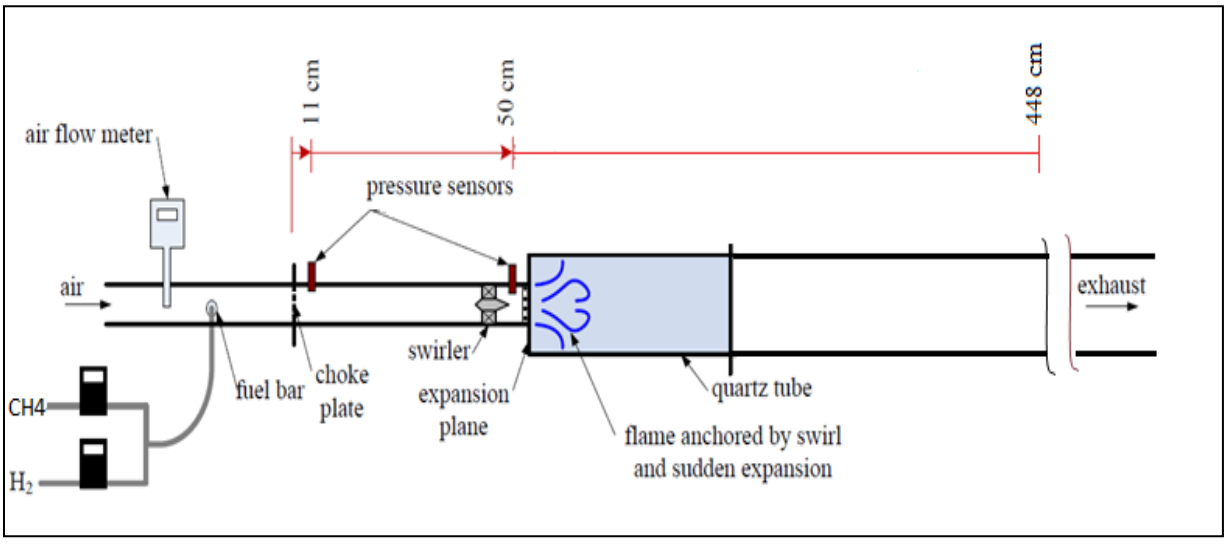

Figure 4.1: Experimental set-up of a premixed swirl stabilized combustor.

The schematic diagram of the swirl stabilized combustor used in the current study is shown in Figure 4.1. It consists of a combustor inlet pipe of 38 mm diameter that has a sudden expansion to the combustion chamber of 76 mm diameter. Premixed fuel-air mixtures are supplied to the combustor via a choked plate 100mm upstream of the combustion chamber. The fuel and air are mixed upstream of the choke plate to eliminate acoustically driven equivalence ratio oscillations while the choke plate prevents the equivalence ratio from coupling with the chamber acoustics, allowing the equivalence ratio to be controlled without oscillation. The combustor is equipped with an axial swirler 100 mm upstream of the expansion plane. The swirler has eight vanes and is used to create a swirling flow with an estimated swirl number of 0.7. The combustion chamber where the flame is anchor is made of optical accessible quartz tube, 40 mm in length. The combustor with an overall length of 4.4 m empties into an exhaust trench at near atmospheric pressure. Air is supplied by an Atlas Copco GA 30 FF air compressor capable of delivering up to 110 g/s air at 883 kPa. Methane is supplied by Sierra C100M Smart-Trak digital mass flow controllers capable of delivering up to 2.3 g/s methane while, Sierra C100L Smart-Trak capable of delivering up to 0.3 g/s of hydrogen is used in supplying hydrogen. The uncertainty in the flow rate is ±1% of the full scale. This allows the equivalence ratios to be measured with the accuracy of 0.002. Pressure is measured at 0.11 m and 0.5 m downstream of the choke plate using Kulite high intensity microphones. The pressure sensors were calibrated to give the same amplitude by adjusting the gains to ensure that they all read the same amplitude at a given axial location. Spatially-integrated Chemiluminescence measurements are taken using a Hamamatsu H930602 photomultiplier tube (PMT). An optical band pass filter is placed

in front of the photomultiplier tube to measure CH* Chemiluminescence emitted by the flame. The CH* Chemiluminescence intensity from the combustor is used as the surrogate for the heat release rate fluctuation[131, 132]. The dynamic flame shapes at a given operating regime were studied using a NAC GX-1 high-speed CMOS camera with Nikon 60mm f/1.8 lens. This was achieved by taking High-speed, spatially resolved Chemiluminescence measurements of the flame at speeds up to 500 Hz. The camera has a resolution of 1280 x 1024 pixels and a monochrome bit depth of 12 bits per pixel. A BG-39 optical colored glass filter with 1-mm thickness is placed in front of the camera, to reduce an infrared radiation from the flame. Analog signals from the pressure sensors, mass flow controllers and PMT are sampled using a National Instruments PCIe-6259 data acquisition card. A custom Matlab code controls the experiment and manages data collection from the various instruments.

4.2 Experimental Procedure

Series of experiments were conducted to show the dependence of hydrogen on the stability map of an atmospheric swirl stabilized combustor. Experiments were carried out at varying fuel composition of 0%H_2, 20%H_2, 40%H_2 and 50%H_2 on volume basis. For each fuel composition, equivalence ratio sweep test was conducted. This is achieved by gradually decreasing the equivalence ratio by 0.01 from the combustor near flash back limit up to flame blow off. All experiments were carried out at a fixed Reynolds number of 20,000 based on the combustor inlet diameter of 38 mm corresponding to velocity of ≈ 8 m/s at 300K. During each experimental run, dynamic pressure and Chemiluminescence measurements were recorded.

4.3 Data Analysis

The temporal pressure measurement at a distance of 50mm from the choke plate is reported in this work by its amplitude in term of the overall sound pressure level (OASPL) as given in eq. (4.1).

$$\boldsymbol{OASPL = 10log_{10}\overline{\left[\frac{P(t)-\overline{P(t)}}{P_0}\right]^2}} \quad (4.1)$$

P (t) is the pressure measured in an interval $t_1 < t < t_2$ and $P_0 = 2 * 10^{-5} Pa$. The over bar represent the mean value. The CH* integrated Chemiluminescence intensity is presented in section 4.4.2 is normalized by its mean as given in equation. (4.2).

$$\boldsymbol{I^* = \frac{I(t)}{\overline{I(t)}}} \quad (4.2)$$

Where I^* is the amplitude of the normalized intensity, I (t) is the integrated intensity over a time interval $t_1 < t < t_2$.

4.4 Results and Discussion

4.4.1 Combustor Stability Map

In this section, we present the stability map of the combustor at different fuel compositions. The stability map for each composition is presented by the overall sound pressure level (OASPL) obtained at different equivalence ratios from near flash back limit up to the blow of limit. Figure 4.2 shows the effect of hydrogen (H_2) addition to methane on the OASPL as a function of equivalence ratio. For the case of 0%H_2, near

the blow off equivalence ratio, the combustor was observed to be in a stable mode (mode I). As the equivalence ratio is increased there is a marginal increase in the OASPL up till the transition point (equivalence ratio). The transition point is characterized by the sudden increase in the sound pressure level signifying a shift in the dynamic mode of the combustor from stable (low frequency low amplitude) mode to unstable mode (high frequency high amplitude) or from an unstable mode to another unstable mode due to change in the frequency and pressure amplitude. The transition equivalence ratio at 0%H_2 is 0.68.A further increase in the equivalence ratio does not significantly affect the OASPL of the combustor up till the flash back limit. Similar trend was observed at 20% H_2. There is, however, a shift in the acoustic response of the combustor to region of lower equivalence ratio such that the transition of the combustor to unstable mode occurs at equivalence ratio of 0.61. At higher H_2 content in CH_4 (40% H_2 and 50%H_2), two transition points were observed, the first transition from stable to unstable mode occur at $\emptyset = 0.52$ and $\emptyset = 0.47$ respectively for 40% H_2 and 50% H_2 composition. The second transition occurs at $\emptyset = 0.8$ and $\emptyset = 0.67$ respectively for 40% H_2 and 50% H_2 composition. Figure 4.3 shows the frequency spectral map for the conditions presented in Figure 4.2. The spectral map is colored with the OASPL data. The frequency response at 0% H_2 (Fig 4.3a) shows that, as the equivalence ratio is increased beyond $\emptyset = 0.68$, the acoustic mode around 120 Hz is excited and the combustor operates in an unstable mode. At 0% H_2 and 20% H_2, the combustor was observed to exhibit a bi-modal (mode I and mode II) state. In mode I, the combustor is in a stable mode at low resonance frequency and amplitude, while in mode II, the combustor operates in an unstable mode at an acoustic frequency of $\approx$ 120Hz. Two modes of instabilities were observed at 40% H_2 and

50% H_2 composition are mode II (≈120Hz) and mode III (≈180Hz) instabilities. The mode II instability range was observed to decrease with increasing hydrogen contents in the fuel. In addition, the transition from 120 Hz to 180 Hz instabilities was also observed to shift to region of lower equivalence ratio. This suggests the strong dependence of the combustor stability regime on the hydrogen composition in the fuel. The lean blow off equivalence for all the flame understudy was also observed to decrease with increasing hydrogen content in methane. This can be attributed to the hydrogen higher resistance to strain as compared to methane.

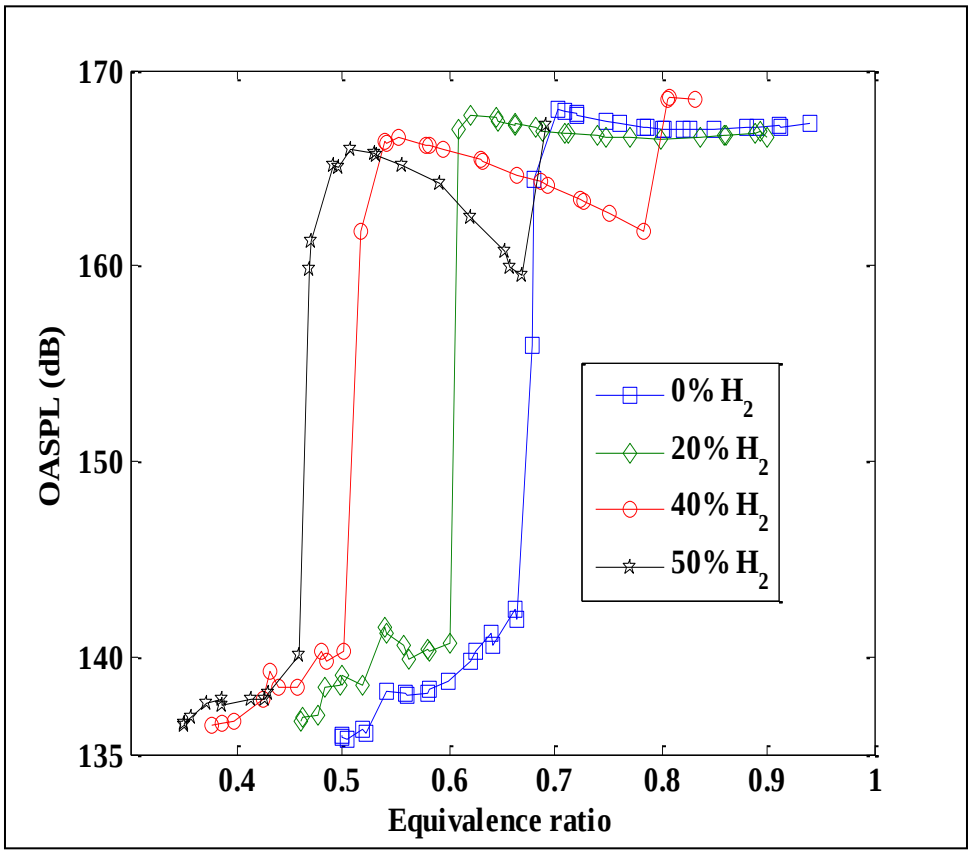

Figure 4.2: Overall sound pressure level at 0.11m from the choke plate for different H_2 compositions.

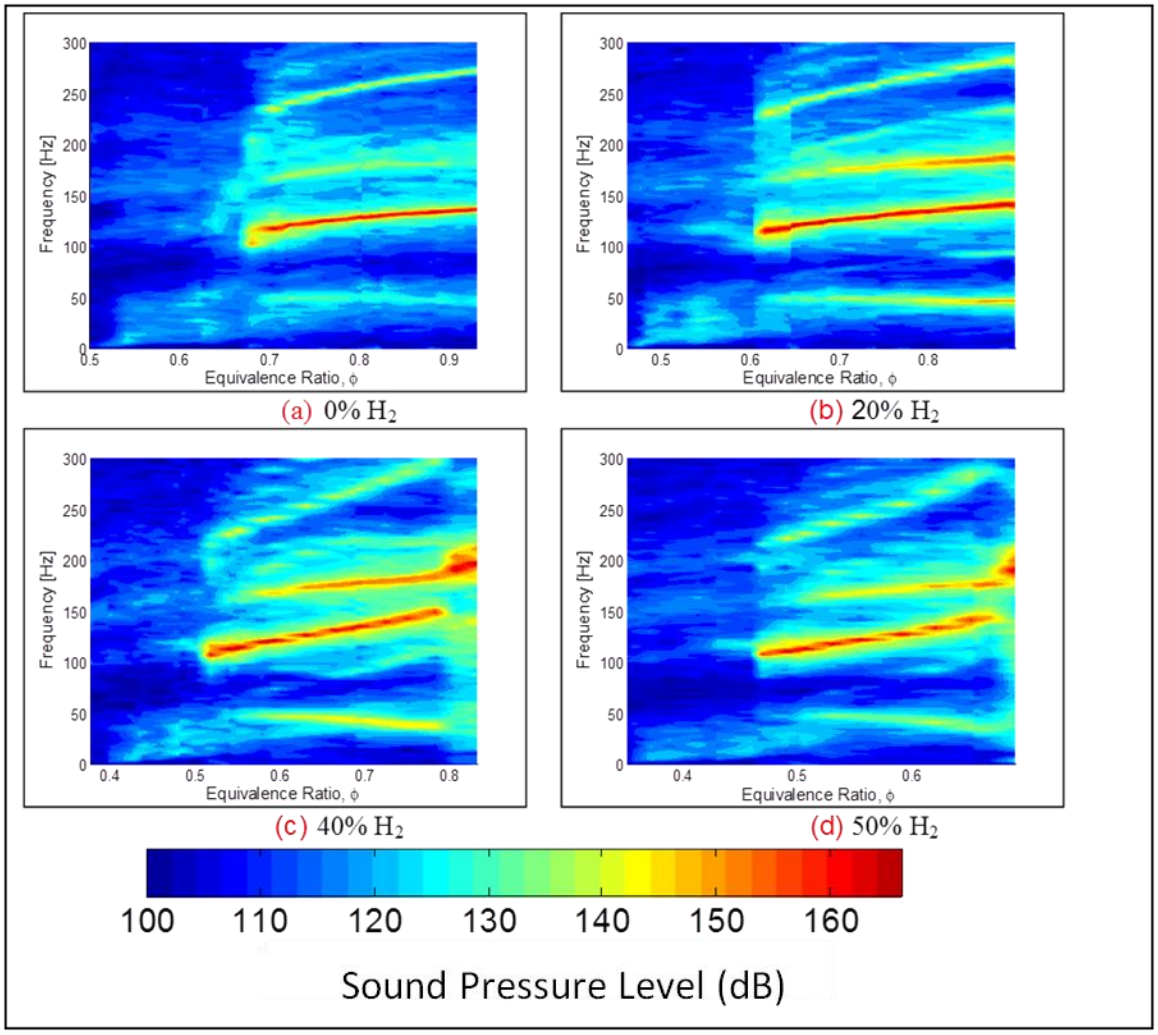

Figure 4.3: Frequency spectral map of the sound pressure level for different H_2 compositions.

4.4.2 Heat Release

The heat release at different operating conditions is quantified by the normalized amplitude of the Chemiluminescence intensity. Figure 4.4 shows the normalized Chemiluminescence intensity at conditions corresponding to those discussed in Fig.4.2. Similar trends observed in the OASPL (Fig. 4.2) were also observed including the transition points. Substantial heat release was observed at the transition point necessitating a sudden increase in the resonance frequency and pressure level of the combustor. There is a shift in the intensity curves to the region of lower equivalence ratio

as the hydrogen concentration in the fuel mixtures increased, similar to those observed in the pressure response curves. There is also an observed downward trend in the normalized intensity as the combustor approach the flash back limit despite the relatively constant pressure amplitude. Though the CH* signal which is used as the surrogate for the heat release increases with increase in the equivalence ratio. The decrease can be attributed to the fact that the Chemiluminescence intensity is normalized with its mean value which increases with increasing equivalence ratio. Figure 4.4 shows the instantaneous Chemiluminescence intensity and pressure oscillation in the combustor for a case of $0\%H_2$ at $\emptyset = 0.7$ corresponding to mode II. It can be seen that the Chemiluminescence and pressure are nearly in phase. The phase difference between the intensity and pressure is, thus, quantified and presented in section 4.4.4. The phase between heat release rate and pressure oscillations can be used to identify the degree of the thermo-acoustic coupling in the combustor.

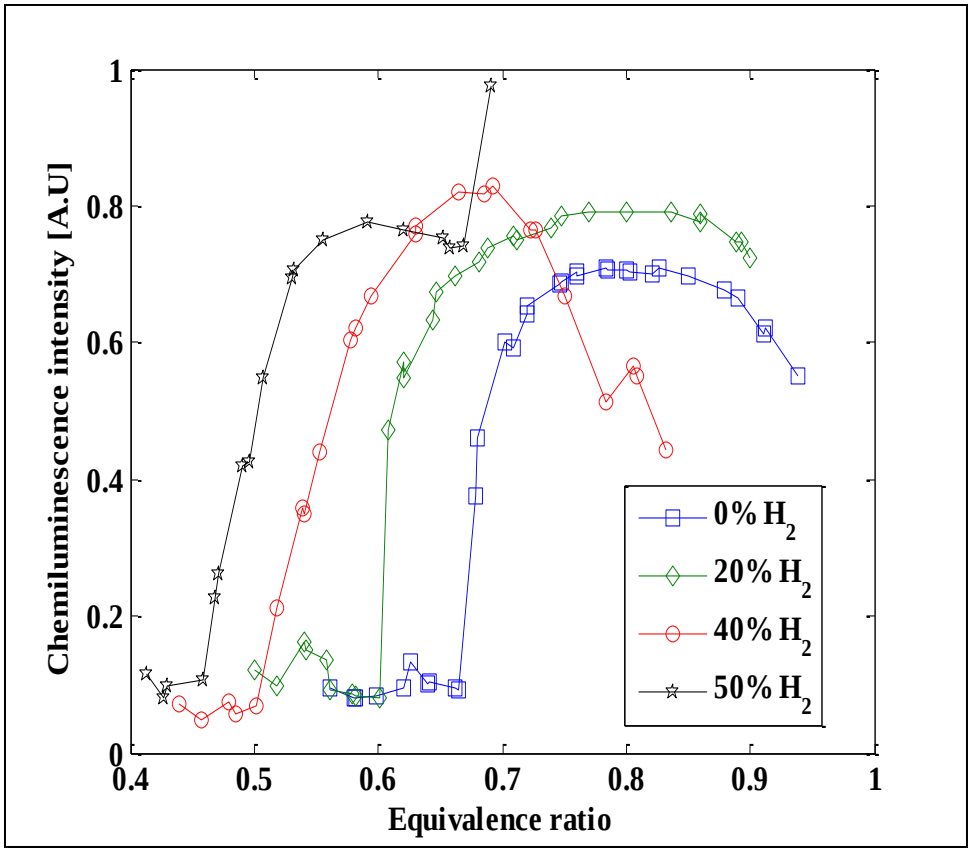

Figure 4.4: Normalized Chemiluminescence intensity amplitude for different H_2 compositions.

4.4.3 Flame Images

The phase averaged Chemiluminescence images highlighting the dynamic nature of flame motions for Mode II instability is presented in Figure 4.6. The images were taken at 500Hz and an exposure time of 1.0 ms for mode II (0%H_2,$\emptyset = 0.7$). The images are assemblage of 40 images phase averaged at 45 degrees interval. The brightest images, corresponding to the maximum heat release is observed at an angle of 90.The length of the flame at this point is ≈ 1.5 of the combustor diameter, while, the length of the flame at an angle of 270 degrees is ≈ 0.5 of the combustor diameter. The dynamic change in the flame area and shape is responsible for the unsteady heat release and when in phase with

the pressure oscillation in the combustor will lead to the growth of the instability. Figure 4.7 shows the normalized intensity of the flame at different phase angles. The dynamics in the flame was earlier explained by Gounder et.al. [83]. They suggest that the increase heat release will cause the pressure in the chamber to rise which reduces the injection of fresh charges. The reduction in the fresh charges results in the decrease of the amount of heat release which leads to drop in the chamber pressure. The drop in the chamber pressure enables fresh charges to be admitted to the combustor and the next cycle begins.

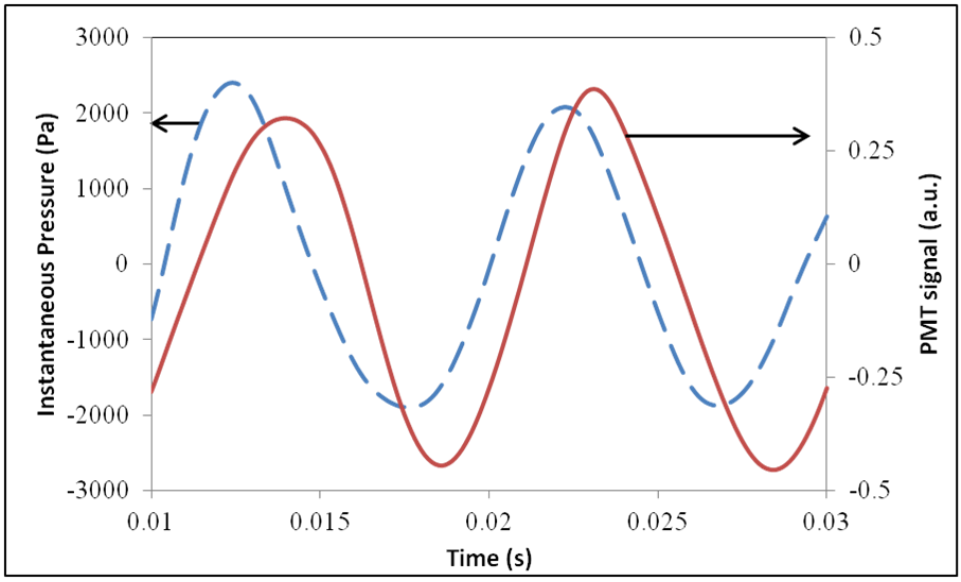

Figure 4.5: Instantaneous pressure and PMT signal with time

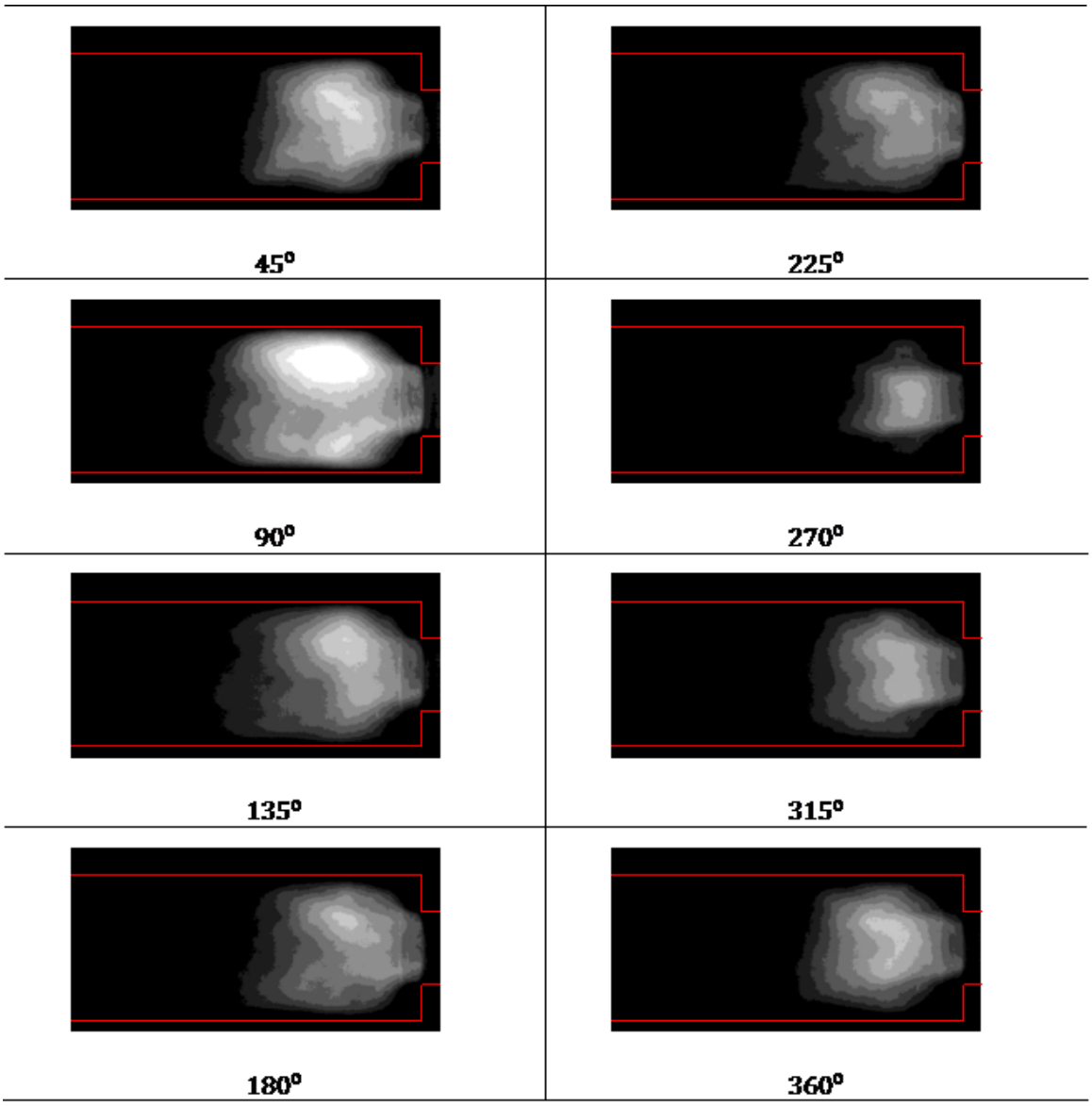

Figure 4.6: Phase resolved Chemiluminescence images for mode II instability ($0\%H_2$, Ø = 0.7)

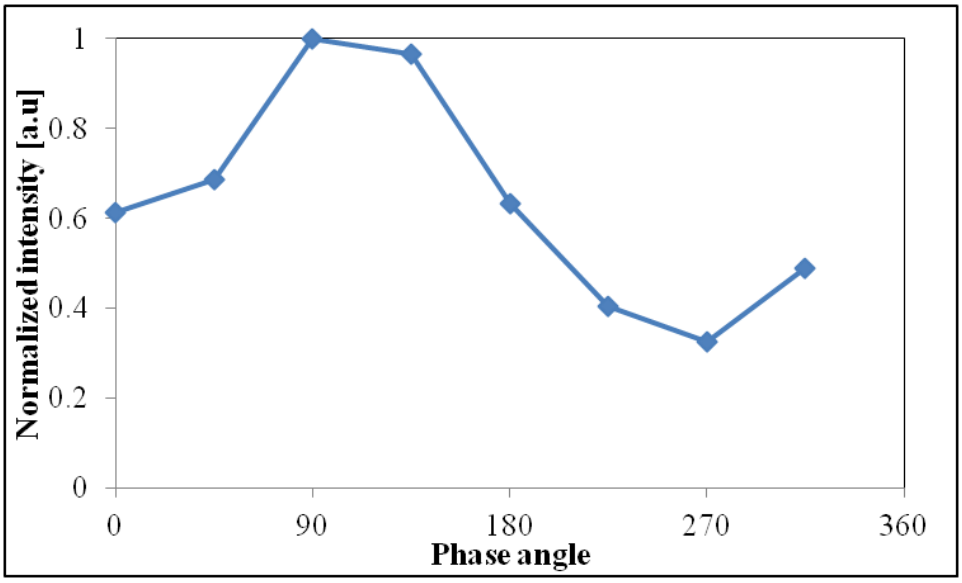

Figure 4.7: Normalized intensity of images presented in Fig.4.6

The effect of hydrogen contents in methane on the flame macrostructure is presented in Fig. 4.8. The flame was generally observed to have bubble flame structure at relatively low equivalence ratio. This flame oscillates at low frequency and low amplitude. At relatively higher equivalence ratio the flame transit to cone flame and is stabilized in the inner recirculation zone (IRZ). A further increase in the equivalence ratio lead the flame being stabilized in the outer recirculation zone (ORZ), thus, the flame became unsteady. This is accompanied by the flame oscillating at high frequency and high pressure amplitude similar to the case presented in Fig. 4.3. The instability is characterized by the appearance of flame in the ORZ. Similar flame structure was observed at different hydrogen contents in the fuel as presented. The increasing presence of hydrogen in the fuel mixtures, however, leads to early transition from one macrostructure to another. For instance at $\emptyset = 0.53$, flame with 0% H_2 has a bubble flame while flame with 10% H_2 and 20% H_2 has a V flame stabilized in the inner recirculation zone (IRZ) and outer

recirculation zone (ORZ) respectively. These observations are in line with the early transition observed in acoustic response and heat release at higher hydrogen contents.

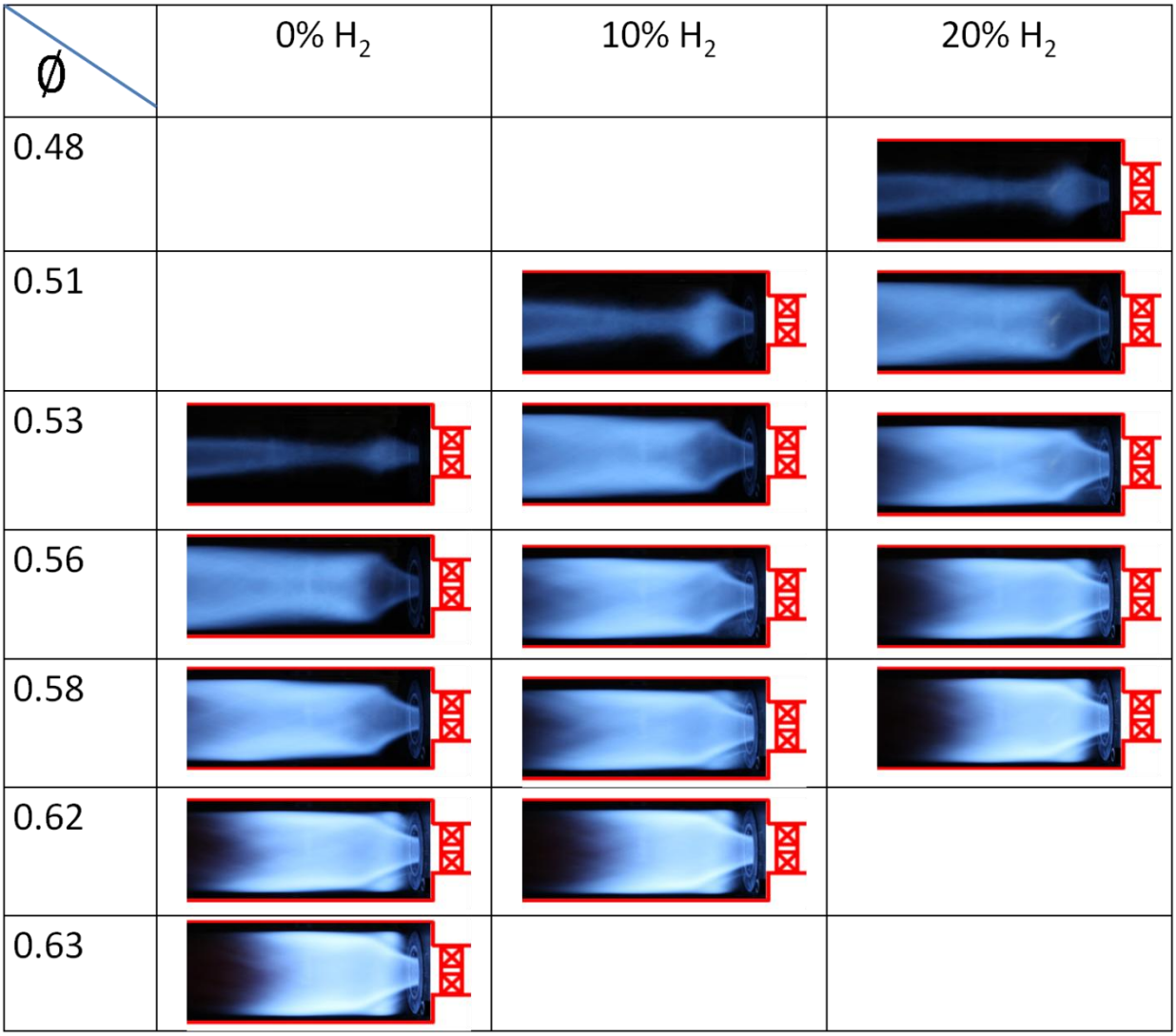

Figure 4.8: Flame images at different H_2/CH_4 compositions.

4.4.4 Phase Angle

The phase angle θ_{qp} between the heat and pressure oscillation has been used [91, 133] as a metric to identify the onset of instability. According to Raleigh criteria, the phase angle θ_{qp} for instability is expected to be in the range of: $-\frac{\pi}{2} < \theta_{qp} < \frac{\pi}{2}$.

The phase angle is computed according to equation (4.3).

$$\boldsymbol{\theta_{qp} = arg\left(\frac{\bar{q}(\omega_n)}{\bar{P}(\omega_n)}\right)} \quad (4.3)$$

Where $\bar{q}(\omega_n)$ and $\bar{P}(\omega_n)$ were obtained by taking the Fourier transform of the time varying pressure P(t) and Chemiluminescence intensity q(t) and ω_n is the frequency at which both $|\bar{P}(\omega)|$ and $|\bar{q}(\omega)|$ is maximum.

Figure 4.9 shows the phase angle θ_{qp} as a function of equivalence ratio at different compositions. The computed phase was colored with the peak frequency at each equivalence ratio. In all cases presented, the heat release was observed to lead the pressure such that $\theta_{qp} > 0$. This indicates that the heat release and the pressure oscillation are positively coupled. For flame with 0%H_2, weak coupling between the heat release and pressure was observed as the flame approaches instability. At $\emptyset = 0.68$, the phase angle approaches zero signifying that the heat release and pressure are in phase and suggesting a strong thermo-acoustic coupling of the flame. This point also signifies the transition from stable to unstable flame. A further increase in the equivalence ratio lead to increase phase angle signifies that the heat release is leading the pressure more rapidly. Despite similar amplitude of the OASPL the phase angle (Fig.4.9a) varies with equivalence ratio and frequency. These suggest that the phase can be quantitatively used in identifying the state of the combustor. Similar trend was observed at 20% H_2, the onset of instability however shift to the region of lower equivalence ratio (i.e. $\emptyset = 0.61$). At higher hydrogen content (40%H_2 and 50%H_2), the phase angle approaches zero at two different conditions (i.e. $\emptyset = 0.52$ and $\emptyset = 0.8$) for 40% H_2 representing two mode transitions. The first transition is from mode I to unstable mode II instabilities and the

transition from mode II to mode III instabilities. In the earlier, the instabilities are being triggered at the maximum coupling between the acoustic and heat release. While the later result from weak coupling that could not be sustain the instabilities and thus, lead to the transition to mode III. The range of transition from mode II to mode III instabilities was observed to reduce at 50%H_2. The hydrogen composition shift the critical equivalence ratio at which the transition occur suggesting that there exist a parameter that encapsulate the effect of the operation condition (i.e. the equivalence ratio and the hydrogen composition in the fuel) on the mode transition.

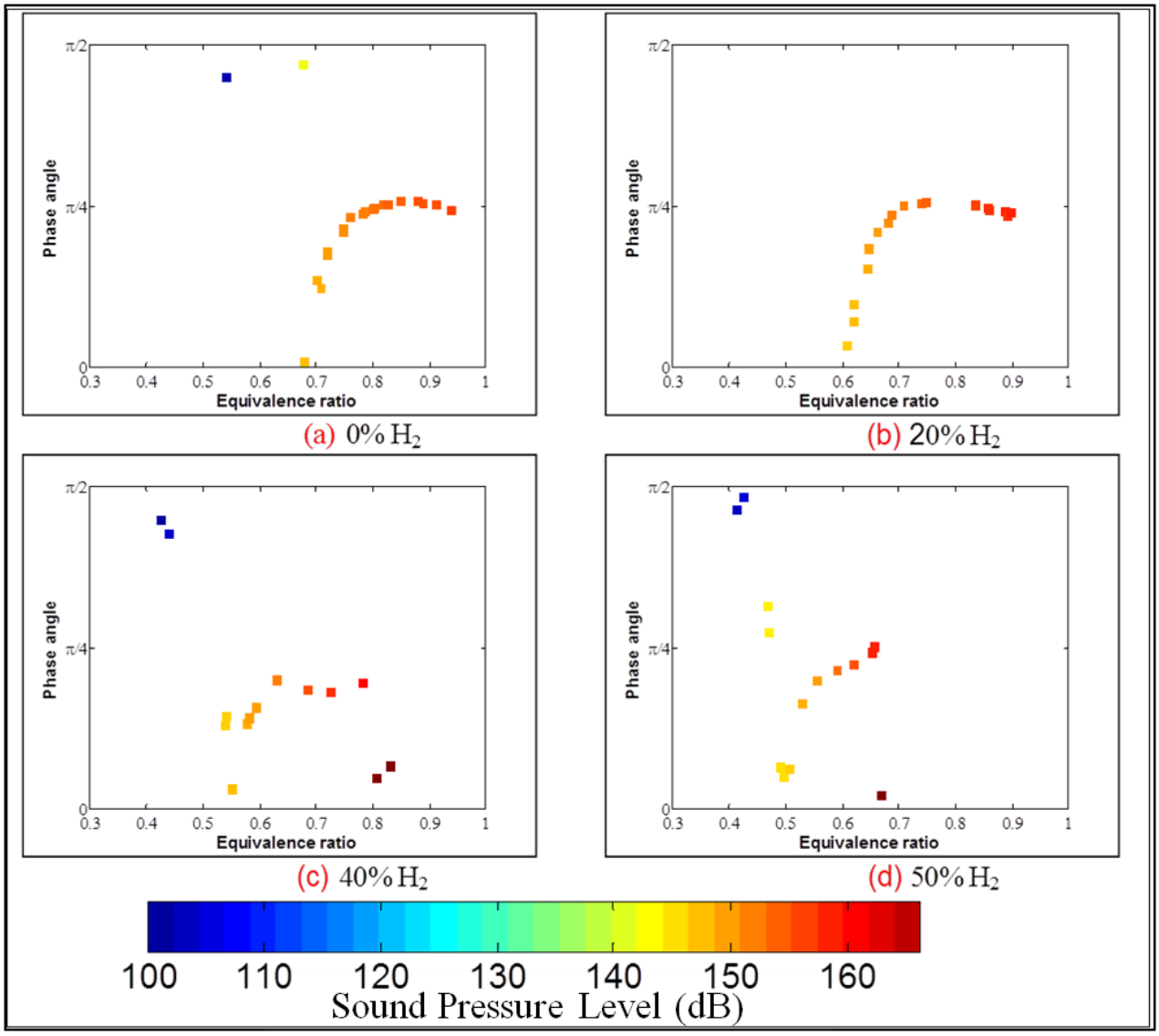

Figure 4.9: Phase angle for different H_2 compositions.

4.5 Scaling of Combustor Instability

By isolating other operating condition such as the inlet temperature, swirls number etc. The flame propensity to become unstable was observed to depend only on the percent of H_2 content in CH_4/H_2 mixtures. The increasing presence of hydrogen was observed to lower the critical equivalence ratio at which the transition occur. At this condition the

flame were observed to have the same macrostructure. This implies that the flame properties at this condition can be explored in combustion scaling. Speth[89] has previously used the strained flame consumption speed to collapse the OASPL for syngas fuel in a swirl stabilized combustor onto a family of curves. Hong[91] further their study by the use of non-dimensional strained consumption speed to correlate the phase angle at different compositions of propane –hydrogen and inlet temperature in backward step combustor. In both studies the consumption speed at given extinction stain rate is used in the scaling of the combustor. In the present study, the extinction strain rate is used to correlate the instability data of swirl stabilized combustor burning different compositions of CH_4/H_2. This is based on the assumption that the extinction strain rate is the property of the mixture and independent of combustor geometry. The extinction strain rate was computed using the extinction module coupled to the OPPDIFF model in CHEMKIN-PRO and GRI3.0 chemistry mechanism The procedure is based on the methodology described by Kee et al. [134].

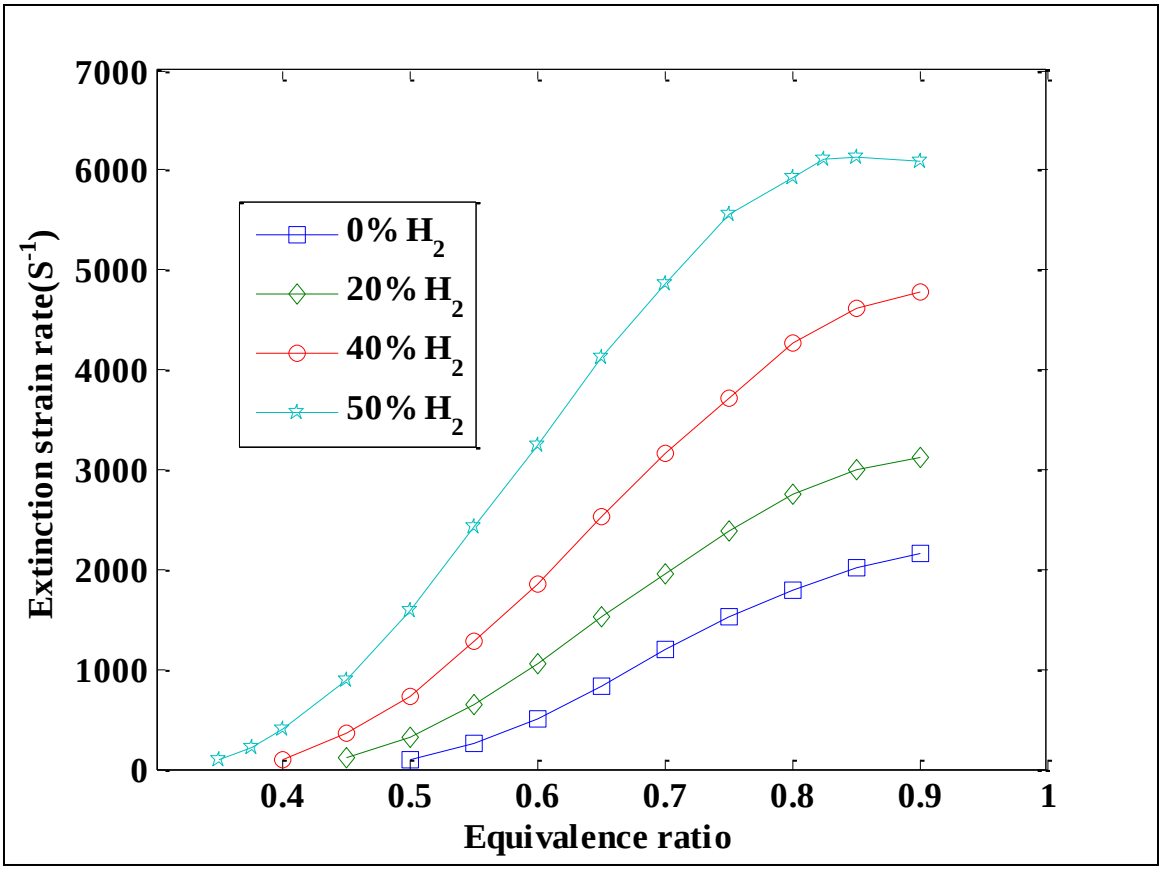

Figure 4.10: Extinction strain rate for different H_2 compositions.

Figure 4.10 shows the extinction strain rate plotted as a function of equivalence ratio for different H_2 compositions. Increasing the equivalence ratio increases the extinction strain rate for all the composition. Fuel burning richer have higher heat release and flame temperature that lead to increase flame resistance to extinction[135]. For a given equivalence ratio, increasing the hydrogen content in the CH_4/H_2 mixtures also increases the flame extinction strain rate. Hydrogen higher resistance to strain and extinction is due to its shorter time scale which make it to respond quickly to unsteadiness [136] under unsteady strain conditions.

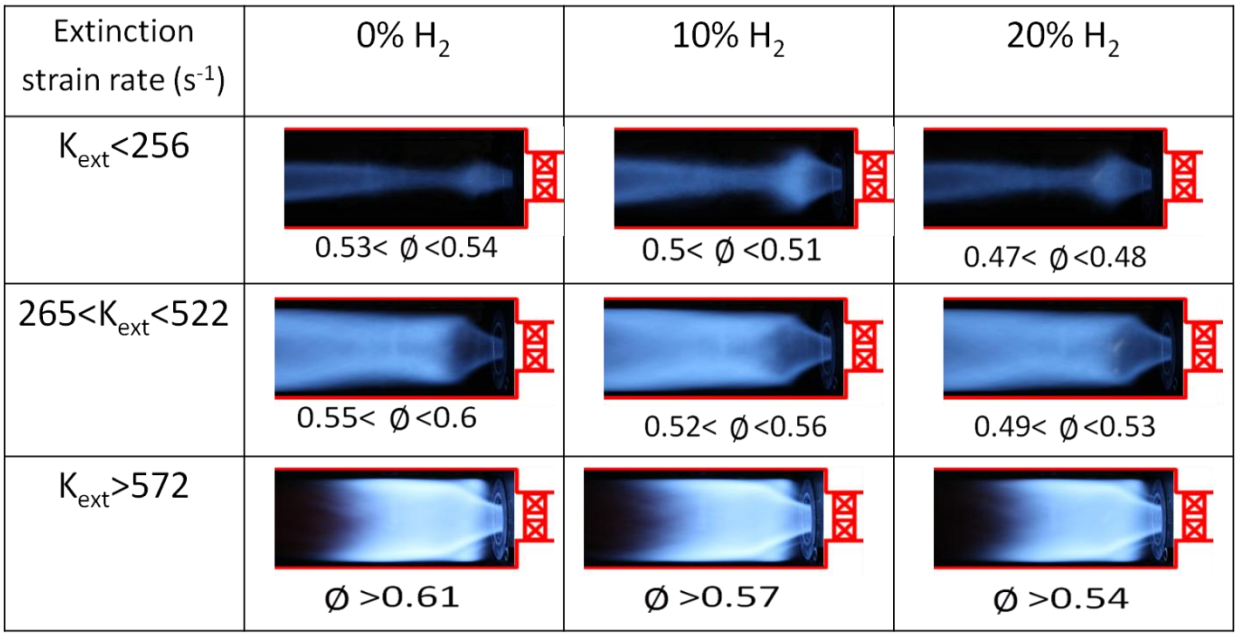

Figure 4.11: Flame shapes for different CH_4/H_2 mixtures plotted as a function of extinction-strain rate.

Different flame shapes presented in Fig.4.8 is now grouped based on the extinction strain rate shown in Fig. 4.10. Flame at different equivalence ratios and CH_4/H_2 mixtures that result in $K_s < 256s^{-1}$ will have a bubble flame macrostructure. Similarly, flame that have $K_s > 572s^{-1}$ will be stabilized in the ORZ. This implies that combination of operating condition that result in the same K_s will similarly have the same flame macrostructure. This observation was further extended to the pressure amplitude and phase angle presented in Fig 4.12 and 4.13 respectively. Figure 4.12 shows that the pressure amplitude can be scaled using the extinction strain rate suggesting that these transitions are linked to the flame shape and stabilization. The transition to first instabilities for CH_4/H_2 mixtures is observed at extinction strain rate of ~$1000s^{-1}$ at a given set of prevailing condition, while the transition to mode III instabilities occurs at K_s of ~$4300s^{-1}$. Mixture compositions of 0%H_2 and 20% H_2 could not achieve K_s=4300S s^{-1} at

temperature of 300K as observed in Fig. 4.10. Thus, the mode III instabilities are not visible at mixtures containing less than 40% H_2. Similar transition regime can be identified in phase angle at similar extinction strain rate. The collapse of the OASPL and phase data with the extinction strain rate implies that the stability of the combustor and its acoustic foot print for different operating conditions can be encapsulated in the extinction strain rate. This property can be used in the scaling of the combustor instability. It can be concluded that, by knowing the extinction strain rate of the CH_4/H_2- air mixtures, the stability of the combustor under study can determined.

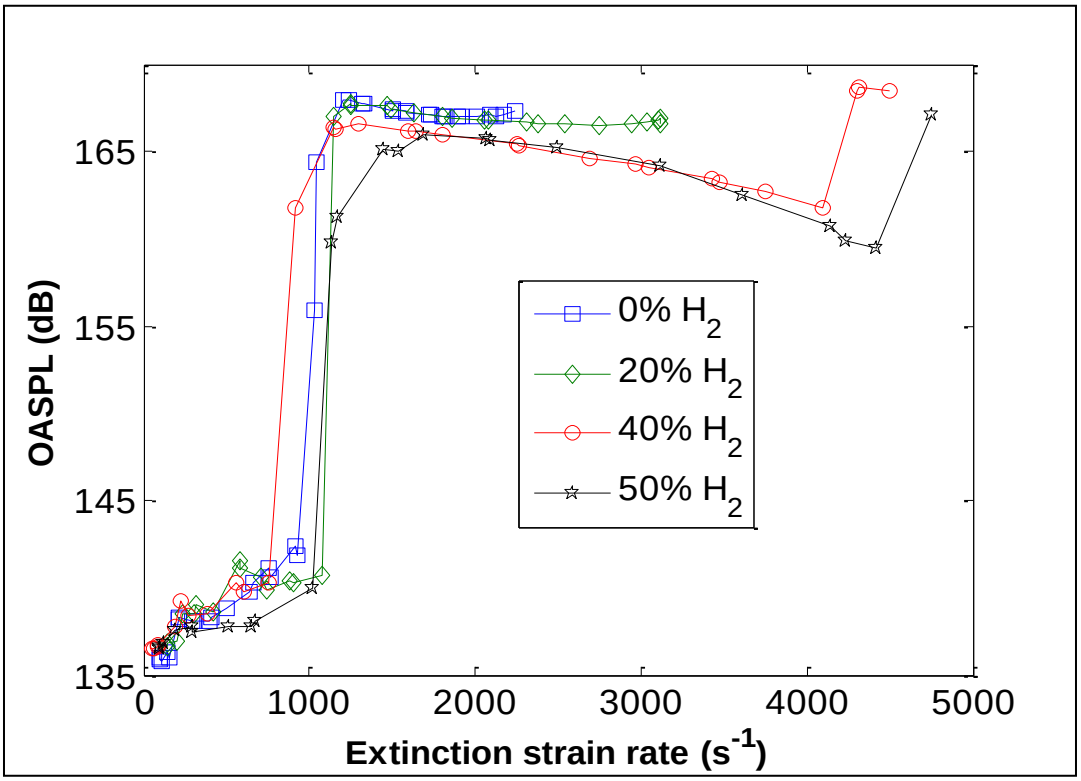

Figure 4.12: Overall sound pressure levels as a function of extinction strain rate.

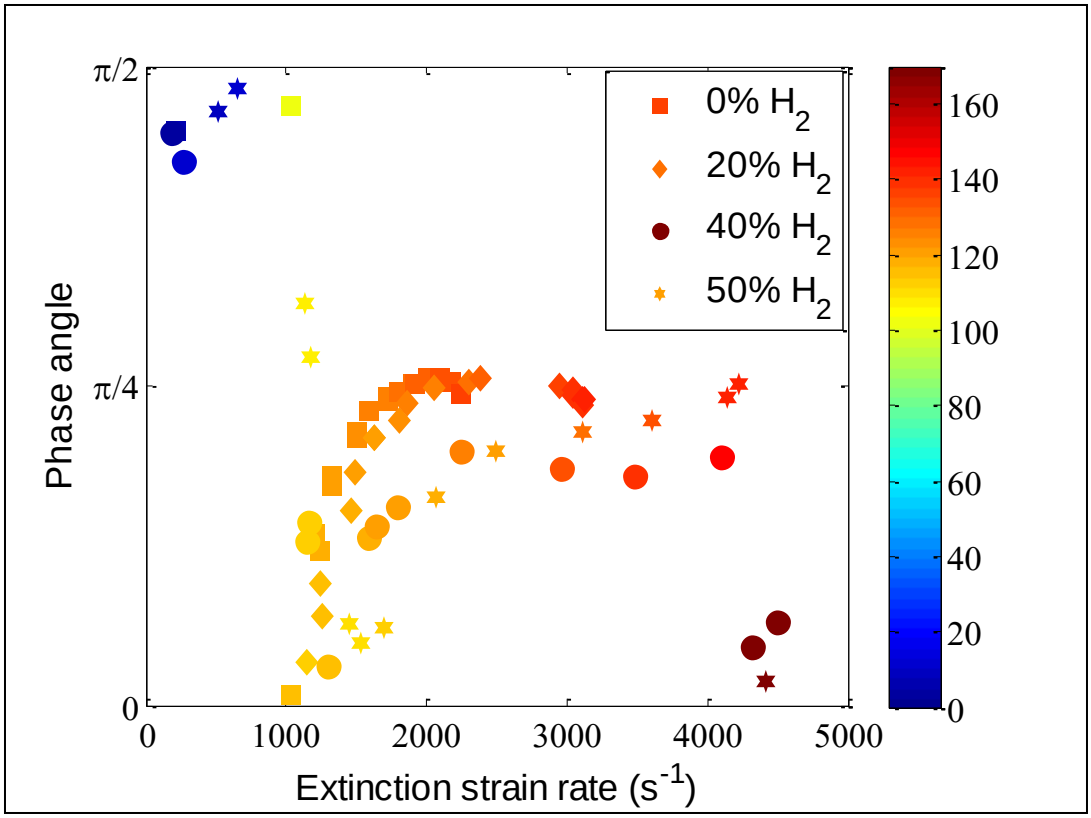

Figure 4.13: Phase angle as a function of extinction strain rate.

4.6 Acoustic Frequency

In this section, we are presenting the acoustic energy balance conducted to examine how these operating regimes are related to the acoustic natural frequency of the combustor using lumped acoustic elements. Figure 4.14 shows the schematic diagram of the swirl-stabilized combustor used in the acoustic modeling. The simplified form of the combustor is divided into six different blocks, with each block having constant acoustic impedance and cross-sectional area. The surface connecting two blocks is referred as an interface.

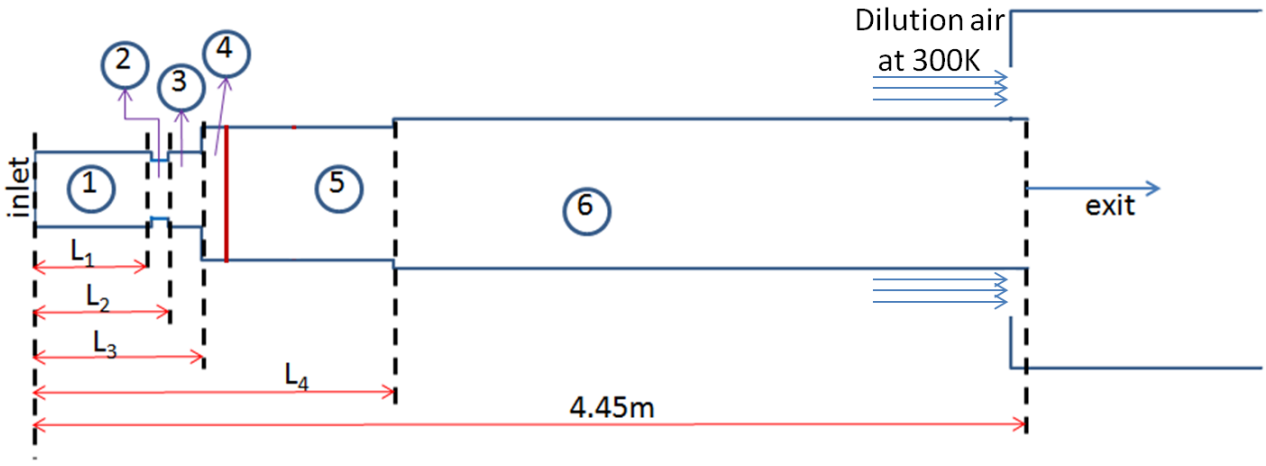

Figure 4.14: schematic diagram of the swirl-stabilized combustor used in acoustic model.

The combustor is divided to six blocks. For six blocks there will be 12 constants. The matching condition for the pressure (Eq.2.31) and velocity (Eq.2.32) at the interface will give 10 equations while the BC at the inlet and outlet of the combustor will give additional two equations.

The matching order for the pressure and the velocity in the combustor is implemented using equation presented in section 2.6.

For the first block:

The inlet BC is a choked orifice which can be modeled as

$$\hat{\boldsymbol{u}}_{\boldsymbol{i}}(\boldsymbol{x}=\boldsymbol{0})=\boldsymbol{0} \tag{4.4}$$

In the first three interfaces, there is only area discontinuity (i.e. change in cross sectional area). The matching condition for the pressure and velocity can be obtained for the momentum and mass conservation equation as,

$$\hat{\boldsymbol{P}}_{\boldsymbol{i}}(\boldsymbol{L}_{\boldsymbol{i}})=\hat{\boldsymbol{P}}_{\boldsymbol{i+1}}(\boldsymbol{L}_{\boldsymbol{i}}) \tag{4.5}$$

$$\boldsymbol{S}_{\boldsymbol{i}}\hat{\boldsymbol{u}}_{\boldsymbol{i}}(\boldsymbol{L}_{\boldsymbol{i}})=\boldsymbol{S}_{\boldsymbol{i+1}}\hat{\boldsymbol{u}}_{\boldsymbol{i+1}}(\boldsymbol{L}_{\boldsymbol{i}}) \tag{4.6}$$

Where S_i is the cross sectional area of the n^{th} block and L_i is the location of the i^{th} interface.

The natural frequencies of the combustor depend on two sets of parameters. The state variables (temperature, pressure and mixture composition) and the unsteady heat release rate. The un-steady heat release induces velocity jump and is model by the modified form of the n-τ model [137] as given in equation (4.7) Where n represents the gain and τ is the phase (time delay) of the flame transfer function

$$\dot{\boldsymbol{q}}' = \boldsymbol{\rho C_p (T_b - T_u) n u'(x, t - \tau)\delta\left(x - L_f\right)} \tag{4.7}$$

Where $\rho, C_p, T_b and\ T_u$ are the unburned mixture density, specific heat at constant pressure, burned gas temperature and unburned gas temperature, respectively.

The matching condition at the flame location is modeled as [91];

$$\widehat{\boldsymbol{P}}_{\boldsymbol{i}}\left(\boldsymbol{L_f}\right) = \widehat{\boldsymbol{P}}_{\boldsymbol{i+1}}\left(\boldsymbol{L_f}\right) \tag{4.8}$$

$$\widehat{\boldsymbol{u}}_{\boldsymbol{i+1}}\left(\boldsymbol{L_f}\right) = \widehat{\boldsymbol{u}}_{\boldsymbol{i}}\left(\boldsymbol{L_f}\right)\left(\mathbf{1} + \left(\frac{\boldsymbol{T_b}}{\boldsymbol{T_u}} - \mathbf{1}\right).\boldsymbol{n e^{i\omega\tau}}\right) \tag{4.9}$$

For the interface that account for temperature discontinuity, the matching condition is;

$$\widehat{\boldsymbol{P}}_{\boldsymbol{i}}(\boldsymbol{L_i}) = \widehat{\boldsymbol{P}}_{\boldsymbol{i+1}}(\boldsymbol{L_i}) \tag{4.10}$$

$$\widehat{\boldsymbol{u}}_{\boldsymbol{i}}(\boldsymbol{L_i}) = \widehat{\boldsymbol{u}}_{\boldsymbol{i+1}}(\boldsymbol{L_i}) \tag{4.11}$$

This shows that for acoustic temperature jump the velocity and pressure are continuous. Because the density and sound pressure also jump across the discontinuity, the matching condition will be implemented in block 5 and block 6. The interface between region 5 and 6 is assumed to be the location of the flame while other interfaces are due to area discontinuity. The flame length is very small compared to the acoustic length of the combustor.

The temperature distribution downstream of the flame location is computed to accounts for the temperature discontinuities due to heat losses from the combustor to the surroundings. A 2-D axisymmetric calculation using ANSYS fluent 12 was carried out to determine the temperature profile for region downstream of the flame. The obtained temperature profile was then curve fitted and serve as input in the acoustic model. Figure 4.15 shows the gas temperatures at different regions in the combustor for 0% H_2 at equivalence ratio of 0.5 and 0.9 respectively. These temperatures were extrapolated using the polynomial equation. The acoustic impedance variations are, thus, computed in the regions downstream of the flame based on these temperatures.

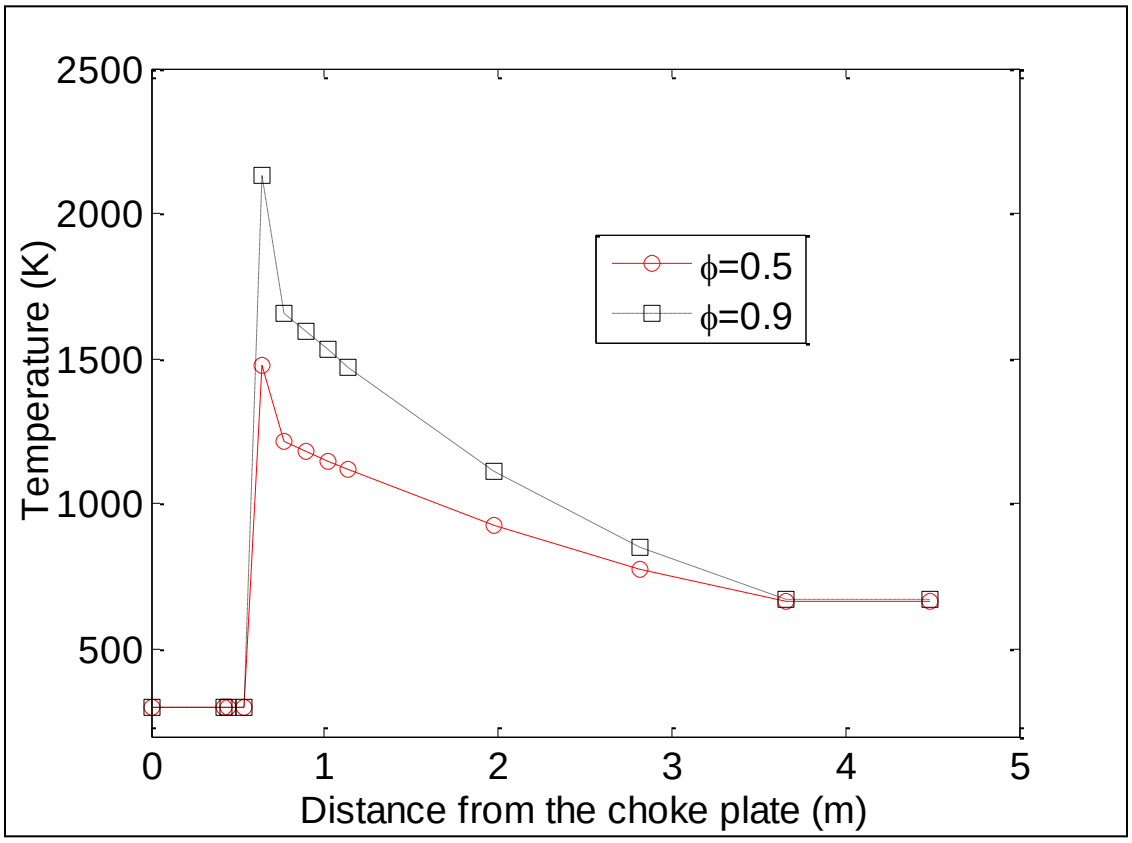

Figure 4.15: Temperature distribution in the combustor downstream of the flame location

The exit boundary condition is modeled as;

$$\widehat{\boldsymbol{P}}_{\boldsymbol{i}}(\boldsymbol{x}=\boldsymbol{L})=\mathbf{0} \tag{4.12}$$

By implementing the BC and matching order, A system of equation AX=0 is obtained. The equations are solved numerically and different values of Eigen-frequencies of the combustor are obtained. The effect of unsteady heat release for a given n and τ was initially isolated while varying the equivalence ratio and mixture compositions, thus, varying the state of the combustor. This was achieved by setting n=0. It was observed that combustor natural frequency is independent of the state variables with the exception of the geometrical features of the combustor. The effect of unsteady heat release on the natural frequency was thereafter studied. For gain of the order of 1, the natural frequency is obtained for varying τ between the values of 0 and 0.006 at interval of 0.001. The limit of τ is set such that $0 < \omega\tau_{uq} < 2\pi$, where $\omega = 2\pi f$. The gain was then increased to an order of 2 and all the calculations were repeated. We observed the effect of gain (n) to be insignificant on the acoustic frequency, this was similarly observed in a backward facing step combustor [91]. Figure 4.16 shows that the result obtained from the model forms a cluster of values depending on different values of n and τ. The model results are given as the shaded region with experimental values given as the symbol. The model was observed to predict reasonably the experimental result. The predicted result also suggests that all the frequencies observed are purely acoustic frequencies.

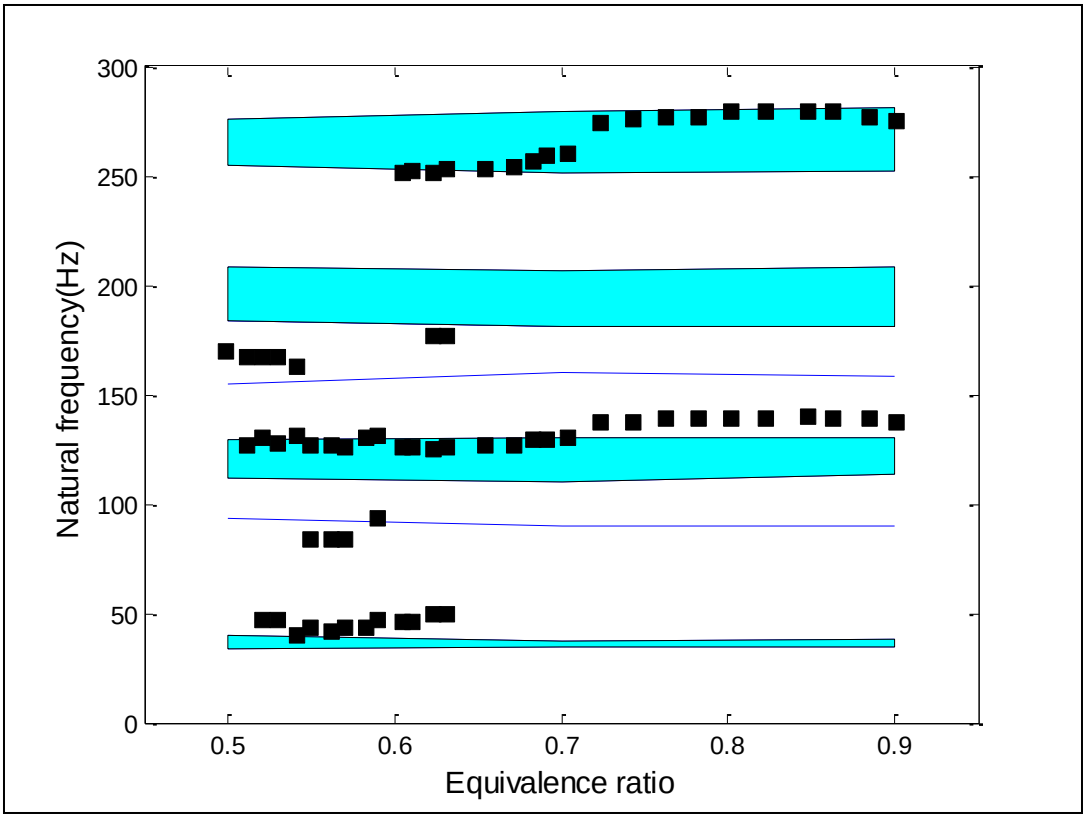

Figure 44.16: Acoustic frequencies of the combustor as predicted by the model (shaded areas and continuous line). The experimental data are overlaid using dark squares.

CHAPTER 5

NUMERICAL STUDY OF FLOW IN A MODEL GAS TURBINE COMBUSTOR

The numerical study of combustion characteristics and emission for model gas turbine combustor experimentally reported in chapter 3 is presented in this section. The numerical calculations were carried out for selected global mechanisms and validated against experimental results. The effect of heat transfer at the wall, swirler angle and preheat temperature was thereafter investigated.

5.1 Computational Scheme

A 2-D axisymmetric condition was used to model the combustion in the model gas turbine combustor because of the axial symmetry of the combustor. Additionally, the combustor axis of the flow was parallel to the gravity force. A schematic diagram of the computational geometry of the combustor is given in Fig. 5.1. More than 70,000 structured, non-uniform grid meshes were used to model the combustor. More cells are used in the high property gradient region (i.e., vicinity of the wall, inlet and outlet) to minimize false diffusion errors.

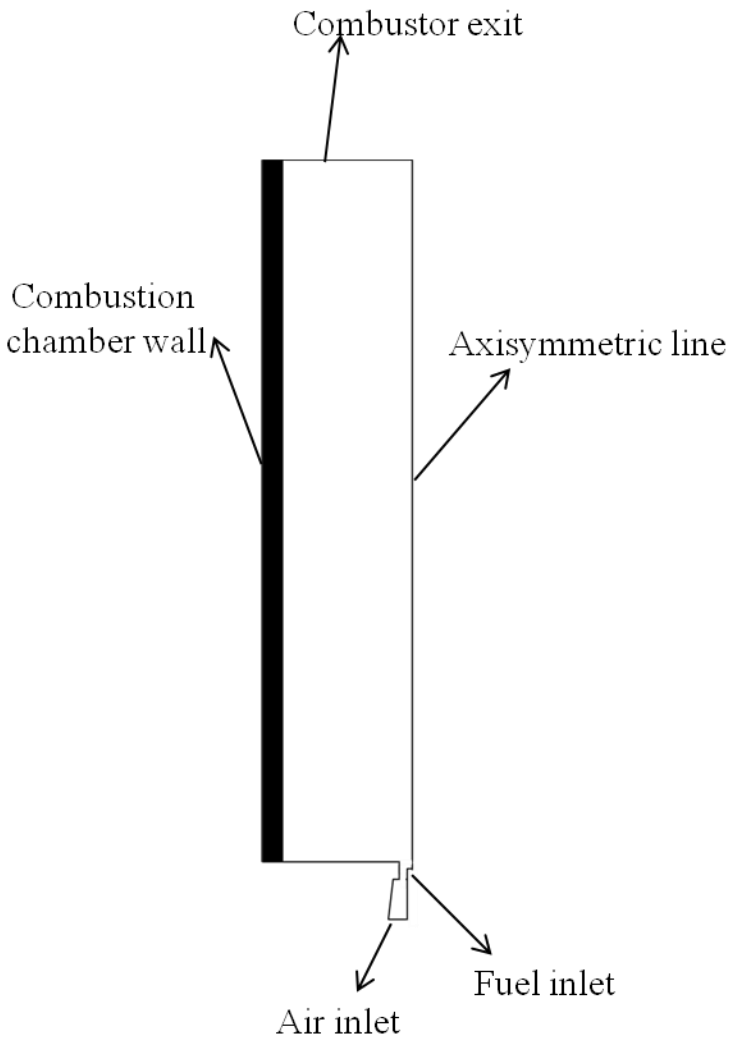

Figure 5.1: Schematic of the computational domain

5.2 Combustion Chemistry

The combustion is modeled using a global chemical mechanism with the one-step model by Westbrook and Dryer [93], a two-step mechanism with an irreversible CO/ CO_2 step (2sCM1) and a two-step mechanism with reversible CO /CO_2 step (2sCM2). The 2sCM1 [68, 138-140] and 2sCM2 [141-143] models have been extensively used in methane and natural gas combustion modeling. Boudier [143] reported that the laminar flame speeds

and the adiabatic flame temperatures obtained using 2sCM2 give a good agreement with the GRI 3.0 mechanism in the lean region (Ø= 0.5-0.8). Our studies, however, indicate that 2sCM2 significantly under-predicts the temperature under ultra-lean conditions in turbulent reacting flow (see section 5.4). Thus, we modified the 2sCM2 reaction mechanism by optimizing the reaction order for oxygen, under ultra-lean combustions (see Table 5.1). This optimization was based on the assumption that reducing the reaction order of O_2 relative to CH_4 and CO increased the reactivity of these gases (CH_4 and CO). Details of the optimization procedure are not given in this paper. The details of the reaction mechanisms used in modeling methane oxidation studied and their Arrhenius constants are summarized in Table 5.1. In modeling the oxidation of hydrogen-enriched methane, the 1-step global mechanism for hydrogen developed by Marinov et al. [144] (see Table 5.2) was incorporated with the respective global reaction mechanisms of methane given in Table 5.1.The obtained equations were used to model the combustion of hydrogen-enriched methane. De and Acharya [145] similarly incorporated the H_2 global reaction mechanism developed by Marinov et al. [144] into the 2sCM2 global reaction mechanism in the large eddy simulation (LES) modeling of hydrogen-enriched methane. They used the CH_4-H_2 coupled equations to perform parametric studies on the effects of the swirl number, premixedness and geometry in a premixed swirl combustor. Various global reaction mechanisms of CH_4 and H_2 have also been coupled and used in the CFD modeling of hydrogen-enriched methane [68, 141, 142, 146]. In the present study, the coupled equations of CH_4 and H_2 were variously used to numerically study the combustion characteristics and emissions of H_2-enriched CH_4.

Table 5.1 : Chemical reaction mechanisms for the oxidation of methane

	Reaction	A	E_a	Order	Equation #
Westbrook	$CH_4 + 2\ O_2 => CO_2 + 2\ H_2O$	1.3E+09	48400	$[CH_4]^{-0.3}[O_2]^{1.3}$	(5.1)
2sCM1	$CH_4 + 1.5\ O_2 => CO + 2\ H_2O$	2.8E+12	48500	$[CH_4]^{-0.3}[O_2]^{1.3}$	(5.2)
	$CO + 0.5\ O_2 => CO_2$	1.64E+13	39900	$[CO]\ [O_2]^{0.25}$	(5.3)
2sCM2	$CH_4 + 1.5\ O_2 => CO + 2\ H_2O$	2E+15	34500	$[CH_4]^{0.9}[O_2]^{1.1}$	(5.4)
	$CO + 0.5\ O_2 <= > CO_2$	1E+9	12000	$[CO]\ [O_2]^{0.5}[CO_2]$	(5.5)
Modified-2sCM2	$CH_4 + 1.5\ O_2 => CO + 2\ H_2O$	2E+15	34500	$[CH_4]^{0.9}[O_2]^{0.5}$	(5.6)
	$CO + 0.5\ O_2 <= > CO_2$	1E+9	12000	$[CO]\ [O_2]^{0.25}[CO_2]$	(5.7)

Note: The temperature exponent b is zero in all cases

Table 5.2 : Global reaction mechanism of hydrogen

	Reaction	A	E_a	Order	Equation #
Hydrogen (By Marinov et al.) [144]	$H_2 + 0.5\ O_2 => H_2O$	1.8E+16	35002	$[H_2]\ [O_2]^{0.5}$	(5.8)

Note: The temperature exponent b is zero in all cases; the parent mechanism identities were retained

5.3 Solution Procedure and Boundary Conditions

The partial differential equations for the conservation of mass, momentum, energy, radiation and species with the appropriate boundary conditions are solved numerically using ANSYS-FLUENT 14 codes. In addition, heat conduction within the combustion chamber wall was also considered. The pressure is discretized using the standard second-order scheme, whereas other equations are discretized using a second-order upwind scheme. The SIMPLE algorithm is used for pressure-velocity coupling. Further details of the calculation procedure can be found in previous studies [147]. The solution is said to converge when the maximum residual of the continuity, momentum, turbulent kinetic

energy and dissipation rate equations are less than 10^{-4}. The residuals for the energy, radiation and species and NO equations are set to 10^{-6}. The inlet velocity of the fuel and air is supplied depending on the operating condition of the combustor (fuel energy level, fuel composition and equivalence ratio). The effect of the air swirler is considered by implementing the appropriate axial and tangential velocity boundary conditions. The conjugate heat transfer is solved at the inner wall with a no-slip boundary condition and a no species flux normal to the wall surface applied. The mixed (convection-radiation) heat transfer equation given in equation (2.21) is implemented at the outer wall. The combustor is modeled to discharge to the surroundings at atmospheric conditions (i.e., zero gauge pressure).

5.4 Results and Discussion

5.4.1 Flame shapes

The calculated temperature field and images obtained under different operating conditions are shown in Fig. 5.2. At 0%H_2 and Ø=0.5, a deep blue flame was observed with the flame appearing in the outside recirculation zone (ORZ). The blue flame signified complete combustion and the absence of unburned hydrocarbon (UHC) in the flame. When the methane was enriched with up to 50% hydrogen (50%H_2: Ø=0.5), a yellow plume was observed in the flame. Similar observations were previously reported by Cozzi and Coghe [69] for the combustion of natural gas enriched with hydrogen. They attributed the yellowish plume to UHC based on their flame emission spectrum measurements. The UHCs observed in the hydrogen-enriched methane are due primarily to higher reactivity of hydrogen as compared to methane, thereby leading to the rapid

consumption of the oxygen in the reaction zone. This implies that the presence of hydrogen in the fuel mixture inhibits the oxidation of methane.

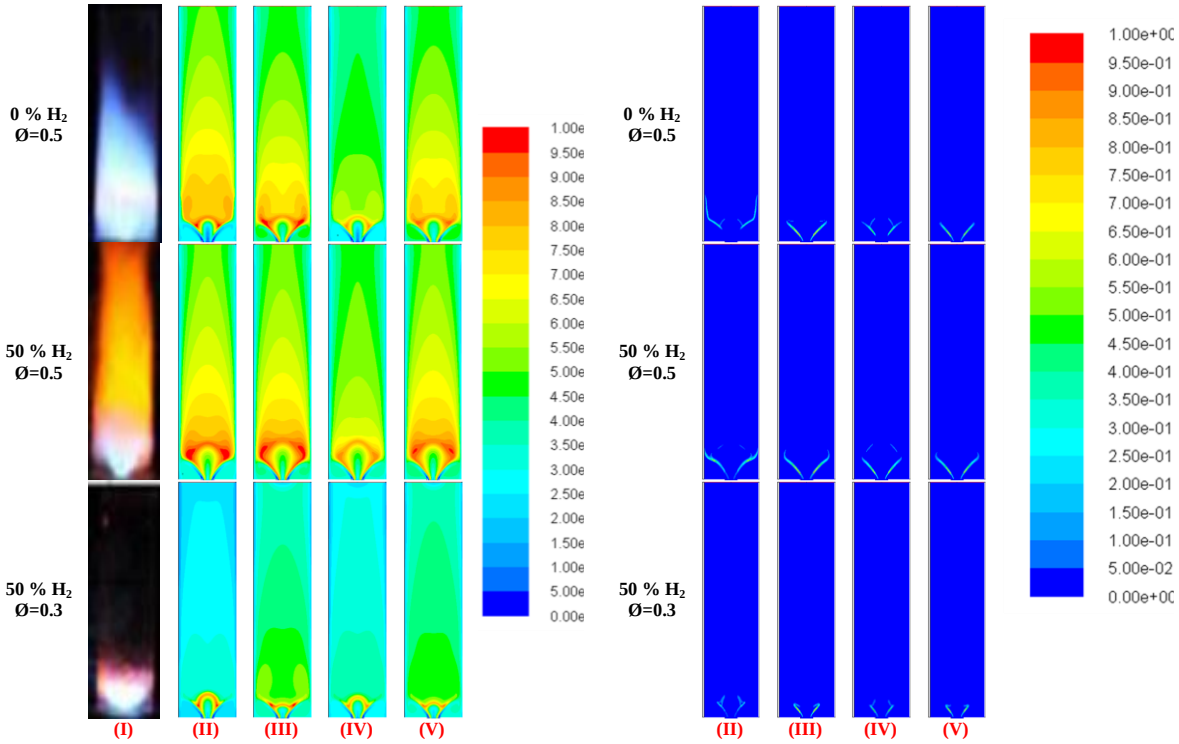

(a) Temperature **(b)** heat of reaction

Figure 5.2: Comparison between the experimental and numerical (contours of the temperature and heat of reactions) flame shapes at 3.67 MW/m^3.(I) Present experimental results (II) Westbrook, (III) 2sCM1, (IV) 2sCM2 and (V) Modified-2sCM2

Figure 5.3 shows the methane conversion for 0% H_2 and 50% H_2 plotted along the combustor axis. The depletion of methane is more rapid for the case of 0% H_2 as compared to 50% H_2. At a location in which nearly all the methane for the case of 0% H_2 has been consumed, only approximately half of the initial methane in the fuel mixture is consumed for 50% H_2 case. The role of hydrogen content on the flow-flame structure and its effect on UHCs and residence time is further discussed in section 5.4.3.

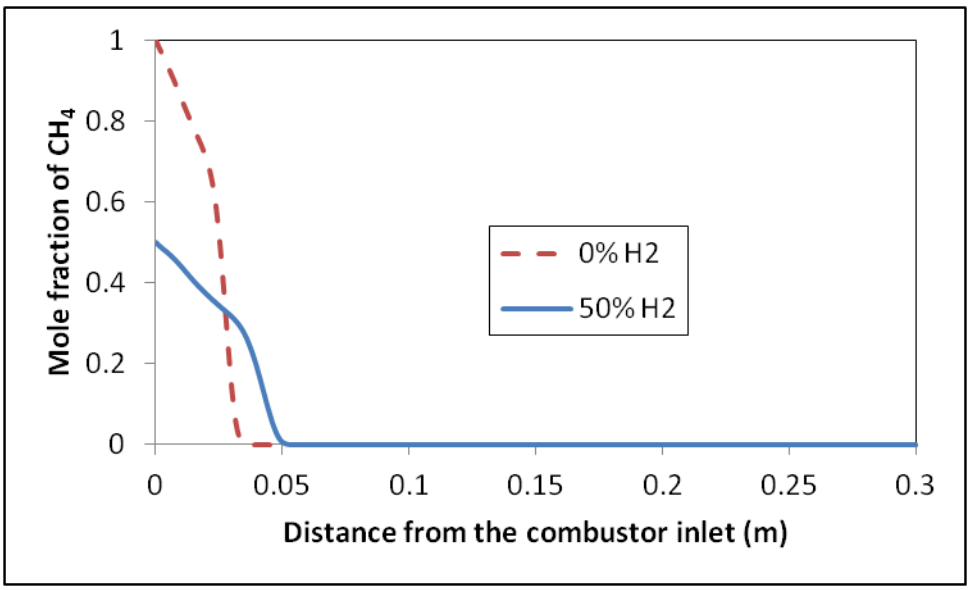

Figure 5.3: The predicted methane conversion along the combustor center line using Modified 2sCM1. Ø=0.5: 3.67 MW/m^3

The flame shapes are numerically characterized by the temperature and the computed heat of reaction. The highest flame temperature occurs in the heat release region and, thus, in the vicinity of the flame zone. The temperature contour shows that the high-temperature region occurs at distance away from the nozzle for the case of the Westbrook and 2sCM2 models. The location of the high-temperature region coincides with the heat of reaction zone (Fig.5.2b) thereby indicating that the flame is stabilized away from the nozzle (lifted flame). This result indicates that, under this condition (0% H_2: Ø = 0.5), the mechanisms (Westbrook and 2sCM2) could not capture the attachment of the flame to the nozzle. However, in the case of the 2sCM1 and Modified 2sCM2 models, the highest temperature and heat of reaction zone were observed to be from the nozzle exit signifying flame attachment to the nozzle. A high-temperature region was also observed in the ORZ (for the 2sCM1 and Modified-2sCM2 models) suggesting presence of hot combustion products (in the ORZ) as observed in the experiment. The flame attachment to the nozzle

was captured by all the mechanism under study (at 50%H_2: Ø=0.5) based on the temperature and heat reaction calculations shown in Fig. 5.2. A further increase in the equivalence ratio to 0.3 increases the Reynolds number from approximately 12,500 (at Ø=0.5) to approximately 19,000 (at Ø=0.3) based on the burner diameter, thus implying that increasing the equivalence ratio enhances the turbulence level in the combustor. This behavior leads to the formation of a compact flame near the fuel nozzle and a significant reduction in the amount of UHCs in the flame. Under this ultra-lean condition, all the studied reaction models studied captured the flame attachment to the nozzle, with a reduction in the reaction zone that was similar to the experimental observations. The blow off for pure methane at this combustor energy level is Ø=0.35. The Westbrook and 2sCM2 models could not achieve combustion at Ø < 0.45. This result indicates that these mechanisms (Westbrook and 2sCM2) are limited to the study of ultra-lean combustions of hydrogen-enriched methane.

5.4.2 Temperature profile

In this section, we discussed the temperature profile along the combustor center line. Figure 5.4 shows the axial temperature for different fuel energy. The temperature measurements were recorded starting at 10cm from the burner (combustor dump plane), to operate within the working range of the thermocouple. In general, the temperature was observed to decrease as the distance from the combustor burner increased. This is due to the mixing of the combustor product with the excess air supplied and the transfer of the heat to the surroundings via the combustor wall. As the combustor energy level increased (Fig. 5.4b and Fig. 5.4c), there is an observed increase in the temperature distribution in the combustor. This increase is attributed to the fact that the increase in fuel energy

produces a corresponding increase in the thermal energy release as well as an ensuing increase in the temperature distribution of the combustor. At an energy level of 2.75 MW/m^3, a similar trend in the temperature was observed between the experimental and numerical calculations. However, various discrepancies were observed near the flame. This area constitutes reactive regions in which most of the heat is released. The discrepancies could be attributed to the implemented kinetic scheme. Similar temperatures were, however, obtained in from the experimental observations and numerical calculations as the combustion products approached the combustor exit, indicating that the heat released is complete and that the produced temperature is due solely to heat transfer between the gases and the wall of the combustor. This result suggests that the applied discrete ordinate (DO) radiation model was able to correctly capture the radiation characteristics between the gases and the combustor walls. The one-step mechanism of Westbrook produced the largest over-prediction for the combustor temperature. This temperature over-prediction can be attributed to the absence of the intermediary species of CO in the reaction zone. The over-prediction of the temperature was similarly observed by Al-Abbas and Naser [148] in modeling a 100 kW furnace using the one-step global mechanism for propane. Figure 5.4 further shows that by changing the combustor flow rate (fuel and air) and by extension combustor energy level, the predictability of the models presented are consistent (especially at typical gas turbine conditions,> 3.45 MW/m^3).

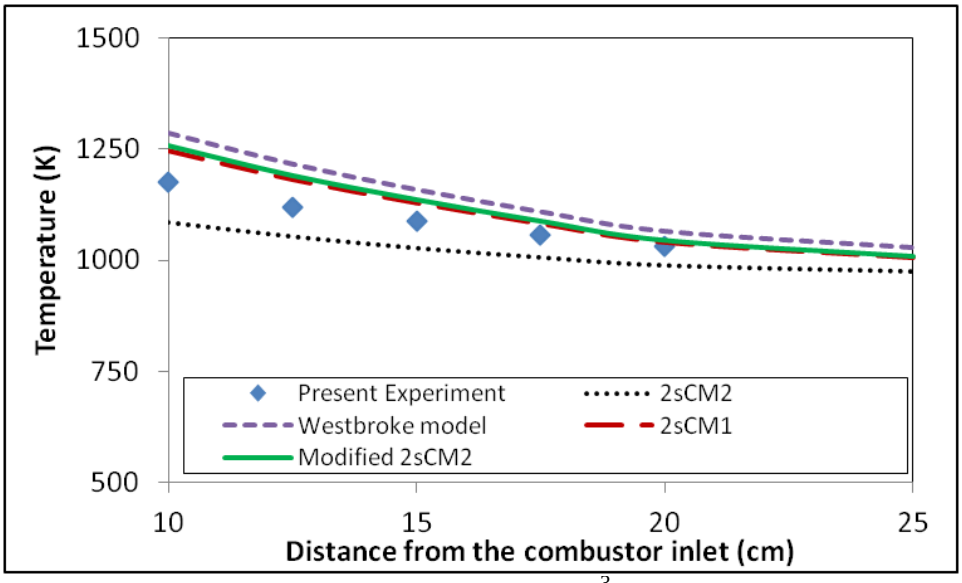

a) 2.75 MW/m^3

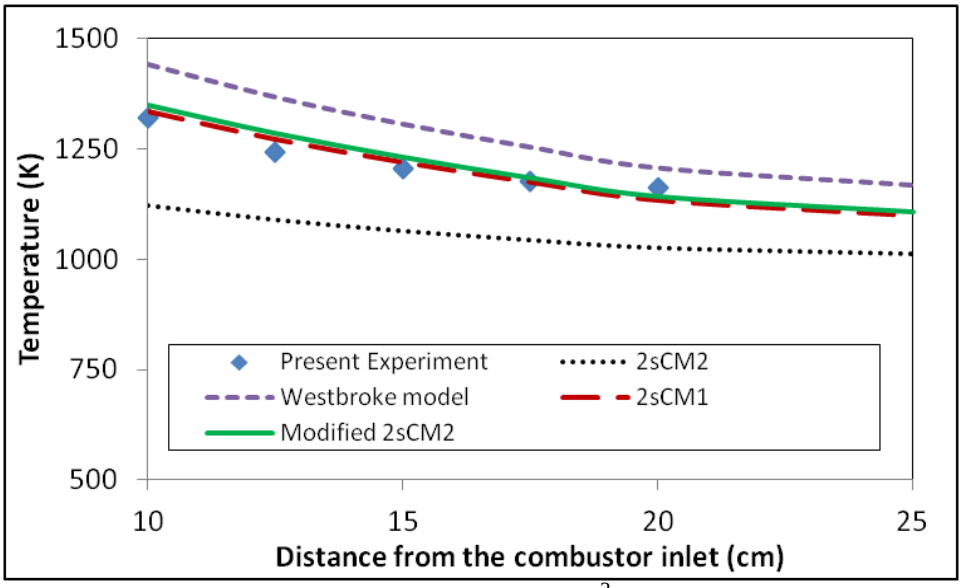

b) 3.67 MW/m^3

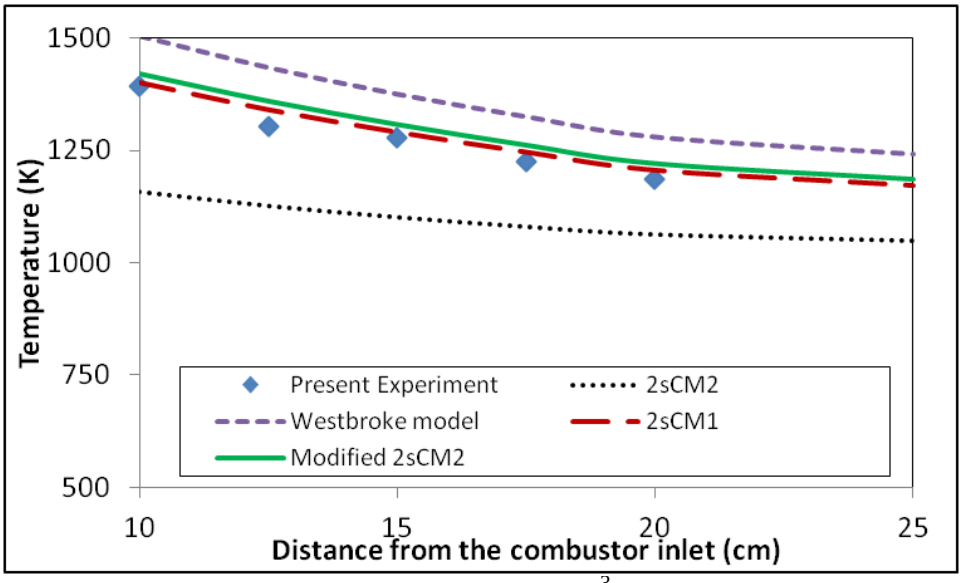

c) 4.59 MW/m^3

Figure 5.4: Experimental and predicted temperatures at 0% H_2: Ø=0.5

The use of the two-step mechanism (2sCM2) with a reversible reaction of CO/CO_2 produced an under-prediction of the temperature under ultra-lean conditions. To improve the prediction capability of this mechanism, we optimized the order for O_2 by reducing the rate of reaction of O_2 relative to CH_4 and CO in Equations (5.4) and (5.5), respectively. This optimization leads to the modified version of the 2sCM2 model presented in Table 5.1. The modified 2sCM2 model shows a substantial improvement in the predicted temperature and gave a similar prediction with 2sCM1 mechanism. At higher energy level (see Fig.5.4b and 5.4c), the discrepancies observed based on the over-prediction of the Westbrook mechanism become more significant. The over-prediction of temperature will substantially affect the prediction of the major species and will lead to the over-prediction of NOx. At this high energy level ($\geq$ 3.67 MW/m^3), the combustor operates within the range of a typical gas turbine combustor (> 3.45 MW/m^3). The predicted temperature by 2sCM1 and Modified-2sCM2 is within 5% of the

experimentally observed values, especially at a fuel energy input of 3.67 and 4.59 MW/m^3. This result suggests that these two mechanisms can be used to capture the temperature distribution in the model gas turbine combustor at 0% H_2.

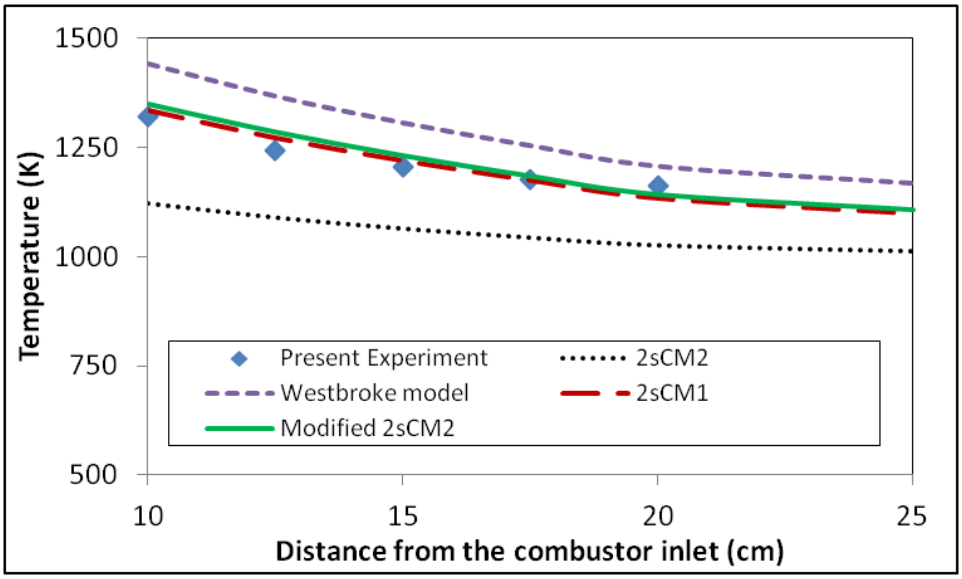

a) 0% H_2

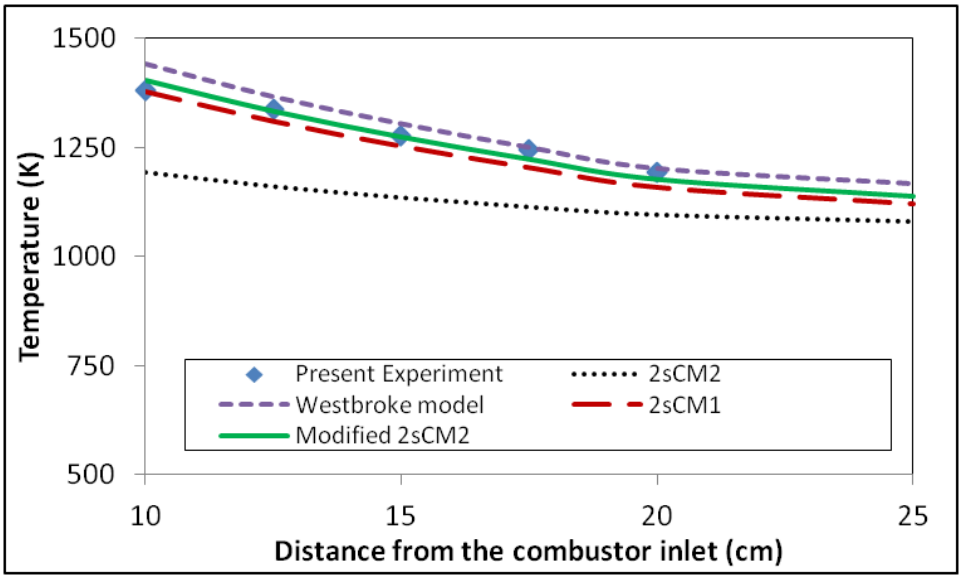

b) 30% H_2

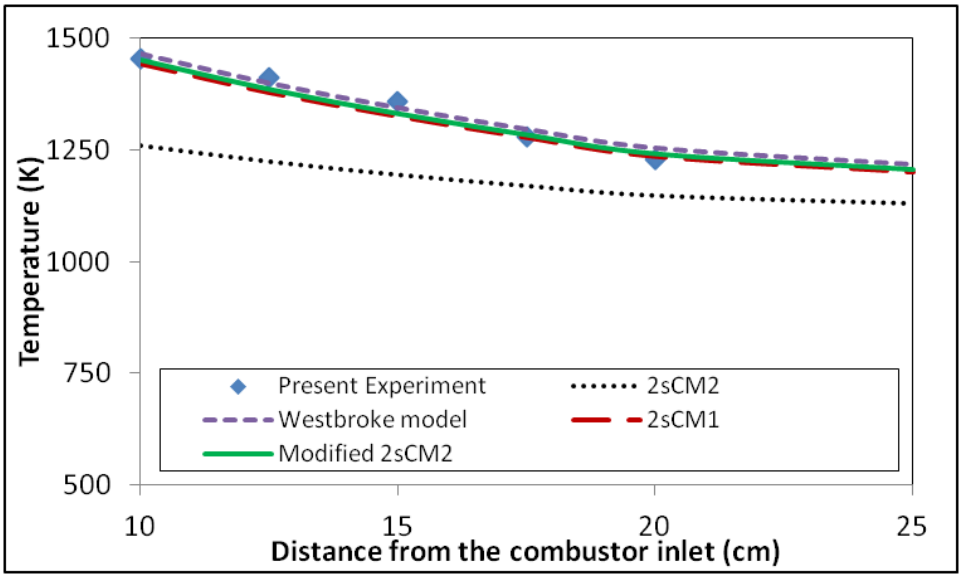

c) 50% H_2

Figure 5.5: Experimental and predicted temperatures at 3.67 MW/m^3: Ø=0.5

To model the effect of the hydrogen enrichment of methane on the combustion characteristics, the one-step global reaction mechanism of hydrogen developed by Marinov et al. [144] was coupled to the respective methane global mechanisms (Table 5.1). Figure 5.5 shows that the combustor temperature increases as the methane's hydrogen content increases. This increase in temperature is due to the higher adiabatic temperature of H_2 as compared to methane. The higher temperature observed in the combustion of hydrogen-enriched methane will increase unwanted NOx emissions. Thus, the combustion is performed under lean conditions to reduce the combustion temperature and to reduce NOx emissions. This reduction is imperative because the temperature is a driving factor for the thermal NOx formation. At 50% H_2 and Ø =0.3 (Fig. 5.6), all the studied mechanisms under-predict the temperature profile in the combustor. The 2sCM1 and Modified-2sCM2 mechanisms continue to predict the temperature within 10% of the experimental values.

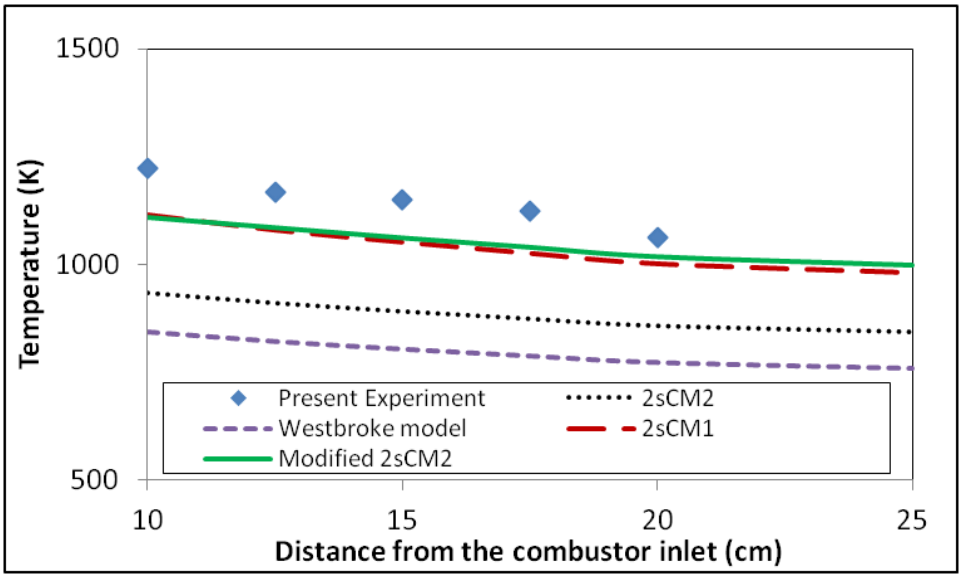
1500
1000
500
Temperature (K)
10
15
20
25
Distance from the combustor inlet (cm)
Present Experiment
2sCM2
Westbroke model
2sCM1
Modified 2sCM2

a) Ø=0.3

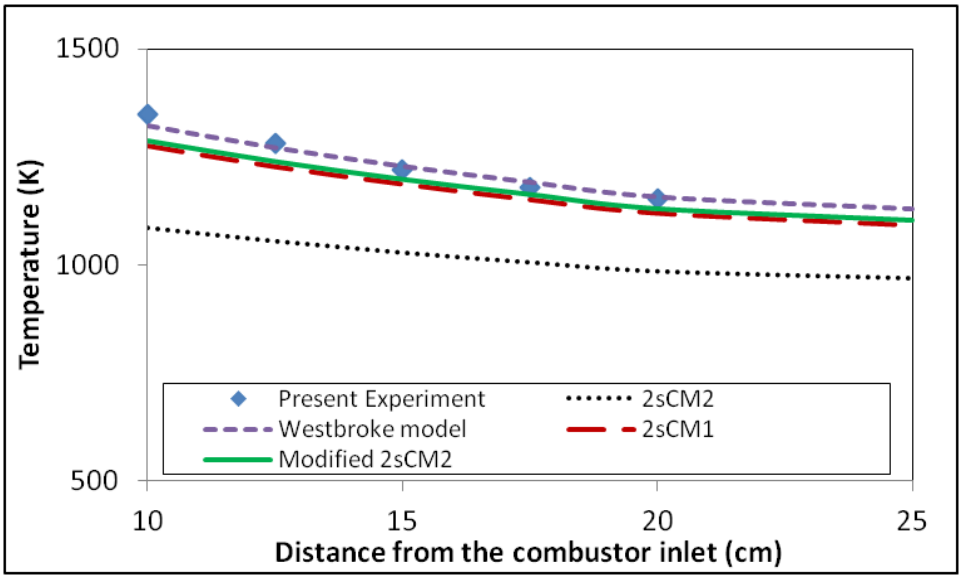
1500
1000
500
Temperature (K)
10
15
20
25
Distance from the combustor inlet (cm)
Present Experiment
2sCM2
Westbroke model
2sCM1
Modified 2sCM2

b) Ø=0.4

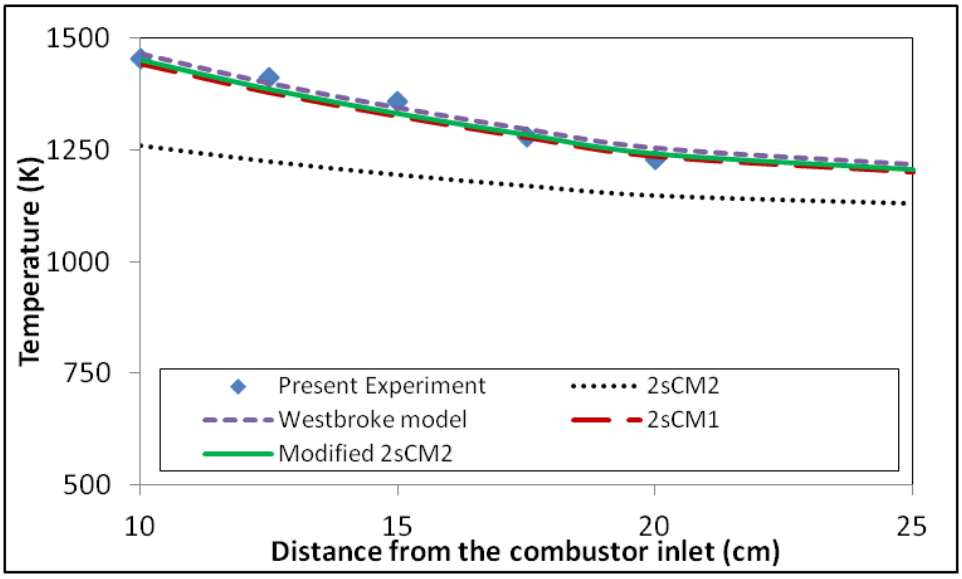

c) Ø=0.5

Figure 5.6: Experimental and predicted temperatures at 50%H_2: 3.67 MW/m^3

Because of the limited measuring range of the type-R thermocouple (0-1450°C) used in the experiment, we could not advance the thermocouple into the flame. Therefore, the maximum temperature, which is the controlling factor for species dissociation and NOx emissions, could not be directly measured. However, we present the maximum temperature obtained via the numerical calculations in Fig.5.7. The observed maximum temperature increases with increasing combustor energy level. The increased fuel energy input increased both the thermal energy released and the turbulence level in the combustor. For instance, at fuel energy inputs of 2.75 MW/m^3 and 3.67 MW/m^3, the Reynolds number at the combustor inlet is 9,200 and 12,300, respectively. These Reynolds numbers imply that the increased turbulence enhances the mixing of the fuel, air and combustion product and favors maximum heat release. The maximum combustor temperature was also observed to increase with increasing hydrogen content in the CH_4-H_2 mixture (Fig.5.7b) because of the higher reactivity and adiabatic temperature of

hydrogen compared to that of methane. The Westbrook mechanism produced the highest combustor temperature. This is due to the absence of intermediary species, such as CO, which is obtainable in other studied mechanisms. The 2sCM1 and Modified-2sCM2 mechanisms, which previously exhibited a similar flame structure (temperature contour) and temperature profile downstream of the flame, exhibited a significant difference in their predicted maximum temperature. The lower temperatures observed for the Modified-2sCM2 mechanisms are due to the reversible reaction in the oxidation of CO to CO_2. The tendency for the dissociation of CO_2 at high temperatures (i.e., the reaction zone), which tends to lower the maximum temperature, was not captured by the 2sCM1 mechanism. Bibrzycki and Poinsot [149] similarly reported that an insufficient CO_2 decomposition to CO could cause an increased predicted flame temperature.

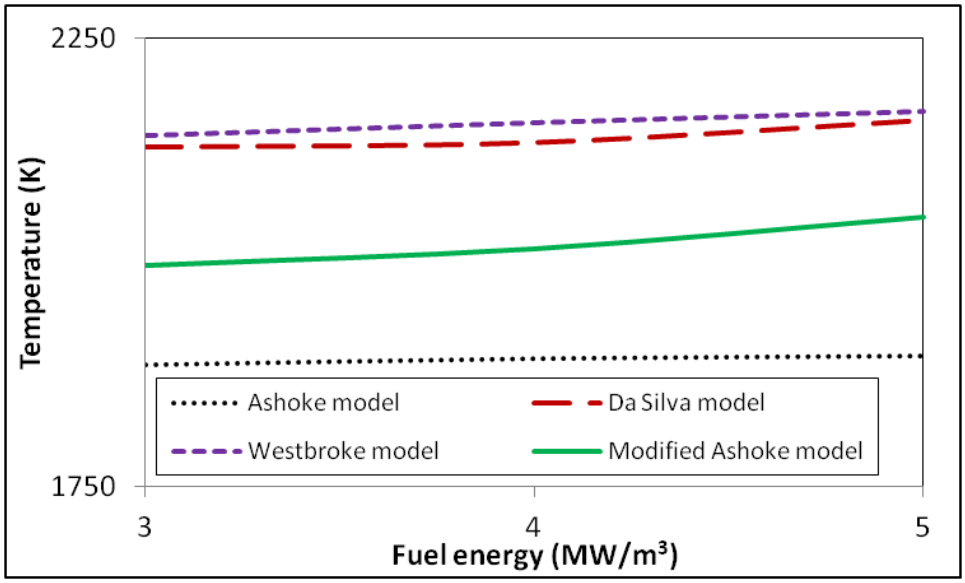

a) Effect of combustor energy level at 0%H_2: Ø=0.5

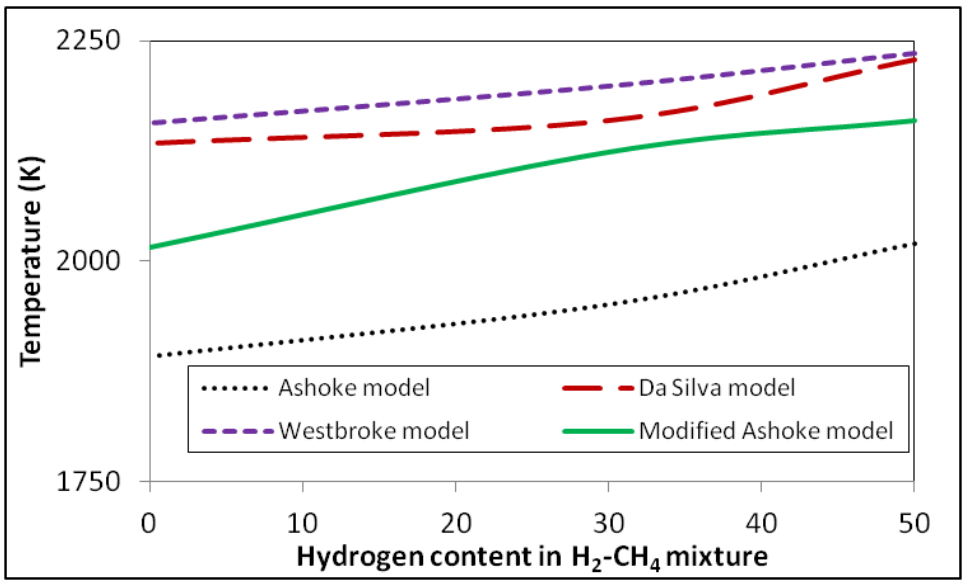

b) Effect of hydrogen contents in CH_4-H_2 mixture Ø = 0.5: 3.67 MW/m^3

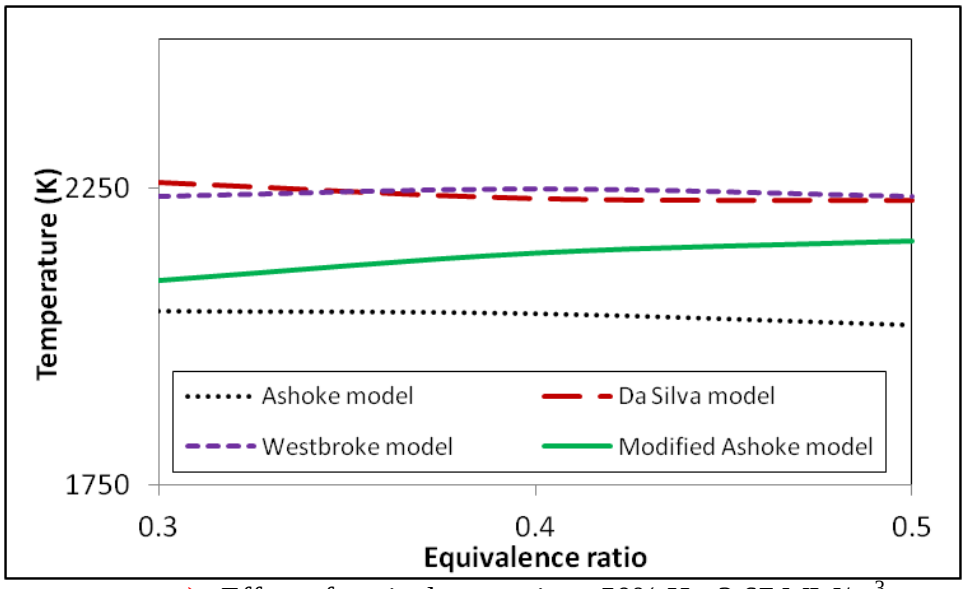

c) Effect of equivalence ratio at 50% H_2: 3.67 MW/m^3

Figure 5.7: Predicted maximum temperatures in the combustor at different operating conditions.

For the effect of equivalence ratio on the maximum temperature, three scenarios were observed. A nearly constant maximum temperature was observed in the Westbrook model, thereby suggesting that the maximum combustion temperature is independent of

the equivalence ratio. In the second scenario, a decrease in the maximum temperature in the 2sCM1 and 2sCM2 models was observed as the equivalence ratio increased. For the Modified-2sCM2 model, the maximum combustor temperature was observed to increase as the equivalence ratio increased. The trend observed in the Modified-2sCM2 model is expected because of the increase in the adiabatic temperature with increased equivalence ratio, whereas the trends predicted by the Westbrook, 2sCM1 and 2sCM2 models are not realistic.

5.4.3 Flow field

To study the effect of the fuel composition on the flow-flame structure, we overlaid the stream line of the flow pattern onto the computed heat of reaction and temperature contour for the case of 0 and 50% H_2 (Figure 5.8). We generally observed three different recirculation zone patterns: the outer recirculation zone (ORZ), the inner recirculation zone (IRZ) and the wake recirculation zone (WRZ). The ORZ is generally formed by the sudden expansion at the dump plane of the combustor. The IRZ is formed by the vortex break down of the flow. The WRZ is formed around the bluff body inserted into the fuel pipe. The contour of the heat of reactions shows that the flames are anchored at the inner shear layer of the flow (between the jet flow and the IRZ) and terminate at the onset of the IRZ. The disappearance of the active reaction zone is due to the vortex rolling up the flame. The vortex roll-up results in the recirculation of a high-temperature combustion product that preheats the incoming fresh charge to the combustor, thus stabilizing the flame. The higher mass diffusivity of hydrogen leads to an increase in the WRZ for 50% H_2 as compared to 0% H_2. The WRZ at 50% H_2 shifts the IRZ away from the combustor axis. The reduction in the size of the IRZ due to hydrogen addition led to a decrease in

the level of turbulence and the amount of hot gas re-circulated. Thus, a complete combustion could not be achieved under this condition. A strategy that could increase the size and strength of the IRZ, such as by increasing the swirl number, can be implemented to improve the combustion efficiency. To quantify the IRZ, we plotted the axial velocity along the combustor axis in Fig. 5.9.

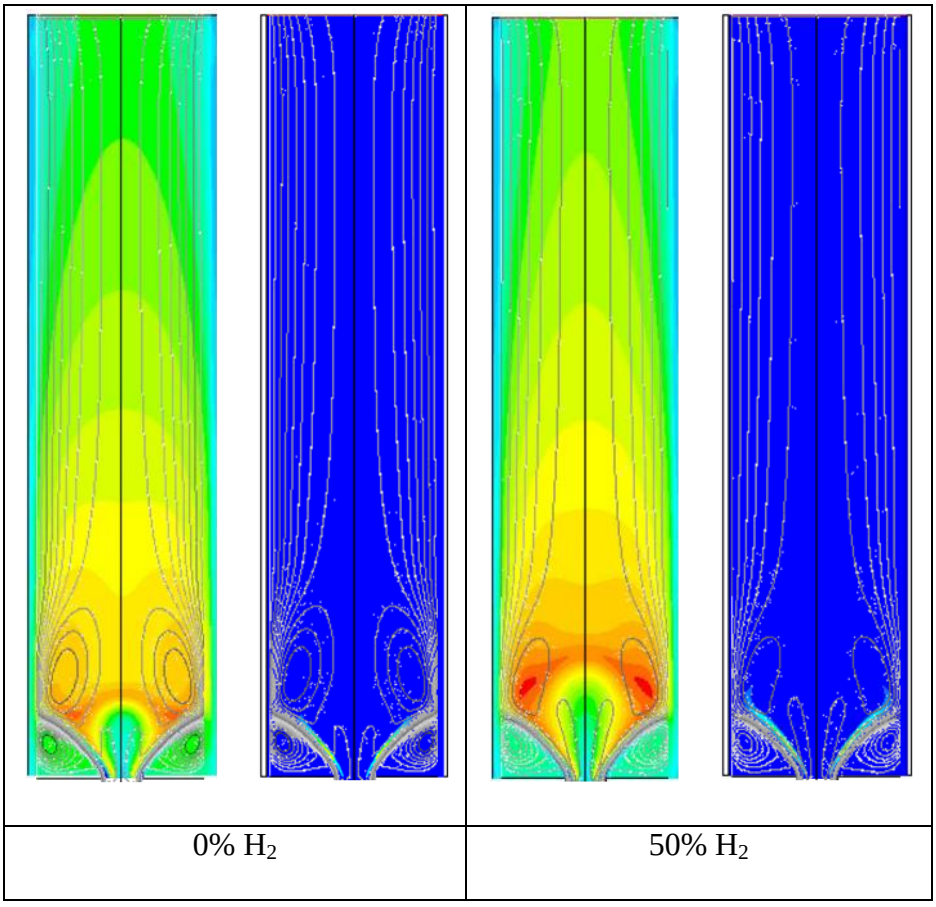

Figure 5.8: The stream line of the flow overlaid on the computed heat of reaction and temperature contour using the Modified-2sCM2 model.

The combustor is generally characterized by a velocity jump at the inlet of the combustion chamber (Fig. 5.9) due to the sudden increase in temperature resulting from the chemical reaction or from the inlet condition (Reynolds number). To isolate the

effects of the sudden temperature increase and inlet condition we considered three cases. In case 1, increasing the energy level (Fig. 5.9a) from 2.75 MW/m^3 to 4.59 MW/m^3 increases both the combustor temperature and Reynolds number (from ~9,200 to ~15,400). Thus, an increase in the velocity jump occurs. For a given energy level with a similar Reynolds number, the velocity jump increases with increasing hydrogen contents in the H_2-CH_4 mixture. This is due to hydrogen higher reactivity and adiabatic flame temperature of hydrogen compared to methane. For case 3 (Fig. 5.9c), an increase in the equivalence ratio led to a velocity jump despite a decrease in the Reynolds number. We can conclude that the velocity jump in the combustor is due to the sudden temperature increase resulting from combustion.

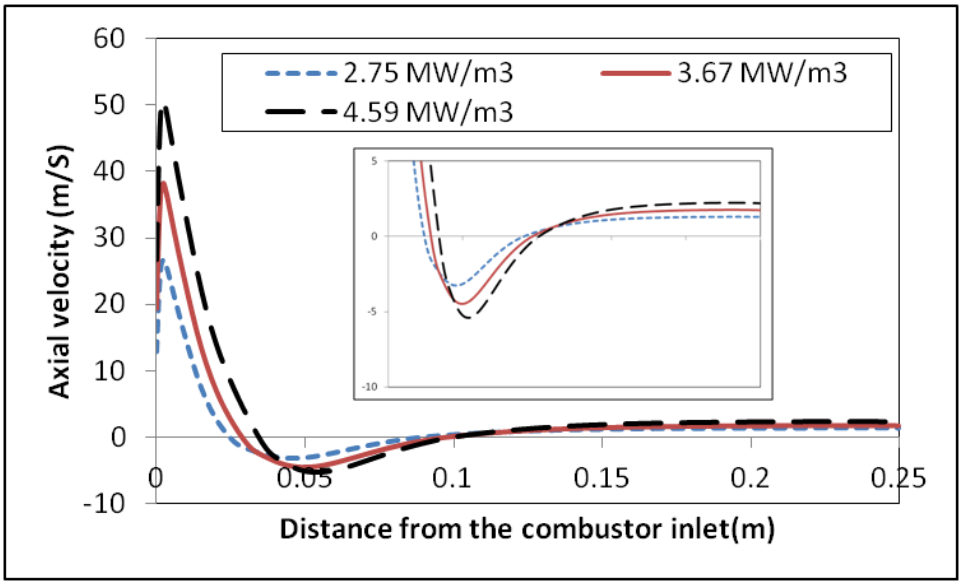

a) Effect of combustor energy level at 0%H_2: Ø=0.5

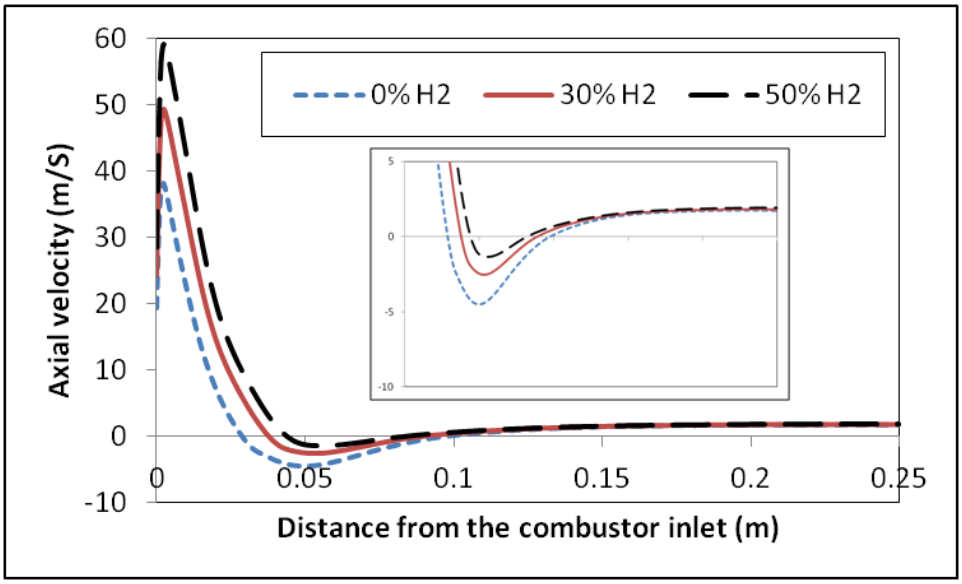

b) Effect of hydrogen contents in CH_4-H_2 mixture Ø=0.5: 3.67 MW/m^3

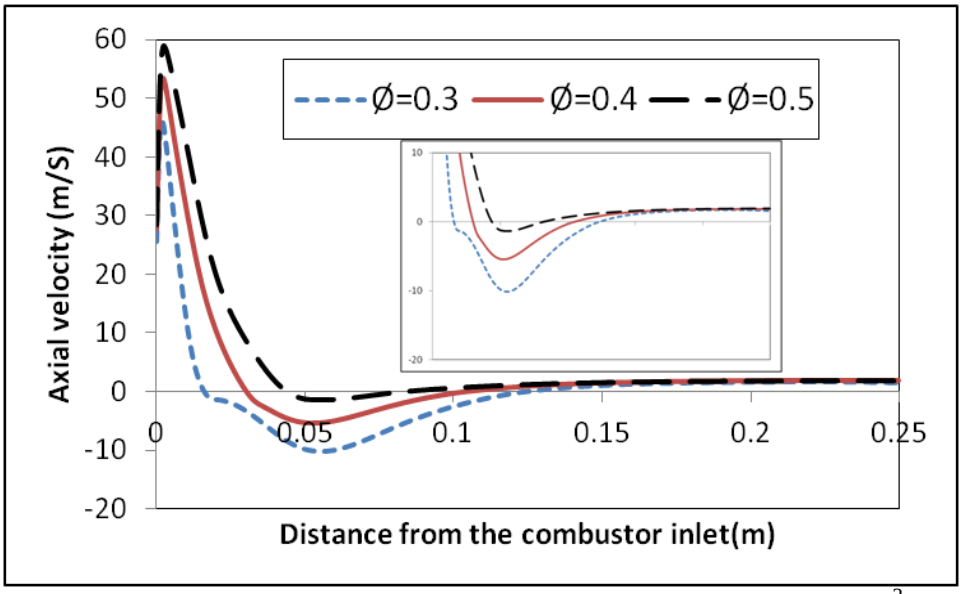

c) Effect of equivalence ratio at 50%H_2: 3.67 MW/m^3

Figure 5.9: Axial velocity along the combustor center line using Modified 2sCM1.

Downstream of the combustor inlet, a vortex breakdown due to adverse pressure gradients produces an inner recirculation zone (IRZ). An inset of the expanded view of the recirculation velocity is given in each figure. The size and strength of the recirculation gases depend on the operating conditions. For instance, at a lower

equivalence ratio and/or lower hydrogen contents in CH_4-H_2, the size and strength of recirculation that is required in stabilizing the flame increases. Strategies that can increase the IRZ could be implemented to further enhance the turbulence and increase the residence time for the complete burnout of the UHCs observed in the flame of hydrogen-enriched methane.

5.4.4 Emissions

CO_2 Emissions

One of the benefits of enriching the methane with hydrogen is the reduction in CO_2 emissions, which contribute to the global warming. Figure 5.10 shows the experimental and predicted CO_2 emission under varying operating condition. A very good agreement was generally observed between the experimental observations and the numerical calculations of the CO_2 emissions on a volume basis, except for 2sCM2 model. This deviation of 2sCM2 model is not surprising because this model has previously under-predicted the combustor temperature under various operating conditions. To quantify the CO_2 emissions from the combustor, we computed and presented the CO_2 emission rate from the combustor in Fig. 5.11.

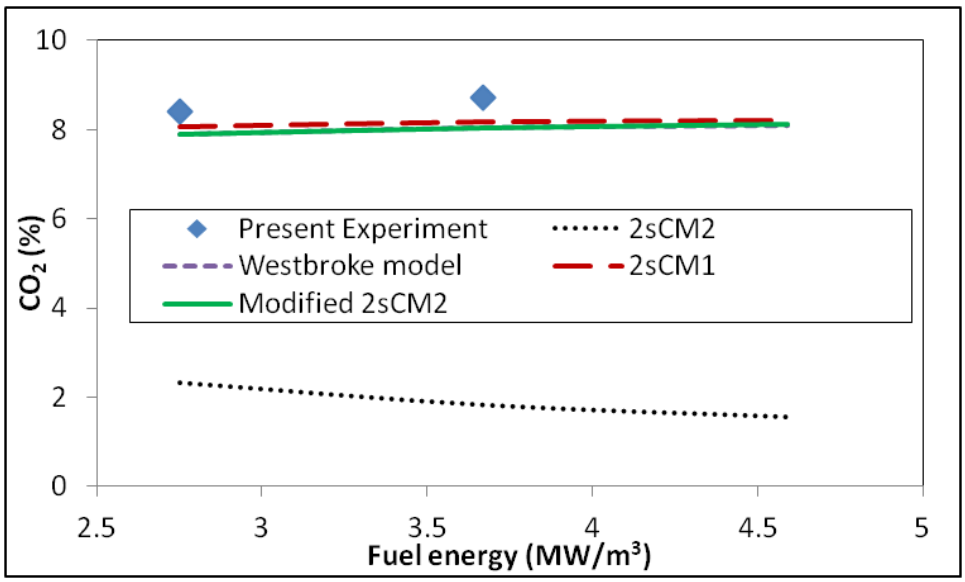

a) Effect of combustor energy level at 0%H_2: Ø=0.5

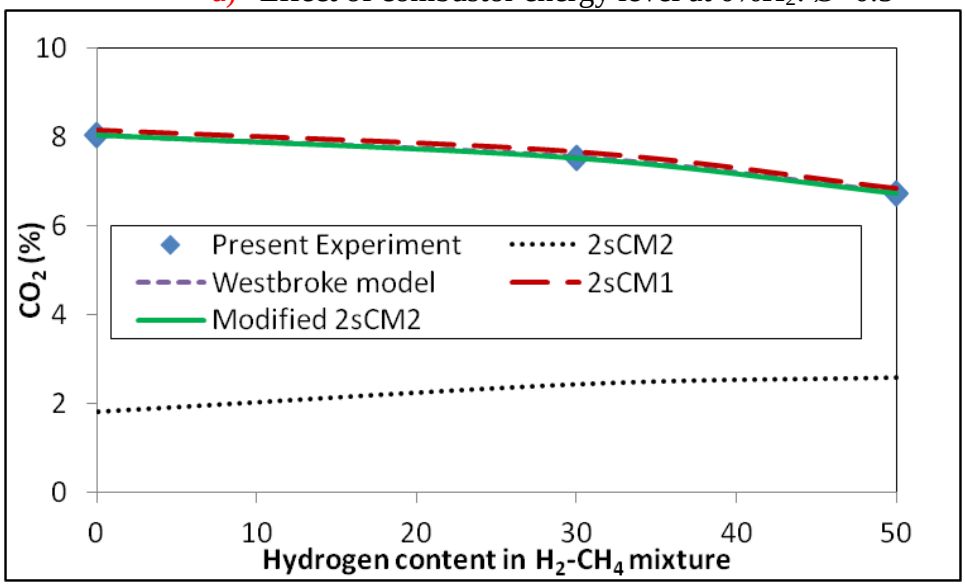

b) Effect of hydrogen contents in CH_4-H_2 mixture Ø=0.5: 3.67 MW/m^3

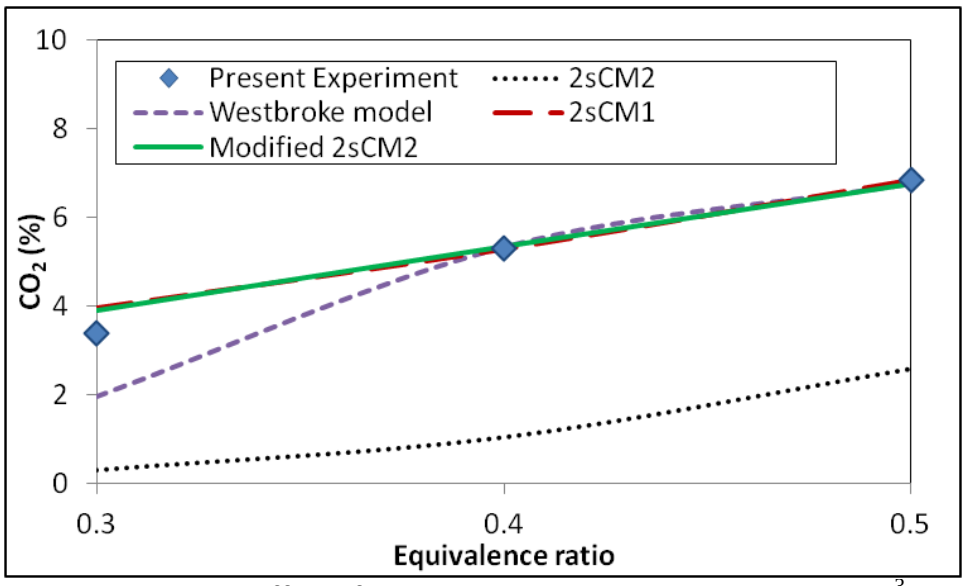

c) Effect of equivalence ratio at 50%H_2: 3.67 MW/m^3

Figure 5.10: Experimental and predicted CO_2 emission from the combustor under different operating conditions.

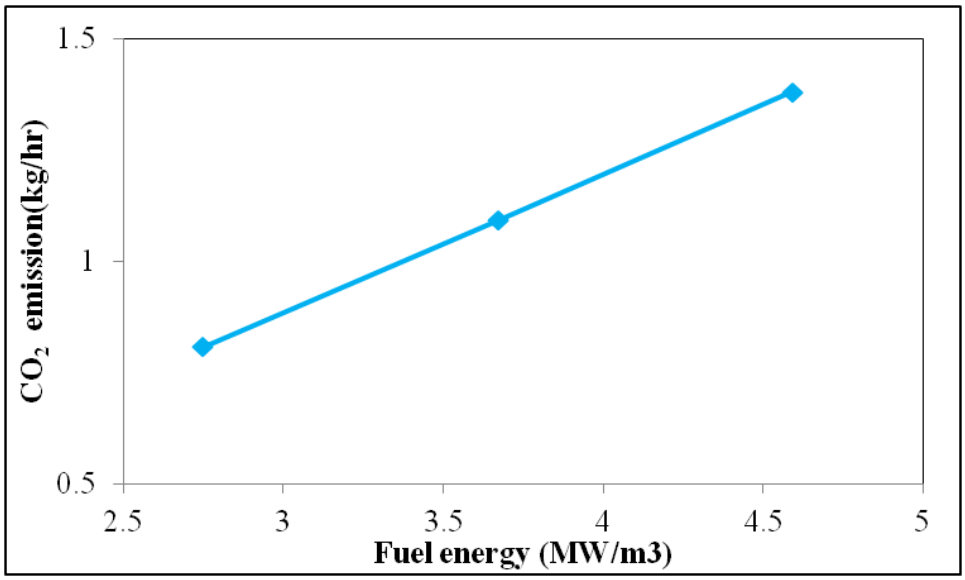

a) Effect of combustor energy level at 0%H_2: Ø=0.5

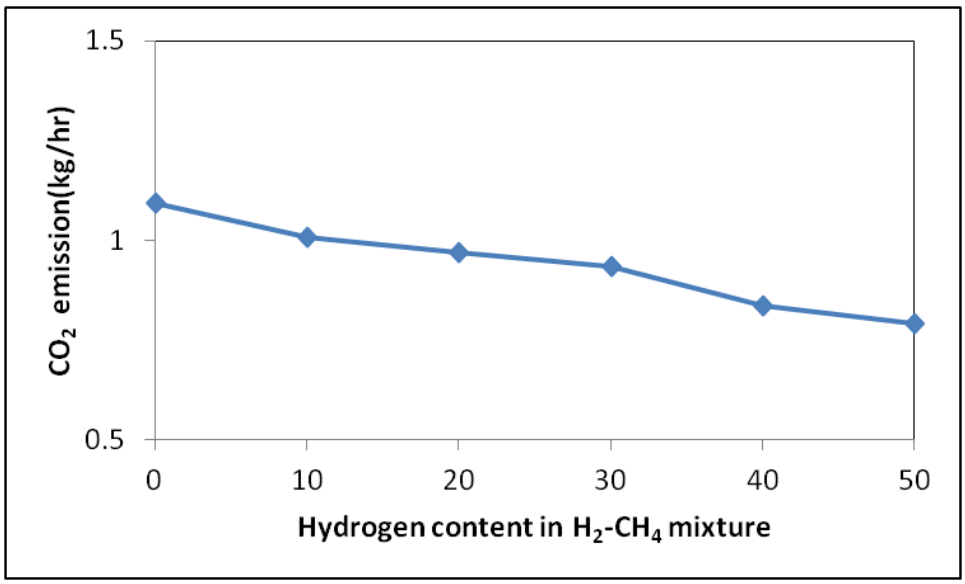

b) Effect of hydrogen contents in CH_4-H_2 mixture Ø = 0.5: 3.67 MW/m^3

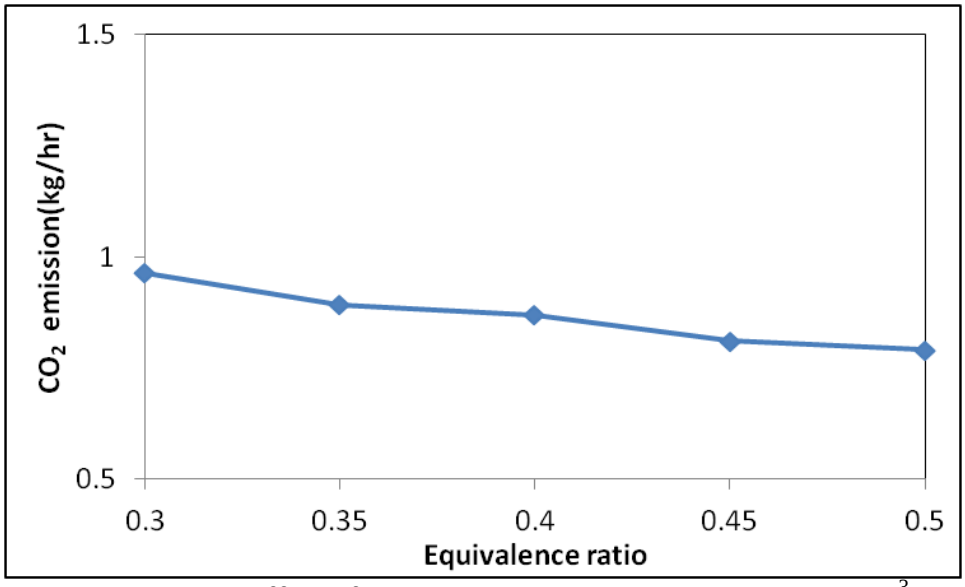

c) Effect of equivalence ratio at 50% H_2: 3.67 MW/m^3

Figure 5.11: Predicted CO_2 emission in kg/hr from the combustor under different operating conditions using the Modified-2sCM2 model.

In Fig. 5.11a, we observed that increasing the energy level (the amount of fossil fuel supplied) in the combustor increased the CO_2 emission rate as expected. This relationship implies that to stabilize the CO_2 concentration in line with the objectives of the UNFCCC, the use of carbon-based fuel, such as natural gas, should be reduced. An

increase in the enrichment of the methane with H_2 (Fig. 5.11b) results in a decrease in the CO_2 emission rate. This relationship is also expected, and the decreased CO_2 can be attributed to the reduction in the fossil fuel in the fuel mixture. Increasing the H_2 content in the fuel mixture by 50% leads to a decrease in the CO_2 emission rate of approximately 30%. This decrease is significant because of the amount of CO_2 emitted from power plants. Figure 5.11c shows that burning leaner mixtures increased the CO_2 emission rate. This result implies that more of the unburned fuel (i.e., UHCs and CO) was able to achieve complete combustion, thus improving the efficiency of the combustor. The increase in the combustion efficiency can be seen by the drastic reduction in soot (UHCs) with decreased equivalence ratio (see Fig. 5.2).

CO Emission

The CO emissions are used to depict the level of combustor inefficiency under a given operating condition. Figure 5.12 shows the emissions of CO from the combustor at different operating conditions. For 0% H_2, we observed a near-zero CO emission when the combustor was operated under typical gas turbine conditions (energy input > 3.45),as a result of the high strength of the IRZ observed under these operating conditions. These findings indicate that more hot gases are re-circulated during the continuous ignition of the fresh charges that favor the complete burnout of the CO. At Ø > 0.5 (Fig 5.12c), near-zero CO emissions were observed for fuel compositions of up to 40% H_2, beyond which a significant increase in the CO emissions was observed. This indicates that the 40% H_2 composition in CH_4 is critical for CO emissions in the combustor under the Ø=0.5 operating condition. We previously identified the inhibition of methane oxidation and reduced IRZ as being responsible for the higher CO when the methane and hydrogen

content in the fuel are of the same order (50% H_2). We thereafter perform an equivalence ratio sweep test at 50% and obtained the optimal equivalence ratio of 0.4 (i.e., $Ø_m$=0.4). The CO emissions at the optimal equivalence ratio were 9 PPM. A further decrease in the equivalence ratio led to an increase in the CO emissions. The high CO emissions at a lower equivalence ratio (Ø < 0.4) could be due to either of the following factors. (1) The excess supplied air serves as a heat sink, convecting heat away from the reaction zone. This convection could lead to localized flame extinction and increased CO emissions. Further insights into the role of heat transfer on emissions are presented in section 5.5. (2) At Ø=0.5 (Fig.5.2), a yellow plume in the flame was attributed to UHCs [69]. A decrease in the equivalence ratio to approximately 0.3 increases both the size and strength of the IRZ and the Reynolds number at the burner, which enhances turbulence mixing. This led to the drastic reduction in the UHCs. The reduction in the equivalence ratio to 0.3 also led to a reduction in the residence time of the combustion product by approximately 50%. The combustion residence time under this condition (Ø=0.3) is, however, not sufficient for the complete burnout of the UHCs at Ø=0.5 to CO_2 at Ø=0.3 (i.e., UHC-CO-CO_2). Thus, CO emissions were observed at Ø=0.3. Strategies that increase the combustion residence time, such as increasing the size of the combustor, increasing the burner diameter to lower the flow velocity or increasing the swirl number, can be implemented to mitigate high CO emissions at higher hydrogen contents.

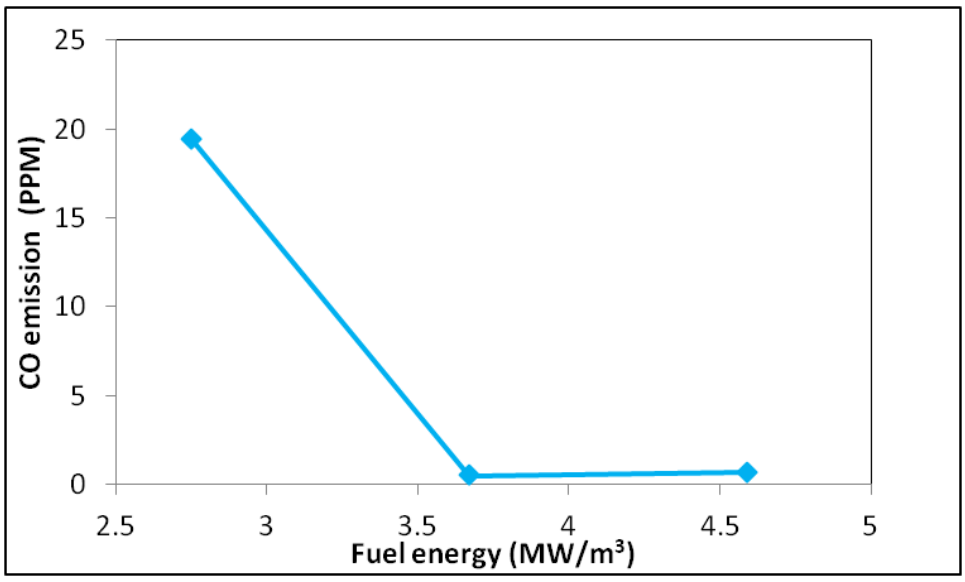

a) Effect of combustor energy level at 0%H_2: Ø=0.5

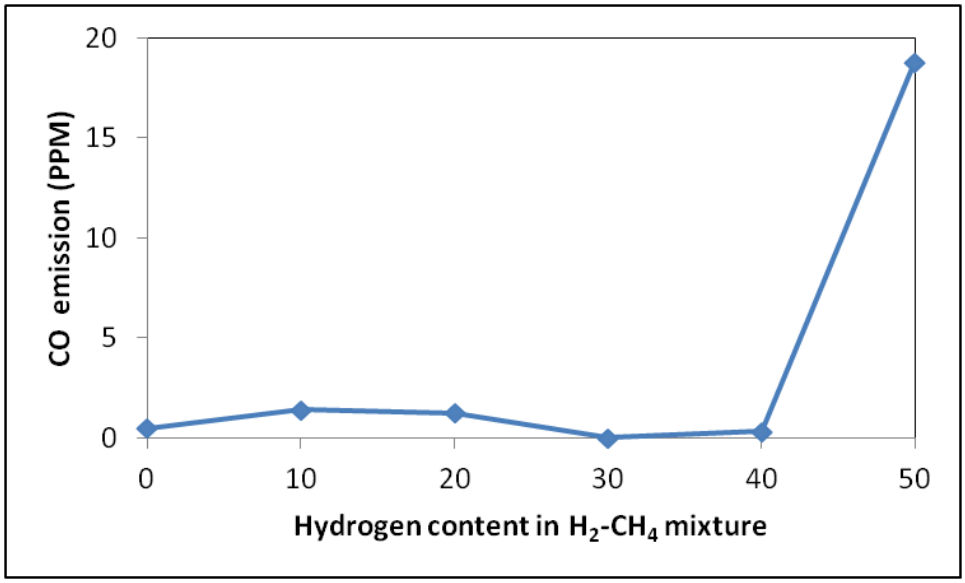

b) Effect of hydrogen contents in CH_4-H_2 mixture Ø = 0.5: 3.67 MW/m^3

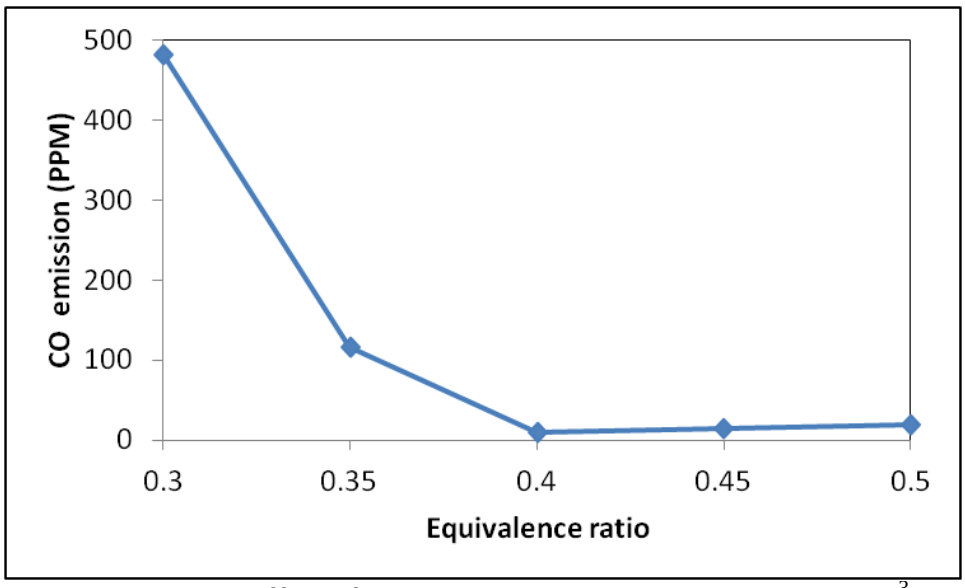

c) Effect of equivalence ratio at 50% H_2: 3.67 MW/m^3

Figure 5.12: Predicted CO emissions from the combustor under different operating conditions using the Modified-2sCM2 model.

NOx Emissions

NOx emissions are an important metric for gas turbine combustors. The NOx emissions from the combustor depend on competing factors such as the combustor temperature, the oxygen availability and the residence time of the combustion product. The measured and = predicted NOx emissions are given in Fig. 5.13. The measured NOx emissions were observed to be relatively constant, despite the increase in the energy level. This is unexpected because the increased energy level increases the combustor temperature distributions. The increase in energy level, however, decreases the combustion-product residence time. Thus, the residence time at higher energy level does not favor NOx formation. . However, increasing the equivalence ratio and hydrogen contents in the CH_4-H_2 mixture increases the NOx emissions. This increase can be attributed to the increase in

the adiabatic temperature at these conditions. This trend was observed experimentally and through numerical calculations.

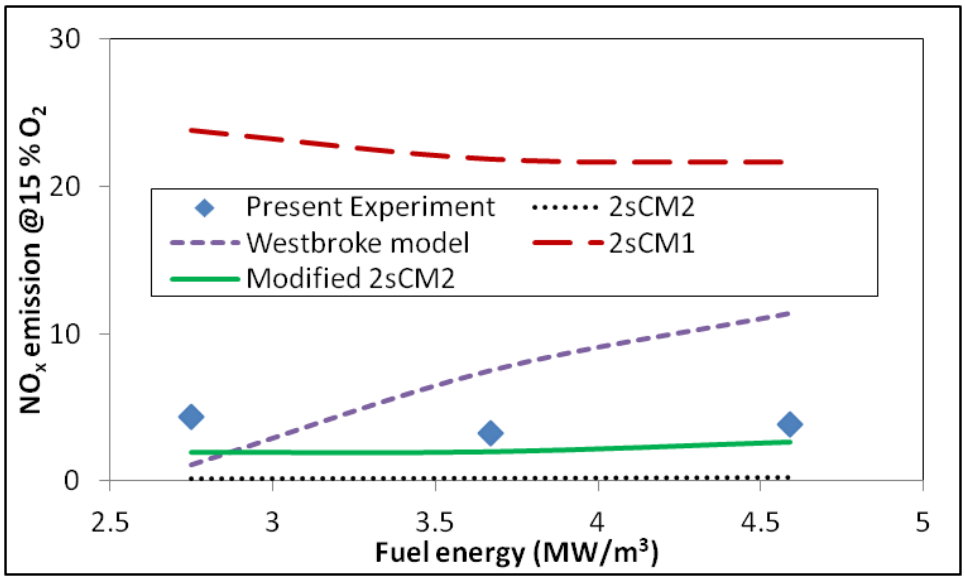

a) Effect of combustor energy level at 0%H_2: Ø=0.5

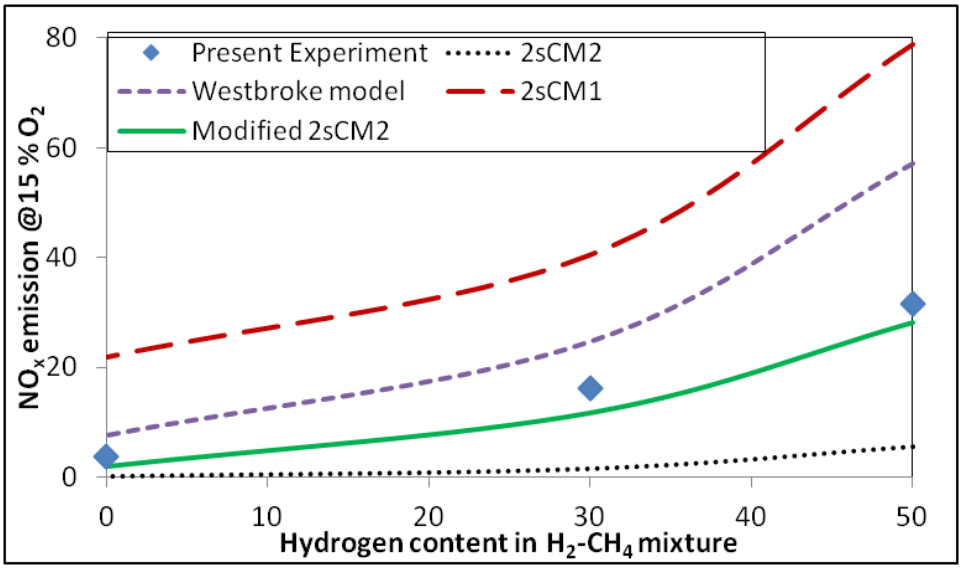

b) Effect of hydrogen contents in CH_4-H2 mixture Ø = 0.5: 3.67 MW/m^3

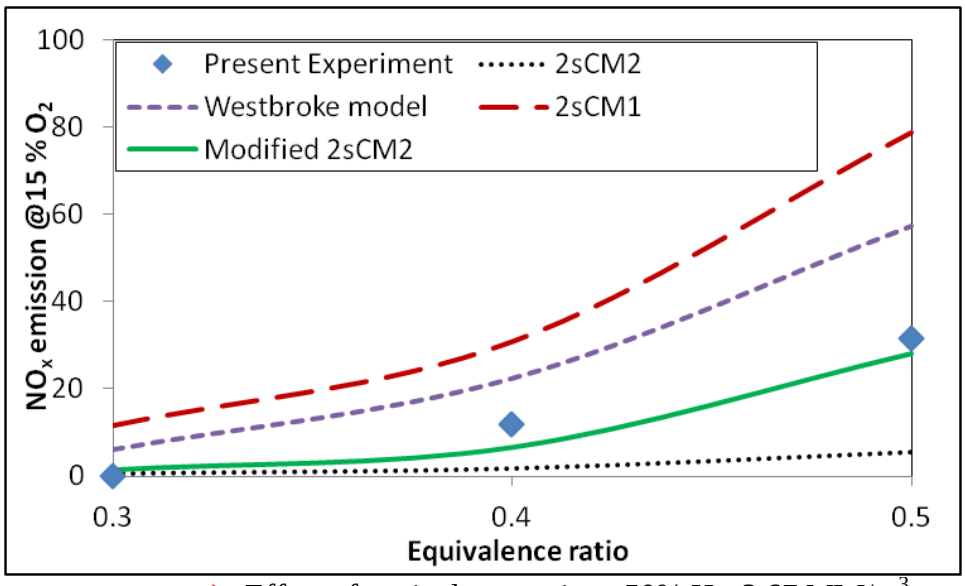

c) Effect of equivalence ratio at 50% H_2: 3.67 MW/m^3

Figure 5.13: NOx emission from the combustor at different operating conditions.

The 2sCM2 mechanism generally under-predicts the NOx emissions under all conditions because of the significant under-prediction of the combustor temperatures. The Modified-2sCM2 developed good predictions of the NOx, whereas the Westbrook and 2sCM1 models significantly over-predict the NOx under all operating conditions. The 2sCM1 model produced the maximum over-prediction of NOx emissions, despite displaying a lower maximum temperature compared to the global mechanism of the Westbrook model. Unlike the Westbrook mechanism, the 2sCM1 mechanism involves the oxidation of CH_4 to CO, leaving more oxygen in the reaction zone. The presence of more oxygen at higher temperatures could result in a higher amount of NOx. The 2sCM1 mechanism displayed a similar temperature distribution compared to the Modified-2sCM2 mechanism; its prediction of a higher combustion temperature led to a substantial over-prediction of NOx. This suggests that the escalation of the temperature in the reaction zone due to the absence of the CO_2/CO dissociation step in the 2sCM1 mechanism

resulted in the over-prediction of NOx. In this study, the combustor maximum temperature controls the NOx emissions. Thus, accurate prediction of the combustor maximum temperature is critical to an accurate NOx prediction. The Modified-2sCM2 mechanism presented in this paper was observed to be consistent in the prediction of the combustor temperature, the major species and the NOx emissions with a reasonable degree of accuracy. This mechanism is thus recommended for use in the combustion modeling of methane and hydrogen-enriched methane under ultra-lean conditions. One of the objectives of this paper is to identify the role of the operating conditions on the emissions of a fuel-flexible combustor. Thus, we numerically performed the equivalence ratio sweep test at different fuel compositions and noted an equivalence ratio at which the CO and NOx emissions from the combustor were optimized. From fig. 5.14, the optimal equivalence ratio for 40 and 50% H_2 is 0.4. This value indicates that a further decrease in the equivalence ($Ø < 0.4$) for the case of 50%, for instance, will lead to a substantial increase in CO emissions, whereas an increase in the equivalence ratio will also lead to an increase in NOx emissions. Similar equivalence ratio sweep tests were performed for other fuel compositions, and the observed optimal equivalence ratios and their corresponding CO and NOx emissions are summarized in table 5.3.

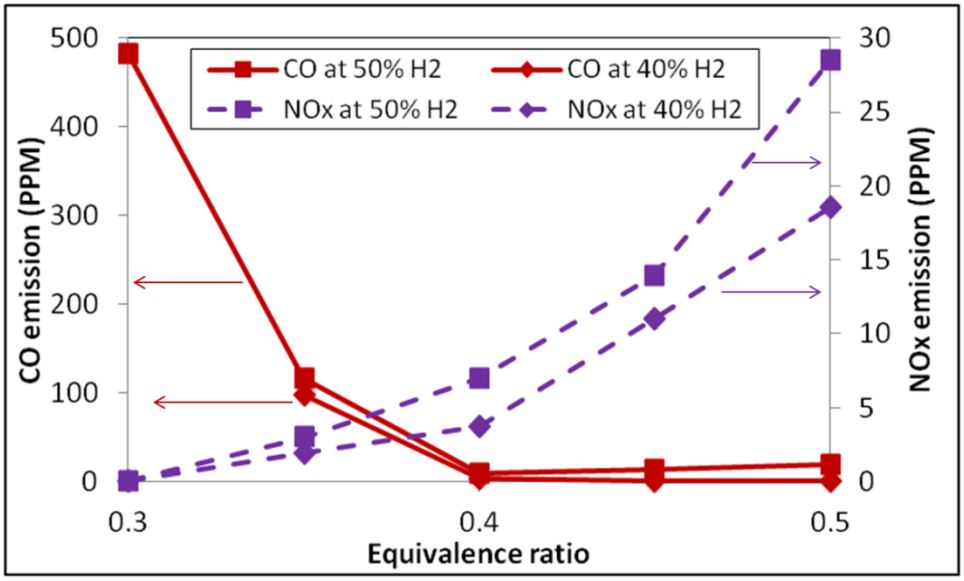

Figure 5.14 : The CO and NOx emissions from the combustor at different equivalence ratios.

Table 5.3: CO and NOx emission at the optimal equivalence ratio for different fuel compositions

Fuel composition	Wobbe index (WI)	Optimum equivalence ratio ($Ø_m$)	CO emission (PPM)	NOx emission (PPM)
0%H_2	46.91	0.5	1	2
10%H_2	45.67	0.5	1	4
20%H_2	44.43	0.45	1	3
30%H_2	43.19	0.45	0	5
40%H_2	41.94	0.4	4	4
50%H_2	40.72	0.4	9	7

5.4.5 Effect of Wall Thermal Boundary Conditions

The combustion chamber wall serves two purposes. 1) The wall conducts heat from the post-combustion zone upstream of the flame, preheating the incoming reactant and thus enhancing the ignition and flame stability. 2) The wall allows heat loss to the ambient surroundings. The thermal conductivity of the wall influences the amount of heat loss and the wall temperature profile. Norton et al. [92] reported that the wall thermal conductivity plays a vital role in the stability of the flame and the integrity of the materials. Excessive heat losses will lead to thermal quenching [150] and reduce the combustion efficiency. Therefore, we investigated the role of the chamber material and, by extension, the heat loss from the emissions from the combustor. Simulations were carried out for the experimental base case (quartz glass), mild steel and adiabatic wall conditions. The convective heat transfer at the wall was enhanced for the steel material such that the maximum wall temperature was within the working range of the steel (less than the creep temperature of approximately 650 K). These parameters are set to simulate the near-experimental conditions in which the wall is cooled via a water jacket or forced air convection. The computed rate of heat loss from the combustor at 50% H_2 is 2.98 kW and 2.39 kW for the steel and quartz glass material, respectively. The wall temperature profile for different fuel compositions and equivalence ratios is presented in Fig.5.15. The wall temperature for the quartz glass and steel material peaked in the vicinity of the flame and decreased thereafter. The temperature decrease is due to the heat energy loss from the combustion products. The steel material was observed to develop lower wall temperatures because of its higher thermal conductivity and wall heat losses. The temperature at the hotspot for the quartz glass (900-1100 K) was below its working

temperature (1473-1573 K). Thus, the quartz was stable throughout the experiment. The hotspot temperature of mild steel falls within the range of its creep temperature (0.4-0.6 melting temperature). For an adiabatic wall, the wall temperature increases downstream of the burner approaching the flue gas temperature. The wall temperature was also observed to increase in the vicinity of the outer recirculation zone (ORZ). These results suggest that the combustion continues in the ORZ. Figure 5.16 shows that by increasing the heat transfer at the wall, the combustion gas residence time increases. This increase can be attributed to the higher heat loss lowering the combustion temperature and gas expansion rate. Thus, the combustion product for the mild steel wall will remain for a longer period of time in the combustor compared to the case of adiabatic wall conditions. Depending on the prevailing conditions, the increased residence time can either lead to the complete combustion of CO to CO_2 or the decomposition of CO_2 to form more CO. The increased residence time of high-temperature combustion products will also favor the formation of more NOx in the combustor.

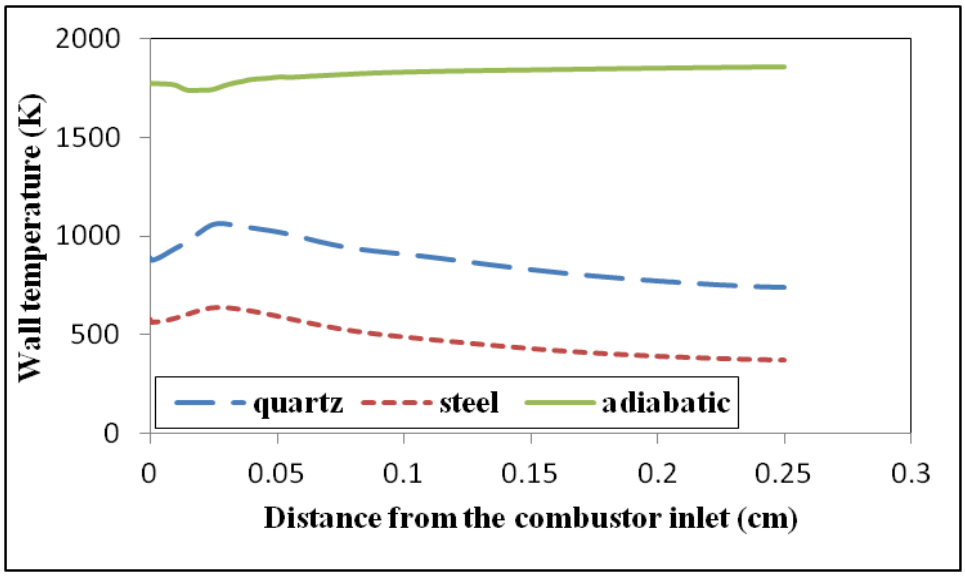

a) Combustor wall temperature at 0% H_2: Ø=0.5

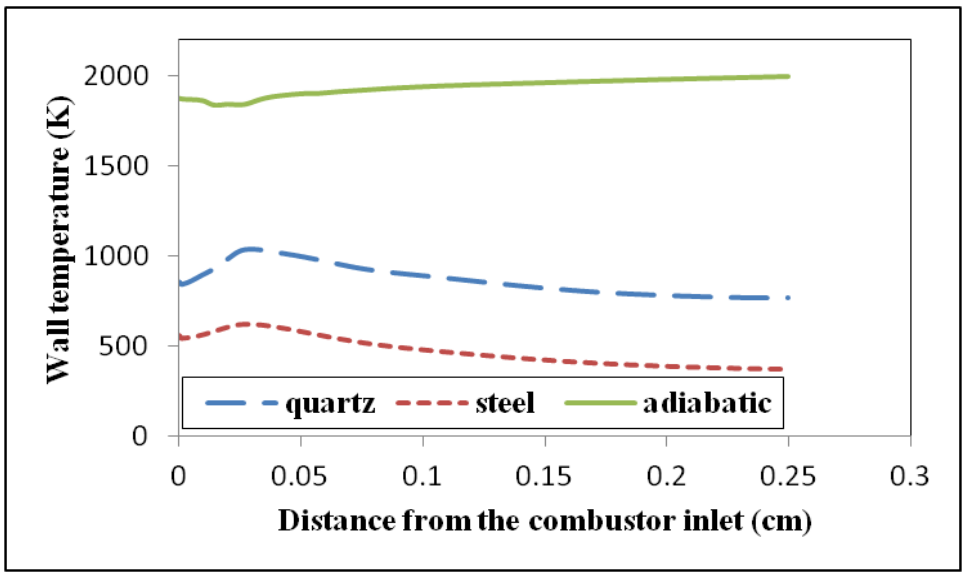

b) Combustor wall temperature at 50%H_2: Ø=0.5

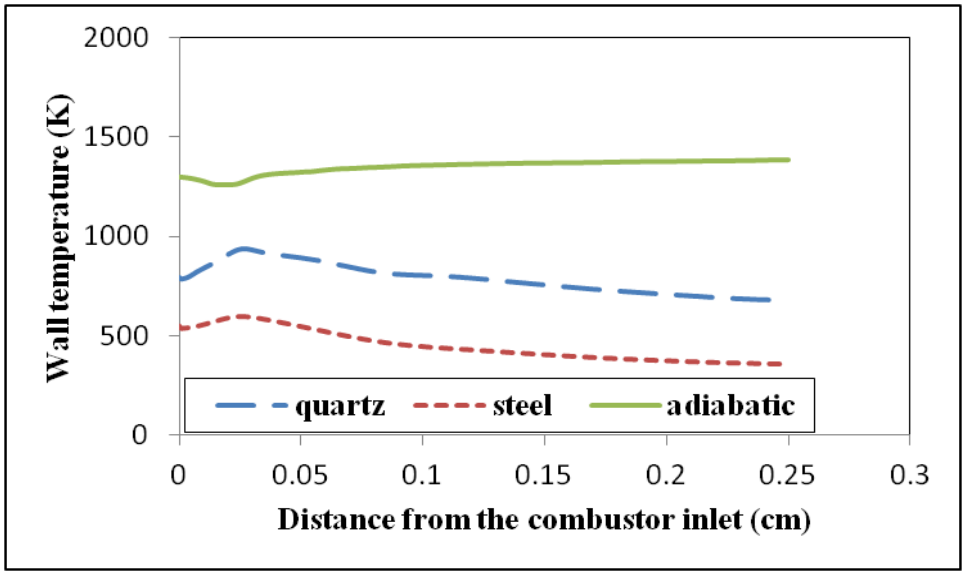

c) Combustor wall temperature at 50%H_2: Ø=0.3

Figure 5.15: Predicted combustor wall temperature under different operating conditions

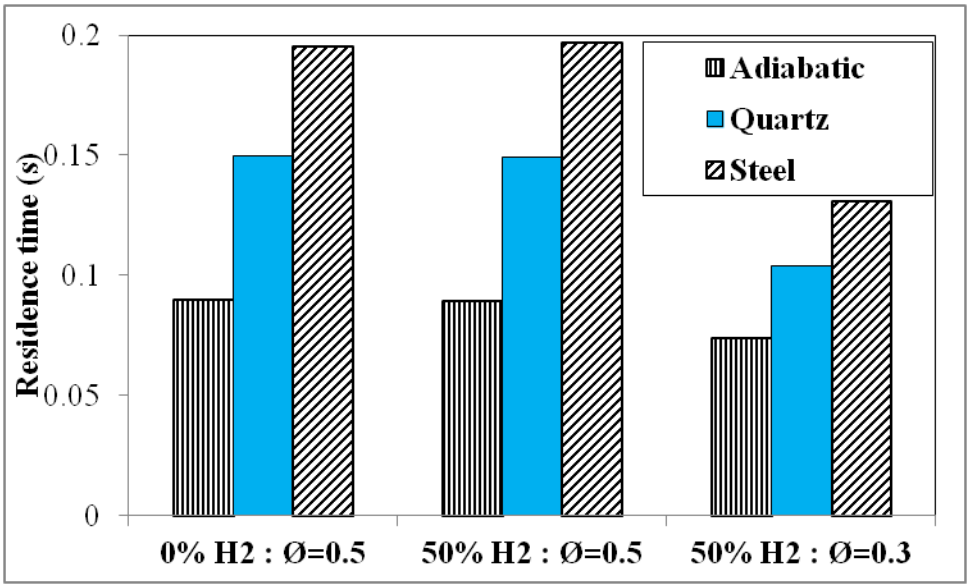

Figure 5.16: Predicted combustor residence time at different operating conditions

The CO emissions at 0% H_2: Ø=0.5 (Fig.5.17a) for a steel wall are higher than the CO emissions under other studied wall conditions despite having the highest combustion residence time. The higher CO emissions for the steel case can be attributed to the higher heat losses at the combustion chamber wall leading to thermal extinction of the flame. Higher CO emissions are also observed in the adiabatic wall case when compared to the quartz glass wall case. Higher combustor temperatures appear to favor the thermal dissociation of CO_2 to CO/O_2 at elevated temperatures. Increasing the hydrogen content to 50% H_2, the CO emissions were observed to increase for quartz and adiabatic wall conditions. The inhibition of methane oxidation in the presence of hydrogen has been attributed to the increased CO emissions. As suggested earlier, the enhanced residence time of the high-temperature combustion product observed for the steel case leads to a nearly complete burnout of the UHCs. The computed CO emissions of 5.15 PPM are observed for the steel case, as compared to 18.78 PPM and 62.93 PPM observed for the quartz glass and adiabatic case, respectively. A further decrease in the equivalence ratio

leads to a drastic increase in CO emissions, especially for steel and quartz glass conditions. The CO emissions for steel are approximately 9,576 ppm (not shown in Fig.5.17a). The role of excess air on the CO emission was earlier discussed in section 5.4.4. The effects of the decrease in the equivalence ratio and the ensuing flame extinction by the excess air on the CO emissions were not significant for the adiabatic wall case as compared to the steel and quartz glass combustion chambers. This is due to the relatively higher combustion temperature under adiabatic wall conditions partially offsetting the effect of the heat sink from the excess air. Thus, a marginal increase in the CO emission is observed. Figure 5.17b shows that the NOx emissions follow the trend of the combustion temperature (not shown). The combustor with the adiabatic wall displayed the highest NOx emissions because of the higher combustion temperature.

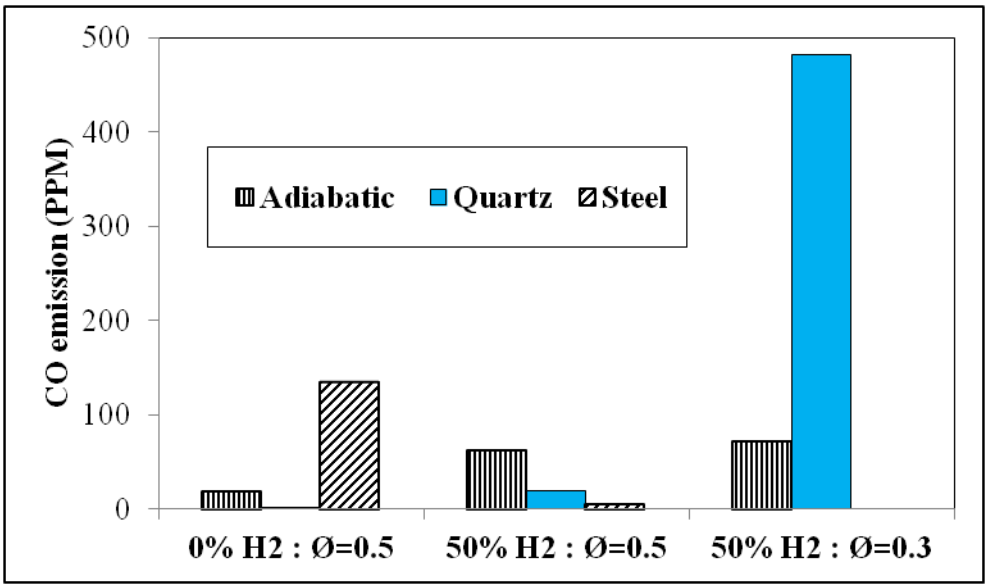

a) CO emission

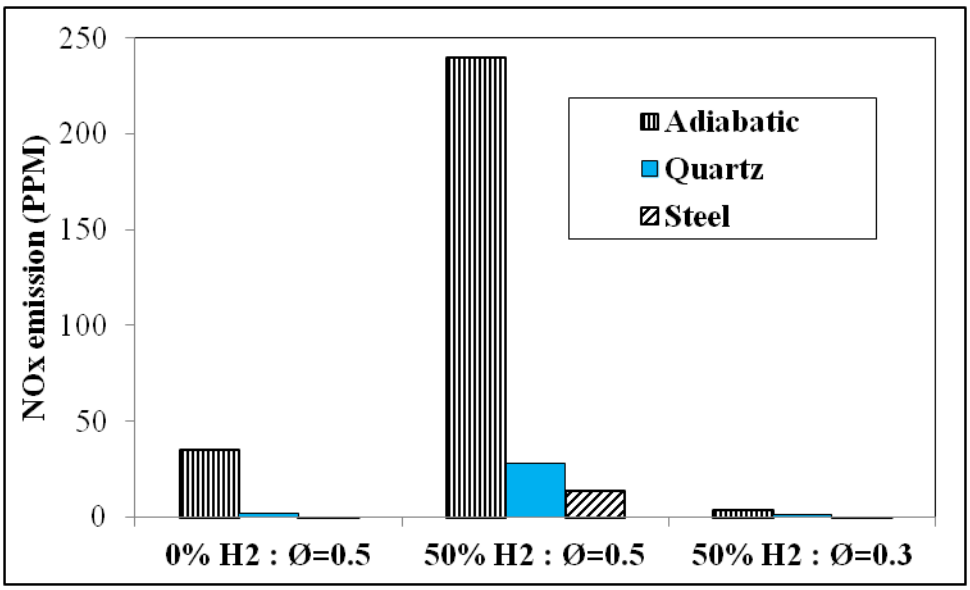

b) NOx emission

Figure 5.17: Emissions from the combustor under different operating conditions

5.4.6 Effect of Swirl Number

In this section, we present the result of the effect of swirl number (SN) on the combustion characteristics at different conditions. Three cases of swirl number of 0.38, 0.67 and 1.15 were investigated and presented.

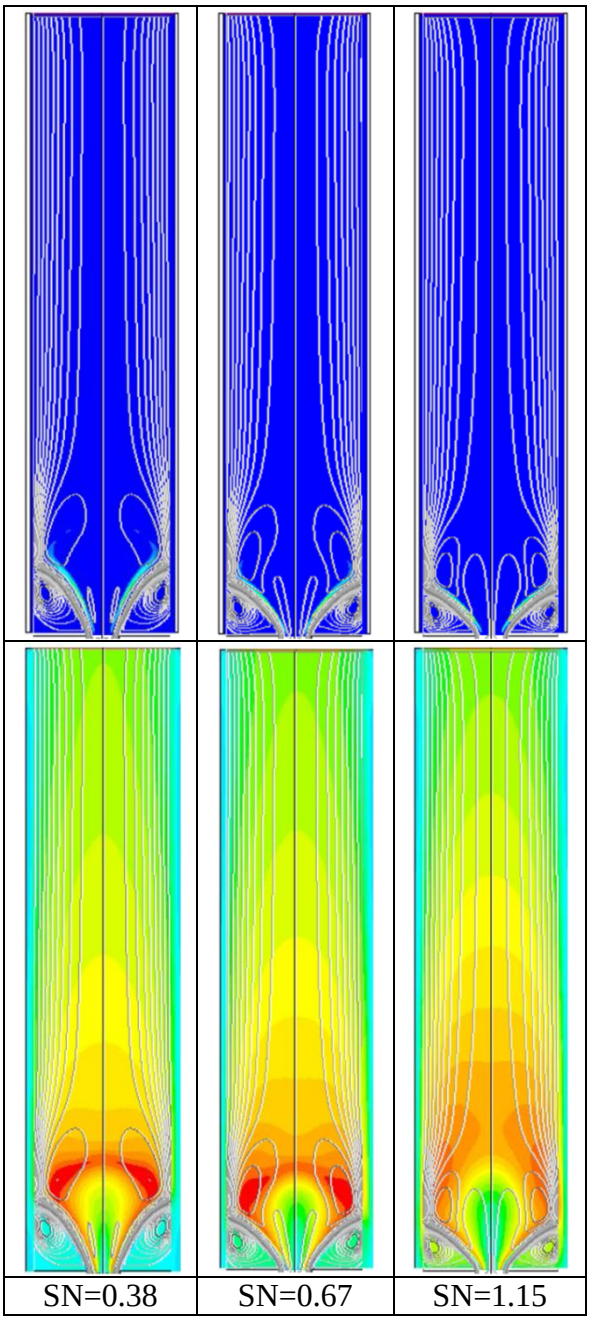

Figure 5.18: The computed heat of reaction and temperature contour for different SN for 50%H_2: Ø = 0.5

Figure 5.18 shows that the stream line of the flow pattern overlay on the computed heat of reaction and temperature contour for 50% H_2: Ø = 0.5. Details of the flow pattern can be found in section 5.4.3. As the SN increases, the recirculation region becomes wider

enabling the IRZ to move towards the combustor inlet, thus, leading to a more compact flame. As SN increases, the size of the WRZ increases due to the reduced axial component of the velocity. The increase in size of the WRZ forces the IRZ to shift towards the combustor wall leading to an increase in the flame angle. It also gives room for the IRZ to approach the combustor inlet, thus, allowing the early attainment of the ignition temperature by the fresh charges. The temperature contour on the same figure shows that the hot combustion product in the eye of the IRZ plays an important role in preheating of the incoming charges and flame stabilization. The local hotspot in the flame was observed to decrease at higher SN. This is due to improve mixing and turbulence at higher SN. The temperature contour further shows that downstream of the IRZ, the combustion is near completion, such that the heat transfers downstream of the flame is due to heat exchange between the combustion products and wall of the combustor.

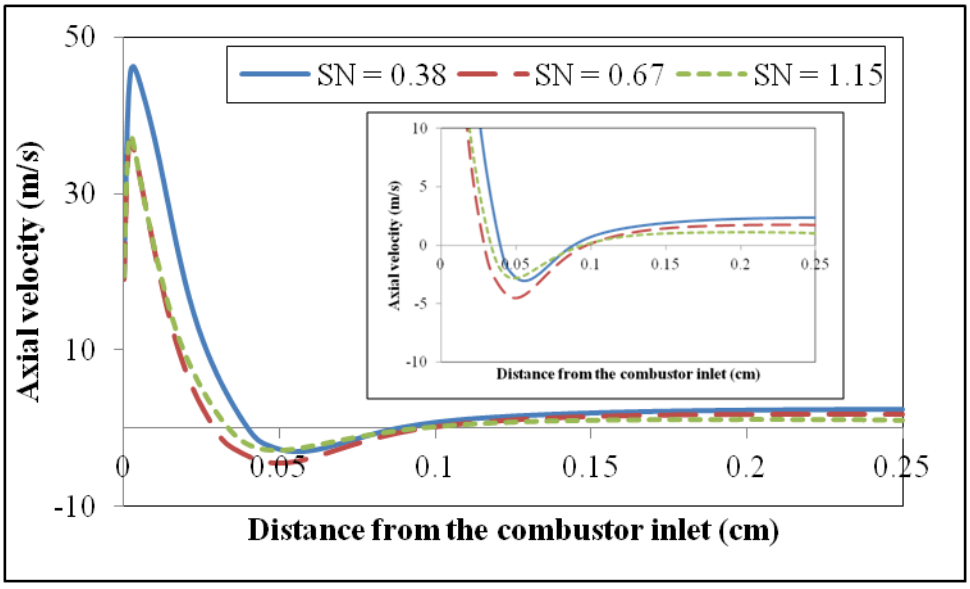

a) 0% H_2: Ø=0.5

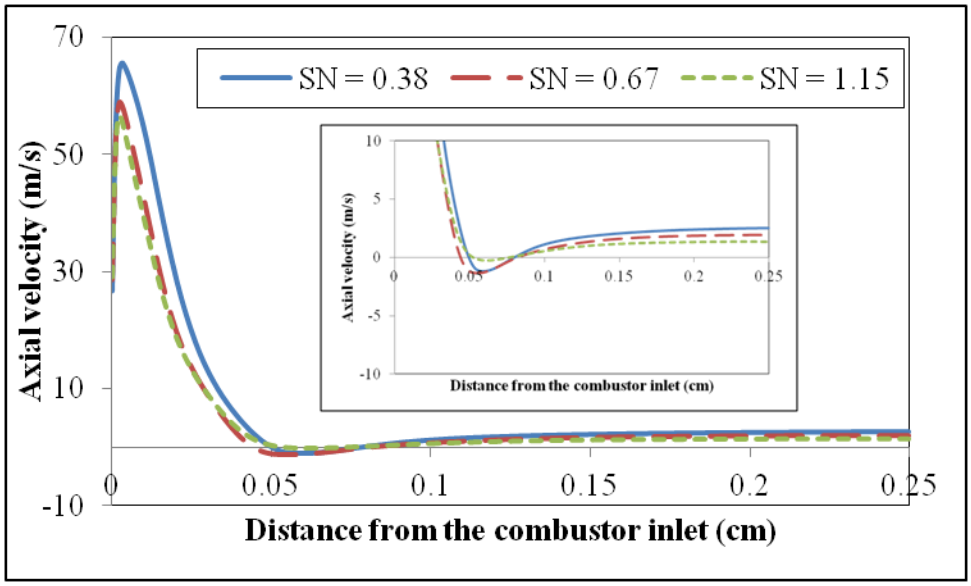

b) 50% H_2: Ø=0.5

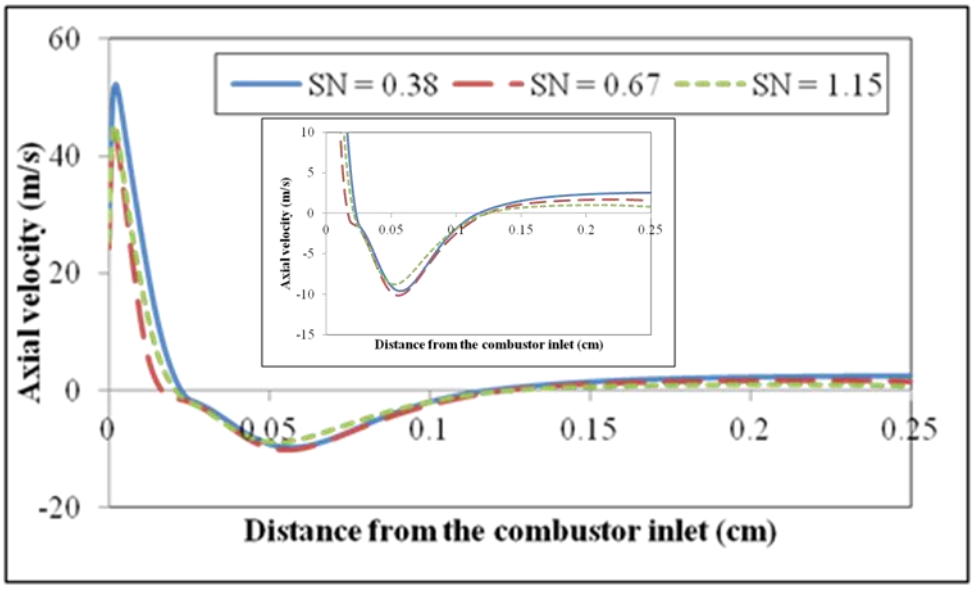

c) 50% H_2: Ø=0.3

Figure 5.19 : Effect of swirl number on the axial velocity profile along the combustor axis under different operating conditions

Figure 5.19 shows the axial velocity along the combustion center line. An inset of the expanded view of the recirculation region is given in each figure. The IRZ in the

combustor serves as aerodynamic blockage resulting in the acceleration the flow at the combustor inlet. Hence, higher axial velocities are generally observed at the combustor inlet. We generally observed higher axial velocity at SN of 0.38 at all operating conditions. Cases with SN of 0.67 are found to be optimum based on the fact that the highest size and strength of the recirculation zone is observed at these conditions.

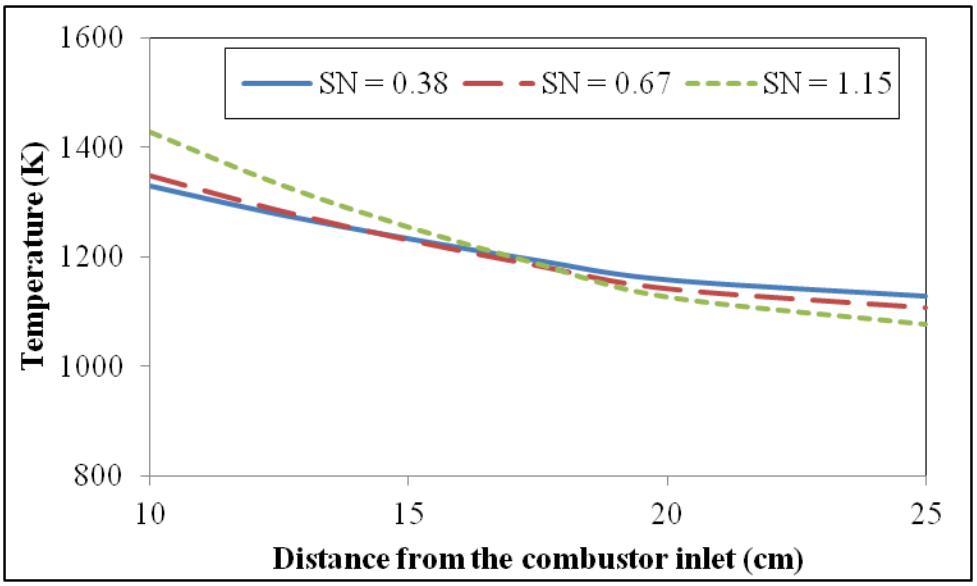

a) 0% H_2: Ø=0.5

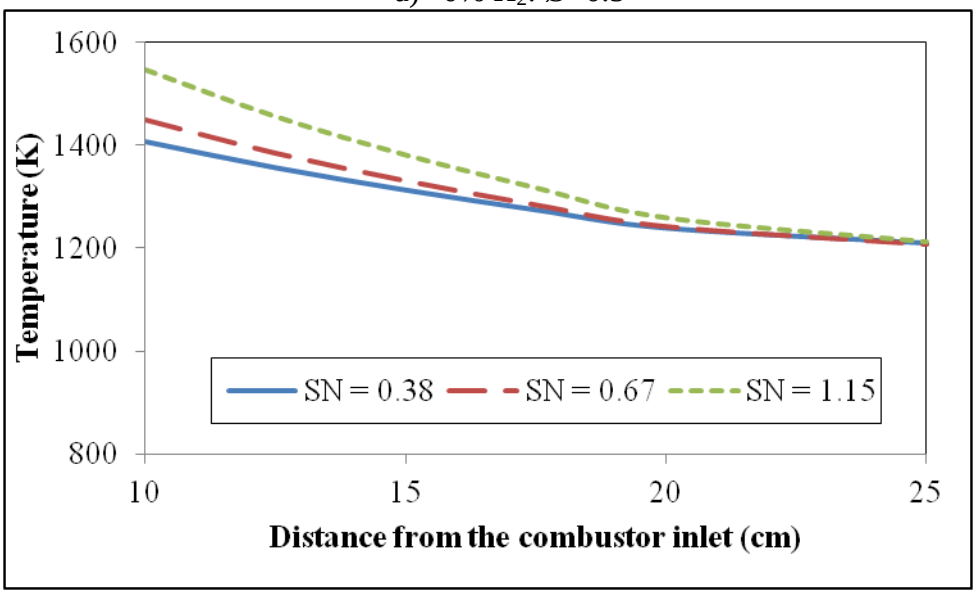

b) 50% H_2: Ø=0.5

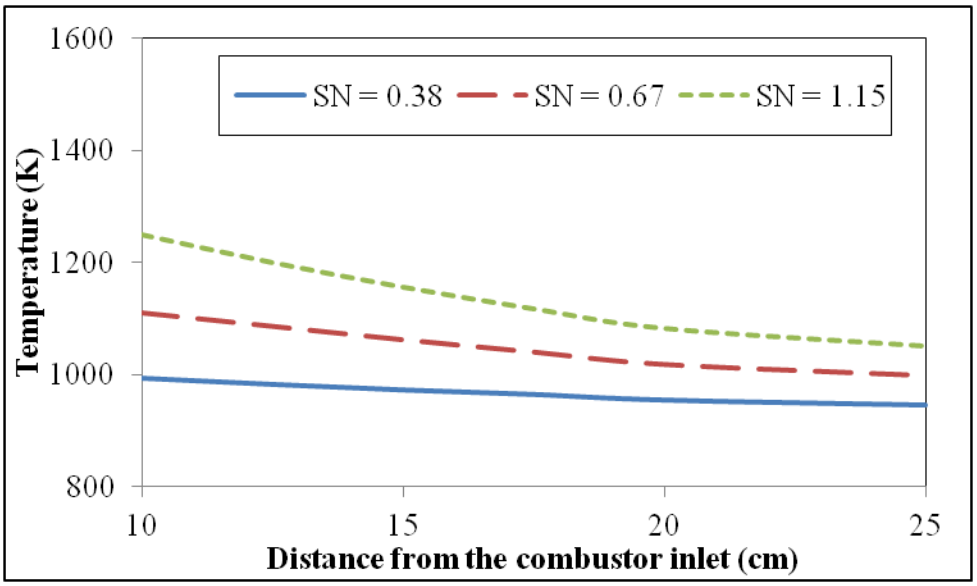

c) 50% H_2: Ø=0.3

Figure 5.20 : Effect of swirl number on the temperature profile along the combustor axis under different operating conditions

Figure 5.20 shows the temperature profile along the combustion center downstream of the flame. A larger recirculation zone comprising of both the IRZ and WRZ led to the increase level of turbulence and amount of hot gas re-circulated. It also increases the combustion residence time. A more compact flame is ensued at this condition. This implies that higher heat release intensity will be observed at these conditions, thus, leading to higher flame temperature. The heat transfers downstream of the RZ are generally due to loss from the combustion product to the wall and the excess air supplied. At 0% H_2 and SN=0.38 (Fig. 5.20a), the flame became less compact and the reaction and heat release continues as the exhaust gas approaches the combustor exit leading to higher temperature at the combustor exit as compared to the case of SN= 1.15. While for higher SN cases, the temperature is essentially due to heat loss from the combustion

product to combustor wall and excess air. For cases with hydrogen in the fuel mixtures, we generally observed higher temperature as the SN increases (Fig. 5.20b and Fig. 5.20c). Consider a case of 50% H_2: Ø=0.5 (Fig. 5.2a) where UHCs are observed in the combustor. Increasing the SN can be a means of improving the combustion efficiency due to increase residence time and turbulence. Thus, more of the fuel that hitherto goes unburned are combusted and release more heat energy leading to increase combustion temperature.

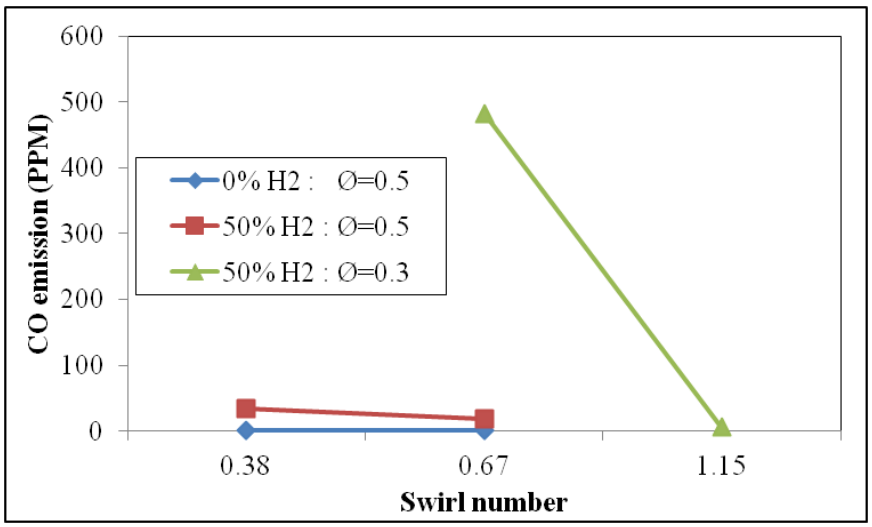

a) CO emissions

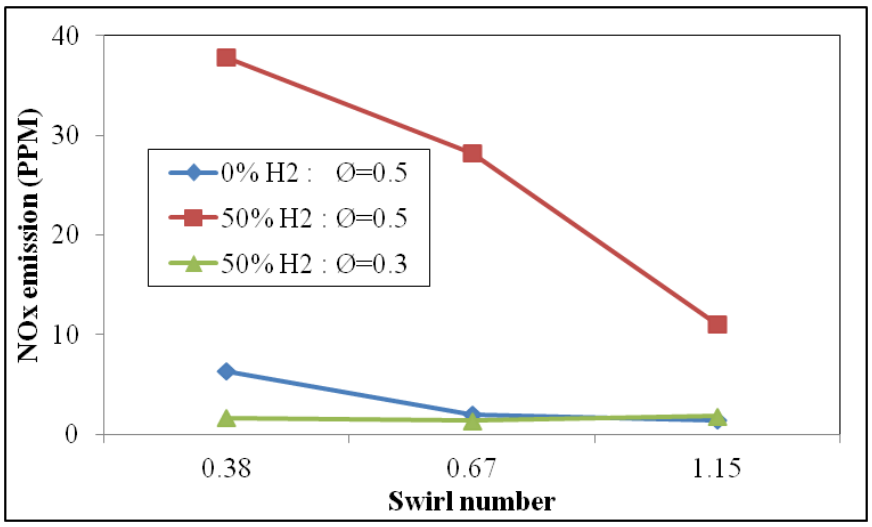

b) NOx emissions

Figure 5.21 : Effect of swirl number on the combustor emissions under different operating conditions.

The effects of SN on the emission at different operating conditions are summarized in Fig. 5.21. For 0% H_2, the SN of up to 0.67 gave near zero CO emission, a further increase in the SN, however, drastically increase the CO emission. The CO emission at this condition is 10,463ppm (not shown on the graph). This high CO can be attributed to higher turbulence observed at SN = 1.15, leading to local flame extinction. Similar trend was observed for case of 50%H_2: Ø = 0.5, the CO emission at this condition is higher than that of 0% H_2 case, the reasons suggested have been previously discussed in section 5.4.4. An increase in the SN continuously decrease the CO emissions for the case of 50% H_2, Ø=0.3. At this operating conditions (Re= ~19,500), the CO is solely dependent on the residence time of the combustion product. Thus, an increase in the SN increases the computed residence time. The increased residence time enable the complete burnout of CO to CO_2. The increase SN also increases the turbulence mixing, thus, reducing the

local hotspot in the combustor. Figure 5.21b shows that the NOx emission decreases with increasing SN. This is expected because the combustion maximum temperature similarly decreases with SN.

CHAPTER 6

NUMERICAL STUDY OF SYNGAS IN A PACKAGE BOILER

In the present study, the effects of replacing methane by syngas as fuel on the combustion and emissions characteristics are investigated numerically. The syngas used in this work comprised of only CO and H_2 gas. Due to composition variation that characterizes syngas production, different syngas compositions of 67%CO: 33%H_2, 50%CO: 50%H_2 and 33%CO: 67%H_2 by volume were studied and compared to methane combustion. As a basis for comparison, the volume of the fuel supplied was computed in such a way as to maintain a constant fuel energy supply of 200 MW which is the boiler continuous rating value. The effect of excess air factor on emission characteristics of the boiler was also presented.

6.1 Boiler Description and Solution Procedure

The three-dimensional view of the package boiler considered in the present study is given in Fig.6.1. The boiler is 12 m long, 6 m wide and 6 m high with the tube bank section of 2 m wide [151]. The boiler has two vertically aligned burners with a firing rate of 200 MW. Fuel is introduced through the nozzles with both the radial and axial velocity components and is surrounded by the primary air. The primary air passage has a swirler of 45^o swirl angle resulting in tangential and axial velocity component while the secondary air flows through the annular opening surrounding the primary air with no swirl component. The boiler is used for saturated steam (50 atm-drum pressure)

production in the tube bank at the rate of 240 tons/h. The front, side, rear and top walls of the furnace has a constant temperature boundary condition corresponding to the saturated temperature of the boiler pressure, while the bottom wall is maintained at adiabatic condition.

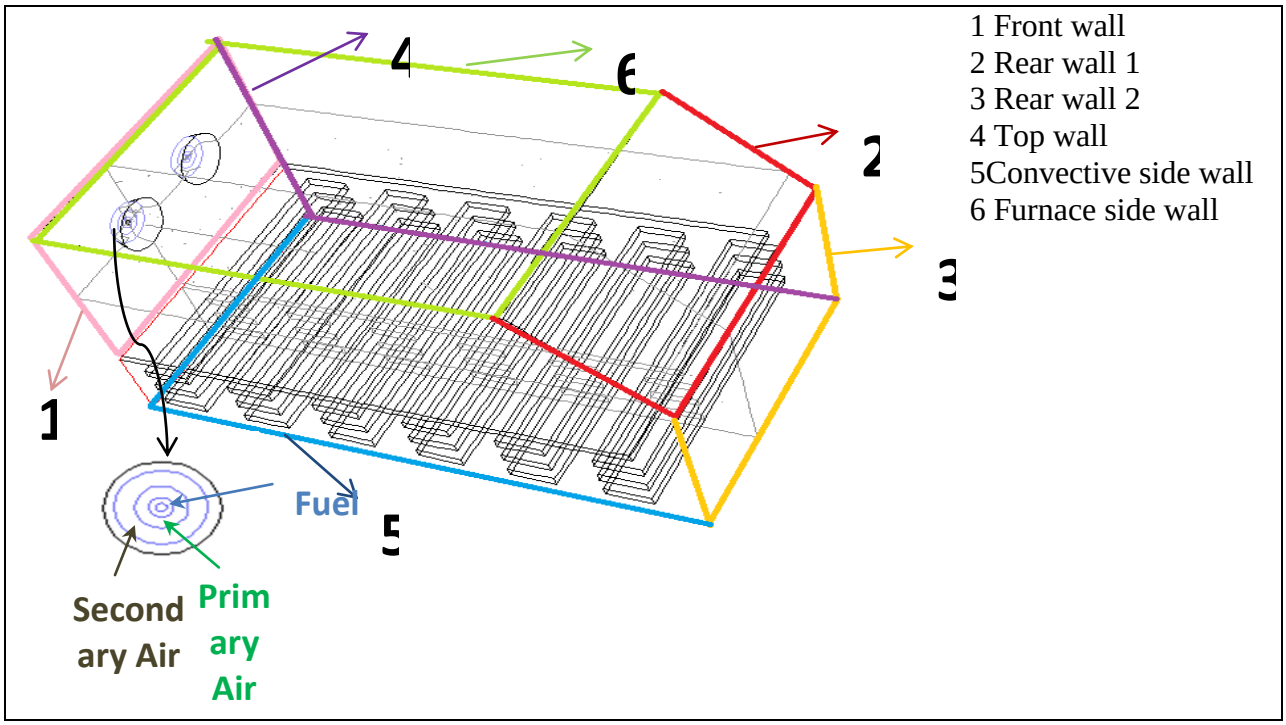

Figure 6.1: Schematic diagram of the package boiler

The set of governing equations presented in section 2.4 were solved numerically under the appropriate boundary conditions. The details of the calculation procedure can be found in previous works[151, 152]. About 400,000 cells were used to model the boiler. In order to minimize the diffusion errors, more grids were used in regions of large property gradients and in the vicinity of the walls. The solution procedure solves the partial differential equations for the conservation of mass, momentum, energy, radiation and

species using ANSYS-fluent 14 codes. The convergence criteria were set to 10^{-3} for the continuity, momentum, turbulent kinetic energy and dissipation rate equations. While residual of 10^{-6} is set for energy, radiation and species equations. NO was post processed from a converged combustion simulation with convergence criteria of 10^{-6}.

6.2 Syngas Chemistry Validation

In validating the syngas chemistry mechanism in turbulent combustion, data obtained from Jurgen et al.[45] were used. In their work, syngas fuel (40% CO, 40% H_2, and 20% N_2) and air were supplied through fuel nozzle of 0.024 m diameter and annular orifice of 0.05 m diameter respectively into the combustion chamber of 1 m length and 0.1m in diameter. The corresponding fuel and air inlet velocities are 4.13 and 2.88 m/s respectively. Syngas mechanism having 21 elementary steps with 11 species presented in Table 6.1 was used to model the combustion. The comparison between the probe measurement of the species concentration and the predicted values presented in Fig. 6.2 shows good prediction of CO and O_2 at a distance of 0.065 m from the burner.

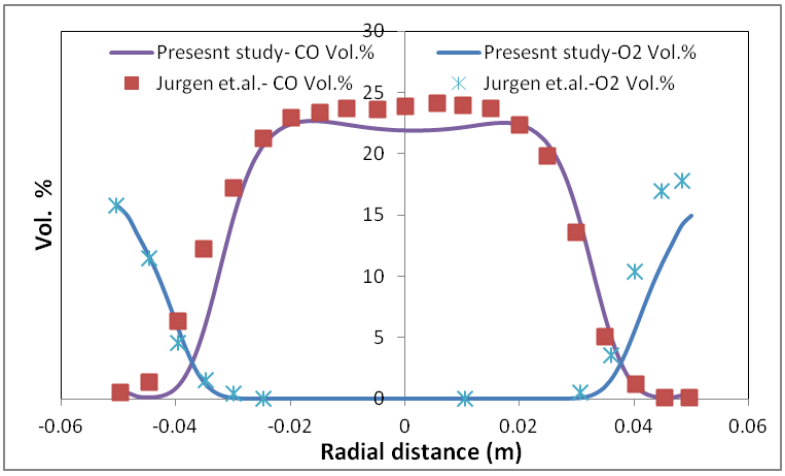

Figure 6.2: Comparison of the experimental and predicteded radial distribution of carbonmonoxide and oxygen.

Table6.1: Syngas-air combustion equations [45].

	Reaction	A [cm, mol, s]	β	E_a [kJ/mol]
R1	$H + O_2 = OH + O$	2.0E+014	0	16790.86
R2	$O + H_2 = OH + H$	5.06E+004	2.67	6281.64
R3	$H_2 + OH = H + H_2O$	1.00E+008	1.600	3296.07
R4	$OH + OH = H_2O + O$	1.50E+009	1.14	100.31
R5	$H + H + M = H_2 + M$ CO/0.75 / O_2 / 0.4/ CO_2 /1.5/ H_2O /6.5/ N_2/ 0.4	1.80E+018	-1.00	0.00
R6	$H + OH + M = H_2O + M$ CO/0.75 / O_2 / 0.4/ CO_2 /1.5/ H_2O /6.5/ N_2/ 0.4	2.20E+022	-2.000	0.00
R7	$O + O + M = O_2 + M$ CO/0.75 / O_2 / 0.4/ CO_2 /1.5/ H_2O /6.5/ N_2/ 0.4	2.9E+17	-1.0	0.00
R8	$H + O_2 + M = HO_2 + M$ CO/0.75 / O_2 / 0.4/ CO_2 /1.5/ H_2O /6.5/ N_2/ 0.4	2.30E+018	-0.80	0.00
R9	$HO_2 + H = OH + OH$	1.50E+014	0.000	1003.152
R10	$HO_2 + H = H_2 + O_2$	2.50E+013	0.000	692.65
R11	$HO_2 + H = H_2O + O$	3.00E+013	0.00	1719.69
R12	$HO_2 + O = OH + O_2$	1.80E+013	0.00	-406.038
R13	$OH + HO_2 = H_2O + O_2$	6.0E+013	0.000	0.00
R14	$HO_2 + HO_2 = H_2O_2 + O_2$	2.50E+011	0.000	-1241.998
R15	$OH + OH + M = H_2O_2 + M$ CO/0.75 / O_2 / 0.4/ CO_2 /1.5/ H_2O /6.5/ N_2/ 0.4	3.23E+022	-2.00	0.00
R16	$H_2O_2 + H = H_2 + HO_2$	1.7E+012	0.00	3749.88
R17	$H_2O_2 + H = H_2O + OH$	1.00E+013	0.00	3582.688
R18	$H_2O_2 + O = OH + HO_2$	2.8E+013	0.00	6401.07
R19	$H_2O_2 + OH = H_2O + HO_2$	5.4E+012	0.00	1003.152
R20	$CO + OH = CO_2 + H$	6.0E+006	1.5	-740.42
R21	$CO + O + M = CO_2 + M$ CO/0.75 / O_2 / 0.4/ CO_2 /1.5/ H_2O /6.5/ N_2/ 0.4	7.1E+013	0.000	-4538.07

6.3 Results and Discussion

6.3.1 Effect of Syngas Composition

In order to have insight of combustion dynamics in the boiler, one of the fuel ignition parameters i.e. the fuel thermal capacity was computed by the mass weighted sum of the product of density and specific heat capacity of constituents of the fuel. The computed thermal capacity was plotted along the center line of the lower burner(y=-2.24 m, z=2.198 m) as shown in Fig.6.3. Similar values were observed for the upper burner. Lower values of the fuel thermal capacity were observed for syngas fuel of 67%CO: 33%H_2. This indicates that the amount of thermal energy that is required to heat the fuel to reach its self ignition temperature is minimal that make it susceptible to early combustion as compared to other syngas fuel composition. Methane fuel was observed to have relatively high thermal capacity which may cause delay in the combustion. Beside the thermal capacity, the fuel-air mixing rate which can be characterized by the turbulent viscosity is exhibited in Fig.6.4. High turbulent viscosity was observed for syngas fuel of 50%CO: 50%H_2 and 33%CO: 67%H_2 which shows that there is better mixing of fuel and air which will enables it to achieve local stoichiometric condition earlier for combustion initiation as compared to 67%CO: 33%H_2 and methane fuel. The combination of the fuel (thermal capacity) and flow (turbulent viscosity) properties can be used to explain the temperature contours in a vertical plane passing through the axes of the two burners shown in Fig.6.5. Very low thermal capacity of 67%CO: 33%H_2 favors its early combustion while good mixing exhibited by 50%CO: 50%H_2 and 33%CO: 67%H_2 was able to offset the effect of high fuel thermal capacity that would have delay the combustion. On the other hand, methane that has high thermal capacity, and relatively

low mixing rate resulted in the delay in combustion as observed in the temperature contour (Fig.6.5d) and heat release contour (Fig.6.6d). The heat release is due to the effects of fuel combustion and can, thus, be used to characterize the flame. At low hydrogen content in the syngas (67%CO: 33%H_2), the flame is shown to be short indicating rapid consumption of fuel and high rate of energy release leading to rapid increase in temperature with possible flame interaction between the two burners. From the numerical point of view, combustion of hydrogen involves chain branching and chain propagation while the combustion of CO involves only its oxidation to form CO_2. Therefore, the rate of chain termination by the CO overwhelms chain branching and chain propagation by H_2. As the syngas gets enriched with hydrogen, the flame becomes elongated due to the presence of more H radical that enhance chain branching and chain propagation with a resultant increase in the reaction zone length (Fig.6.6c). The increase in the heat release region, (Fig.6.6) depict that the fuel energy are released more evenly within the boiler. This similarly results in a more even temperature distribution in the boiler and lowers the maximum furnace temperature. This is of an important advantage as the local hotspots that can aid the formation of thermal NO_X are minimized with lower risk of thermal degradation of the boiler material. Increasing H_2 content in the syngas also results in reduction of the production rate of high thermal capacity carbon dioxide (CO_2) that cools and shortens the flame.

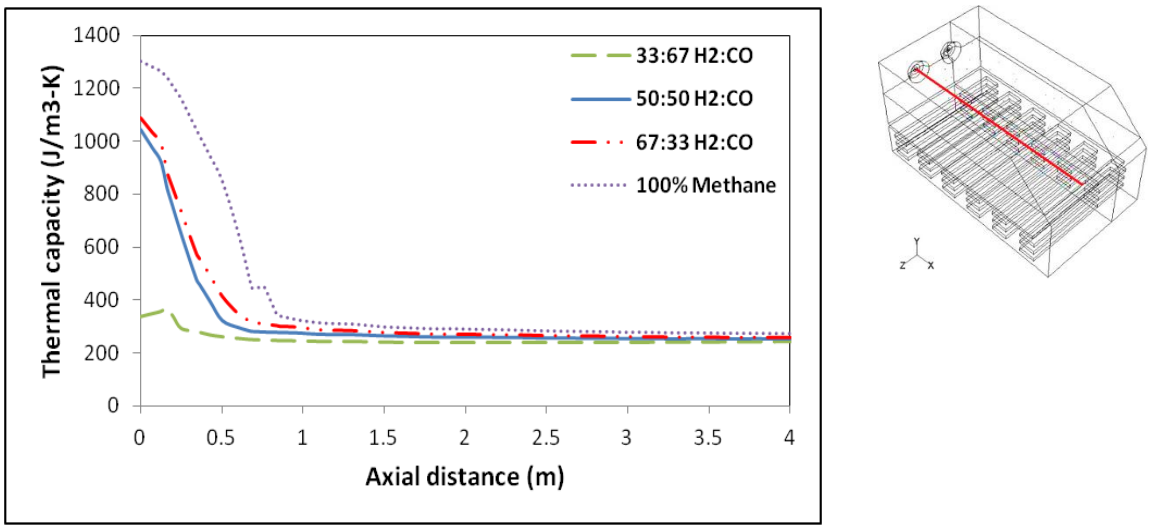

Figure 6.3: The thermal capacity of the gases mixture along the axis of the lower burner.

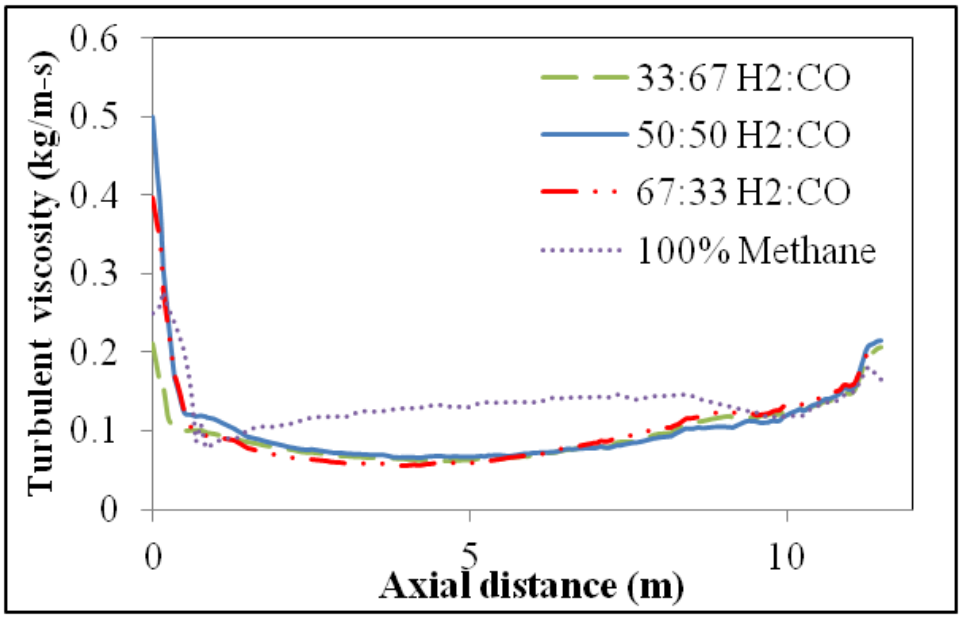

Figure 6.4: The Turbulent viscosity of the gases mixture along the axis of the lower burner.

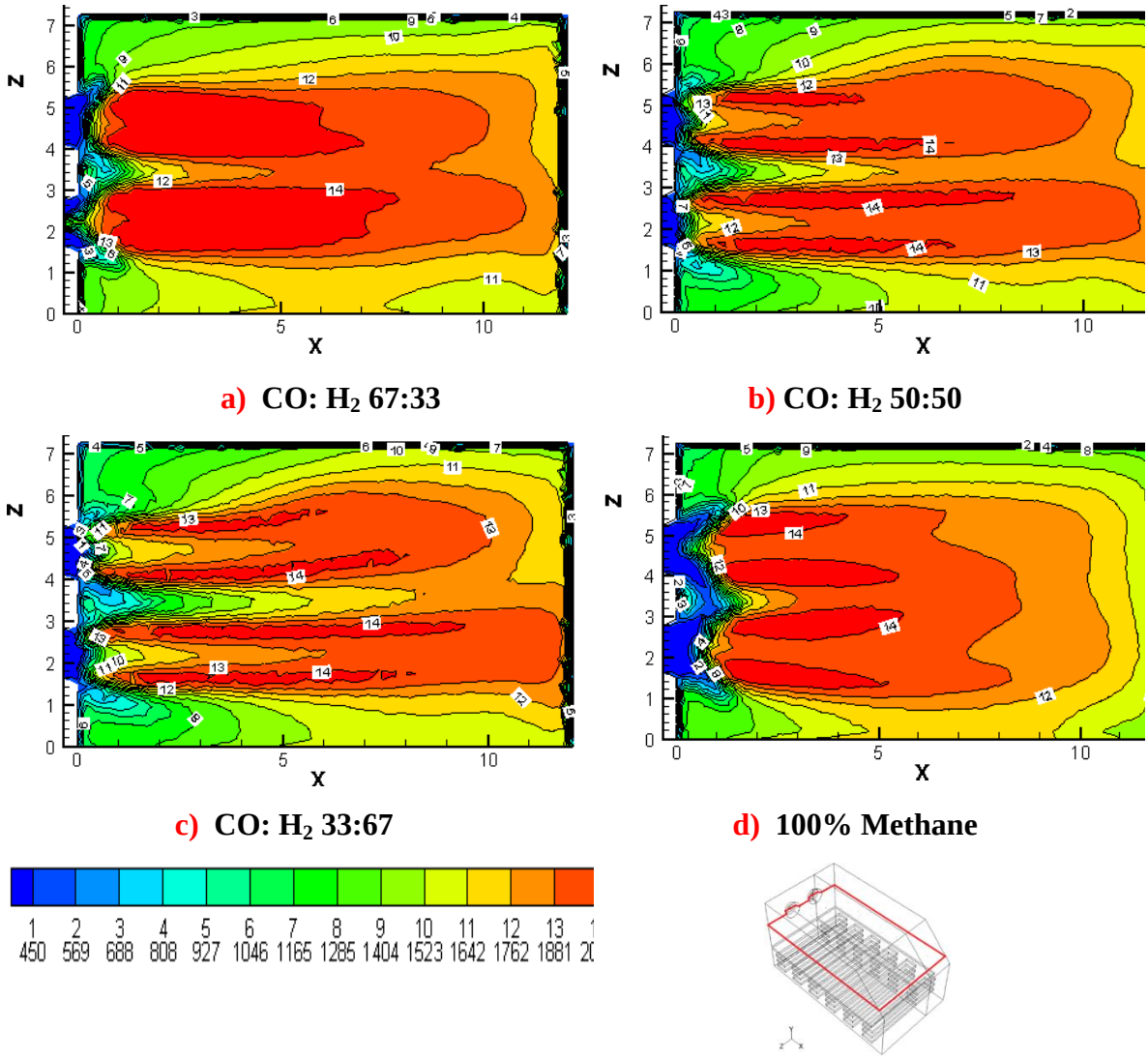

Figure 6.5: Temperature (K) distributions at a vertical plane passing through the two burners, y =-2.24 m

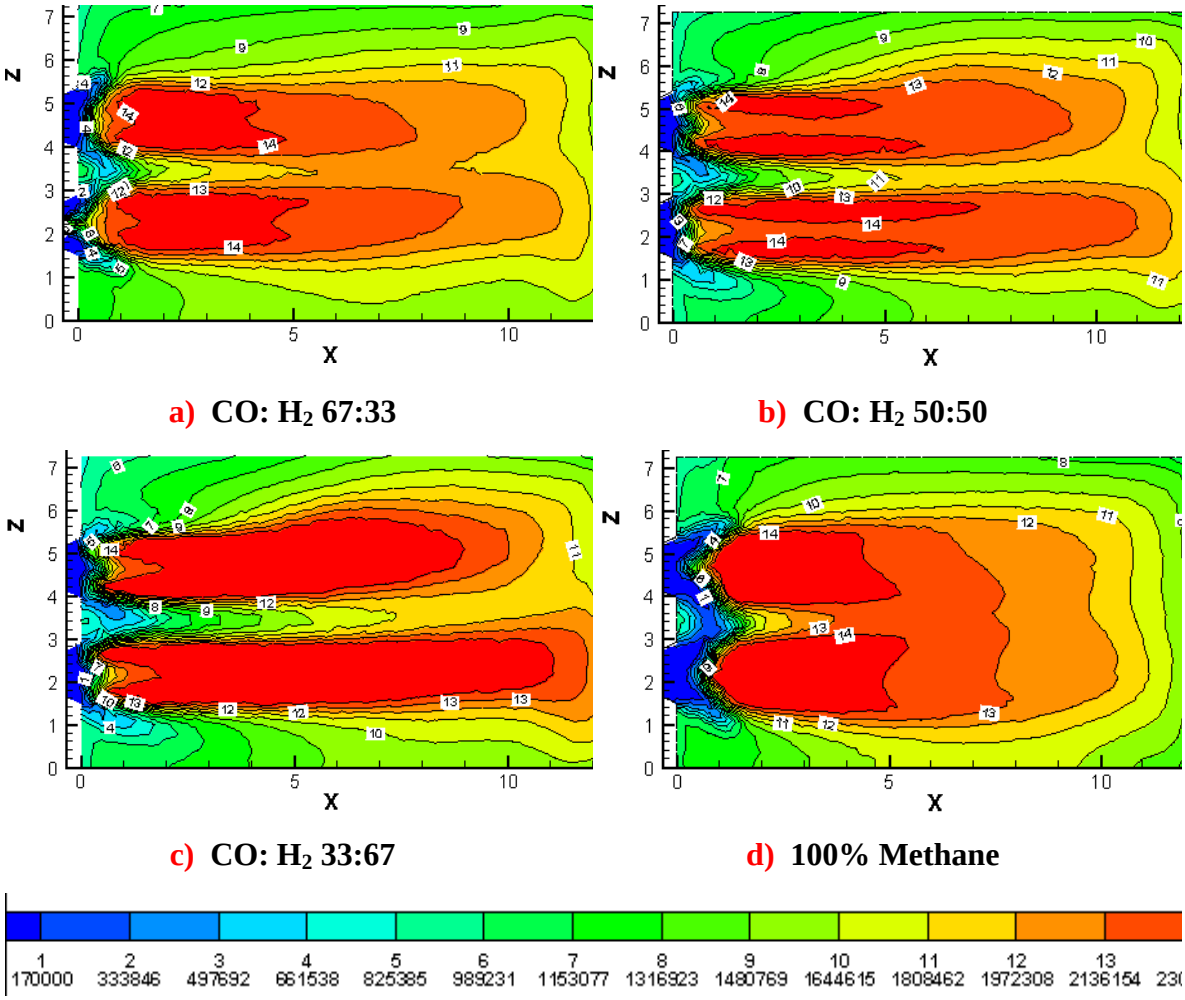

Figure 6.6: The heat release per kg of the gaseous mixture (J/kg) at a vertical plane passing through the axis of the two burners, y =-2.24 m.

The concentration of the heat release close to the burner discussed earlier in the case of 67%CO: 33%H_2 enables the incoming mixture to quickly reach self ignition temperature and anchoring of the flame to the burner as exhibited in Fig.6.6. The resultant short flame characteristics of 67%CO: 33%H_2 syngas and methane also discussed earlier can be observed by the peak temperature attained in the vicinity of the burner. However, for syngas of 33%CO: 67%H_2, slow rise in temperature may be attributed to initial chain

branching reaction of hydrogen that consumes energy. As the reaction zones become flooded with H radical, species recombination ensues and the amount of heat liberated in the exothermic steps continues to increase until temperature reaches its maximum value which decreases thereafter due to the heat loss at the rear walls that quenches the flame. Further insight into the delay in achieving the maximum temperature for syngas of 33%CO: 67%H_2 is observed in the plot of the fuel mole fraction along the center line of the lower burner shown in Fig.6.8. Syngas of 33%CO: 67%H_2 has the lowest fuel consumption rate, thus, have slow rise in temperature (Fig. 6.7). Despite the delay in methane fuel ignition due to its high thermal capacity, it has high mixing rates downstream of the burner which leads to more rapid fuel consumption compared to syngas fuels.

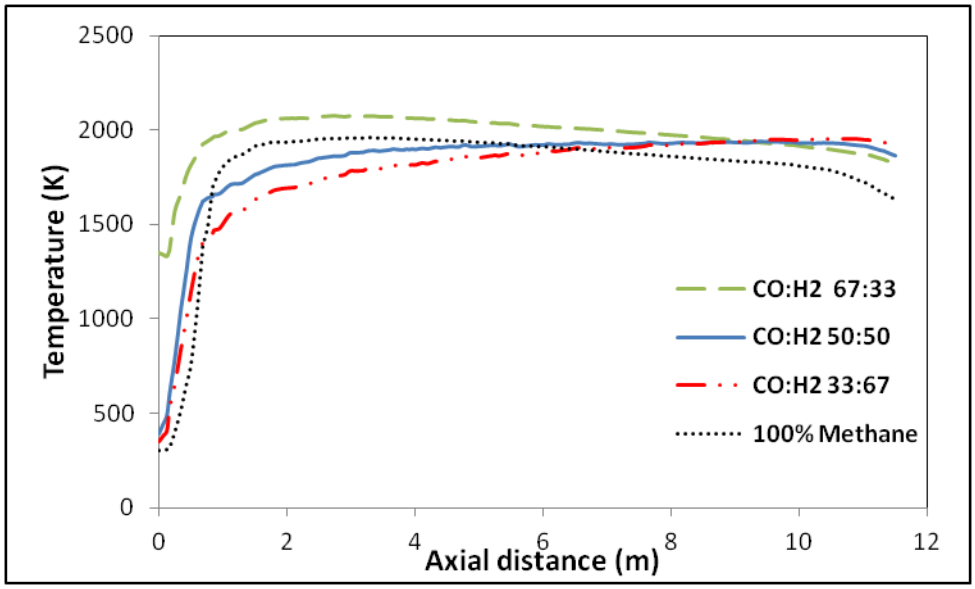

Figure 6.7: The Temperature distribution along the axis of the lower burner.

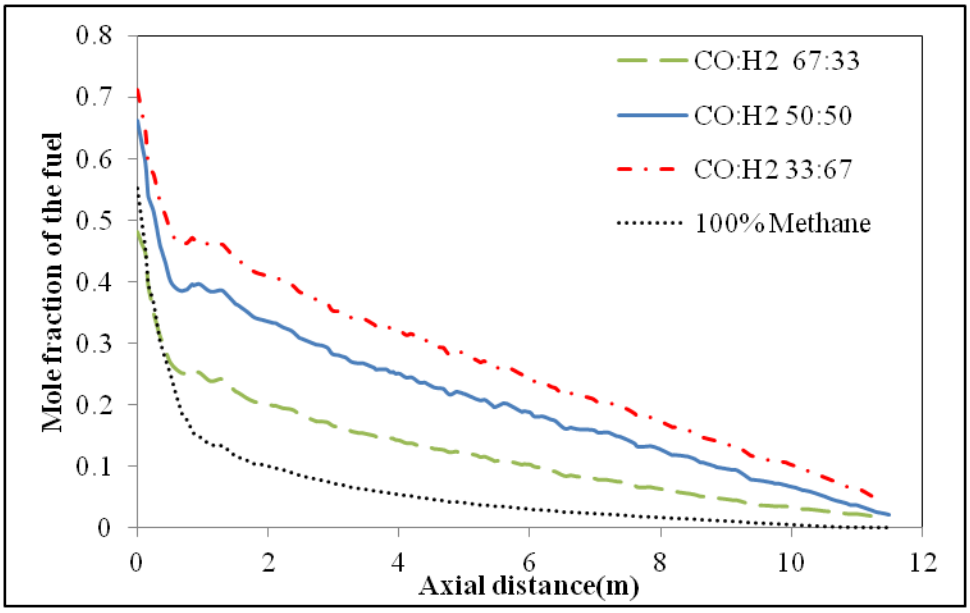

Figure 6.8: The mole fraction of the fuel along the axis of the lower burner.

Figure 6.9 indicates that the maximum boiler temperatures are highest for syngas (67%CO: 33%H_2) and methane fuel. The observed higher temperature will to lead to higher thermal NOx formation. The exit temperature was observed to increase with increase H_2 content in syngas fuel. The higher exit temperature is due to the increase in the observed flame length for syngas fuel with higher H_2. Thus, there is no enough residence time for the combustion product to mix with the excess air supplied.

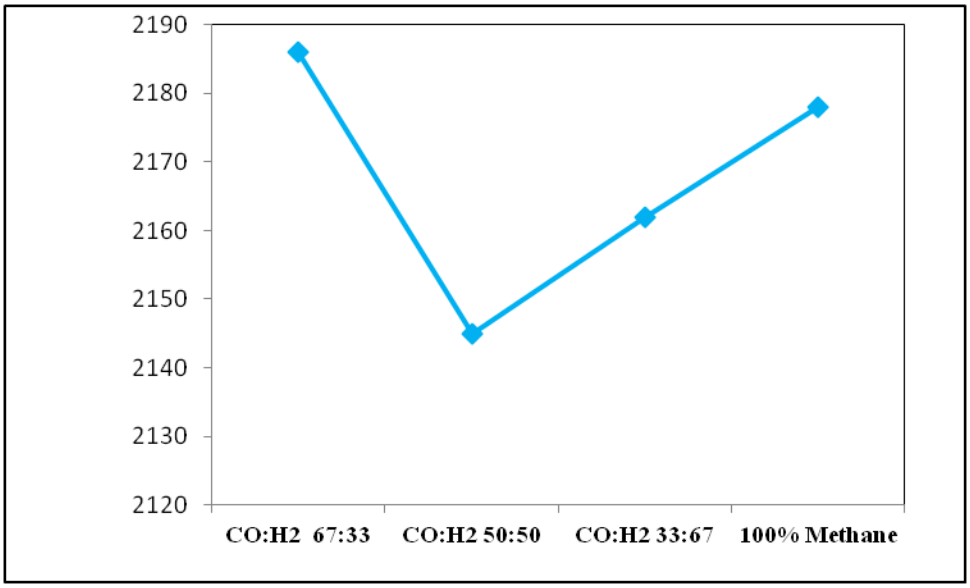

(a) Maximum temperature (K),

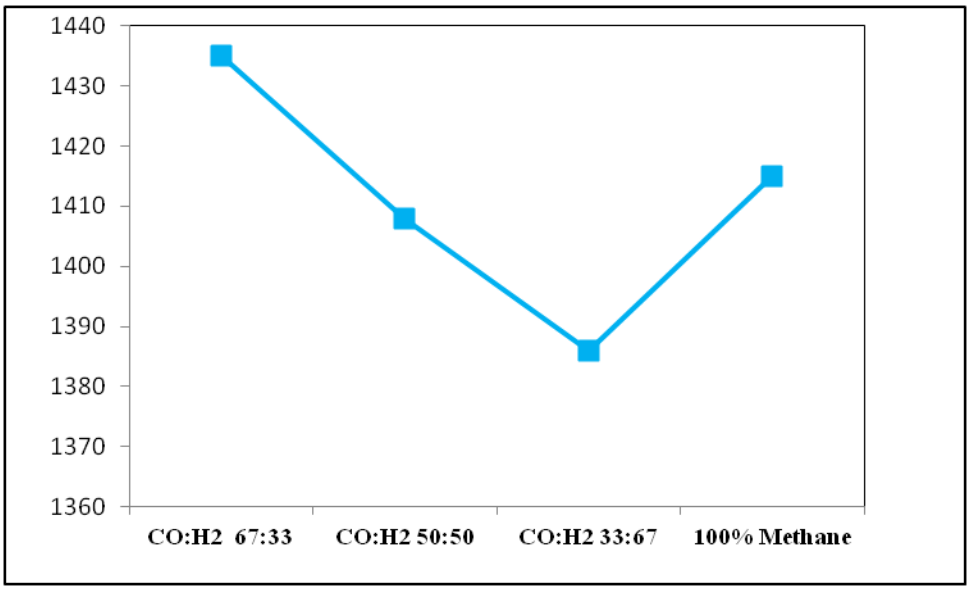

(b) Average temperature (K)

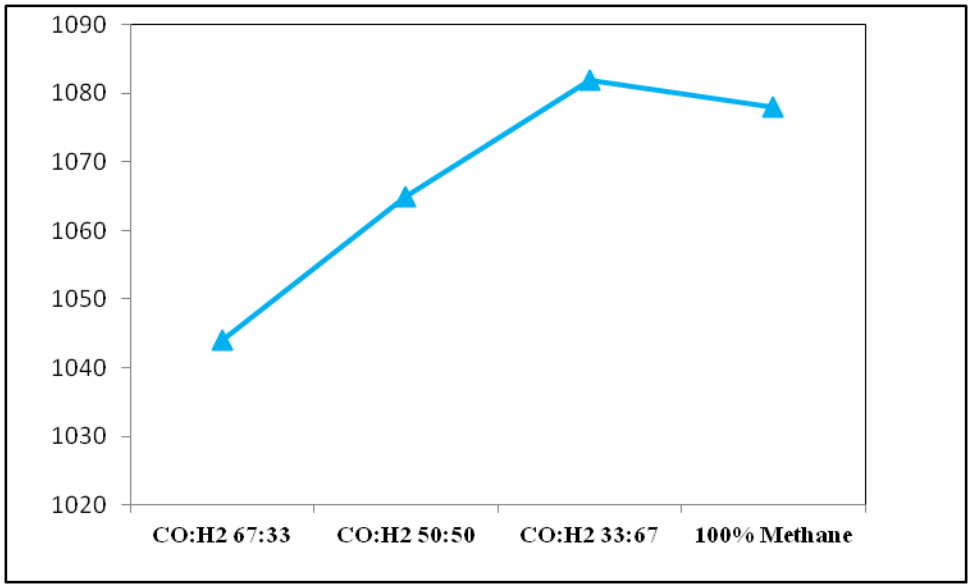

(c) Exhaust temperature (K).

Figure 6.9: Boiler temperature characteristics for different fuel compositions: a) Maximum temperature (K), b) Average temperature (K) and c) Exhaust temperature (K).

.

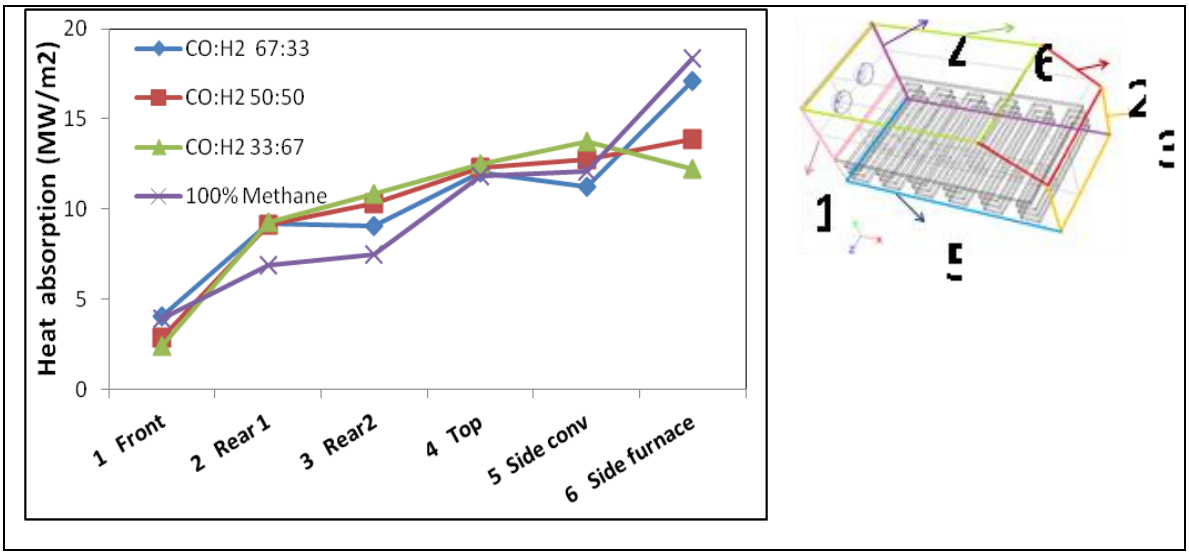

Figure 6.10: Heat loss through the package boiler walls at different compositions.

The different flame structures observed in different mixture compositions affect the heat absorption pattern to the boiler walls (Fig.6.10). More energy is absorbed by the front and

furnace sidewall (mainly in the furnace) in the case of CH_4 and syngas that are characterized by short flames while more energy is absorbed by to the rear walls and the convective side of the boiler by syngas fuels that have long flame characteristics. This means that significant part of the heat is available for steam generation in the convection part of the boiler. Thus, care must be taken to avoid pipe rupture due to higher available thermal energy that results in high temperature values.

6.3.2 Emission Rates

The effect of fuel composition on the emission characteristics of the boiler is summarized in Fig.6.11. Increasing the hydrogen content of the syngas reduces the carbon dioxide emission rate. This is expected due to decrease of CO in the fuel. This scenario fits into the much desired carbonless environment. It also reduces the challenge of capturing the carbon dioxide and its sequestration. CO_2 emission rate in syngas (33%CO: 67%H_2) was observed to be similar to that of the methane due to their similar C: H ratio. CO emission rate was observed to be highest in 67%CO: 33%H_2 syngas, this is due to CO fuel that escapes to the exit unburned. The unburned CO will lower the combustion efficiency. For this syngas fuel (33%CO: 67%H_2), the combustion can be improved by increasing the swirl angle for better mixing and/or increase the fuel-air opening to enhance the CO residence time in the furnace for complete combustion to CO_2 due to slow burning of CO. Negligible CO emission was observed at higher H_2 due to more active reaction zone that provides the required thermal energy for complete conversion of CO to CO_2. The NO emission which was post combustion processed and calculated using the extended Zeldovich mechanism [15]. Figs.6.11 shows that NOx emissions profiles have similar trend as that of the boiler maximum temperature (Fig.6.9a). Therefore, any strategy that

will lower the maximum temperature will also result in lowering NOx emission. Of all the compositions studied, 50%CO: 50%H_2 syngas was observed to be optimum in terms of the emission and maximum temperature which can affect life span of the boiler material. The contribution of the thermal and prompt NOx to the total NOx emission was also plotted in Fig.6.12. The thermal NOx was observed to be the NOx controlling parameter in the boiler. The prompt NOx was also significant in syngas fuel and increase with increasing CO concentration in the syngas. This may be attributed to more fuel rich zone in the furnace and can be as a result of more syngas fuel supplied to compensate for its lower heating value (i.e. CO = 11.4 MJ/m^3, H_2 = 9.8 MJ/m^3 and CH_4 = 31.5 MJ/m^3).

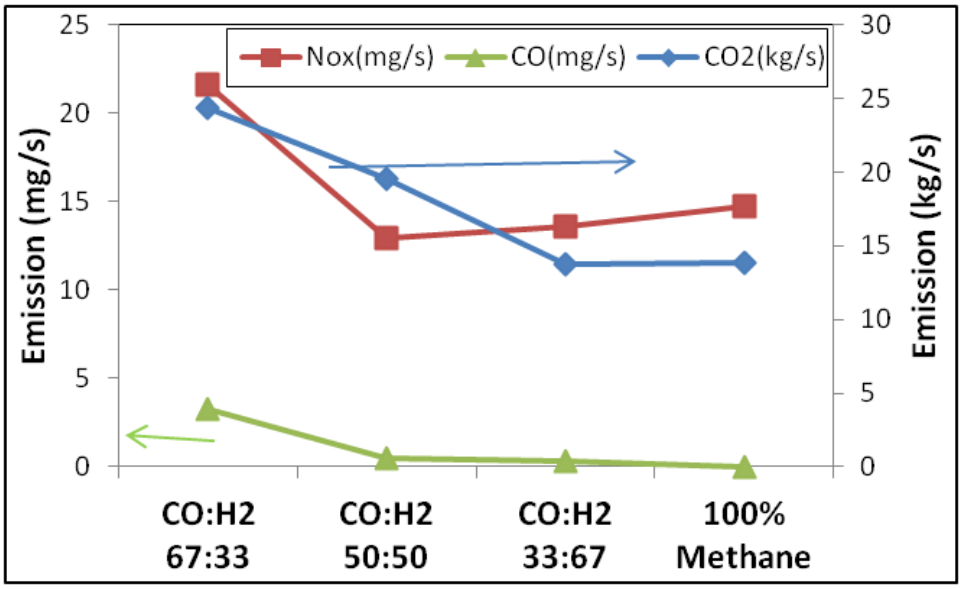

Figure 6.11: Emission rates at the exit section of the package boiler

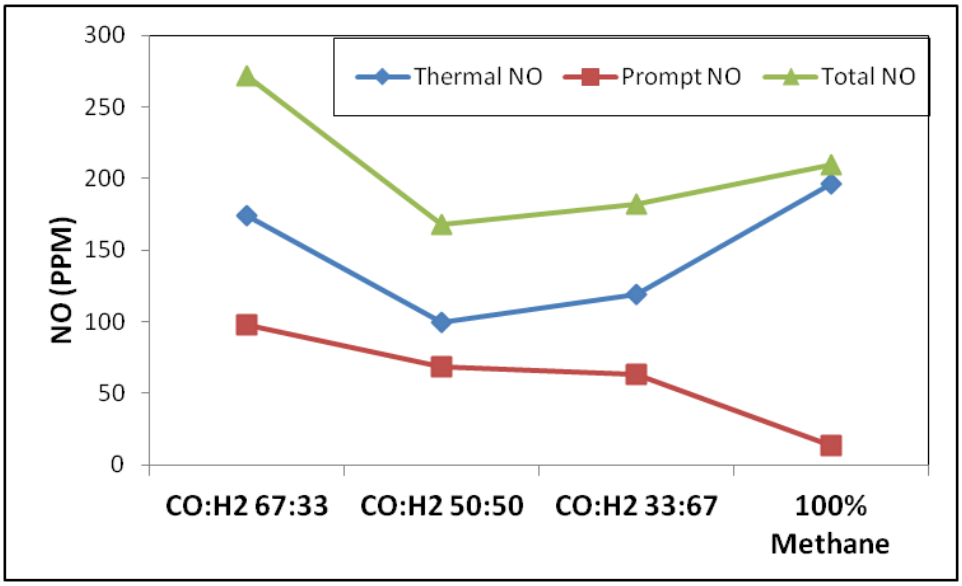

Figure 6.12: Influence of fuel composition on thermal and prompt NO at the exit section

6.3.3 Effect of Excess Air

The effect of excess air of 5%, 15% and 25% on the combustion dynamics and emission characteristics of the syngas using 50%CO: 50% H_2 as the representative syngas was also carried out. The effect of the excess air factor on the temperature distribution, fuel consumption rate and flame structure in the boiler was observed to be insignificant. It, however, reduces the maximum temperature in the boiler as seen in Fig.6.13. This may be due to the reduction of the adiabatic flame temperature with increasing excess air. The exit temperature was, however, observed to increase with increasing excess air due to the availability of more oxidizer that will enable the complete combustion of the residual fuel (especially CO) that might go to the exhaust unburned. The impact of the excess air on the emission is given in Fig.6.14. The increase in excess air supply increases the oxygen concentration in the reaction zone that favors the conversion of CO to CO_2 as seen in the increase in CO_2 and decrease in CO (Fig.6.14). NOx emission was observed to follow similar trend to maximum temperature in the furnace (Figs.6.14 and 6.15). In quantitative

terms, an increase in excess air from 5% to 25% decreases the NOx production rate by ~30%, which is promising. Most of the reduction in the NOx production is from the prompt NOx route. This means that the presence of more excess air reduces the fuel rich zone which consequently reduces the prompt and total NOx production.

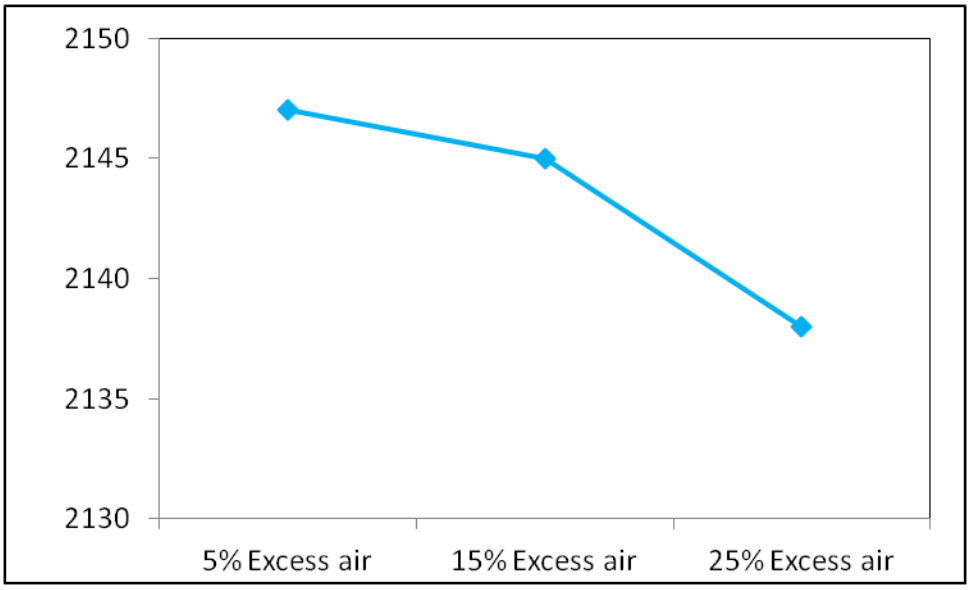

a) Maximum temperature (K),

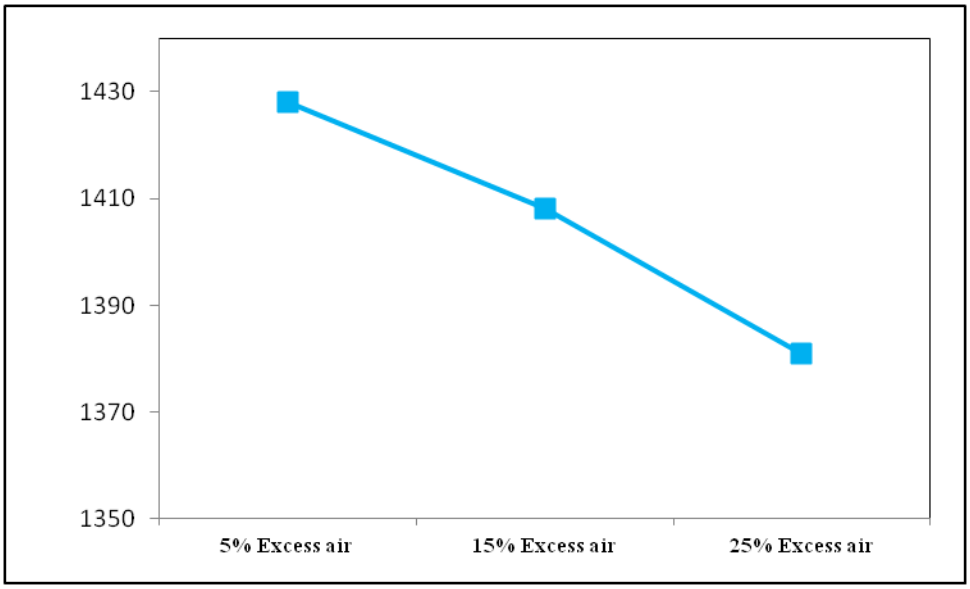

b) Average temperature (K)

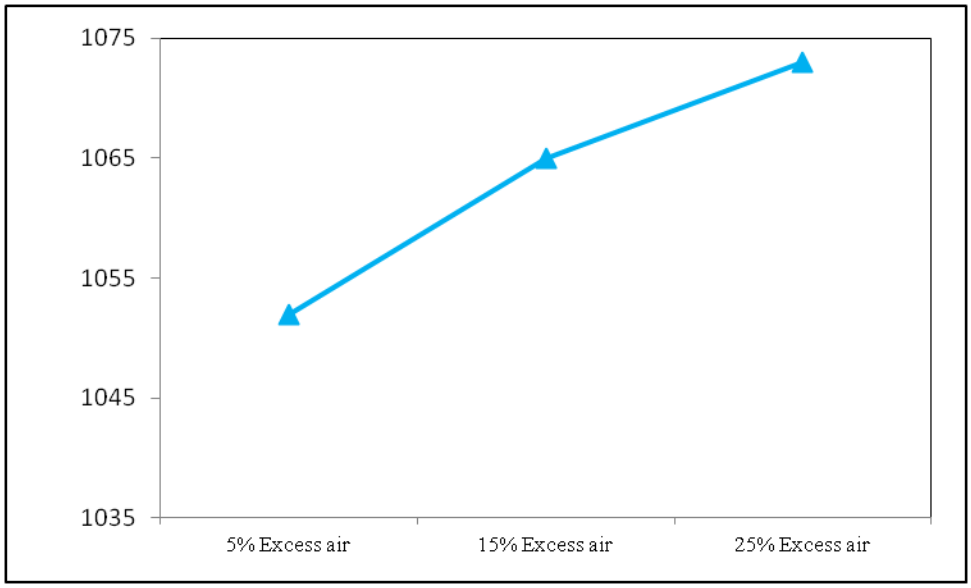

c) Exhaust temperature (K).

Figure 6.13: Boiler temperature characteristics for different excess air ratios

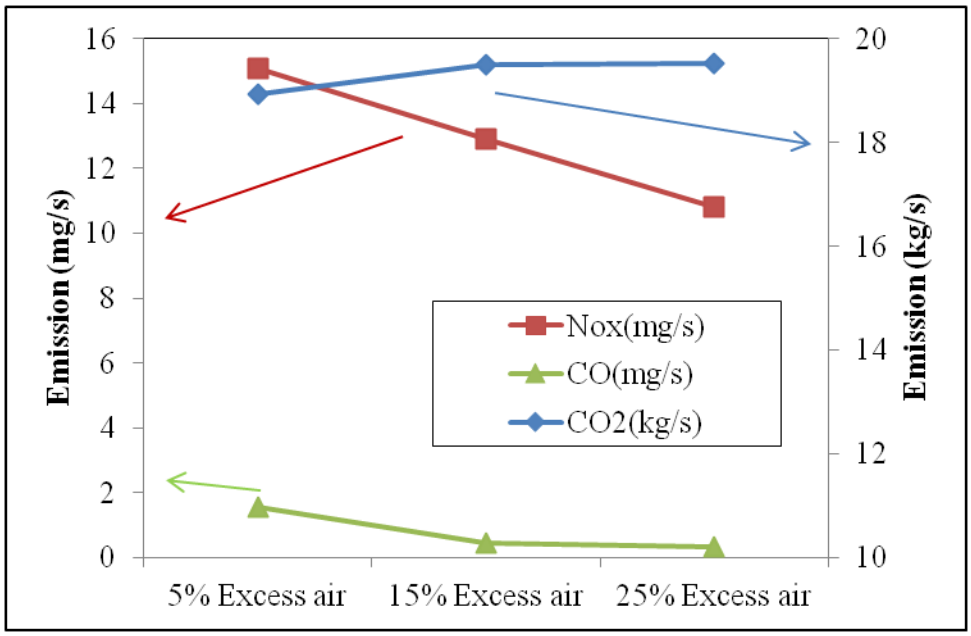

Figure 6.14: Emission rates at the exit section of the package boiler for CO: H_2 50:50 syngas

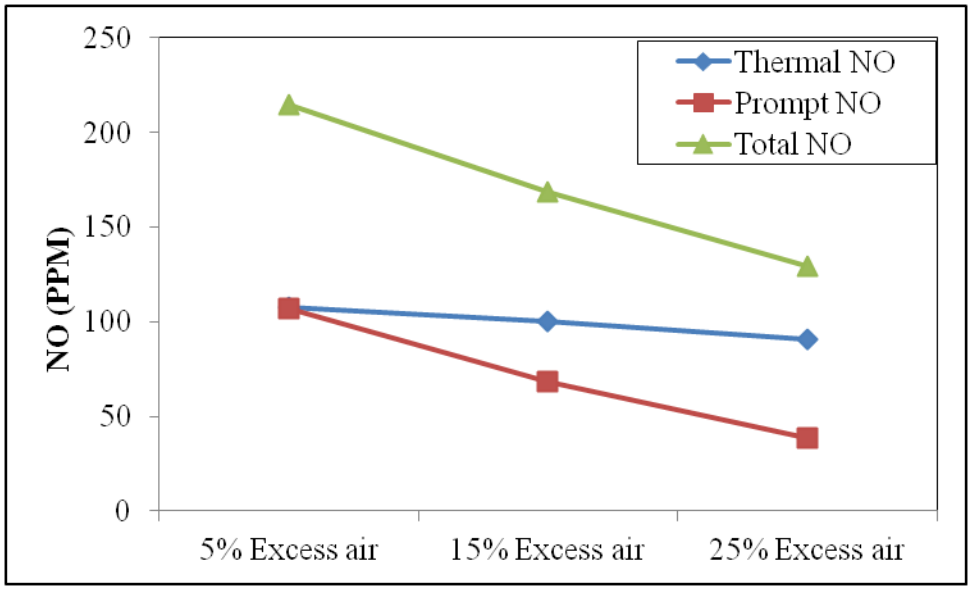

Figure 6.15: Influence of excess air factor on thermal and prompt NO at the exit section

CHAPTER 7

CONCLUSIONS AND RECOMMENDATIONS

7.1 Conclusions

Syngas is a potential energy source for the future due to its wide availability as a product of biofuel and fossil fuel gasification as well as a product of methane reforming. The composition of the syngas, however, depends on the source and method of production. Thus, this research work studied the effect of different syngas compositions and fuel energy inputs delivered to the combustor on the combustion characteristics, emission and combustor stability.

In the first part of this work, experiments were carried out in two laboratory scale swirl stabilized combustor; non-premixed combustor and a premixed combustor using mixture of methane and hydrogen as the characteristics syngas. In the non-premixed combustor, the temperature profile within the combustor, still flame images and emission data were taken to characterize the combustion. Deep blue flames were generally observed at 0% H_2, with the appearance of yellow luminous plume in the flame as the methane is enriched with H_2. The yellowish plume is attributed to the presence of unburned hydrocarbon (UHC) in the flame. The height, width and brightness of the yellow plume were observed to increase with increasing H_2 in the fuel mixture. This implies that the presence of hydrogen in the fuel mixture inhibits the oxidation of methane leading to the formation of unburned hydrocarbon (UHCs) in the flame. Increased hydrogen content in the fuel mixture, however, extends the flame blow off limit

(LBO) due to its resistance to extinction strain. The combustor NOx emission increased with increasing percentage of hydrogen in the fuel mixture due to increased combustor temperature. The extended LBO observed in hydrogen-enriched methane was employed to achieve zero NOx emission without the flame prone to instability. Measured temperatures decreased with increasing axial distance due to the cooling of the combustor by the ambient air as well as the continuous mixing of the combustion product and the excess air. The temperature data were used to validate the numerical model using ANSYS-Fluent 14 software. Increasing the H_2 content to 50% in methane decreases the CO_2 emission up to about 30%. This is very significant owing to the amount of CO_2 emission from power plants.

In the premixed combustor, equivalence ratio sweep test was carried out at different fuel compositions (H_2/CH_4 mixture) to show the dependence of hydrogen on the thermo-acoustic instability. The dynamic pressure and Chemiluminescence intensity measurement as well as the Chemiluminescence images were taken at all operating conditions to identify distinct operating modes in the combustor at different CH4/H2-air fuel compositions. The premixed combustor was generally observed to exhibit a bi-modal state (stable → unstable). The combustor was in a stable mode near the lean blow off limit. As the equivalence ratio is increased up till the transition point (equivalence ratio), the combustor shift from stable to an unstable mode. The unstable modes are due to flame–vortex interactions driven by acoustically-coupled velocity oscillations in the flame-anchoring region. The computed phase angle shows that the heat release lead the pressure such that $\theta_{qp} \geq 0$. This indicates that the heat release and the pressure oscillation are positively coupled with the instabilities triggered at maximum coupling

(θ_{qp} approaches zero). Despite similar amplitude of the OASPL the phase angle varies with equivalence ratio and frequency. This implies that the phase can be quantitatively used in identifying the state of the combustor. With increasing H_2 content in the CH_4/H_2, the stability map of the combustor including the transition point shift to region of lower equivalence ratio. This suggests, there is a strong dependence of the combustor stability regime on the hydrogen composition in the fuel. The lean blow off equivalence for all the flame understudy was also observed to decrease with increasing hydrogen content in methane due to hydrogen resistance to extinction strain as compared to methane. Irrespective of the hydrogen composition, the flame macro images shows that the flame transit as: Bubble flame> cone flame stabilized in IRZ> cone flame stabilized in the ORZ. The flame transition equivalence ratio however depends on the hydrogen contents. Similar flame shapes were observed at the same extinction strain rates irrespective of the CH_4/H_2 mixture. These flame shapes are linked to the stability of the combustor. The collapse of the OASPL and phase data with the extinction strain rate suggest that the stability of the combustor and its acoustic footprint for different operating conditions can be encapsulated in the extinction strain rates. This property can be used in the scaling of the combustor instability.

In the second part of this dissertation, numerical study of combustion in a non-premixed combustor was carried out using ANSYS-FLUENT 14 codes. Global mechanism with one-step by Westbrook and Dryer, two-step mechanism with irreversible and reversible CO/CO_2 step (2sCM1 and 2sCM2) were used for combustion modeling. Results showed that the Westbrook and 2sCM1 over predicted the NOx emission at all conditions studied. The over prediction could be attributed to the escalation of the

temperature in the reaction zone. The absence of intermediary species of CO and irreversible CO/ CO_2 step in Westbrook and 2sCM1, respectively, is suggested for the temperature escalation. On this basis, a modified 2sCM2 mechanism was proposed for modeling CH_4 and CH_4/H_2 under ultra-lean conditions. The modified 2sCM2 mechanism presented gave good predictions of the combustor temperature, major species and NOx emissions. The effect of the thermal boundary condition of the combustor was observed to have effect on the thermal quenching of the active species and gas expansion rate. This implies that the residence time of the combustion product can be influenced by the thermal boundary condition of the combustor. The increase/decrease combustor residence time will lead to complete burn out of the CO (or decomposition of CO_2) as well as reduced NOx formation in the combustor depending on the prevailing conditions. The equivalence ratio sweep test was thereafter carried out numerically to show that, there exists an equivalence ratio where the emissions (CO and NOx) from the combustor are optimum for any given fuel composition. Based on the numerical model developed, the effect of replacing methane with syngas fuel (CO/H_2) of different compositions on the flame stability and emission characteristics in a 200 MW package boiler were investigated. Of all the fuel compositions studied, syngas fuel of 50% CO: 50% H_2 was observed to be optimum in terms of emission control with lowest maximum temperature thereby having a tendency to improve the life span of the boiler material.

The observations from this study have several implications.

1) The present study provides a basis for ultra-lean combustion towards achieving zero NOx emission in a fuel-flexible combustor. 2) The enrichment of methane with hydrogen at the same fuel energy input decreased the fuel density thereby leads to high

fuel injection velocity. The issue of high injection velocity needs to be addressed by redesigning of the burner to reduce the gas inlet velocity when using hydrogen-enriched fuels. 3) Hydrogen-enriched methane has higher flame temperatures as compared to methane. Data of obtainable temperature at different operating conditions presented in this study can serve as guide when changing fuel from natural gas to syngas (CH_4/H_2). This will enable the operator to operate within safe limit and protect integrity of the combustor material. Similar data are required for other fuel mixtures. 4) The combustion residence time has also been shown to have significant influence on emission from the combustor. In combustor design, while minimum residence times required for CO burn out, may not be sufficient for zero NOx emission. Thus, a trade off may be required for optimum emission in line with environmental regulations. The residence time of the combustion product can be influence by changing the swirl number of the combustor. 5) The collapse of the combustor dynamic response for different syngas (CH_4/H_2) with the extinction strain rate has indicated a means of predicting the combustor instability for arbitrary change in fuel compositions (CH_4/H_2). This method could be extended to fuel mixtures such syngas (CO/H_2).

7.2 Recommendations

Suggestions and ideas for future research are summarized as follows:

1. The use of combustion diagnostic equipment such as has high-resolution particle image velocimetry (PIV) and Planar Laser Induced Fluorescence (PLIF) of CH* and OH* radicals can be used to resolve the flame and flow structures and their

interactions. Result from this measurement can further be used to validate the numerical models developed.

2. Experiments can be carried out under partially premixed conditions to study the effect of the different fuels composition on the combustion stability and emission. This is to achieve low emissions with reduced tendency for flash black.
3. The use of intrusive measuring probe will have influence on the flow structure and affect parameters being measured. Thus, temperature and emission measurement required for validation can be measured using laser facilities.
4. This study should also be extended both numerically and experimentally such that combustion characteristics and emission of practical syngas (CO/H_2) that contains trace amounts of CH_4, CO_2, N_2, C_2H_6 and C_3H_8 can be studied.
5. The modified 2sCM2 chemical mechanism presented can be investigated at fundamental level at different conditions to examine the level of its accuracy. The mechanism can also be tested outside the range of this study.
6. In reality the flame and flow are not fully axisymetry, thus, a 3-D numerical calculation that will better resolve the flame/flow structure can be carried out.
7. The effect of air preheating obtainable in gas turbine can be incorporated in the combustor, this enables the combustor to achieve lean burning without suffering from combustor blow off.
8. The acoustic response of premixed combustor running CH_4/H_2 was collapse using the extinction strain rate. This study can be extended for syngas fuel.
9. The global flame shapes were taken for the non-premixed flames, high speed Chemiluminescence images should be taken to study the dynamic flame shape.

REFERENCES:

[1] Electricity/Heat in the World. Available: http://www.iea.org/stats/electricitydata.asp?COUNTRY_CODE=29

[2] International Energy Outlook 2013. Available: http://www.eia.gov/forecasts/ieo/

[3] S. Solomon, G.-K. Plattner, R. Knutti, and P. Friedlingstein, "Irreversible climate change due to carbon dioxide emissions," Proceedings of the national academy of sciences, vol. 106, pp. 1704-1709, 2009.

[4] R. S. Tol, "The marginal damage costs of carbon dioxide emissions: an assessment of the uncertainties," Energy policy, vol. 33, pp. 2064-2074, 2005.

[5] M. Emadi, M. Burkhalter, T. Salameh, T. Gentry, and A. Ratner, "Examination of thermo-acoustic instability in a low swirl burner," in Spring technical meeting of the central states section of the combustion institute. Ohio, USA, 2012.

[6] K. Venkataraman, L. Preston, D. Simons, B. Lee, J. Lee, and D. Santavicca, "Mechanism of combustion instability in a lean premixed dump combustor," Journal of Propulsion and Power, vol. 15, pp. 909-918, 1999.

[7] S. Hermeth, G. Staffelbach, L. Y. Gicquel, V. Anisimov, C. Cirigliano, and T. Poinsot, "Bistable swirled flames and influence on flame transfer functions," Combustion and Flame, vol. 161, pp. 184-196, 2014.

[8] Actual Generating Capacity and Peak Load chart. Available: http://www.data.gov.sa/dataset/actual-generating-capacity-and-peak-load-chart

[9] Annual Reports - Saudi Electricity Company. Available: www.se.com.sa/en-us/Lists/AnnualReports/Attachments/11/AnnualReport2013En.pdf

[10] S. M. Shaahid and M. A. Elhadidy, "Economic analysis of hybrid photovoltaic-diesel-battery power systems for residential loads in hot regions-A step to clean future," Renewable and Sustainable Energy Reviews, vol. 12, pp. 488-503, 2008.

[11] Saudi Arabia Looks to Secure $109 Billion to Develop its Solar Industry. Available: http://oilprice.com/Latest-Energy-News/World-News/Saudi-Arabia-Looks-to-Secure-109-Billion-to-Develop-its-Solar-Industry.html

[12] Saudi Arabia Starts Survey of Renewable Energy Potential Available: http://www.bloomberg.com/news/2013-07-02/saudi-arabia-starts-survey-of-renewable-energy-potential.html

[13] Y. Ding and E. Alpay, "Adsorption-enhanced steam–methane reforming," Chemical engineering science, vol. 55, pp. 3929-3940, 2000.

[14] S. Blakey, L. Rye, and C. W. Wilson, "Aviation gas turbine alternative fuels: A review," Proceedings of the Combustion Institute, vol. 33, pp. 2863-2885, 2011.

[15] J. r. D. Warnatz, Robert W; Maas, Ulrich, Combustion: Physical and Chemical Fundamentals, Modeling and Simulation, Experiments, Pollutant Formation, 4th Edition. ed., 2006.

[16] T. Lieuwen, V. McDonell, D. Santavicca, and T. Sattelmayer, "Burner development and operability issues associated with steady flowing syngas fired combustors," Combustion Science and Technology, vol. 180, pp. 1169-1192, 2008.

[17] S. Gadde, J. Wu, A. Gulati, G. McQuiggan, B. Koestlin, and B. Prade, "Syngas capable combustion systems development for advanced gas turbines," ASME Paper GT20006-90970, 2006.

[18] D. Sanchez, R. Chacartegui, J. M. Munoz, A. Munoz, and T. Sanchez, "Performance analysis of a heavy duty combined cycle power plant burning various syngas fuels," International Journal of Hydrogen Energy, vol. 35, pp. 337-345, 2010.

[19] E. O. Oluyede and J. N. Phillips, "Fundamental impact of firing syngas in gas turbines," Proceedings of ASME Turbo Expo 2007 (GT2007), pp. 14-17, 2007.

[20] M. C. Lee, S. B. Seo, J. H. Chung, S. M. Kim, Y. J. Joo, and D. H. Ahn, "Gas turbine combustion performance test of hydrogen and carbon monoxide synthetic gas," Fuel, vol. 89, pp. 1485-1491, 2010.

[21] A. E. E. Khalil and A. K. Gupta, "Distributed swirl combustion for gas turbine application," Applied Energy, vol. 88, pp. 4898-4907, 2011.

[22] D. R. Noble, Q. Zhang, A. Shareef, J. Tootle, A. Meyers, and T. Lieuwen, "Syngas mixture composition effects upon flashback and blowout," 2006, pp. 8-11.

[23] D. M. G. Gregory P. Smith, Michael Frenklach, Nigel W. Moriarty, Boris Eiteneer, Mikhail Goldenberg, C. Thomas Bowman, Ronald K. Hanson, Soonho Song, William C. Gardiner, Jr., Vitali V. Lissianski, and Zhiwei Qin. (2013, 4th March). GRI-Mech 3.0 Available: www.me.berkeley.edu/gri_mech

[24] S. G. Davis, A. V. Joshi, H. Wang, and F. Egolfopoulos, "An optimized kinetic model of H2/CO combustion," Proceedings of the Combustion Institute, vol. 30, pp. 1283-1292, 2005.

[25] J. Li, Z. Zhao, A. Kazakov, M. Chaos, F. L. Dryer, and J. J. Scire, "A comprehensive kinetic mechanism for CO, CH2O, and CH3OH combustion," International Journal of Chemical Kinetics, vol. 39, pp. 109-136, 2007.

[26] Z. M. Nikolaou, J.-Y. Chen, and N. Swaminathan, "A 5-step reduced mechanism for combustion of CO/H2/H2O/CH4/CO2 mixtures with low hydrogen/methane and high H2O content," Combustion and Flame, 2012.

[27] O. A. Marzouk and E. D. Huckaby, "A comparative study of eight finite-rate chemistry kinetics for CO/H2 combustion," Engineering applications of computational fluid mechanics, vol. 4, pp. 331-356, 2010.

[28] A. Frassoldati, T. Faravelli, and E. Ranzi, "The ignition, combustion and flame structure of carbon monoxide/hydrogen mixtures. Note 1: Detailed kinetic modeling of syngas combustion also in presence of nitrogen compounds," International Journal of Hydrogen Energy, vol. 32, pp. 3471-3485, 2007

[29] P. Boivin, C. Jimenez, A. L. Sanchez, and F. A. Williams, "A four-step reduced mechanism for syngas combustion," Combustion and Flame, vol. 158, pp. 1059-1063, 2011.

[30] N. Slavinskaya, M. Braun-Unkhoff, and P. Frank, "Reduced reaction mechanisms for methane and syngas combustion in gas turbines," Journal of engineering for gas turbines and power, vol. 130, 2008.

[31] A. Cuoci, A. Frassoldati, T. Faravelli, and E. Ranzi, "Accuracy and Flexibility of Simplified Kinetic Models for CFD Applications," in Combustion Colloquia-32 nd Combustion meeting, II-6, 2009, pp. 26-28.

[32] J. Natarajan, S. Nandula, T. Lieuwen, and J. Seitzman, "Laminar flame speeds of synthetic gas fuel mixtures," ASME Paper# GT2005-68917, 2005.

[33] C. Dong, Q. Zhou, Q. Zhao, Y. Zhang, T. Xu, and S. Hui, "Experimental study on the laminar flame speed of hydrogen/carbon monoxide/air mixtures," Fuel, vol. 88, pp. 1858-1863, 2009.

[34] N. Bouvet, S. Y. Lee, I. Gokalp, and R. J. Santoro, "Flame speed characteristics of syngas (H2-CO) with straight burners for laminar premixed flames," 2007.

[35] H. Sun, S. I. Yang, G. Jomaas, and C. K. Law, "High-pressure laminar flame speeds and kinetic modeling of carbon monoxide/hydrogen combustion," Proceedings of the Combustion Institute, vol. 31, pp. 439-446, 2007.

[36] J. Fu, C. Tang, W. Jin, L. D. Thi, Z. Huang, and Y. Zhang, "Study on laminar flame speed and flame structure of syngas with varied compositions using OH-PLIF and spectrograph," International Journal of Hydrogen Energy, vol. 38, pp. 1636-1643, Feb 6 2013.

[37] C. Prathap, A. Ray, and M. R. Ravi, "Effects of dilution with carbon dioxide on the laminar burning velocity and flame stability of H2/CO mixtures at atmospheric condition," Combustion and Flame, vol. 159, pp. 482-492, 2012.

[38] J. Natarajan, T. Lieuwen, and J. Seitzman, "Laminar flame speeds of H2/CO mixtures: Effect of CO2 dilution, preheat temperature, and pressure," Combustion and Flame, vol. 151, pp. 104-119, 2007.

[39] S. Yousefian, A. Ghafourian, and M. Darbandi, "Numerical study of syngas premixed flame structure and extinction," Chia Laguna, Cagliari, Sardinia, Italy, September 11-15, 2011.

[40] E. Monteiro and A. Rouboa, "Measurements of the Laminar Burning Velocities for Typical Syngas-Air Mixtures at Elevated Pressures," Journal of Energy Resources Technology, vol. 133, p. 031002, 2011.

[41] K. W. Chun, H.-J. Chung, S. H. Chung, and J. H. Choi, "A numerical study on extinction and NOx formation in nonpremixed flames with syngas fuel," Journal of mechanical science and technology, vol. 25, pp. 2943-2949.

[42] D. E. Giles, S. Som, and S. K. Aggarwal, "NOx emission characteristics of counterflow syngas diffusion flames with airstream dilution," Fuel, vol. 85, pp. 1729-1742, 2006.

[43] G. J. Rortveit, J. E. Hustad, S.-C. Li, and F. A. Williams, "Effects of diluents on NOx formation in hydrogen counterflow flames," Combustion and Flame, vol. 130, pp. 48-61, 2002.

[44] C. Ghenai, "Combustion of Syngas Fuel in Gas Turbine Can Combustor," Advances in Mechanical Engineering, vol. 2010, 2010.

[45] J. J. J. Louis, J. B. W. Kok, and S. A. Klein, "Modeling and measurements of a 16-kW turbulent nonadiabatic syngas diffusion flame in a cooled cylindrical combustion chamber," Combustion and Flame, vol. 125, pp. 1012-1031, 2001.

[46] J. Wang, Z. Huang, C. Tang, H. Miao, and X. Wang, "Numerical study of the effect of hydrogen addition on methane-air mixtures combustion," International Journal of Hydrogen Energy, vol. 34, pp. 1084-1096, 2009.

[47] G. A. Karim, "Hydrogen as a spark ignition engine fuel," International Journal of Hydrogen Energy, vol. 28, pp. 569-577, 2003.

[48] J. Wang, Z. Huang, C. Tang, and J. Zheng, "Effect of hydrogen addition on early flame growth of lean burn natural gas-air mixtures," International Journal of Hydrogen Energy, vol. 35, pp. 7246-7252, 2010.

[49] S. R. Bell and M. Gupta, "Extension of the lean operating limit for natural gas fueling of a spark ignited engine using hydrogen blending," Combustion Science and Technology, vol. 123, pp. 23-48, 1997.

[50] M. Emadi, D. Karkow, T. Salameh, A. Gohil, and A. Ratner, "Flame structure changes resulting from hydrogen-enrichment and pressurization for low-swirl premixed methane-air flames," international journal of hydrogen energy, vol. 37, pp. 10397-10404, 2012.

[51] M. Ilbas, A. P. Crayford, I. Yilmaz, P. J. Bowen, and N. Syred, "Laminar-burning velocities of hydrogen-air and hydrogen-methane-air mixtures: an experimental study," International Journal of Hydrogen Energy, vol. 31, pp. 1768-1779, 2006.

[52] D. M. Wicksall, A. K. Agrawal, R. W. Schefer, and J. O. Keller, "The interaction of flame and flow field in a lean premixed swirl-stabilized combustor operated on H2/CH4/air," Proceedings of the Combustion Institute, vol. 30, pp. 2875-2883, 2005.

[53] Y. Zhang, J. Wu, and S. Ishizuka, "hydrogen addition effect on laminar burning velocity, flame temperature and flame stability of a planar and a curved CH4/H2/air premixed flame," international journal of hydrogen energy, vol. 34, pp. 519-527, 2009.

[54] H. Miao, Q. Jiao, Z. Huang, and D. Jiang, "Effect of initial pressure on laminar combustion characteristics of hydrogen enriched natural gas," International Journal of Hydrogen Energy, vol. 33, pp. 3876-3885, 2008.

[55] D. Littlejohn, D. R. Noble, T. Lieuwen, and R. K. Cheng, "Laboratory investigations of low-swirl injectors operating with syngases," Journal of engineering for gas turbines and power, vol. 132, p. 011502, 2009.

[56] B. Taupin, G. Cabotaa, G. Martins, D. Vauchelles, and A. Boukhalfa, "Experimental study of stability, structure and CH— chemiluminescence in a pressurized lean premixed methane turbulent flame," Combustion science and technology, vol. 179, pp. 117-136, 2007.

[57] I. Yilmaz, "Effect of Swirl Number on Combustion Characteristics in a Natural Gas Diffusion Flame," Journal of Energy Resources Technology, vol. 135, p. 042204, 2013.

[58] A. E. E. Khalil and A. K. Gupta, "Dual Injection Distributed Combustion for Gas Turbine Application," Journal of Energy Resources Technology, vol. 136, p. 011601, 2014.

[59] J. Wan, A. Fan, K. Maruta, H. Yao, and W. Liu, "Experimental and numerical investigation on combustion characteristics of premixed hydrogen/air flame in a micro-combustor with a bluff body," international journal of hydrogen energy, vol. 37, pp. 19190-19197, 2012.

[60] E. Hu, Z. Huang, J. Zheng, Q. Li, and J. He, "Numerical study on laminar burning velocity and NO formation of premixed methane-hydrogen-air flames," International Journal of Hydrogen Energy, vol. 34, pp. 6545-6557, 2009.

[61] E. Hu, Z. Huang, J. He, and H. Miao, "Experimental and numerical study on lean premixed methane-hydrogen-air flames at elevated pressures and temperatures," International Journal of Hydrogen Energy, vol. 34, pp. 6951-6960, 2009.

[62] Z. Huang, Y. Zhang, K. Zeng, B. Liu, Q. Wang, and D. Jiang, "Measurements of laminar burning velocities for natural gas-hydrogen-air mixtures," Combustion and Flame, vol. 146, pp. 302-311, 2006.

[63] A. Rouboa, "Measurements of the Laminar Burning Velocities for Typical Syngas-Air Mixtures at Elevated Pressures," 2011.

[64] S. Gersen, N. B. Anikin, A. V. Mokhov, and H. B. Levinsky, "Ignition properties of methane/hydrogen mixtures in a rapid compression machine," International Journal of Hydrogen Energy, vol. 33, pp. 1957-1964, 2008.

[65] F. Halter, C. Chauveau, N. Djebaili-Chaumeix, and I. Gokalp, "Characterization of the effects of pressure and hydrogen concentration on laminar burning velocities of methane-hydrogen-air mixtures," Proceedings of the Combustion Institute, vol. 30, pp. 201-208, 2005.

[66] E. Hu, Z. Huang, J. He, C. Jin, and J. Zheng, "Experimental and numerical study on laminar burning characteristics of premixed methane-hydrogen-air flames," International Journal of Hydrogen Energy, vol. 34, pp. 4876-4888, 2009.

[67] R. W. Schefer, D. M. Wicksall, and A. K. Agrawal, "Combustion of hydrogen-enriched methane in a lean premixed swirl-stabilized burner," Proceedings of the Combustion Institute, vol. 29, pp. 843-851, 2002.

[68] M. Ilbas, I. Yilmaz, T. N. Veziroglu, and Y. Kaplan, "Hydrogen as burner fuel: modelling of hydrogen-hydrocarbon composite fuel combustion and NOx

formation in a small burner," International journal of energy research, vol. 29, pp. 973-990, 2005.

[69] F. Cozzi and A. Coghe, "Behavior of hydrogen-enriched non-premixed swirled natural gas flames," International Journal of Hydrogen Energy, vol. 31, pp. 669-677, 2006.

[70] O. Tuncer, S. Acharya, and J. H. Uhm, "Dynamics, NOx and flashback characteristics of confined premixed hydrogen-enriched methane flames," International Journal of Hydrogen Energy, vol. 34, pp. 496-506, 2009.

[71] R. W. Schefer, "Hydrogen enrichment for improved lean flame stability," International Journal of Hydrogen Energy, vol. 28, pp. 1131-1141, 2003.

[72] C. Park, C. Kim, Y. Choi, S. Won, and Y. Moriyoshi, "The influences of hydrogen on the performance and emission characteristics of a heavy duty natural gas engine," international journal of hydrogen energy, vol. 36, pp. 3739-3745, 2011.

[73] A. E. E. Khalil and A. K. Gupta, "Hydrogen addition effects on high intensity distributed combustion," Applied Energy, vol. 104, pp. 71-78, 2013.

[74] A. E. E. Khalil and A. K. Gupta, "Fuel flexible distributed combustion for efficient and clean gas turbine engines," Applied Energy, vol. 109, pp. 267-274, 2013.

[75] J. R. Dawson, V. M. Rodriguez-Martinez, N. Syred, and T. O'Doherty, "The effect of combustion instability on the structure of recirculation zones in confined swirling flames," in Combustion science and technology vol. 177, ed, 2005, pp. 2349-2371.

[76] A. Alves, P. T. Lacava, C. A. Martins, D. S. de Almeida, and R. Corá, "Measurements of the flow behavior and the emissions generated by low swirl injectors in a lean premixed gas turbine combustor," 2013.

[77] K. T. Kim and D. A. Santavicca, "Interference mechanisms of acoustic/convective disturbances in a swirl-stabilized lean-premixed combustor," Combustion and Flame, vol. 160, pp. 1441-1457, 2013.

[78] Y. Huang, S. Wang, and V. Yang, "Systematic analysis of lean-premixed swirl-stabilized combustion," AIAA journal, vol. 44, pp. 724-740, 2006.

[79] Y. Huang and V. Yang, "Effect of swirl on combustion dynamics in a lean-premixed swirl-stabilized combustor," Proceedings of the Combustion Institute, vol. 30, pp. 1775-1782, 2005.

[80] I. Boxx, C. M. Arndt, C. D. Carter, and W. Meier, "High-speed laser diagnostics for the study of flame dynamics in a lean premixed gas turbine model combustor," Experiments in fluids, vol. 52, pp. 555-567, 2012.

[81] J. Lee and D. Santavicca, "Experimental diagnostics for the study of combustion instabilities in lean premixed combustors," Journal of Propulsion and Power, vol. 19, pp. 735-750, 2003.

[82] M.-K. Kim, J. Yoon, S. Park, M.-C. Lee, and Y. Yoon, "Effects of unstable flame structure and recirculation zones in a swirl-stabilized dump combustor," Applied Thermal Engineering, vol. 58, pp. 125-135, 2013.

[83] J. Gounder, I. Boxx, P. Kutne, S. Wysocki, and F. Biagioli, "Phase Resolved Analysis of Flame Structure in Lean Premixed Swirl Flames of a Fuel Staged Gas

Turbine Model Combustor," Combustion science and technology, vol. 186, pp. 421-434, 2014.

[84] S. Tachibana, K. Kanai, S. Yoshida, K. Suzuki, and T. Sato, "Combined effect of spatial and temporal variations of equivalence ratio on combustion instability in a low-swirl combustor," Proceedings of the Combustion Institute, 2014.

[85] D. Davis, P. Therkelsen, D. Littlejohn, and R. Cheng, "Effects of hydrogen on the thermo-acoustics coupling mechanisms of low-swirl injector flames in a model gas turbine combustor," Proceedings of the Combustion Institute, vol. 34, pp. 3135-3143, 2013.

[86] Y. Huang and V. Yang, "Bifurcation of flame structure in a lean-premixed swirl-stabilized combustor: transition from stable to unstable flame," Combustion and Flame, vol. 136, pp. 383-389, 2004.

[87] H. Murat Altay, D. E. Hudgins, R. L. Speth, A. M. Annaswamy, and A. F. Ghoniem, "Mitigation of thermoacoustic instability utilizing steady air injection near the flame anchoring zone," Combustion and Flame, vol. 157, pp. 686-700, 2010.

[88] R. L. Speth, H. M. Altay, D. E. Hudgins, and A. F. Ghoniem, "Dynamics and stability limits of syngas combustion in a swirl-stabilized combustor," in ASME Turbo Expo 2008: Power for Land, Sea, and Air, 2008, pp. 767-776.

[89] R. L. Speth and A. F. Ghoniem, "Using a strained flame model to collapse dynamic mode data in a swirl-stabilized syngas combustor," Proceedings of the Combustion Institute, vol. 32, pp. 2993-3000, 2009.

[90] R. L. Speth, H. M. Altay, D. E. Hudgins, A. M. Annaswamy, and A. F. Ghoniem, "Vortex-driven combustion instabilities in Step and Swirl-stabilized combustors," in the 46th AIAA Aerospace Sciences Meeting, Reno, NV, 2008.

[91] S. Hong, S. J. Shanbhogue, R. L. Speth, and A. F. Ghoniem, "On the phase between pressure and heat release fluctuations for propane/hydrogen flames and its role in mode transitions," Combustion and Flame, vol. 160, pp. 2827-2842, 2013.

[92] D. G. Norton and D. G. Vlachos, "Combustion characteristics and flame stability at the microscale: a CFD study of premixed methane/air mixtures," Chemical engineering science, vol. 58, pp. 4871-4882, 2003.

[93] C. K. Westbrook and F. L. Dryer, "Simplified reaction mechanisms for the oxidation of hydrocarbon fuels in flames," Combustion science and technology, vol. 27, pp. 31-43, 1981.

[94] C. Yin, L. A. Rosendahl, and S. K. Kær, "Chemistry and radiation in oxy-fuel combustion: a computational fluid dynamics modeling study," Fuel, vol. 90, pp. 2519-2529, 2011.

[95] C. V. da Silva, H. A. Vielmo, and F. H. R. Franca, "Validation of a Numerical Simulation of the Combustion of Natural Gas In a Cylindrical Chamber. ," in 18th International Congress of Mechanical Engineering-COBEM, 2005.

[96] W. C. Reynolds, "Fundamentals of turbulence for turbulence modeling and simulation," Lecture Notes for Von Karman Institute, Agard Report No. 755, 1987.

[97] T.-H. Shih, W. W. Liou, A. Shabbir, Z. Yang, and J. Zhu, "A new k-e eddy viscosity model for high reynolds number turbulent flows," Computers & Fluids, vol. 24, pp. 227-238, 1995.

[98] M. A. Habib, R. Ben-Mansour, H. M. Badr, S. F. Ahmed, and A. F. Ghoniem, "Computational fluid dynamic simulation of oxyfuel combustion in gas-fired water tube boilers," Computers & Fluids, vol. 56, pp. 152-165.

[99] "ANSYS FLUENT 12.0 Theory Guide. April 2009."

[100] W. W. L. T.-H. Shih, A. Shabbir, Z. Yang, and J. Zhu. , " A New k-e Eddy-Viscosity Model for High Reynolds Number Turbulent Flows - Model Development and Validation. ," Computers Fluids vol. 24, pp. 227–238, 1995.

[101] V. Y. a. S. A. Orszag, " Renormalization Group Analysis of Turbulence: I. Basic Theory.," Journal of Scientific Computing, vol. 1, pp. 1-51, 1986.

[102] V. Yakhot and S. A. Orszag, "Renormalization group analysis of turbulence. I. Basic theory," Journal of scientific computing, vol. 1, pp. 3-51, 1986.

[103] L. M. Smith and S. L. Woodruff, "Renormalization-group analysis of turbulence," Annual Review of Fluid Mechanics, vol. 30, pp. 275-310, 1998.

[104] S. A. Orszag, V. Yakhot, W. S. Flannery, F. Boysan, D. Choudhury, J. Maruzewski, and B. Patel, "Renormalization group modeling and turbulence simulations," Near-wall turbulent flows, pp. 1031-1046, 1993.

[105] D. G. Norton and D. G. Vlachos, "A CFD study of propane/air microflame stability," Combustion and Flame, vol. 138, pp. 97-107, 2004.

[106] M. Bidi, R. Hosseini, and M. R. H. Nobari, "Numerical analysis of methane-air combustion considering radiation effect," Energy Conversion and Management, vol. 49, pp. 3634-3647, 2008.

[107] F. R. Centeno, C. V. da Silva, and F. H. R. Franca, "The influence of gas radiation on the thermal behavior of a 2D axisymmetric turbulent non-premixed methane-air flame," Energy Conversion and Management, vol. 79, pp. 405-414, 2014.

[108] M. A. Nemitallah and M. A. Habib, "Experimental and numerical investigations of an atmospheric diffusion oxy-combustion flame in a gas turbine model combustor," Applied Energy, vol. 111, pp. 401-415, 2013.

[109] C. Galletti, G. Coraggio, and L. Tognotti, "Numerical investigation of oxy-natural-gas combustion in a semi-industrial furnace: Validation of CFD sub-models," Fuel, vol. 109, pp. 445-460, 2013.

[110] A. Coppalle and P. Vervisch, "The total emissivities of high-temperature flames," Combustion and Flame, vol. 49, pp. 101-108, 1983.

[111] B. Magnussen, "On the structure of turbulence and a generalized eddy dissipation concept for chemical reaction in turbulent flow," 1981.

[112] I. R. Gran and B. F. Magnussen, "A numerical study of a bluff-body stabilized diffusion flame. Part 2. Influence of combustion modeling and finite-rate chemistry," Combustion Science and Technology, vol. 119, pp. 191-217, 1996.

[113] S. B. Pope, "Computationally efficient implementation of combustion chemistry using in situ adaptive tabulation," combustion Theory and modelling, vol. 1, p. 41, 1997.

[114] L.-Y. Jiang and I. Campbell, "A critical evaluation of NOx modeling in a model combustor," Journal of engineering for gas turbines and power, vol. 127, pp. 483-491, 2005.

[115] T. Ishii, C. Zhang, and S. Sugiyama, "Effects of NO Models on the Prediction of NO Formation in a Regenerative Furnace," Journal of Energy Resources Technology, vol. 122, pp. 224-228, 2000.

[116] J. M. Lobert and J. Warnatz, "Emissions from the combustion process in vegetation," Fire in the environment: The ecological, atmospheric, and climatic importance of vegetation fires, pp. 15-37, 1993.

[117] P. Gobbato, M. Masi, A. Toffolo, A. Lazzaretto, and G. Tanzini, "Calculation of the flow field and NO x emissions of a gas turbine combustor by a coarse computational fluid dynamics model," Energy, vol. 45, pp. 445-455, 2012.

[118] G. G. De Soete, "Overall reaction rates of NO and N 2 formation from fuel nitrogen," in Symposium (international) on combustion, 1975, pp. 1093-1102.

[119] S. Hubbard and A. Dowling, "Acoustic instabilities in premix burners," AIAA paper, vol. 2272, 1998.

[120] J. Y. Ren, W. Qin, F. N. Egolfopoulos, and T. T. Tsotsis, "Strain-rate effects on hydrogen-enhanced lean premixed combustion," Combustion and Flame, vol. 124, pp. 717-720, 2001.

[121] A. F. Ghoniem, A. Annaswamy, S. Park, and Z. C. Sobhani, "Stability and emissions control using air injection and H 2 addition in premixed combustion," Proceedings of the Combustion Institute, vol. 30, pp. 1765-1773, 2005.

[122] P. K. Bose and R. Banerjee, "An experimental investigation on the role of hydrogen in the emission reduction and performance trade-off studies in an existing diesel engine operating in dual fuel mode under exhaust gas recirculation," Journal of Energy Resources Technology, vol. 134, p. 012601, 2012.

[123] O. Askari, H. Metghalchi, S. K. Hannani, H. Hemmati, and R. Ebrahimi, "Lean Partially Premixed Combustion Investigation of Methane Direct-Injection Under Different Characteristic Parameters," Journal of Energy Resources Technology, vol. 136, p. 022202, 2014.

[124] V. K. Arghode and A. K. Gupta, "Hydrogen addition effects on methane-air colorless distributed combustion flames," International Journal of Hydrogen Energy, vol. 36, pp. 6292-6302, 2011.

[125] S. Nordlund and J. Kovac, "Advanced SGT6-5000F Development," in 18th Symposium of the Industrial Application of Gas Turbines Committee, Banff, Alberta, Canada, 2009.

[126] Anoon, Saudi Arabia Makes Huge Push to Expand Gas Turbine Generation Capacity. Available: http://www.powermag.com/saudi-arabia-makes-huge-push-to-expand-gas-turbine-generation-capacity/

[127] Anoon, Siemens wins $967m contract from Saudi Aramco for combined cycle power plant. Available: http://www.power-technology.com/news/newssiemens-wins-967m-contract-from-saudi-aramco-for-combined-cycle-power-plant

[128] N. Li and S. Thompson, "A simplified non-linear model of NOx emissions in a power station boiler," 1996.

[129] C. Ji, E. Dames, Y. L. Wang, H. Wang, and F. N. Egolfopoulos, "Propagation and extinction of premixed C5–C12 in alkane flames," Combustion and Flame, vol. 157, pp. 277-287, 2010.

[130] R. Sankaran and H. G. Im, "Effects of hydrogen addition on the Markstein length and flammability limit of stretched methane/air premixed flames," Combustion science and technology, vol. 178, pp. 1585-1611, 2006.

[131] A. F. Ghoniem, S. Park, A. Wachsman, A. Annaswamy, D. Wee, and H. M. Altay, "Mechanism of combustion dynamics in a backward-facing step stabilized premixed flame," Proceedings of the Combustion Institute, vol. 30, pp. 1783-1790, 2005.

[132] Y. Hardalupas, C. Panoutsos, and A. Taylor, "Spatial resolution of a chemiluminescence sensor for local heat-release rate and equivalence ratio measurements in a model gas turbine combustor," Experiments in fluids, vol. 49, pp. 883-909, 2010.

[133] P. Langhorne, "Reheat buzz: an acoustically coupled combustion instability. Part 1. Experiment," Journal of Fluid Mechanics, vol. 193, pp. 417-443, 1988.

[134] R. J. Kee, J. A. Miller, G. H. Evans, and G. Dixon-Lewis, "A computational model of the structure and extinction of strained, opposed flow, premixed methane-air flames," in Symposium (International) on Combustion, 1989, pp. 1479-1494.

[135] C. Vagelopoulos and F. Egolfopoulos, "Laminar flame speeds and extinction strain rates of mixtures of carbon monoxide with hydrogen, methane, and air," in Symposium (International) on Combustion, 1994, pp. 1317-1323.

[136] E. R. Hawkes and J. H. Chen, "Direct numerical simulation of hydrogen-enriched lean premixed methane–air flames," Combustion and Flame, vol. 138, pp. 242-258, 2004.

[137] L. Crocco, "Research on combustion instability in liquid propellant rockets," in Symposium (International) on Combustion, 1969, pp. 85-99.

[138] D. Garréton and O. Simonin, "Aerodynamics of steady state combustion chambers and furnaces. ," presented at the ASCF Ercoftac CFD Workshop, EDF,Chatou, France, 1994.

[139] A. O. Nieckele, Naccache, M.F., Gomes, M.S.P.,Carneiro, J.E. and Serfaty, R, "Evaluation of models for combustion processes in a cylindrical furnace," 2001.

[140] Y. S. Sanusi, Mokheimer, E.M.A.,Habib, M.A., "Effect of swirl on combustion and emission dynamics of methane-air in a cylindrical furnace " presented at the 4th SAS-Combustion Institute Annual meeting, KAUST Thuwal KSA, 2014.

[141] L. Selle, G. Lartigue, T. Poinsot, R. Koch, K.-U. Schildmacher, W. Krebs, B. Prade, P. Kaufmann, and D. Veynante, "Compressible large eddy simulation of turbulent combustion in complex geometry on unstructured meshes," Combustion and Flame, vol. 137, pp. 489-505, 2004.

[142] A. De and S. Acharya, "Dynamics of upstream flame propagation in a hydrogen-enriched premixed flame," International Journal of Hydrogen Energy, vol. 37, pp. 17294-17309, 2012.

[143] G. Boudier, "Methane/air flame with 2-step chemistry: 2S-CH4-CM2," CERFACS technical report2007.

[144] N. Marinov, C. Wcstbrook, and W. Pitz, "Detailed and global chemical kinetics model for hydrogen," Transport phenomena in combustion, vol. 1, p. 118, 1996.

[145] A. De and S. Acharya, "Parametric study of upstream flame propagation in hydrogen-enriched premixed combustion: Effects of swirl, geometry and premixedness," International Journal of Hydrogen Energy, vol. 37, pp. 14649-14668, 2012.

[146] A. Giauque, L. SELLE, L. Gicquel, T. Poinsot, H. Buechner, P. Kaufmann, and W. Krebs, "System identification of a large-scale swirled partially premixed combustor using LES and measurements," Journal of Turbulence, 2005.

[147] S. V. Patankar and D. B. Spalding, "A calculation procedure for heat, mass and momentum transfer in three-dimensional parabolic flows," International Journal of Heat and Mass Transfer, vol. 15, pp. 1787-1806, 1972.

[148] A. H. Al-Abbas and J. Naser, "Numerical study of one air-fired and two oxy-fuel combustion cases of propane in a 100 kW furnace," Energy & Fuels, vol. 26, pp. 952-967, 2012.

[149] J. Bibrzycki and T. Poinsot, "Reduced chemical kinetic mechanisms for methane combustion in O2/N2 and O2/CO2 atmosphere," Working note ECCOMET WN/CFD/10, vol. 17, 2010.

[150] J. Hua, M. Wu, and K. Kumar, "Numerical simulation of the combustion of hydrogen–air mixture in micro-scaled chambers. Part I: Fundamental study," Chemical engineering science, vol. 60, pp. 3497-3506, 2005.

[151] M. A. Habib, M. Elshafei, and M. Dajani, "Influence of combustion parameters on NOx production in an industrial boiler," Computers and Fluids, vol. 37, pp. 12-23, 2008.

[152] S. Z. Shuja and M. A. Habib, "Fluid flow and heat transfer characteristics in axisymmetric annular diffusers," Computers and Fluids, vol. 25, pp. 133-150, 1996.

CURRICULUM VITAE

Personal

Name: SANUSI, Yinka Sofihullahi

Date: 16th December, 1979

Nationality: Nigerian

Gender /Marital Status: Male /Married

Current Contact Address: Dept. of Mechanical Engineering.
Ahmadu Bello University,
Zaria, Nigeria.

Contact #: +966501914095

Email address: sanusi@kfupm.edu.sa, yinkasan@yahoo.com

Education

PhD Mechanical Engineering

King Fahd University of Petroleum and minerals, Dhahran, Saudi Arabia. May 2015

M.Sc Mechanical Engineering

Ahmadu Bello University, Zaria, Nigeria 2010

B.ENG. Mechanical Engineering

University of Ilorin. Nigeria 2003

PhD Scholar

Reaction gas dynamics Laboratory

Massachusetts Institute of Technology (MIT)

Cambridge, MA. USA **(Summer & Fall Semesters)** 2014

Professional service/ Honor Societies

Member, Council of Registration of Engineering in Nigeria (COREN) R 19,364

Corporate Member Nigerian society of Engineers.